Application of a perforated shadow band to the decomposition of global solar irradiance

by
Michael John Brooks

Dissertation presented for the degree of
Doctor of Philosophy in the Faculty of Engineering
at Stellenbosch University

Promoter: Prof. Theodor W. von Backström
Co-promoter: Prof. E. Ernest van Dyk

December 2015

DECLARATION

By submitting this thesis electronically, I declare that the entirety of the work contained therein is my own, original work, that I am the sole author thereof (save to the extent explicitly otherwise stated), that reproduction and publication thereof by Stellenbosch University will not infringe any third party rights and that I have not previously in its entirety or in part submitted it for obtaining any qualification.

December 2015

ABSTRACT

The earth’s atmosphere causes pronounced spatial and temporal variability in downwelling solar radiation at the planet’s surface. Since the characterisation of sun strength is important in solar resource assessment studies, and in the Earth sciences generally, more effective methods are sought to measure irradiance at ground stations. The general drive is towards greater spatial coverage, reduced instrument uncertainty, lower costs and higher temporal data resolution.

This study investigates a new method of measuring the principle components of solar irradiance at 1-minute intervals using a single pyranometer and a novel shading structure. The perforated shadow band decomposes global horizontal irradiance (GHI) to obtain the diffuse horizontal and direct normal irradiance components (DHI and DNI). The design of the band and its positioning relative to the thermopile sensor of a radiometer are described. A ray trace-derived model of pyranometer exposure is presented as a function of the local hour angle.

In operation, the band produces a composite output trace incorporating both global and diffuse fragments that require separation and reconstitution as independent time-series. DNI values can then be calculated from these components. Gaps between data fragments must be filled using appropriate interpolation techniques to lower statistical uncertainty. The structure of the trace is dependent on atmospheric turbidity and the nature of the prevailing cloud field.

A test programme was run at the US National Renewable Energy Laboratory in Colorado to establish performance of the system relative to collocated reference instruments. The band functioned most effectively under clear sky conditions, where it produced GHI, DHI and DNI measurements with root mean square differences of 2.7%, 13.6% and 2.0% respectively. Mean bias differences were 0.1% for GHI, 7.9% for DHI and –0.3% for DNI.

The presence of cloud introduces stochasticity to the perforated band output trace. In such a case the ray trace model of pyranometer exposure can be used to identify and separate GHI and DHI data. Uncertainties rise for GHI and DNI under partly cloudy conditions. As the inaugural study on perforated band performance, this work tested several approaches to filling measurement gaps, including numerical interpolation and data replacement by radiometric decomposition models. A key finding of the study is that uncertainties may be lowered by interpolating adaptively according to the prevailing clearness index. Tests run at a southern hemisphere ground station suggest that the system’s performance is not location-dependent.

It may be concluded that the perforated shadow band system is most effective in sunny regions where the average daily clearness index remains above approximately 0.7. This would include large parts of continental Africa in the south-western and northern desert areas. The best potential for deploying the band is in existing sub-optimal measurement schemes utilising a single pyranometer, where it would enable the direct measurement of two radiometric components rather than one.

OPSOMMING

Die aarde se atmosfeer veroorsaak beduidende ruimtelike en tydafhanklike veranderlikheid in afwellende sonstraling op die planeet se oppervlakte. Aangesien die karakterisering van sonsterkte belangrik is in hulpbronbeoordelingstudies, en in die aardwetenskappe in die algemeen, is doeltreffender metodes in aanvraag om bestraling by grondstasies te meet. Die algemene stukrag is in die rigting van groter ruimtelike dekking, verminderde instrument-onsekerheid, laer koste en hoër data-resolusie met tyd.

Hierdie studie ondersoek ’n nuwe metode om die hoofkomponente van sonbestraling teen 1-minuut intervalle te meet deur ’n enkele piranometer en ’n nuutgeskepte skadubandstruktuur te gebruik. Die geperforeerde skaduband breek die globale horisontale bestraling (GHB) op om die diffuse horisontale en direkte normale bestralingskomponente (DHB en DNB) te verkry. Die ontwerp van die band en sy plasing relatief tot die termostapelsensor van ’n radiometer word beskryf. ’n Straalnavolgmodel van piranometerblootstelling word voorgestel as ’n funksie van die plaaslike uurhoek.

In bedryf lewer die band ’n saamgestelde uitsetverloop wat beide globale en diffuse breukdele inkorporeer, wat skeiding en hersamestelling as onafhanklike tydreeks vereis. DNB-waardes kan dan uit hierdie komponente bereken word. Gapings tussen die data-breukdele moet gevul word deur geskikte interpolasietegnieke te gebruik om statistiese onsekerheid te verminder. Die struktuur van die verloop hang af van atmosferiese turbiditeit en die aard van die heersende wolkveld.

’n Toetsprogram is by die US National Renewable Energy Laboratory in Colorado bedryf om die vertoning van die stelsel te bevestig relatief tot aanliggende verwysings-instrumente. Die band het die doeltreffendste gewerk onder skoon lugtoestande, waar dit GHB-, DHB- en DNB-metings gelewer het met wortelgemiddelde kwadraat afwykings van 2.7%, 13.6% en 2.0% onderskeidelik. Gemiddelde afwykingsneigings was 0.1% vir GHB, 7.9% vir DHB en –0.3% vir DNB.

Die teenwoordigheid van wolke bring wisselvalligheid in die geperforeerde band se uitsetverloop mee. In so ’n geval kan die straalvolgmodel van piranometerblootstelling gebruik word om die afsonderlike GHB- en DHB-data te identifiseer en te skei. Onsekerhede in GHB en DNB ontstaan onder gedeeltelik-bewolkte toestande. Synde die inleidende studie oor geperforeerde bandvertoning, toets hierdie werk verskeie benaderings vir die invul van meetgapings, insluitende numeriese interpolasie en datavervanging deur radiometriese dekomposisie-modelle. ’n Sleutelbevinding van die studie is dat onsekerhede verminder kan word deur aanpasbaar te interpoleer volgens die heersende helderheids-indeks. Toetse gedoen by die suidelike halfrond-grondstasie doen aan die hand dat die stelsel se gedrag nie afhanklik is van die ligging nie.

Die gevolgtrekking kan gemaak word dat die geperforeerde-skaduband stelsel die effektiefste werk in sonnige streke waar die daaglikse helderheidsindeks bo

ongeveer 0.7 bly. Dit sluit groot dele van kontinentale Afrika in die suidwestelike en noordelike woestynareas in. Die beste potensiaal vir die ontplooiing van die skaduband is in bestaande sub-optimale meetstelsels wat ‘n enkele piranometer gebruik, waar dit die direkte meting van twee radiometriese komponente moontlik maak, eerder as een.

To my parents …

... et in honore Maria, Regina caeli, qui nos deducit ad Christum.

ACKNOWLEDGEMENTS

My sincere thanks to the following:

- My supervisors, Professor Theo von Backström and Professor Ernest van Dyk, for their sage wisdom, encouragement and patience. Your guidance is deeply appreciated.
- The United States National Renewable Energy Laboratory in Golden, Colorado, for supporting the perforated band test programme. I am especially grateful to Tom Stoffel, Steve Wilcox, Afshin Andreas, Ibrahim Reda, Peter Gotseff, Dr Manajit Sengupta, Bev Kay and the staff at the NREL Solar Radiation Research Laboratory for maintaining the test equipment. Above all, I am indebted to Senior Scientist Daryl Myers, now retired, who hosted me during visits to NREL, offered advice and generously shared his encyclopedic knowledge of radiometry whenever I asked. Thank you, Daryl - it has been a privilege working with you.
- Professors Glen Bright and Lance Roberts at the University of KwaZulu-Natal for supporting this research and providing me with time to pursue it. Thanks also to the Mechanical Engineering workshop staff, to my colleagues Jean Pitot, Jared Padayachee, Louw Butler and Shaniel Davrajh for lightening my workload, and to my students who assisted with the UKZN ground station and datasets, including Sven du Clou, Khulisile Kunene and Kai Broughton.
- Professor Wikus van Niekerk of the Centre for Renewable and Sustainable Energy Studies at Stellenbosch University for his support, and fellow members of the Solar Thermal Energy Research Group.
- Dr Tomas Cebecauer and Dr Marcel Suri of GeoModel Solar for providing satellite-derived clearness index data for continental Africa.
- Dr Anette Mienie and Professor Ewa Zawilska at Mangosuthu University of Technology, where the first perforated band prototypes were tested. My thanks also to Mary Watkins and the Florida Solar Energy Center (FSEC) for their assistance.
- The National Research Foundation’s Thuthuka and THRIP programmes, and the Eskom Tertiary Education Support Programme (TESP) for funding this research.

Last but not least, thank you to my family and friends for patiently walking this long journey with me and for administering the humour that made it possible to continue.

TABLE OF CONTENTS

LIST OF FIGURES

LIST OF TABLES

NOMENCLATURE

Symbol	Description	Unit
AST	apparent solar time	hours
D	order of ARIMA differencing process	-
E	broadband solar irradiance	W/m^2
E_o	global horizontal top of atmosphere irradiance	W/m^2
E_{on}	direct normal top of atmosphere irradiance	W/m^2
E_s	exposure state	-
f_w	weighting factor for ARIMA interpolation	-
G	data gap	-
IR	infrared irradiance	W/m^2
K_{T_day}	clearness index over daily period	-
K_{T_hour}	clearness index over 1-hour period	-
k	diffuse fraction	-
k_T	clearness index over 1-minute period	-
k_{T_patch}	clearness index over perforated band patch	-
L	length	m
N	number of data	-
N_s	number of data rows in spread sheet file	-
n	day number; number of polynomial terms	-
P	data patch	-
p	order of ARIMA autoregressive process	-
q	order of ARIMA moving average process	-
R^2	coefficient of determination	-
R_b	band radius	m

Rs	sensor responsivity	μV/W/m^2
t_z	zonal exposure time	minutes
W	width	m
w	ARIMA series value transformed by differencing	-
Z	zenith angle	degrees
z	ARIMA moving average series value	-
α	solar altitude angle	degrees
γ	azimuth angle	degrees
Δl	band displacement	m
δ	declination angle	degrees
φ	latitude [degrees]; persistence factor [-]; autoregressive coefficient [-]	
ψ	persistence factor	-
ω	hour angle	degrees

Subscript	**Description**
a	aperture
$Bird$	Bird and Hulstrom model
bn	direct normal irradiance from reference radiometer
d	diffuse irradiance, calculated or from reference radiometer
f	output from the perforated band
fbn	perforated band direct normal irradiance
fd	perforated band diffuse horizontal irradiance

fg	perforated band global horizontal irradiance
ft	perforated band transition
G	data gap
g	global irradiance from reference radiometer
i	index
int	interpolated
j	index
k	index
L	left data patch
$meas$	measured data
mfr	manufacturer
mod	modelled data
P	data patch
R	right data patch
ref	reference
s	spread sheet or sun
sb	shading band
t	time

Superscript	**Description**
D	order of ARIMA differencing process

ACRONYMS

AMSL	above mean sea level
ABS	absolute

ACF	autocorrelation function
ACR	absolute cavity radiometer
AIS	adaptive interpolation scheme
AR	autoregressive
ARIMA	autoregressive integrated moving average
A001	ARIMA(0,0,1) interpolation scheme
A011	ARIMA(0,1,1) interpolation scheme
A100	ARIMA(1,0,0) interpolation scheme
A101	ARIMA(1,0,1) interpolation scheme
A111	ARIMA(1,1,1) interpolation scheme
B_AIS	adaptive interpolation scheme for DNI
BORCAL	Broadband Outdoor Radiometer Calibration
BMS	Baseline Measurement System
BRB	Boland Ridley and Brown decomposition model
BRL	Boland Ridley and Lauret decomposition model
BSRN	Baseline Surface Radiation Network
CAM	cumulative analysis matrix
CdSPM	cloudy sky processing methodology
CrSPM	clear sky processing methodology
CSP	concentrating solar power
D_AIS	adaptive interpolation scheme for DHI
DHI	diffuse horizontal irradiance
DM	decomposition model
DNI	direct normal irradiance
DPM	data processing methodology

G_AIS	adaptive interpolation scheme for GHI
GeD	global equals diffuse model
GHI	global horizontal irradiance
HC	Howard College
MA	moving average
MBD	mean bias difference
MST	mountain standard time
NASA	National Aeronautics and Space Administration
NIP	normal incidence pyrheliometer
NREL	National Renewable Energy Laboratory
O&H	Orgill and Hollands decomposition model
PACF	partial autocorrelation function
PB	perforated band
PCHIP	piecewise cubic Hermite interpolating polynomial
PIR	precision infrared pyrgeometer
PSP	precision spectral pyranometer
PV	photovoltaic
RE	renewable energy
RMSD	root mean square difference
RSR	Rotating Shadowband Radiometer
RSS	root sum of squares
RTME	ray trace model of pyranometer exposure
SAWS	South African Weather Service
SBS	shadow band stand
SD	standard deviation

SPA	Solar Position Algorithm
SRRL	Solar Radiation Research Laboratory
TOA	top of atmosphere
UKZN	University of KwaZulu-Natal
U_{95}	expanded uncertainty
3OP	3rd order polynomial
4OP	4th order polynomial
5OP	5th order polynomial

1. INTRODUCTION

1.1 Background

Solar radiation is an abundant source of energy that drives the earth's climate, fuels photosynthesis, supports life in its myriad forms and offers humanity a sustainable alternative to conventional power sources. Apart from its abundance, there is also considerable spatial and temporal variability to the resource that defies simple characterisation. The acquisition and analysis of sun strength data is therefore crucial to understanding the role of solar energy in our environment and to deploying solar technologies on a wider scale.

This dissertation proposes and evaluates a novel instrumentation system for characterising the components of broadband solar irradiance. The system comprises a perforated shadow band operated in conjunction with a thermopile pyranometer and data logger. Under certain conditions, the perforated shadow band (PB) enables the extraction of greater amounts of data from a single thermopile pyranometer than is possible with a conventional solid band or an unshaded instrument. It is aimed at improving the coverage of solar measurement networks by reducing the cost of instrumentation and lowering the measurement uncertainty of data generated by existing radiometers of the pyranometric type.

This chapter describes the fundamentals of solar radiation and the rationale for its measurement. The components of sun strength are addressed, including the instrumentation commonly used to characterise the resource. A brief history of solar radiometry in South Africa is provided to contextualise the present study. Having considered existing radiometric methods, the perforated shadow band is proposed as an alternate approach and the outline of the dissertation is then described, including the technical aims of the research.

1.2 Solar radiation and the earth's climate

Solar radiation is the primary driver of the earth's climate, accounting for more than 99.9% of the energy input to the atmosphere (Kandel and Viollier, 2010).

Since measurements began, the average shortwave solar flux at top-of-atmosphere (TOA), referred to as the solar constant, has been estimated and revised many times. Duffie and Beckman (1991) recommended a value of 1367 W/m^2, while Gueymard (2004) confirmed a slightly lower value of 1366.1 W/m^2 using a revised dataset. More recently, this value was lowered again to 1360.8 ± 0.5 W/m^2 by Kopp and Lean (2011). Aside from the seasonal variation due to the earth's eccentric orbit, the solar constant, or total solar irradiance, is highly stable and changes by only about 0.1% within the Sun's 11-year activity cycle (Frohlich and Lean, 2004).

When averaged over the surface area of the earth, the annual solar constant is approximately 341 W/m^2. The planet's annual mean energy budget can be derived from this input value, as illustrated by Trenberth et al. (2009) in Figure 1.1. The irradiance values in the graphic are annualised averages; in practice the measured solar irradiance at a given location on the earth's surface may exceed 1000 W/m^2, depending on sky conditions.

Of the shortwave solar energy intercepted by the earth each year, approximately 30% is reflected back into space by clouds, atmospheric particulates and the planet's surface, while 47% is absorbed by the surface. The remainder is absorbed by the atmosphere which stores energy and exchanges it convectively and by radiation with the ground. Approximately 70% of the input energy is returned to space as longwave radiation.

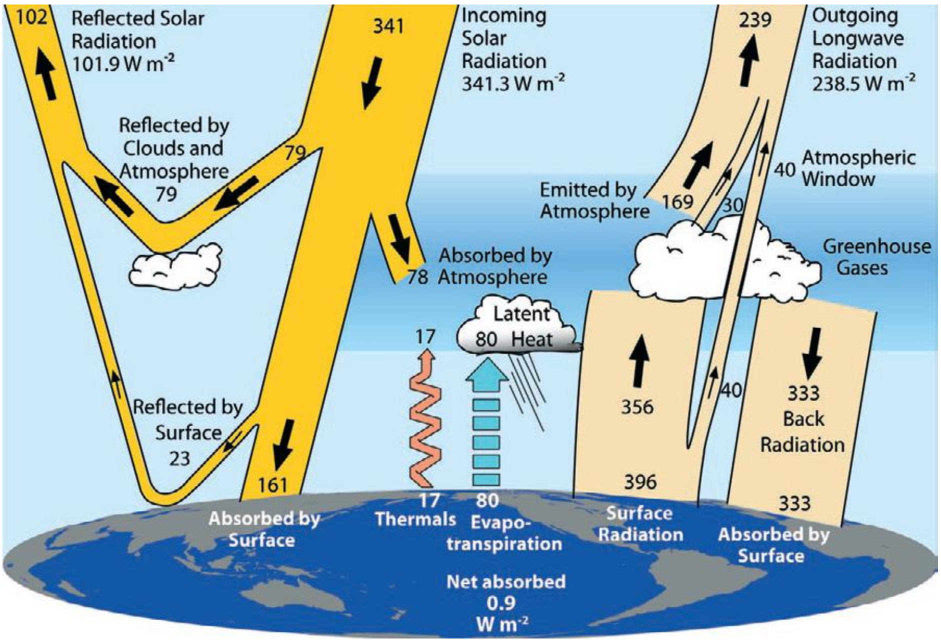

Figure 1.1: Estimation of the global annual mean energy budget of the earth between March 2000 and May 2004 (Trenberth et al., 2009).

Solar radiation thus fuels a complex set of energy exchanges between the ground, the atmosphere and space that drive weather systems and affect most aspects of human, plant and animal life. The study of sun strength by satellite-based instruments and ground-based stations has become an essential tool in understanding the earth's climate.

1.3 Solar radiation as energy source

The world's total energy demand is predicted to grow by 36% between 2013 and 2030 (British Petroleum, 2013). This trend, together with concerns over fossil-fuel consumption, is driving the acceptance of sustainable power sources and lowering their costs. As a result, the contribution by renewable energy (RE) to global consumption is expected to rise from 13% in 2011 to as much as 26% by 2035 (International Energy Agency, 2013). Although biomass, hydropower and wind will remain the dominant RE sources of electricity, solar photovoltaic (PV) and concentrating solar power (CSP) are predicted to grow substantially from their present levels (de Castro et al., 2013; Matsuo et al., 2013; Viebahn et al., 2011).

Solar radiation can be harnessed in several ways, the most common being direct electricity generation by PV panels, conversion of thermal energy to electricity by concentrating systems such as central receiver and parabolic trough plants (Figure 1.2), and the capture of thermal energy for heating.

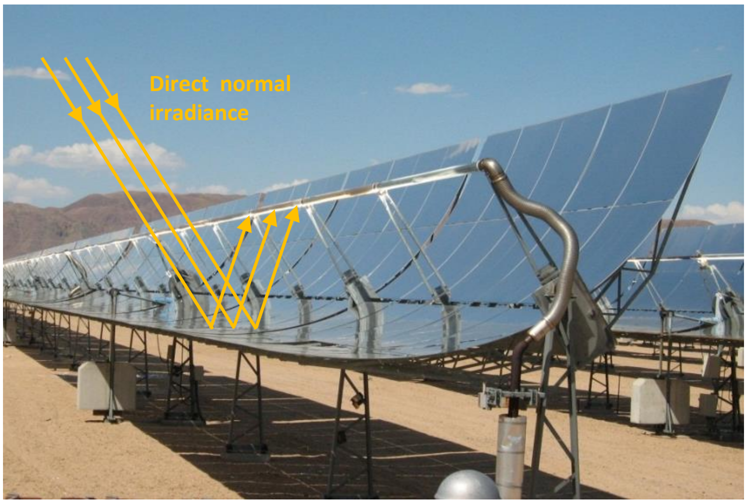

Figure 1.2: Parabolic trough receiver at the Solar Electric Generating System (SEGS) I plant in Daggett, California.

The rate at which CSP systems are being constructed has accelerated globally. At the beginning of 2014 there was 4 GW of operational capacity in parabolic trough, central receiver, compound linear Fresnel and parabolic dish systems, mostly for electricity generation. A further 11 GW has been announced or is now in the planning and construction phases (CSP Today, 2015). Matsuo et al. (2013) estimate the installed capacity of PV to rise from 38.9 GW in 2010 to 525.1 GW by 2035.

South Africa is ideally positioned to exploit solar energy because of its strong resource. Five of the nine provinces receive irradiance levels deemed sufficient to implement CSP projects (Fluri, 2009) and the Northern Cape has among the best resources of any region on Earth.

South Africa’s long-term policy on solar energy is articulated through the Integrated Resource Plan for Electricity (Department of Energy, 2013) which commits the country to installing 17.8 GW of RE-based electricity generating capacity by 2030. Of this, 8.4 GW is dedicated to PV and 1.0 GW to CSP. The implementation is effected through the Renewable Energy Independent Power Producers Procurement Programme (REIPPP), which had allocated 200 MW of CSP capacity and 1048 MW of PV to commercial developers by January 2014 (Giglmayr et al., 2014).

It is not possible to accelerate the roll-out of CSP and PV technologies without an extensive radiometric capacity, including satellite and ground-based measurements. Stoffel et al. (2010) consider solar data as integral to three phases of a CSP project: correct site selection, prediction of the long-term annual output, and development of short-term performance and operating strategies. Optimisation of the mechanical and optical design of solar energy equipment necessarily also requires an understanding of the solar resource. In addition, the financing or ‘bankability’ of solar projects is based on accurate projections of sun strength at a given site (Leloux et al., 2014; Myers, 2010b). In South Africa, the importance of radiometry is illustrated by the growth of commercial enterprises such as CSAfrica and GeoSun Africa (Pty) Ltd that supply stations and monitoring services to clients in the CSP and PV industries.

1.4 The measurement of sun strength

1.4.1 Attenuation and the solar spectrum

As sunlight passes through the atmosphere it is attenuated by water vapour, airborne particles and gases, reducing the flux at the earth’s surface. Even on a cloud-free day, more than 20% of the TOA irradiance may be lost to absorption and scattering. Attenuation forms the basis of numerous transmittance models of clear-sky irradiance, including the REST2 model of Gueymard (2008), given in equation (1.1). The direct normal irradiance at the earth’s surface, E_{bn}, may be obtained by applying band transmittance scaling factors (τ) to the TOA irradiance, E_{on}.

$$E_{bn} = E_{on}\tau_{Ri}\tau_{gi}\tau_{oi}\tau_{ni}\tau_{wi}\tau_{ai} \tag{1.1}$$

The factors in equation (1.1) are for Rayleigh scattering (τ_{Ri}), extinction by mixed gases (τ_{gi}), ozone absorption (τ_{oi}), nitrogen dioxide absorption (τ_{ni}), water vapour absorption (τ_{wi}) and aerosol extinction (τ_{ai}). The transmittances are obtained empirically. The REST2 model has low uncertainties that are comparable to the best radiometers, however it requires accurate input data from a sun photometer which makes it impractical as a general means of measuring sun strength.

At Earth’s surface the sun’s energy is distributed across a range of wavelengths indicated by the blue trace in Figure 1.3. The ordinate represents the flux in W/m^2/nm and has been normalised for readability. The ultraviolet band includes UVA (shaded blue) and UVB (yellow) up to a wavelength of about 380 nm. The infrared band (shaded cream) exceeds 780 nm, and the visible spectrum occurs between 380 and 780 nm (Duffie and Beckman, 1991). The black line centred on

555 nm represents the human eye's spectral ('photopic') response. The typical responses of thermopile (red) and photovoltaic (green) sensors are shown.

The spectral nature of sunlight is of interest in different fields. For example, the ultraviolet spectrum is important to oncology because of its role in the development of skin cancers (de Gruijl, 1999; Medhaug et al., 2009; Utrillas et al., 2013). Photosynthetically active radiation (PAR), which occurs within the visible band is of interest to biologists and the agricultural sector because of its effect on plant growth and crop yields (Alados and Alados-Arboledas, 1999; Oliphant et al., 2006; Parisi et al., 1998). In most thermal engineering applications, the spectral nature of sun strength is less important than its broadband energy content.

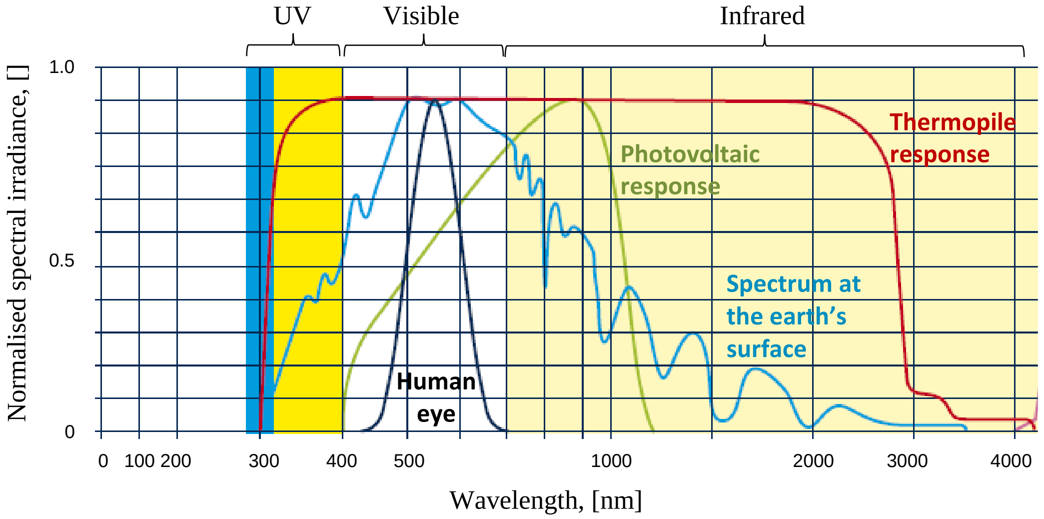

Figure 1.3: Normalised solar energy spectrum at the earth's surface (adapted from Kipp & Zonen (2014)).

1.4.2 Broadband solar radiometry

Radiometry is the acquisition and analysis of sun strength data. As an important field of study it serves the needs of many sectors, including agriculture, physics, environmental science, solar energy engineering, the medical sciences and biology. In order to advance, radiometry needs efficient, accurate and widespread methods of data collection together with effective analytical tools to make sense of the information.

Unlike spectroradiometry that characterises light as a function of wavelength, broadband radiometry aims to measure sun intensity for the full spectrum from 300 to 3000 nm. Irradiance is measured in watts per square metre, while radiation is the time integrated equivalent, measured in joules per square metre.

The sensors used to detect solar irradiance must be capable of responding to the wavelengths present in the spectrum. In the case of sunlight, thermopile detectors composed of a mat of temperature thermocouples, cover the full wavelength range (red line in Figure 1.3) and are commonly used, although they are more expensive than photodiode-based sensors that are similar to photovoltaic cells. Photodiodes have a limited spectral response shown by the green line in Figure 1.3, and their output must be corrected, particularly with respect to diffuse irradiance measured under clear sky conditions (Alados-Arboledas et al., 1995).

Broadband irradiance is highly variable with respect to both space and time. Stoffel et al. (2010) suggest that variability represents the single greatest uncertainty in the forecast output of CSP power plants. Temporal variability at a site is driven mainly by the dynamic nature of cloud fields and results in stochasticity in the output data trace of measurement instruments. There is also the problem of interannual variability in which the resource changes from year to year. This is most pronounced for direct normal irradiance (DNI) and necessitates the installation of ground measurement stations during the early planning stages of solar energy projects so that performance models can be refined and financing secured (Gueymard, 2012).

Gueymard and Wilcox (2011) note that a minimum of 30 years of measurements is necessary to understand precisely the resource at a location. This is illustrated in Figure 1.4 which shows the convergence of annual DNI, global horizontal irradiance (GHI) and global tilt irradiance (GTI) averages towards the long-term average at the National Renewable Energy Laboratory (NREL) in Golden, Colorado. Similar trends are given by Pitz-Paal and Hoyer-Klick (2010).

The spatial variability of solar radiation is a function of topography, climate and differences in ground reflectivity, or albedo. The lack of ground measurement stations has led to gaps in geographic coverage and spurred the development of interpolation techniques for solar data (Bosch et al., 2010; Glasbey et al., 2001; Miller et al., 2008; Rehman and Ghori, 2000).

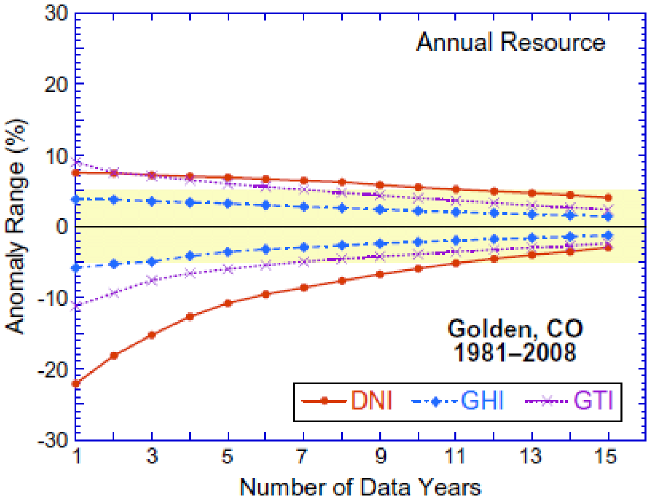

Figure 1.4: Interannual variability of the solar resource at Golden, Colorado, between 1981 and 2008 (Gueymard and Wilcox, 2011).

1.4.3 The components of sun strength and their measurement

The solar energy incident on a surface within the earth's atmosphere per unit time, correctly termed 'irradiance', is composed of several parts. These include direct normal irradiance emanating from the solar disc, diffuse circumsolar irradiance from the disc's aureole, diffuse isotropic irradiance from the sky, atmospheric particulates and translucent clouds, diffuse irradiance reflected off clouds and nearby objects, and a horizon brightening component.

In the case of the exposed horizontal surface of a stationary measurement sensor, irradiance can be grouped into two categories: diffuse irradiance and a component of the DNI which may be absent when the sun is obscured by cloud. The relationship between the components measured in the horizontal plane is commonly given as:

$$E_g = E_{bn}\cos Z + E_d \qquad (1.2)$$

where E_g is the global horizontal irradiance (sometimes called total hemispherical irradiance), E_{bn} is the direct normal irradiance, Z is the solar zenith angle and E_d is the sum of all diffuse horizontal irradiance components. The product $E_{bn}\cos Z$ is the direct horizontal irradiance, that is, the vertical component of direct normal irradiance. Figure 1.5 illustrates the difference between the three solar components, and how they are measured.

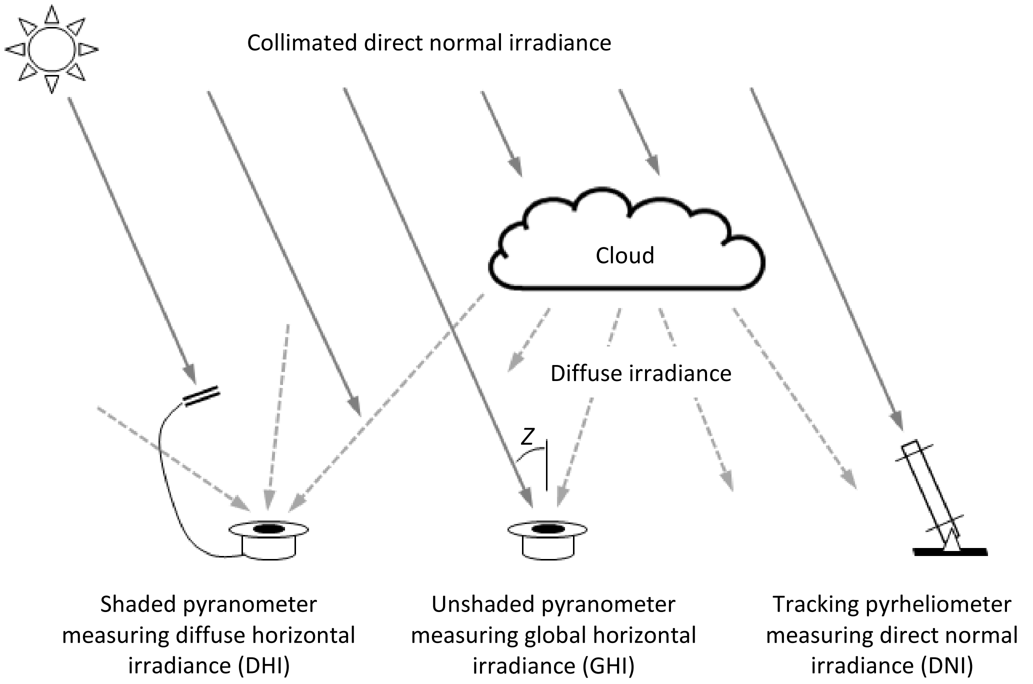

Figure 1.5: The direct normal, global horizontal and diffuse horizontal components of solar irradiance and their measurement.

Broadband sun strength is fully described when the DNI, GHI and DHI components are known contemporaneously. Since they are related through the closure equation (1.2) it is only necessary to measure two components in order to determine the third, although many ground stations measure all three independently to provide redundancy and enable cross-checking of the sensors.

Irradiance is measured with a radiometer that generates a voltage proportional to the solar flux. This is converted to a measurement in watts per square metre by applying a shortwave responsivity factor, determined when the sensor is calibrated.

Radiometers are classified according to the ISO 9060 standard as secondary standard, first class or second class instruments (Table 1.1). Secondary standard sensors are of the best quality and are generally employed for specific research-grade climatological and radiometric measurements, while first and second class instruments are more commonly used in applications such as meteorological networks, equipment testing and agricultural monitoring systems. Often, the choice of sensor is dictated by cost. Surprisingly, ISO 9060 does not classify sensors according to their measurement uncertainty, thus a first class instrument may, under specific conditions, provide more accurate data than a secondary standard sensor.

Table 1.1: Specifications of radiometers according to the ISO 9060 standard (Ammonit, 2014).

ISO 9060 Radiometer Specifications	Secondary Standard	First Class	Second Class
Response time: time to reach 95% response	< 15s	< 30s	< 60s
Zero offset-A: response to 200 W/m² net thermal radiation, ventilated	+ 7 W/m²	+ 7 W/m²	+ 7 W/m²
Zero offset-B: response to 5 K/h change in ambient temperature	± 2 W/m²	± 2 W/m²	± 2 W/m²
Non-stability: % change in responsivity per year	± 0.8%	± 1.5%	± 3%
Non-linearity: % deviation from responsivity at 500 W/m² in range from 100 to 1000 W/m²	± 0.5%	± 1%	± 3%
Directional response (for beam irradiance): the range of errors for a beam of 1000 W/m²	± 10 W/m²	± 20 W/m²	± 20 W/m²
Spectral selectivity: % deviation of the product of spectral absorbance and transmittance from the corresponding mean, from 0.35 to 1.5 μm	± 3%	± 5%	± 10%
Temperature response: % deviation due to change in ambient within an interval of 50K	2%	4%	8%
Tilt response: % deviation in responsivity relative to 0 to 90° tilt at 1000 W/m² beam irradiance	± 0.5%	± 2%	± 5%

The most common types of radiometer are the pyranometer, which measures total hemispherical irradiance in a 180° solid angle field of view, and the pyrheliometer which is typically mounted on a tracker and measures collimated irradiance emanating from the solar disc (Figure 1.6).

Pyranometers are commonly fitted with either a thermoelectric (thermopile) or photodiode detector (Myers, 2013). The thermopile sensor of the Eppley Precision Spectral Pyranometer (PSP) used with the perforated shadow band in this study consists of multiple thermocouple junctions housed beneath a set of glass domes (Figures 1.6 (a) and (b)). The domes filter incoming light to the wavelength range of interest, namely 285 nm to 2800 nm. This coincides with the red line in Figure 1.3 indicating the thermopile sensor's response to visible light. The PSP is ubiquitous in broadband radiometry with over 10 000 having been produced (Kirk, 2013). It is classified as a first class radiometer, while the Kipp & Zonen CMP 11 and 22 models are defined as secondary standard sensors.

Photodiodes make use of photovoltaic sensors and offer certain advantages over the thermopile. They are less expensive, smaller in size and they offer much shorter response times (King et al., 1998). Disadvantages include spectral and temperature-related dependencies that cause variation in the output signal under different cloud conditions. These can be corrected (Alados-Arboledas et al., 1995) but photodiode detectors do not comply with the ISO 9060 or WMO standards and are generally not used in research-grade solar radiometric installations. Their spectral response is indicated by the green line in Figure 1.3.

Duffie and Beckman (1991), Myers (2013) and Vignola et al. (2012) provide useful descriptions of commercially available radiometers, of which there are many, ranging in cost from a few hundred to several thousand US dollars.

Diffuse horizontal irradiance: the shading method

The measurement of diffuse irradiance requires a pyranometer in conjunction with a shading device that occludes the sun and prevents DNI from striking the sensor. This is commonly achieved with a shadow band, as in Figure 1.6 (a), or a shading ball (or disc) mounted on a tracker (Figure 1.7).

The perforated shadow band used in this study is designed for use with an Eppley shadow band stand (SBS) as shown in Figure 1.6 (a). The arms holding the band are inclined at the latitude angle of the site and are adjusted manually along their axis every few days to maintain an occluding position as the declination angle changes. The SBS is widely used with approximately 500 having been sold globally (Kirk, 2013). Kipp & Zonen manufactures a fully circular shading ring for use at higher latitudes where the range of azimuth angles exceeds the occluding limits of the Eppley band.

As an alternate approach, the shading ball occludes less of the sky and is the most accurate method of measuring DHI, however it requires a tracker and is costlier to implement. A ground station developed by the author at the University of

KwaZulu-Natal (UKZN) in Durban, South Africa, operates an automated tracker, Kipp & Zonen radiometers and a shading ball as shown in Figure 1.7.

(a) **(b)** **(c)**

Figure 1.6: (a) Pyranometer with a shadow band for measuring DHI, (b) exposed pyranometer for GHI, and (c) pyrheliometer on a mechanical tracker for measuring DNI (Kunene, 2011).

Figure 1.7: UKZN HC ground station with first class pyrheliometer and secondary standard pyranometers.

Two corrections are often applied to DHI data; the first is for the excessive blocking effect of the shadow band and the second is to account for the thermal offset error of the instrument.

The shadow band introduces an error in DHI by blocking more of the sky than the area around the solar disc. This must be accounted for by a correction factor (f_{sb}) that inflates the instrument output, that is, $f_{sb} > 1$. A number of formulations for f_{sb} based on geometry have been proposed, including that of the South African radiometry pioneer, Drummond (1956), who later worked for the Eppley Laboratory. For ease of use, the Eppley Laboratory publishes a table of correction factors for their solid band that decrease the measurement uncertainty of the system to ±5% versus the reference DHI (Drummond, 1964). Other studies on the shadow band method include those of Ineichen et al. (1983), De Oliveira et al. (2002) and Kudish and Evseev (2008).

An infrared (IR) thermal offset error is caused by the difference in temperature between a shortwave sensor and the sky. This is more pronounced for all-black thermopile instruments like the Eppley PSP because of the positioning of the reference junction inside the sensor casing. If the effective sky temperature is lower than that of the sensor, net radiation is lost skywards, lowering the output signal (Bush et al., 2000; Dutton et al., 2001; Gueymard and Myers, 2009). A correction flux (ΔE_{corr}) can be determined if the net infrared long-wave radiation between the ground and the sky (IR_{net}) is measured. This is achieved using specially tuned sensors called pyrgeometers that detect terrestrial radiation in the wavelength range between about 3.5 and 50 μm. The correction flux is then obtained using equation (1.3) (Reda et al., 2005):

$$\Delta E_{corr} = IR_{net}.RS_{net}.RS_{mfr} \tag{1.3}$$

where RS_{net} is the net infrared responsivity of the pyranometer in [$\mu V/W/m^2$] and RS_{mfr} is the inverse of the instrument manufacturer’s shortwave sensitivity in [$W/m^2/\mu V$]. The output from the pyranometer is adjusted by ΔE_{corr} to yield a final irradiance that is corrected for thermal offset. Typically, the magnitude of ΔE_{corr} is between 1 and 15 W/m^2.

All PB data used in this study from the United States National Renewable Energy Laboratory (NREL) were corrected using equation (1.3). Southern hemisphere data from the University of KwaZulu-Natal (UKZN) ground station were not corrected because pyrgeometers are not installed.

Global horizontal irradiance

An exposed pyranometer is used to measure GHI directly, since it must detect both the DHI and the horizontal component of the DNI simultaneously (Figure 1.6 (b)). In fact, the most accurate way of obtaining GHI is not by direct measurement, but by obtaining DNI and DHI separately, and then summing DHI with the horizontal component of DNI calculated using the zenith angle, as in equation (1.2) (Gueymard and Myers, 2009; Michalsky et al., 1999). This is because diffuse and direct normal irradiance can be measured with lower uncertainties than that with which an exposed pyranometer measures $E_{bn}\cos Z$. This is provided that the DHI component is obtained with a shading ball and not a band. The slightly higher uncertainty of a GHI measurement obtained from an exposed pyranometer is caused by the instrument's variable response to irradiance as a function of the incidence angle. The cosine effect, as it is known, is exacerbated for DNI because of its directional nature and becomes more pronounced at medium to high zenith angles.

Direct normal irradiance

DNI can be measured directly by pointing a pyrheliometer at the sun and following it through the course of the day. This requires a tracker as shown in Figure 1.6 (c). The instrument is an Eppley Normal Incidence Pyrheliometer (NIP) and the tracker is an electrically driven, non-automated ST-1 model that rotates at 15° per hour to keep pace with the sun. Regular adjustment of the clamp is required to maintain alignment with the plane of the ecliptic. The pyrheliometer in Figure 1.7 is a Kipp & Zonen CHP1 mounted on an automated SOLYS 2 tracker that locates the sun using an accurate solar position algorithm and a GPS system. It requires no manual adjustment but is considerably more expensive than the ST-1 device. Both the NIP and CHP1 models are first class instruments, although with traceability to the World Radiometric Reference (WRR) a sensor might be classified as a secondary standard. Other manufacturers of first class pyrheliometers include Eko Instruments, Middleton Solar and Hukseflux.

DNI can also be measured by an absolute cavity radiometer (ACR) which is considered as a primary standard instrument because it does not require calibration against another thermopile sensor. The Hickey-Friedan ACR measures solar irradiance by comparing the output of two thermopiles, one of which is irradiated by solar energy and the second of which is heated electrically (Hickey et al., 1977).

ACRs are unsuitable for continuous use because of their open aperture design and complex operation but they exhibit extremely low measurement uncertainties on the order of 0.3% (PMOD-WRC, 2010) and are used to calibrate other radiometers. The World Standard Group is a set of six ACR-type sensors that defines the World Radiometric Reference for solar irradiance. This is updated every five years at the International Pyrheliometer Comparison in Davos, Switzerland. National laboratories send instruments to be calibrated alongside the WSG, after which they are returned home to transfer the reference to secondary standard field instruments by repeat calibration.

Characterising DNI is important because of its use in CSP projects but it is the most expensive component to measure because of the tracking requirement, and is often calculated instead from DHI and GHI using equation (1.2). Although DNI is directional, the sun subtends an average solid angle of 0.53° at the surface of the earth such that DNI rays are not perfectly parallel (Duffie and Beckman, 1991). The effect is negligible for most applications although it contributes to the spread of focused images in CSP equipment such as heliostats and parabolic troughs, reducing the concentration ratio and the optical efficiency of the system (Stine and Harrigan, 1985).

1.4.4 Alternate instruments

Inevitably, there is a trade-off between the cost of an instrument and its accuracy. Since cost varies inversely with measurement uncertainty, there is an ongoing challenge to introduce better quality low-cost sensors. The need for radiometric ground data from multiple stations distributed over as wide an area as possible is also driving research efforts in radiometer development.

Examples of recently introduced alternatives to traditional radiometers include the Delta-T SPN1 instrument and the Irradiance Rotating Shadowband Radiometer.

Delta-T SPN1 radiometer

The SPN1 sunshine pyranometer contains seven thermopile sensors that each produce a voltage output when exposed to sunlight (Figure 1.8). A shading mask beneath the instrument's glass dome shields the sensors such that at least one sensor is always fully exposed to GHI while one is exposed only to DHI (Delta-T Devices Ltd., 2006). Coupled with an onboard computer processor and software algorithm, the SPN1 is able to determine separate instantaneous values for GHI and DHI from the sensor readings. Direct normal irradiance can then be calculated using equation (1.2). The cost of the instrument was about R87 400 in 2014.

Figure 1.8: A Delta-T Devices Ltd. SPN1 radiometer installed at the UKZN Howard College ground station.

An advantage of the SPN1 is its ability to generate DHI, GHI and DNI values from a single, compact device, making it easier to deploy in monitoring networks than optimal equipment schemes with trackers. Although it is thermopile-based the instrument exhibits some spectral selectivity below 400 nm meaning that it tends to under read diffuse irradiance in very clear conditions, and at high altitudes (Delta-T Devices Ltd., 2007). A further disadvantage is that the instrument requires a power supply for signal conditioning and the onboard heater. In addition, the SPN1 must be run for several weeks alongside a reference sensor when outdoor calibration is required, because of the presence of the mask and multiple thermopiles. The cost is also high compared with an Eppley PSP, however this must be weighed against the greater capabilities of the device.

Rotating Shadowband Radiometer (RSR)

The Rotating Shadowband Radiometer uses a single silicon diode sensor to produce GHI and DHI measurements of irradiance (Michalsky et al., 1986). It does this by rotating an electrically driven arm twice per minute into position over the sensor, blocking DNI and enabling the instantaneous measurement of DHI (Figure 1.9). The device measures GHI five times a minute, from which it builds a continuous measurement history of both components. Direct normal irradiance can be obtained from the closure equation (1.2). The Irradiance RSR2 model cost approximately R83 300 in 2014.

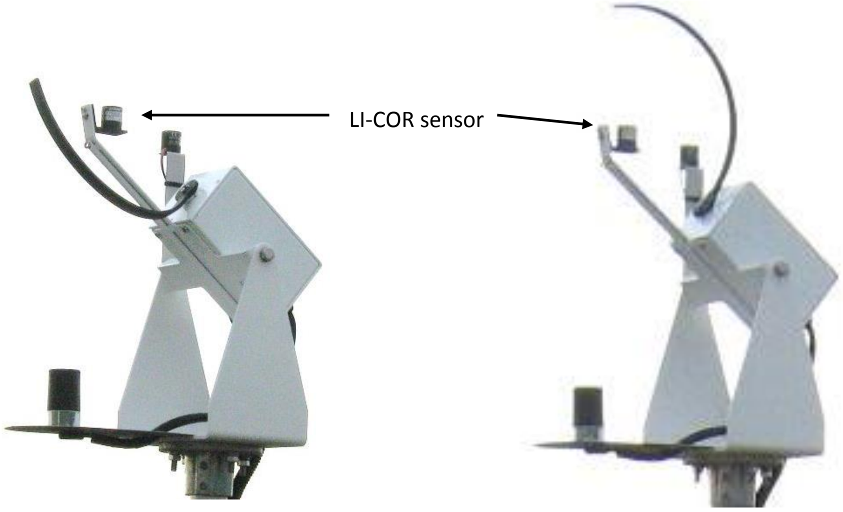

Figure 1.9: RSR2 Rotating Shadowband Radiometer measuring GHI on the left and DHI on the right.

The RSR2 device uses a LI-COR silicon photodiode sensor, which is known to suffer from spectral selectivity (Vignola, 1999). The LI-COR LI-200 sensor responds to radiation in the 400 to 700 nm range, which eliminates the remaining visible wavelengths from 700 to 3900 nm. It typically produces low readings for diffuse irradiance under clear sky conditions.

1.4.5 Optimal and sub-optimal measurement schemes

A measurement scheme refers to the combination of radiometers in use at a ground station, the array of data they provide and the quality of the measurements. Configuring a station can be difficult given the variety of sensors available and the numerous ways in which they may be combined. Consideration must be given to factors including the number of solar components to be measured, the cost of the installation, the desired measurement uncertainty, the availability of sensors and technical backup in a given location, the frequency of maintenance required, the power requirements of the station and the integration of the station with existing networks.

In an attempt to provide guidance, the US National Renewable Energy Laboratory proposed two standard station configurations (Wilcox and Stoffel, 2009). The first is a low-cost, higher uncertainty option comprising silicon photodiode sensors based on the RSR instrument, providing GHI and DHI data. This would be deemed sub-optimal because the resulting data do not exhibit the lowest uncertainty. The second is a more expensive configuration comprising independent measurement of DHI, GHI and DNI using secondary standard or first class thermopiles. The measurement uncertainty for GHI is approximately half that of the cheaper version.

To assist in the selection of station instruments, several studies have compared the relative performance of commercial radiometers. Gueymard and Myers (2009) considered common sources of uncertainty in 12 silicon and thermopile instruments located at the NREL Solar Radiation Research Facility (SRRL), including thermal offset error and seasonal variation. Myers and Wilcox (2009) tested 12 pyranometers and four pyrheliometers over a year-long period, also at SRRL. Michalsky et al. (2011) documented the comparative performance of 33 pyrheliometers over a trial period of ten months.

Gueymard (2009) argued that an optimal scheme should make use of Kipp & Zonen CM22 pyranometers for GHI and DHI, together with a CHP1 pyrheliometer for obtaining DNI. Using this as the reference scheme, Table 1.2 gives a comparison of selected instrument configurations ranging from the optimal setup to less expensive options. The comparison is based mainly on secondary standard Kipp & Zonen and Eppley radiometers.

To facilitate a fair comparison, the calculated costs include radiometers, trackers, shading devices where applicable and a logger, but exclude site preparation, mounting equipment, ventilation, battery backup and remote communications equipment. All of the schemes except 6 and 7 are configured with Kipp & Zonen or Eppley sensors. The least expensive combination of sensors is used to establish the normalised cost and the RSR2 in scheme 6 is the only non-thermopile instrument.

Schemes 1 and 2 incorporate redundancy in that they permit the independent measurement of DHI, GHI and DNI without recourse to calculation. The others measure one or two components and calculate the outstanding values, including the perforated shadow band system. The normalised costs are based on 2014 retail prices of landed sensors in South Africa, converted to US dollars at an exchange rate of ZAR10.50 to $1.

Table 1.2: Notional cost comparison of selected radiometric measurement schemes using commercially available instrumentation, normalised and calculated in 2014 US dollars.

	Measurement scheme	**Normalised Cost**	**Comment**
1*	Tracked pyrheliometer + unshaded pyranometer + shaded pyranometer with tracked occulting disc or ball	1.00	Optimal measurement capability, with thermopile/secondary standard sensors, low uncertainty and redundancy. From $32,500.
2	Tracked pyrheliometer + unshaded pyranometer + shaded pyranometer with shadow band	≥0.57	From $18,550. Full measurement capability with redundancy.
3	Tracked pyrheliometer + unshaded pyranometer	≥0.36	From $11,830. Partial capability. E_{bn} and E_g measured, E_d calculated.
4	Tracked pyrheliometer + shaded pyranometer	≥0.47	From $15,430. Partial capability. E_{bn} and E_d measured, E_g calculated.
5	Pyranometer (unshaded) + pyranometer (shaded)	≥0.35	From $11,250. Partial capability. E_g and E_d measured, E_{bn} calculated.
6	RSR2 silicon photodiode rotating shadow band radiometer	≥0.24	From $7,260. Partial capability. E_g and E_d measured, E_{bn} calculated.
7	Delta-T SPN1 thermopile radiometer	≥0.31	From $10,190. Partial capability. E_g and E_d measured, E_{bn} calculated.
8	Single pyranometer (shaded) + model	≥0.25	From $8,120. Only E_d measured, E_{bn} and E_g derived from model(s).
9	Single pyranometer (unshaded) + model	≥0.15	From $4,990. Only E_g measured, E_{bn} and E_d derived from model(s).
10	Single pyranometer + perforated shadow band on SBS	≥0.27	From $8,680. Partial capability. E_d and E_g measured, E_{bn} calculated.
11	Replace existing solid band with perforated shadow band	≥0.003	From $100. Adds measurement of E_g to E_d. E_{bn} calculated.

*Reference scheme

There is a substantial premium to be paid for scheme 1 which includes a shading disc on a tracker and conforms to Gueymard’s definition of an optimal setup (Gueymard, 2009) with redundancy. This is nearly twice the cost of scheme 2, which utilises high quality instruments but which relies on less expensive pyranometers and a sub-optimal shadow band for DHI. Scheme 4 is potentially optimal but only if CMP22 sensors are used and shading is accomplished with a tracking disc. This would raise the cost substantially over the given value which is based on Eppley sensors and a shadow band.

The RSR2 and SPN1 sensors in schemes 6 and 7 offer good value, but the non-thermopile sensor of the RSR2 limits its use in research-grade applications. Scheme 9 represents one of the most common setups in use, namely a single unshaded pyranometer measuring GHI (Perez et al., 1990b). The output can be used in conjunction with a radiometric decomposition model, described in Chapter 4, to estimate DHI, from which DNI can then be calculated.

Two values are given for the perforated band system. Scheme 10 accounts for the purchase of new components at 27% of the nominal scheme's cost. This places the PB system in a similar range as the RSR2 and SPN1 sensors. Scheme 11 considers the replacement of the solid shadow band in scheme 8 with a perforated band, for which the cost is restricted to the band itself and is negligible. Given that a substantial number of SBS systems have been distributed, this scheme represents an opportunity to extract greater amounts of data from an existing single thermopile radiometer than operating it in the fully shaded state.

The uncertainties associated with several of the schemes in Table 1.2 are addressed in Chapter 5.

1.4.6 Clearness index

As a classification tool in resource assessment analyses, clearness index, k_T, is a measure of the atmosphere's solar energy transmission efficiency and hence, indirectly, of cloud presence. It can be calculated for any one of the solar components as the ratio of the measured flux at the planet's surface to that component's extraterrestrial value at the earth's top of atmosphere (Myers, 2013). In addition, it can be varied for time periods ranging from one minute to monthly, with the minute-based value for GHI as follows:

$$k_T = \frac{E_g}{E_o} \tag{1.4}$$

E_g and E_o are the measured GHI and calculated minute-average of extraterrestrial global horizontal irradiance, respectively. That is, E_o is the component of the direct normal top of atmosphere irradiance (E_{on}) perpendicular to the earth's surface. E_{on} is available for download alongside NREL solar data and is continuously adjusted to account for the variation in Earth-Sun distance. The hourly averaged clearness index for GHI is designated K_{T_hour} and the daily equivalent is K_{T_day}. The value of the parameter lies in its ability to characterise relative sun strength when only the global irradiance is measured (Perez et al., 1990b). Although there are more complex ways to classify the sky condition, such as total sky imaging camera systems, they are more expensive and rarely available.

In this study clearness index is used extensively because GHI values are generated by the perforated band system whose performance is heavily dependent on the sky condition. The metric can thus be used to grade data and inform the processing methodology.

Clearness index is often correlated with the diffuse fraction, *k*, to yield an empirically derived method of calculating diffuse irradiance when GHI is known. This is described in greater detail in Chapter 4.

1.5 Global data availability

The high cost of instrumentation remains a central challenge to the large-scale deployment of radiometric networks and drives the search for lower-cost sensors. Although station density remains limited, a substantial number of monitoring stations are operated throughout the world by government agencies, weather services, research institutes and universities. These are located mostly in Europe and the United States. Stoffel et al. (2010) provide a useful summary of data sources, including satellite-derived measurements. In some cases instruments are integrated into networks and the data are made available to the public (Table 1.3).

Table 1.3: Examples of active solar radiometric monitoring networks (Brooks et al., 2015).

Data source	**Website access**
Baseline Surface Radiation Network (BSRN)	www.gewex.org/bsrn.html
World Radiation Data Center	wrdc-mgo.nrel.gov
Surface Radiation Network	www.esrl.noaa.gov/gmd/grad/surfrad/
Atmospheric Radiation Measurement	www.arm.gov
University of Oregon Solar Radiation Monitoring Laboratory	solardat.uoregon.edu/index.html
Australian Bureau of Meteorology	www.bom.gov.au/climate/data-services/solar/
Southern African Universities Radiometric Network (SAURAN)	www.sauran.net

There are several advantages to systematising the collection of radiometric data through networks of sensors (Brooks et al., 2015). The management of measurement campaigns can be centralised according to accepted principles of metrology, instruments can be properly maintained, data can be subjected to quality control filters and rigorous methods of data analysis can be encouraged among users. Networks may also be better funded and more widely publicised than single installations, broadening public access to solar measurement information.

Perhaps the best known network is the Baseline Surface Radiation Network (BSRN) which falls under the World Climate Research Programme. Data are obtained from research-grade sensors located at more than 50 stations on seven continents, and subjected to rigorous quality checks (Zhang et al., 2013). Other sources of information include the Surface Radiation Network (SURFRAD) and the World Radiation Data Center in Russia which publishes daily totals of global irradiance from more than 1000 stations (Stoffel et al., 2010). SURFRAD maintains seven stations across the United States and is funded by the National Oceanic and Atmospheric Administration. The United States Department of Energy operates the Atmospheric Radiation Measurement programme with instruments located mainly in the United States as well as at three sites in the Western Pacific ocean (US Department of Energy, 2013).

An extensive historical record of solar data for the Pacific Northwest of the United States is available through the University of Oregon’s Solar Radiation Monitoring Laboratory. Measurements from as far back as 1977 can be downloaded for certain of the locations. Lastly, the Australian Bureau of Meteorology operates a network of 10 active stations and makes historical data available to the public from several others.

1.6 South African data availability

Although South Africa (SA) has a history of sporadic radiometric monitoring campaigns, there has been no continuous, coordinated deployment of high-quality ground measurement stations. From the 1980s to the mid-90s the South African Weather Bureau, now the Weather Service (SAWS) maintained a network of thermopile sensors, however this fell into disrepair and no systematic measurement programme was in operation until rehabilitation began very recently. SAWS archived data are not freely available to the public. Ciolkosz (2009) presented results from a network of silicon-based sensors operated by the Agricultural Research Council, but these do not output research-grade data nor is the archive easily accessible.

In the last fifteen years several universities have started radiometric measurement and research programmes, including Mangosuthu University of Technology (Brooks and Harms, 2005; Zawilska and Brooks, 2011), Stellenbosch University and the University of KwaZulu-Natal (Brooks and Roberts, 2009; Kunene et al., 2013; Lysko, 2006). Zawilska et al. (2012) provided a more comprehensive history of radiometric initiatives in South Africa. Given the lack of a long-term, coherent record of sun strength in the region, they argued for the establishment of a formal network utilizing instrumentation at universities and elsewhere.

In 2014 the Southern African Radiometric Network, or SAURAN, was established to address the regional lack of publicly accessible, long-term, high-quality solar data of high-temporal resolution. This was an initiative of the Centre for Renewable and Sustainable Energy Studies at Stellenbosch University and the Group for Solar Energy Thermodynamics at the University of KwaZulu-Natal in Durban (Brooks et al., 2015).

In its initial phase, SAURAN consists of ten ground stations across South Africa, marked in black in Figure 1.10. Six of these are located on university campuses in the cities of Stellenbosch (SUN), Port Elizabeth (NMU), Durban (KZH and KZW), Pretoria (UPR) and Bloemfontein (UFS). Four are on farms in rural areas near the towns of Vanrhynsdorp in the Western Cape, Vryheid (VRY) in KwaZulu-Natal, Graaff-Reinet (GRT) in the Eastern Cape and near Alexander Bay in the Richtersveld region of the Northern Cape (RVD). The ten sites cover a range of climate and vegetation conditions, from desert scrubland through to coastal sub-tropical. Some of the stations are existing facilities that have also contributed historical data to the archive that predate the SAURAN project.

In the project's second phase, stations are planned in the far northern province of Limpopo (UVT), near the town of Alice in the Eastern Cape (UFH) and at the Mangosuthu University of Technology south of Durban. Data from the USP station will be of particular interest given the construction of several CSP and PV power plants in the region, which boasts very high DNI levels. Further stations are planned in the Namibian capital city of Windhoek (PNW), at Gaborone in Botswana (UBG) and on the Indian Ocean island of Reunion.

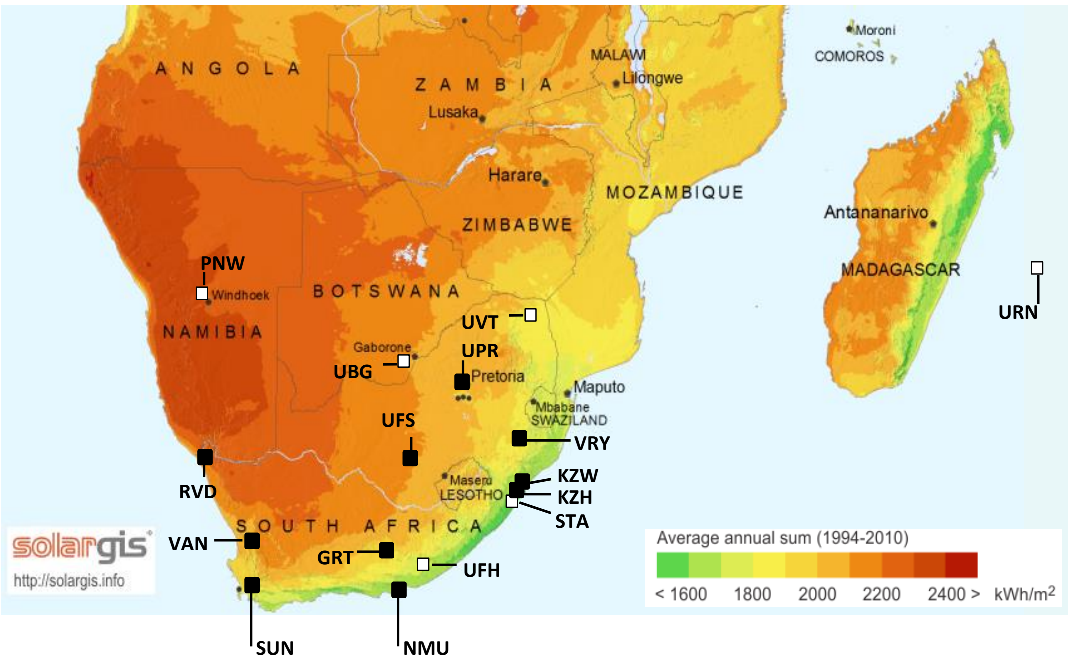

Figure 1.10: Initial SAURAN stations (in black) and planned stations (in white) on a satellite-derived map of annual average global horizontal radiation (Brooks et al., 2015).

The primary aim of the SAURAN initiative is to build a high-quality, long-term dataset of high temporal resolution for public use. To this end, the ten initial stations use research-grade first class and secondary standard thermopile radiometers that are properly maintained and cleaned regularly. All sites measure DNI, DHI and GHI independently so that cross-checking of the radiometric components at a given location is possible through the closure equation (1.2). The responsibility for maintaining sensors belongs to the partner universities that own the stations.

SAURAN data are provided to website users as 1 minute, hourly and daily averages from sensor scans conducted at sub-6 second intervals. Some of the sites host additional radiometers for research purposes. Stellenbosch University operates a CMP11 under a shading ring to provide additional diffuse measurements and UVS-AB-T sensor for recording ultraviolet radiation in the wavelength ranges of 280 to 315 nm and 315 to 400 nm. UKZN has a CUV5 sensor for UV radiation in the 280 to 400 nm range. The KZH station also hosts a Delta-T SPN1 pyranometer and an Eppley Precision Spectral Pyranometer fitted with the perforated shadow band.

1.7 Objectives of the research

Whereas most solar radiometric systems use two sensors to measure GHI and DHI, this research proposes a novel radiometric scheme that generates independent global and diffuse time-series from a single thermopile pyranometer. The key component of the scheme is an innovative shadow band incorporating a series of perforations so as to cyclically shade and expose a radiometer sensor. Used in conjunction with a stationary pyranometer and a data processing methodology, the perforated band system enables the decomposition of global horizontal irradiance to obtain the direct normal and diffuse components. The research has potential to impact solar monitoring programmes by providing an inexpensive measurement scheme that yields competitively low statistical uncertainties under certain cloud conditions.

To date, the approach of occluding and exposing a radiometric sensor has been used in two specific applications. The first is by instrument laboratories to establish the responsivity factor of pyranometers by the shade-unshade calibration method (Reda et al., 2003). Shading is effected manually over brief periods to determine the relationship between GHI and DHI. The second application is in the Rotating Shadowband Radiometer where an electrically driven solid band periodically blocks the sun’s direct normal component, from which the global and diffuse components can be obtained.

The PB system represents a new type of radiometric scheme. The solid shadow band of a conventional diffuse measurement station is replaced by a perforated version such that the accompanying pyranometer is intermittently exposed as the sun traverses the sky. This has the same cyclical shading effect used in the RSR device, however it is mechanically simpler and the switch between GHI and DHI takes place at much lower frequency because the band is static. The output from a pyranometer used with such a device comprises a single curve that alternates between global (exposed) and diffuse (shaded) irradiance. A processing algorithm separates the curve into independent traces and completes the measurement of both components of sun strength, from which DNI can then be calculated.

The study is motivated by the need to expand solar radiometric efforts through the provision of less expensive monitoring techniques. The research has particular application in sun-rich regions such as south-western and northern Africa where the solar resource is strong but underexploited, and where radiometric coverage is limited. While the output from a PB system cannot be classified as optimal, it offers potential advantages to station operators:

1. The perforated band does not require electrical power
2. A secondary standard thermopile sensor can be used
3. Although the normalised cost of a new PB system is not insignificant, it is possible to retrofit the perforated band in place of solid bands at existing measurement stations, such that the investment is negligible

The technical objectives of this research were three-fold:

1. To define the physical geometry of a perforated shadow band that can be retrofitted to existing station architecture.
2. To establish a test programme in which the performance of the PB system is rigorously assessed in conjunction with adequate reference instruments.
3. To characterise the performance of a PB system under all sky conditions through recognised measures of statistical uncertainty.

1.8 Dissertation outline and methodology

Chapter 2 introduces the concept of the perforated shadow band and describes the geometry governing its interaction with the sun’s direct normal component. A ray trace model of pyranometer exposure is then developed to describe the dynamic shading mask that the band creates over the course of a day, and seasonally throughout the year. Performance of the ray trace model is assessed using data from an experimental system. The derivation of a correction matrix is described to account for physical distortion of the band under operational conditions.

Chapter 3 addresses the performance of the PB system under clear sky conditions. A clear sky processing methodology is proposed to disaggregate the composite GHI/DHI data trace into its constituent parts and reconstitute the irradiance fragments as continuous time-series. The perforated band test programme, which was carried out in collaboration with the United States National Renewable Energy Laboratory, is also described. Experimental results from the operation of the system are given. The test methodology compares outputs from the PB system with reference data from collocated instruments at the NREL site. Performance is quantified via several statistical metrics including root mean square difference and mean bias difference.

An important feature of the PB system is its sensitivity to cloud which induces stochasticity in the pyranometer output trace and invalidates the use of visual filtering to separate GHI from DHI data. Chapter 4 addresses the complexities introduced by cloud fields and describes a cloudy sky processing methodology for the PB system. The methodology uses three methods of reconstituting fragmented GHI and DHI traces; numerical interpolation techniques, data replacement via radiometric models and an adaptive approach that monitors clearness index and deploys best-performing techniques in response.

Chapter 5 gives the experimental performance results of the PB system for cloudy sky conditions. In line with best practice, two independent, long-term datasets extending over several years are used to assess the Cloudy Sky Processing Methodology and confirm reproducibility of the statistical results. The chapter includes a comparison between the performance of the PB system and that of alternate measurement schemes, including the SPN1 radiometer, the rotating shadow band system and commercially available satellite data.

Chapter 6 describes PB system performance under southern hemisphere conditions. Results are presented from an experimental trial at the UKZN Howard College ground station in Durban. These shed light on whether the band's performance is affected by geographic location. The chapter concludes by considering the advantages and disadvantages of the system versus existing radiometric schemes. The deployment of the perforated shadow band system is briefly discussed with reference to regions in Africa where it may register lower uncertainties than competing measurement schemes.

The dissertation is concluded with Chapter 7, which summarises the main findings of the study and describes further areas of research that might improve the performance of the PB system.

2 THE PERFORATED SHADOW BAND

2.1 Introduction

The perforated shadow band permits the decomposition of global irradiance, as measured with a pyranometer, to obtain the diffuse and direct normal solar components. The band represents a novel type of radiometric scheme whose concept and performance have not been characterised prior to this study.

The band is introduced in this chapter, which is drawn mainly from the first three sections of the journal article by Brooks (2010). The geometry of the device is described and a time-dependent model of pyranometer exposure is developed with the aid of ray tracing software. Operation of the model is illustrated using experimental data from the NREL Solar Radiation Research Laboratory (SRRL) in Golden, Colorado. A method is described for adjusting the exposure model so as to account for structural deformation of the band in situ.

2.2 Principle of operation

The perforated shadow band is a semi-circular structure similar in dimension to its solid counterpart, from which apertures are cut, as shown in Figure 2.1. The perforations impose a cyclical shade/unshade regime on the sensing thermopile of a horizontally oriented pyranometer located below the band (Figure 2.2). As a result, the instrument output trace cycles between measurements of GHI when exposed and DHI when shaded yielding a characteristic square-wave trace under clear sky conditions (Figure 2.3).

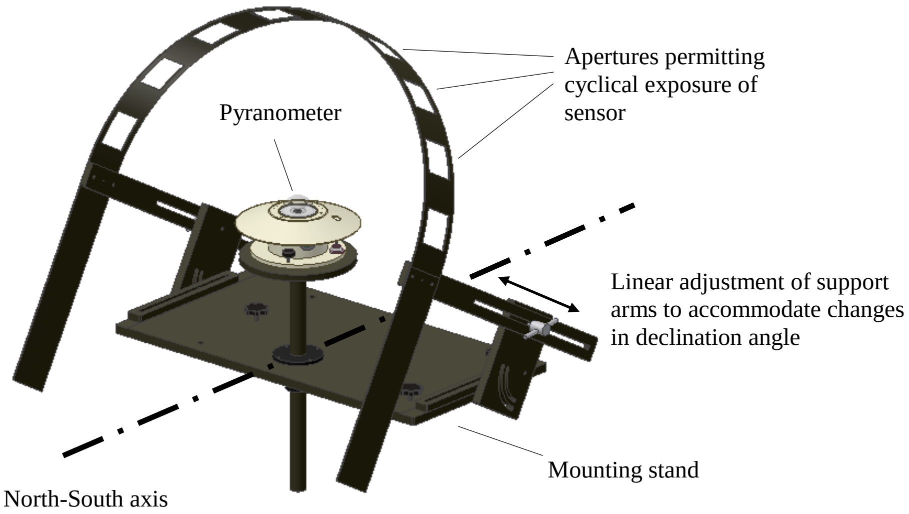

Figure 2.1: Perforated shadow band operated in conjunction with an Eppley Laboratory Precision Spectral Pyranometer, adapted from Brooks (2010).

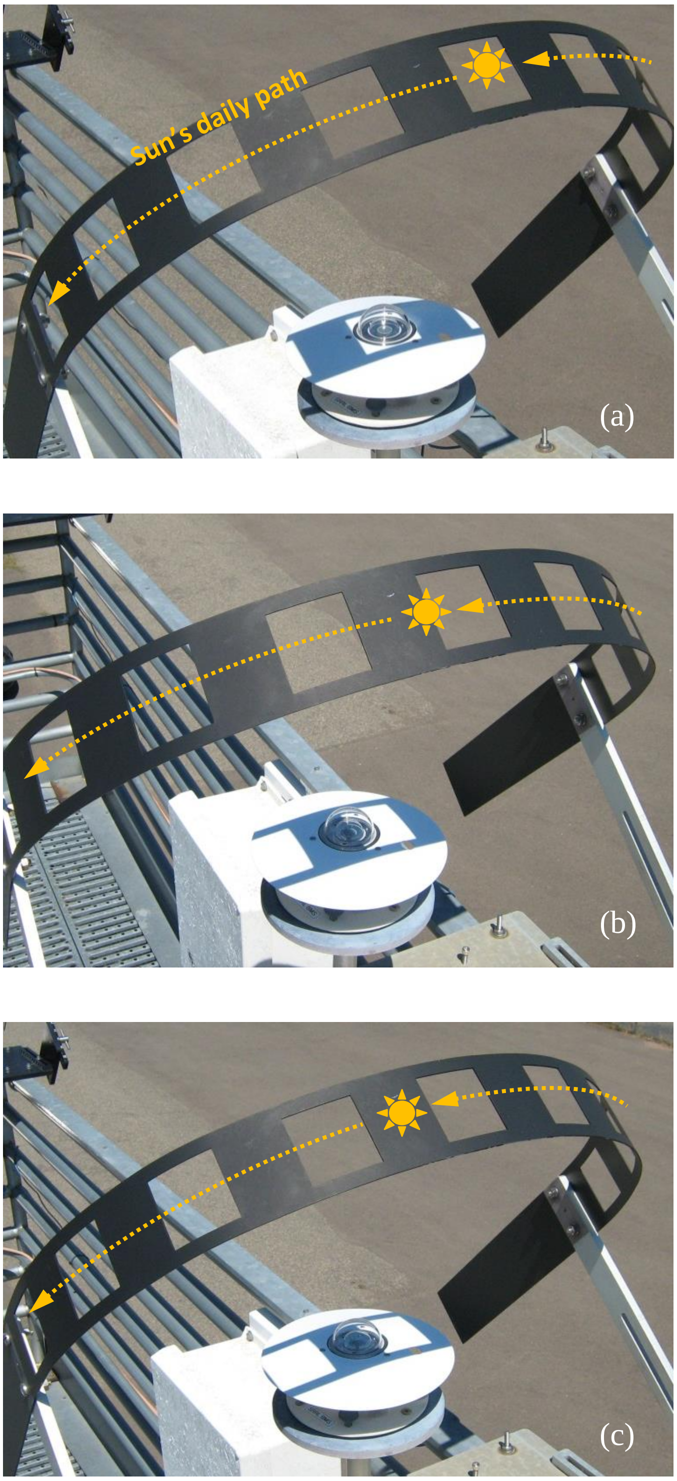

Figure 2.2: Perforated shadow band with an Eppley PSP at NREL SRRL showing (a) full sensor exposure for measurement of GHI, (b) partial sensor exposure and (c) full occlusion for DHI.

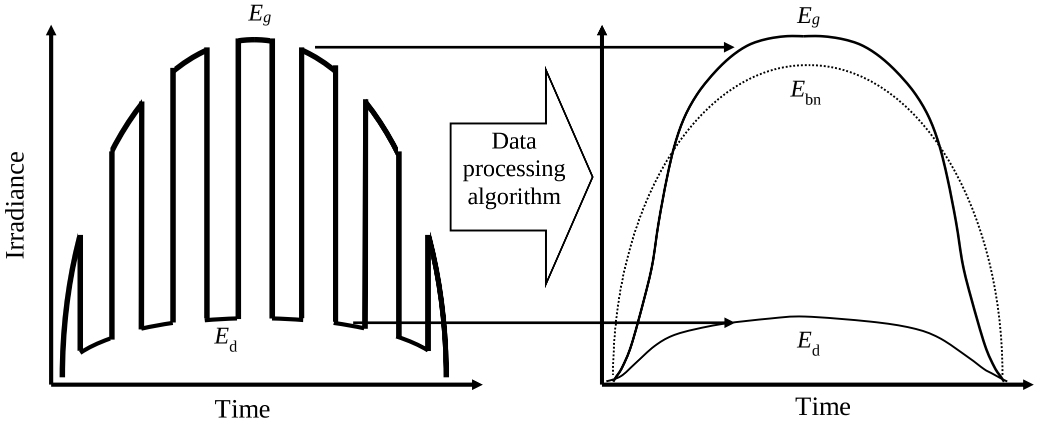

Figure 2.3: (Left) Schematic of square-wave output trace from the PB system under clear sky conditions and (right) its reconstitution as independent diffuse and global horizontal irradiance curves (Brooks, 2010).

A defining feature of the system is its inability to measure both GHI and DHI simultaneously; when one component is recorded, the other is missing. Under clear sky conditions the band generates clearly defined but fragmented upper and lower curves that must be separated and then reconstituted individually. Under partly cloudy and overcast conditions the coherency of the trace is disrupted, although the fragmentation effect remains. Developing appropriate data processing algorithms to separate and reconstitute the DHI and GHI curves with acceptably low uncertainties thus represents the primary challenge of this study.

2.3 The geometry of the perforated shadow band

The geometry of the band is influenced by several factors. First, the greater the number of apertures, the more frequently the sensor can switch between DHI and GHI. Secondly, as the shading mask transitions from exposure to occlusion (Figure 2.2 (b)) the pyranometer generates indeterminate data which represent neither GHI nor DHI, and which are discarded. These factors give rise to competing constraints: the first drives the design towards many smaller apertures, while the second suggests fewer apertures to limit transitional data.

In addition, the band must permit unhampered exposure and occlusion of the pyranometer thermopile (Figures 2.2 (a) and (c)), therefore the geometry of the radiometer also influences the band’s design. Early trials with greater numbers of smaller apertures (Figure 2.4) produced a shading mask that never fully exposed the pyranometer’s outer glass dome. Although this does not affect the measurement of GHI, provided the sensing thermopile is exposed, the apertures were lengthened in response. A minimum of 20 minutes full exposure or occlusion was considered adequate in the GHI and DHI time-series fragments for trend identification during the reconstitution of the curves. This equates to 20 individual 1-minute averages of sun strength from a ground station logger.

Figure 2.4: Alternate aperture configurations.

The total width (W) of the band and the internal aperture width (W_a) are set at 84 mm and 60 mm respectively to ensure lateral occlusion of the solar disc during shading and unobstructed communication between the sun and the outer glass hemisphere of the sensor during exposure, regardless of declination angle or time of day (Figure 2.5).

The aperture length (L_a) in the circumferential direction was determined using a two dimensional analysis, based on a maximum zonal exposure time (t_z) of 30 minutes. This is illustrated in Figure 2.5 for a zenith angle of 0° during the solar noon period of exposure. The PSP measures GHI while the solar disc of diameter W_s is in full sight of the sensor, that is, while the disc appears fully within the window of the band. For a mean radial distance from sensor to band of 320 mm and sun speed of 0.25 deg/min, the arc length (s) of the sun's movement at the band radius and the total aperture length are obtained from equations 2.1 to 2.3:

$$\mu = \left(\frac{0.25\pi t_z}{180}\right) = 0.1309\ \text{rad} \tag{2.1}$$

$$s = 320\varphi = 41.9\ \text{mm} \tag{2.2}$$

$$L_a = s + W_s \approx 45\ \text{mm} \tag{2.3}$$

To account for variation in t_z due to three dimensional effects, and to ensure that the aperture length exceeds the diameter of the outer glass hemisphere of the PSP (48 mm), L_a is extended to 55 mm.

Multiple rectangular apertures of length 55 mm are cut from the band as shown in Figure 2.6. They are equal to the eight alternating solid zones contained between the first and last apertures such that the band has a total of nine apertures and ten shading zones, with zone 1 located to the left of aperture 1 and zone 10 to the right of aperture 9.

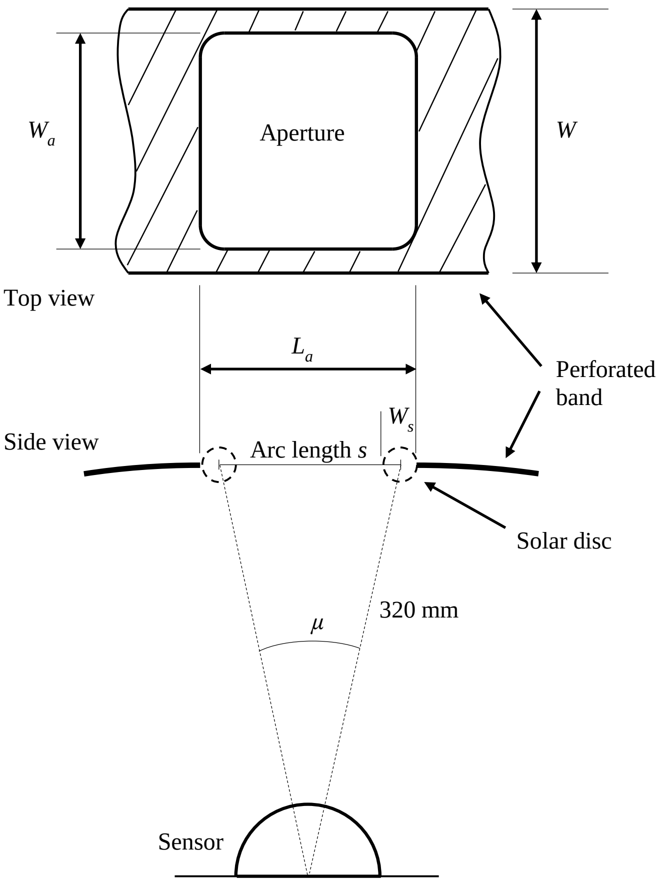

Figure 2.5: Top and side views of perforated shading band geometry with solar disc traversing a single aperture (Brooks et al., 2007).

In this study, three pyranometer exposure states (E_S) are defined as a result of the sun-band interaction. They are: complete shade during which DHI is measured, denoted as $E_S = 0$, transitional exposure ($E_S = 0.5$) when the edge of the aperture throws a creeping shadow over the sensor and full exposure ($E_S = 1$) during which GHI is measured.

The perforated band is manufactured from a strip of stainless steel 1700 mm long, 84 mm wide and 2 mm thick. It is inclined on a polar mount at the local geographic latitude angle, φ, and aligned with true north (Figure 2.7). It is manually adjusted daily or every few days to accommodate changes in the declination angle of the sun, δ, which varies between extrema of +23.45° and –23.45° and is defined as positive in the northern hemisphere and negative in the south. The band is inclined with the upslope pointing north in the northern hemisphere and south in the southern hemisphere.

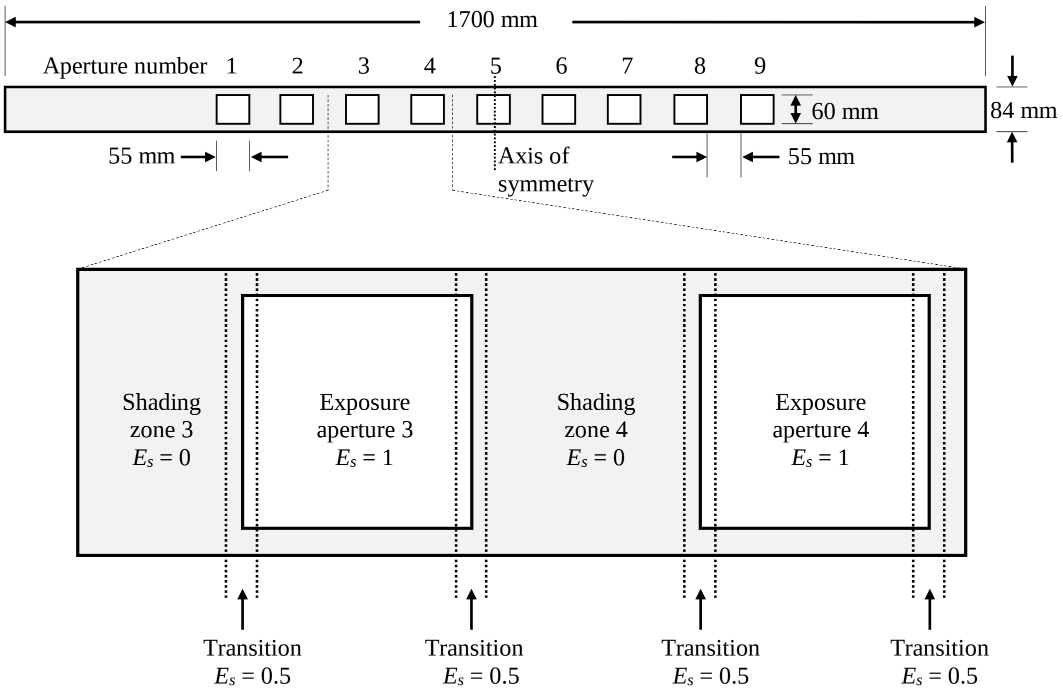

Figure 2.6: Plan view of an unrolled perforated band with close-up of apertures 3 and 4 (Brooks, 2010).

An advantage of the polar mount is that the plane of the band coincides with the plane of the ecliptic at the equinoxes ($\delta = 0°$), thus the maximum travel to the north and south of the equinox position is equal. That is, a band displacement of $+\Delta l$ is required for $\delta = +23.45°$ and $-\Delta l$ for $\delta = -23.45°$. It should be noted that a ray drawn from the centre of the solar disc to the thermopile sensor does not strike the band perpendicularly, apart from twice yearly on the equinoxes.

In Figure 2.7, the PSP sensor (white dash) remains stationary while the band is adjusted along the polar axis through maxima of $\pm\Delta l$. The central solar ray is coincident with the midpoint of the band's outer radius at any instant of the day as the sun traverses the plane of the ecliptic. Some inaccuracy in the band's axial position may be tolerated because aperture width exceeds that of the solar disc.

For a band of radius R_b whose displacement is zero at the equinoxes, Δl may be calculated from equation (2.4) which applies to perforated and solid bands in the northern or southern hemispheres. If intra-day variations of δ are ignored throughout day number n, Δl is given by:

$$\Delta l = \mathrm{R}_b \tan\delta \qquad (2.4)$$

The declination angle may be calculated as follows (Duffie and Beckman, 1991):

$$\delta = 23.45\sin\left[\frac{360(284 + n)}{365}\right] \qquad (2.5)$$

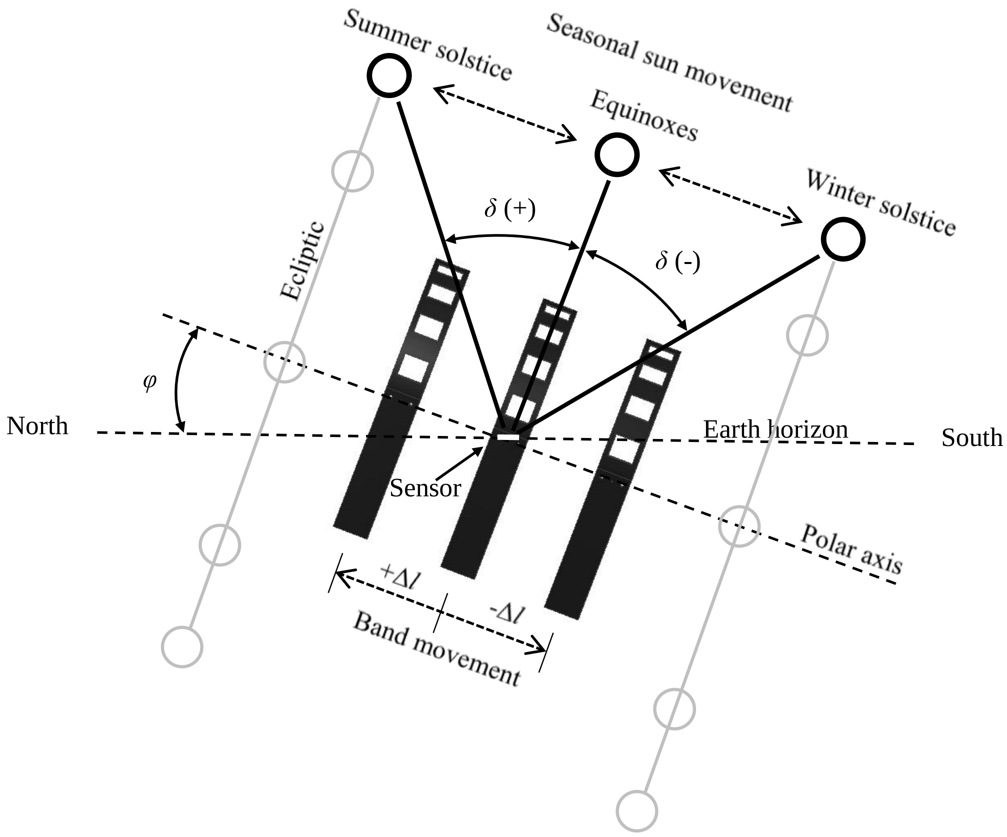

Figure 2.7: Seasonal variation of the perforated band relative to the sensor for latitude *φ* in the northern hemisphere at solar noon (Brooks, 2010).

2.4 Ray trace model of pyranometer exposure

2.4.1 Methodology

In the absence of cloud, hereafter ‘clear sky conditions’, the structure of the PB data trace is coherent and cycles unambiguously between its GHI and DHI components, as in Figure 2.3. This permits the accurate identification and removal of transition data between exposure and shading of the sensor. Under such conditions, the decomposition of the PB trace into fragmented DHI and GHI time-series can be carried out by visual filtering. Reconstituting the separated values into continuous functions can be achieved by curve-fitting, as described in Chapter 3.

Under partly cloudy conditions, the PB trace is chaotic and incoherent, and visual filtering of the transition data is no longer possible (Brooks and Roberts, 2009). Identification of GHI and DHI fragments may also not be possible by inspection. To meet the third aim of this research and characterise the system’s performance under all cloud conditions, it was necessary to provide a non-visual method of identifying the diffuse and global components in the PB trace. This was achieved by the development of a model in which the state of pyranometer exposure is correlated with the sun's hour angle. The model uses a ray tracing approach to determine when the PSP sensor is shaded or exposed for the band geometry in Figure 2.8 on a regularly spaced number of days spanning a generic 365-day year. The steps followed in deriving the model were:

1. Calculate solar position data for a given day number (*n*) from sunrise to sunset in hour angle increments of 0.125°.
2. Calculate perforated band movement (Δl) for day *n* number using equations (2.4) and (2.5).
3. Define the spatial coordinates and angular orientation of the ray trace solar source.
4. Trace light rays, plot sensor flux maps and determine the exposure state of the thermopile for apertures 1 to 5 as a function of day number
5. Mirror the results for apertures 6 to 9 and process the ray trace results to correlate sensor exposure with zenith and hour angles

In positioning the ray-emitting solar source, the model makes use of solar geometric relationships given by Duffie and Beckman (1991) and Sproul (2007), as described in equations 2.6 to 2.11. For daily declination angle δ and zenith angle Z, the hour angle ω is given as:

$$\omega = \cos^{-1}\left[\frac{(\cos Z - \sin\varphi \sin\delta)}{(\cos\varphi \cos\delta)}\right] \qquad (2.6)$$

The sunrise hour angle ω_{sr} is obtained from equation (2.6) by setting $Z = 0°$. For the analysis, a table of daily hour angle values was created using ω_{sr} as the starting point, increasing in 0.125° increments. These were used to step the solar source through the given day during the ray tracing exercise and represent the resolution of the model.

For each value of ω_{sr} the corresponding altitude and zenith angles (α and Z) were generated from equations (2.7) and (2.8):

$$\alpha = \sin^{-1}[\sin\delta \sin\varphi + \cos\delta \cos\varphi \cos\omega] \qquad (2.7)$$

$$Z = 90° - \alpha \qquad (2.8)$$

Azimuth angle is calculated from the following, where $0° \leq \gamma' \leq 360°$:

$$\gamma' = \cos^{-1}\left[\frac{\sin\delta \cos\varphi - \cos\delta \sin\varphi \cos\omega}{\cos\alpha}\right] \qquad (2.9)$$

The above equation is subject to the condition that $\gamma' = \gamma'$ for $\omega < 0$, and $\gamma' = (360° - \gamma')$ for $\omega > 0$. Lastly, the angle is adjusted so that $-180° \leq \gamma \leq 180°$.

$$\gamma = \gamma' - 180° \qquad (2.10)$$

In the ray trace model, light rays emanate from a grid source whose position is defined by spatial displacement relative to the coordinate origin, and by the angular orientation of the emitting face. The values of δ, ω, α and γ obtained above are used to position the grid such that it simulates the sun's position as shown in Figure 2.8. Latitude, declination, zenith, and altitude angles are indicated for the solar noon position.

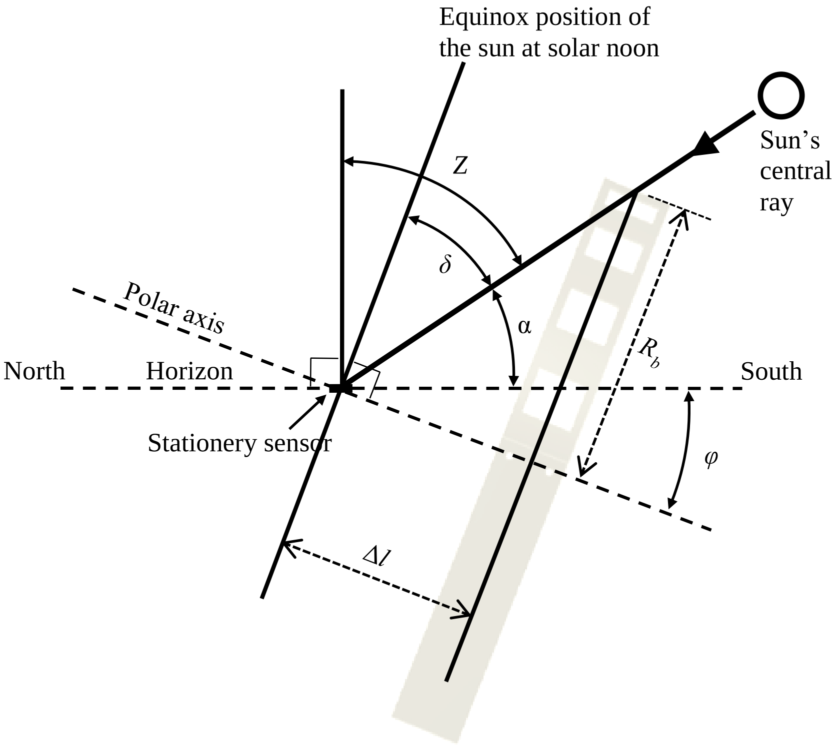

Figure 2.8: Generalised geometry of a shadow band in the northern hemisphere used to establish the ray trace model of pyranometer exposure (Brooks, 2010).

The artificial solar source is defined by spatial coordinates P(x,y,z) relative to the PSP sensor at a defined origin O(0,0,0), and by the angular orientation of the grid. The final orientation of the emitting face is obtained by three successive rotations of the displaced grid about the x-, y- and z-axes, in that order, given by the rotation vector S(ξ,η,ζ) (Figure 2.9). A straight line drawn perpendicular from the centre of the emitting face therefore passes through the centre of the pyranometer sensor for any solar position.

Light rays emanate in the z' direction from the upper surface of the grid source which must be displaced along the solar vector to P after rotation so that the emitting face is perpendicular to OP. OB represents the projection of the solar vector on the plane of the earth's surface. In this case |OP| is set at 1000 mm to ensure it exceeds the distance from the sensor to the outer radius of the band.

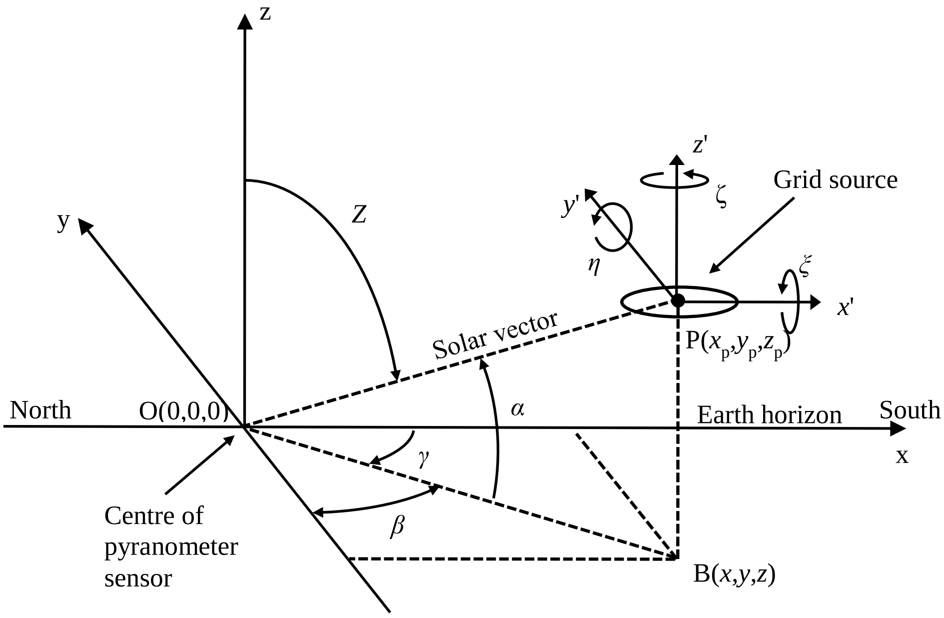

Figure 2.9: Schematic of the translation and rotation required to orient the solar source in the ray trace model (Brooks, 2010).

The components of P and S proceed from Figure 2.8 and are given in equations (2.11) to (2.16):

$$z_p = |\mathrm{OP}|\sin\alpha \tag{2.11}$$

$$y_p = -|\mathrm{OB}|\cos(270° - \gamma) \tag{2.12}$$

$$x_p = -|\mathrm{OB}|\sin\beta = -|\mathrm{OB}|\cos\gamma \tag{2.13}$$

$$\xi = -(90° + \alpha) \tag{2.14}$$

$$\zeta = (90° - \gamma) \tag{2.15}$$

In the above, $|\mathrm{OB}| = \sqrt{(1000^2 - z_p^2)}$ and no rotation about y is required, that is, $\eta = 0°$. The diameter of the grid is 20 mm to ensure that it fully floods the sensor of diameter 11.3 mm. The source generates rays with a half-angle of 0.255° to accommodate the finite size of the solar disc. Tracing is executed using TracePro software and outputs from each run consist of a physical picture of the rays within the model space and an irradiance flux map of the pyranometer sensor, isolated from its surrounding plane. The resulting flux map defines the exposure state of the sensor as occluded ($E_s = 0$), partially exposed ($E_s = 0.5$) or fully exposed ($E_s = 1$), thereby associating each value of ω and Z with a corresponding value of E_s for a given day. In this way, pyranometer exposure is correlated with sun position for the given latitude and day. As an example, Figure 2.10 shows a ray bundle generated by the artificial source positioned according to equations (2.11) to (2.16). A close-up of the first aperture (lower left) shows light rays partially obstructed by the band's lower edge. The irradiance flux map of the sensor (lower right) shows a light region representing the transitional state, $E_s = 0.5$

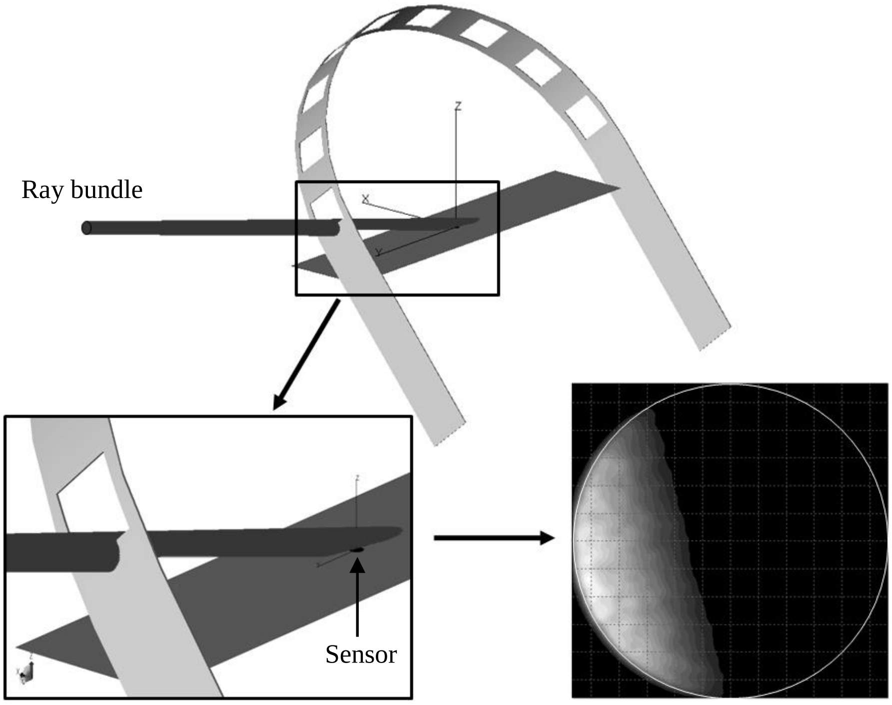

Figure 2.10: Graphic of a perforated band in the ray tracing environment for n = 232, φ = 39.74° and ω = -81.019° (Brooks, 2010).

2.4.2 Model parameters

Ray tracing results are given in Figure 2.11 for a set of daily computational runs spanning a generic year at the NREL SRRL site. The graphs show the hour angle values defining the start and end of sensor exposure ($E_s = 1$) and occlusion ($E_s = 0$), related to each aperture and shading zone of the band respectively as a function of day number. In each case the lower set of markers for each aperture or shading zone represents the values of ω at which full exposure or occlusion of the sensor first occurs and the upper markers represent the end of full exposure or occlusion. For example, a pyranometer sensor at the NREL site will be fully exposed through aperture 6 between hour angle values of 15.2° and 22.3°, and this behaviour will be repeated daily throughout the year.

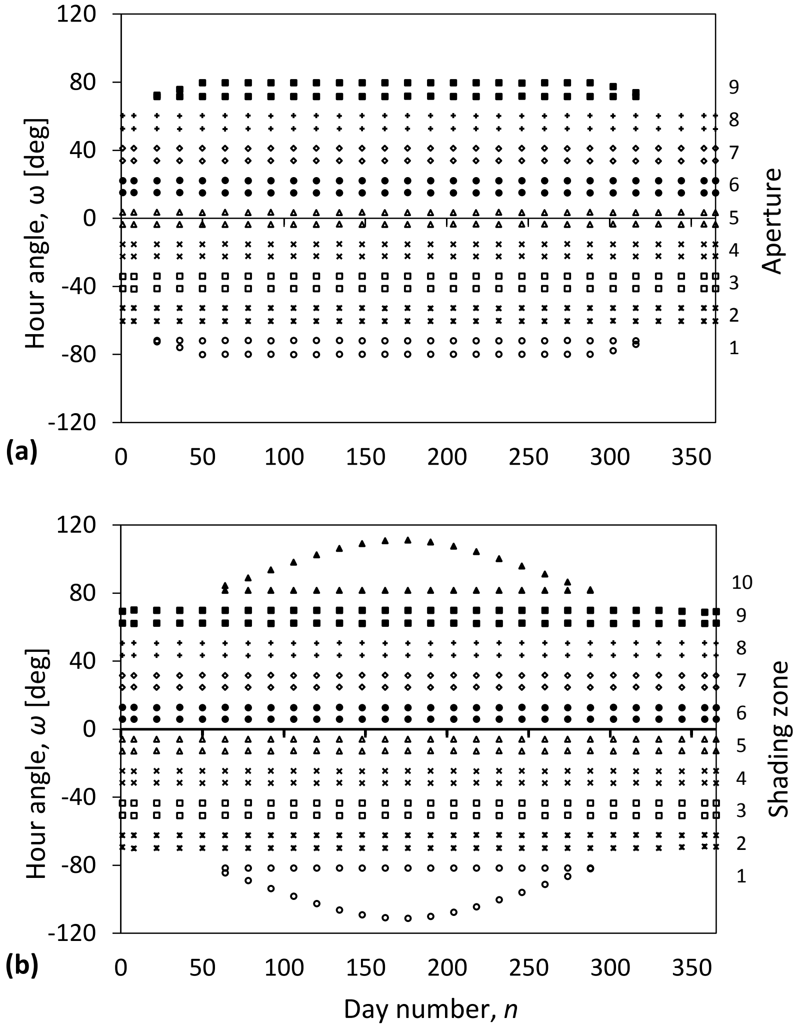

Figure 2.11: Ray tracing-derived hour angle limits for (a) full sensor exposure (E_s = 1), and (b) full sensor shading (E_s = 0) as a function of day number at φ = 39.74° (Brooks, 2010).

In the case of Figure 2.11 (a), the sensor is never fully exposed through apertures 1 and 9 for $1 \leq n \leq 18$ and $326 \leq n \leq 365$ due to the downward manual adjustment of the band in mid-winter. For $1 \leq n \leq 56$ and $289 \leq n \leq 365$ shading zones 1 and 10 fall below the level of the pyranometer and have no influence on the sensor exposure state (Figure 2.11 (b)).

With the exception of exposure data for apertures 1 and 9, and shading data for zones 1 and 10, ω is independent of day number. This is a useful result and is due to the polar mount of the band, its circular shape and the daily adjustment of the band to accommodate for changes in declination angle. These factors result in the sun-band-sensor geometric relationship remaining constant for a given solar time, or hour angle.

As an extension to the model, it is possible to relate zenith angle to exposure and shading for each aperture or zone by reworking equations (2.7) and (2.8):

$$Z = \cos^{-1}[K_1 \sin\delta + K_2 \cos\delta] \tag{2.9}$$

where $K_1 = \sin\varphi$ and $K_2 = \cos\varphi\cos\omega$. For NREL SRRL, $K_1 = 0.64$. K_2 is ω-dependent with values are given in Table 2.1 along with corresponding average hour angle limits for each aperture and zone. These constitute the predictive model of pyranometer exposure for the perforated band. Figure 2.12 gives the resulting zenith angle limits from the ray trace model for exposure and shading states at the NREL test site.

Table 2.1: Annual hour angle limits for onset and completion of full pyranometer exposure ($E_s = 1$) and shading ($E_s = 0$) at NREL SRRL (Brooks, 2010).

E_s = 1 (Exposure)					**E_s = 0 (Shading)**				
Aper-ture	**Start ω**	**K_2**	**End ω**	**K_2**	**Shad. zone**	**Start ω**	**K_2**	**End ω**	**K_2**
1	-79.80*	0.14	-71.77**	0.24	**1**	*Variable*		-81.60†	0.11
2	-60.37	0.38	-52.69	0.47	**2**	-69.83	0.27	-62.33	0.36
3	-41.19	0.58	-33.85	0.64	**3**	-50.65	0.49	-43.38	0.56
4	-22.27	0.71	-15.15	0.74	**4**	-31.61	0.66	-24.63	0.70
5	-3.49	0.77	3.49	0.77	**5**	-12.78	0.75	-5.92	0.77
6	15.15	0.74	22.27	0.71	**6**	5.92	0.77	12.78	0.75
7	33.85	0.64	41.19	0.58	**7**	24.63	0.70	31.61	0.66
8	52.69	0.47	60.37	0.38	**8**	43.38	0.56	50.65	0.49
9	71.77**	0.24	79.80*	0.14	**9**	62.33	0.36	69.83	0.27
					10	81.60†	0.11	*Variable*	

Limits are valid approximately as: *$50 \leq n \leq 294$ **$19 \leq n \leq 325$ †$57 \leq n \leq 288$

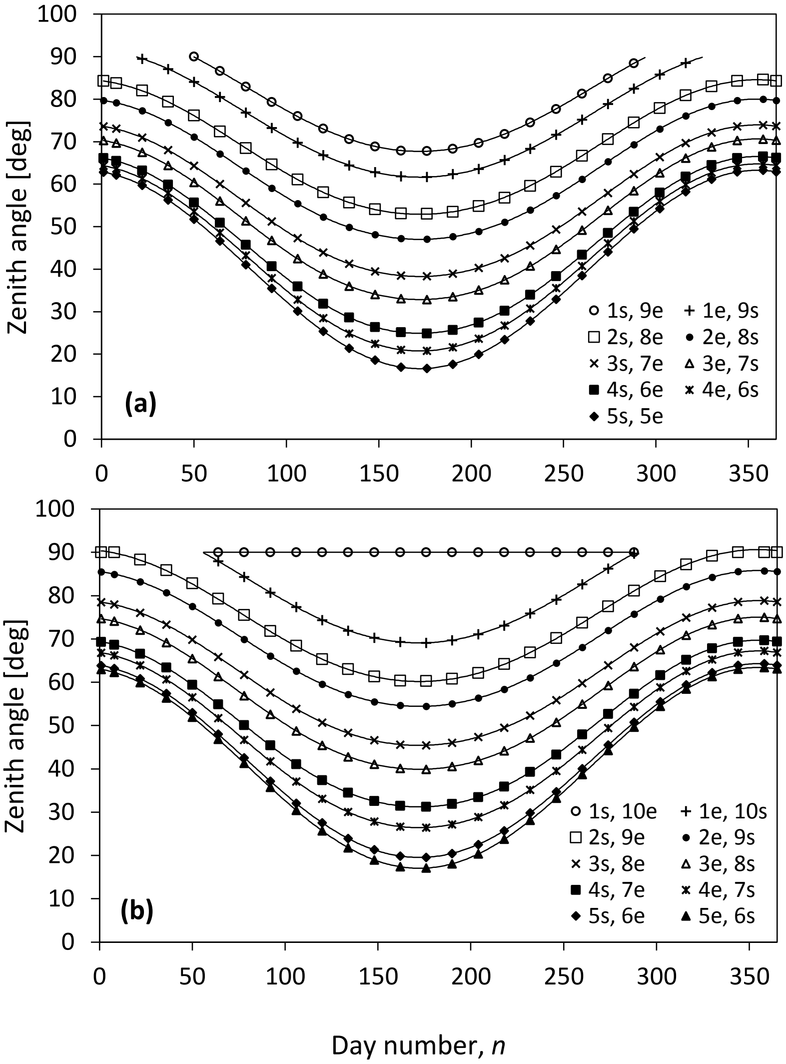

Figure 2.12: Annual zenith angle start (s) and end (e) limits: (a) by band aperture for pyranometer exposure (E_s = 1) and (b) by shading zone (E_s = 0) at φ = 39.74° (Brooks, 2010).

2.4.3 Implementation of the ray trace model

The ray trace model is illustrated in Figure 2.13 (a) to (c) using sample data from NREL SRRL. Under both summer and winter conditions the shading mask correctly identifies GHI, DHI and transition data without recourse to visual filtering. A magnified view of aperture 5 flanked by shading zones 5 and 6 for *n* = 322 is given in Figure 2.13 (c). Predicted shading, exposure and transition states from the ray trace model are superimposed in black. Figures 2.13 (a) and (b) illustrate the seasonal difference in waveforms produced under clear skies, both with respect to magnitude and shape. In summer, the band is adjusted upward in its stand relative to the PSP, activating apertures 1 and 9 and producing a characteristic ‘nine-peak’ waveform versus the ‘seven-peak’ shape of mid-winter.

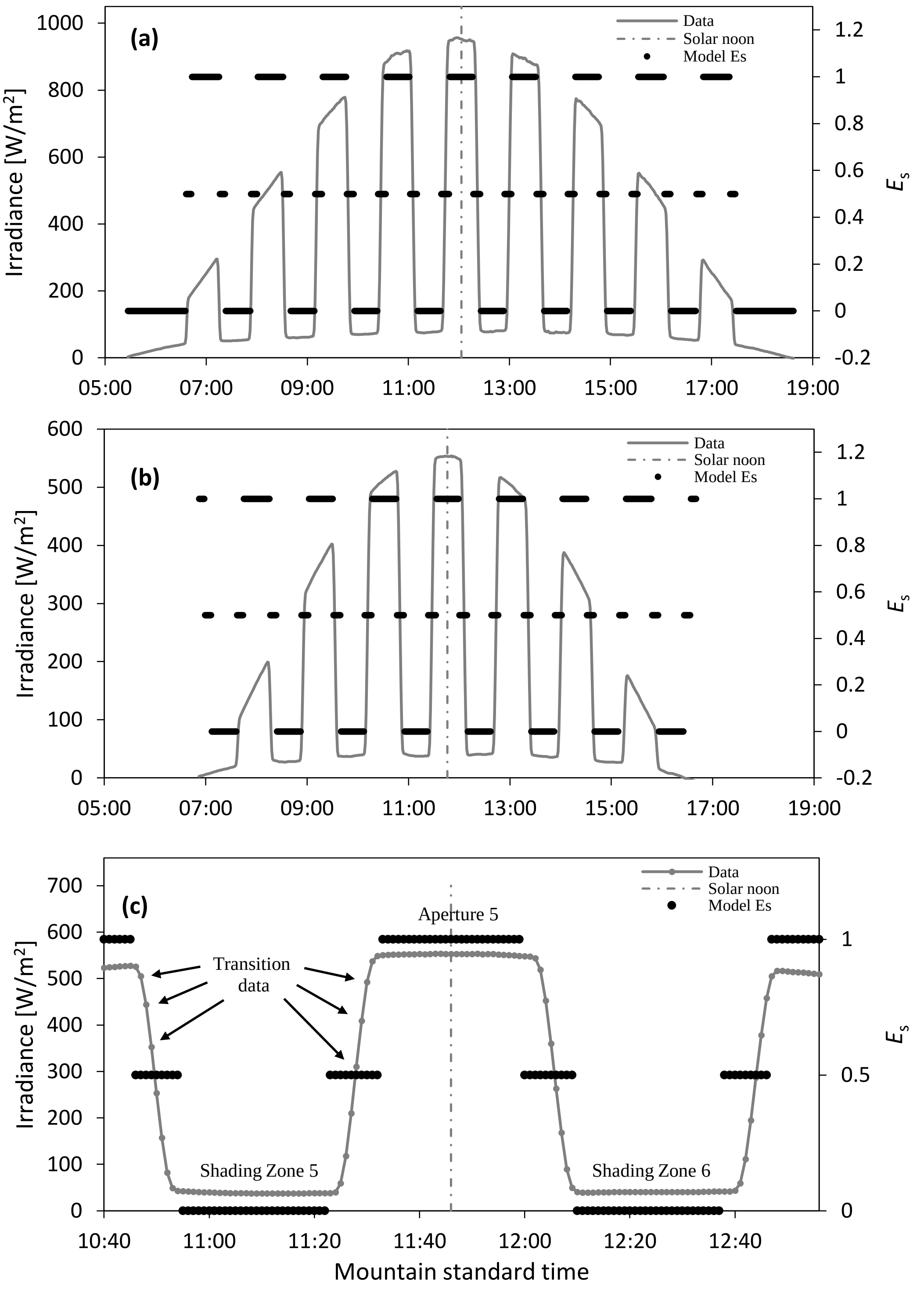

Figure 2.13: Characteristic square wave irradiance data for NREL on clear-sky days: (a) 27 August 2009 (n = 239) and (b) 18 November 2009 (n = 322) (b) (Brooks, 2010).

The potential latitude-dependence of the ray trace model was investigated by comparing the hour angle limits in Table 2.1 with values derived for the UKZN ground station in Durban at latitude $\varphi = -29.87°$ (south). The maximum absolute variation in the hour angle exposure start and end limits for any single aperture was 0.14°, as described in detail in Chapter 6. For shading zones, the maximum difference in predicted hour angle limits was 0.23°.

The model described in Table 2.1 is expected to apply universally except at extreme polar latitudes where a fully circular structure is required to occlude the sensor over the summer months. This universality is due to the semi-circular nature of the band and the use of a polar mount. The only differences between sites will be the tilt of the pyranometer sensor relative to the band, and the variations peculiar to the first and last apertures as they fall below the sensor level in winter.

2.5 Correction factors

2.5.1 Structural deformation

In practice, minor structural deformation of the perforated band is difficult to avoid because of wind loading, the regular adjustments made to the device and deflection of the stand’s support arms.

Two corrections are therefore made to account for deviation of the structure from its idealised shape and to reverse the resulting inaccuracy of the pyranometer exposure model. First, an empirically derived correction factor is applied to the ray trace model to shift the predicted shading mask, where necessary, in accordance with periodically measured locations of peaks and troughs in the data output trace. Second, the transitional period is extended by one minute at the start and end of each crossover phase between GHI and DHI to provide an additional buffer and to prevent confusion between data types.

The first correction factor is obtained by inspection of clear sky days at regular intervals throughout the datasets. The degree to which the model deviates from the trace curve under clear conditions is quantified in the form of a lookup table and read into the processing software to reverse the misalignment. The peaks and troughs of the predicted shading mask are shifted to the left or right of their idealised position by integer multiples of 1 minute, so as to align them with the square-wave trace visible on selected clear days. The correction factors are specified independently for each peak and trough and cover the duration of all datasets used in this study for both the NREL site and the UKZN ground station. On cloudy and partly cloudy days they are obtained by linear interpolation between the clear sky data. The second correction factor is also applied automatically to data generated by the PB system.

Figure 2.14 illustrates the application of the correction factors to an extract of data from NREL SRRL on 20 July 2012. The unadjusted shading mask is shown in red and is noticeably misaligned with the data trace in apertures 1 to 4. The correction procedure shifts the mask to the left (black) and extends the duration of transitional data by 1 minute at the start and end of the crossover from DHI to GHI, and vice versa.

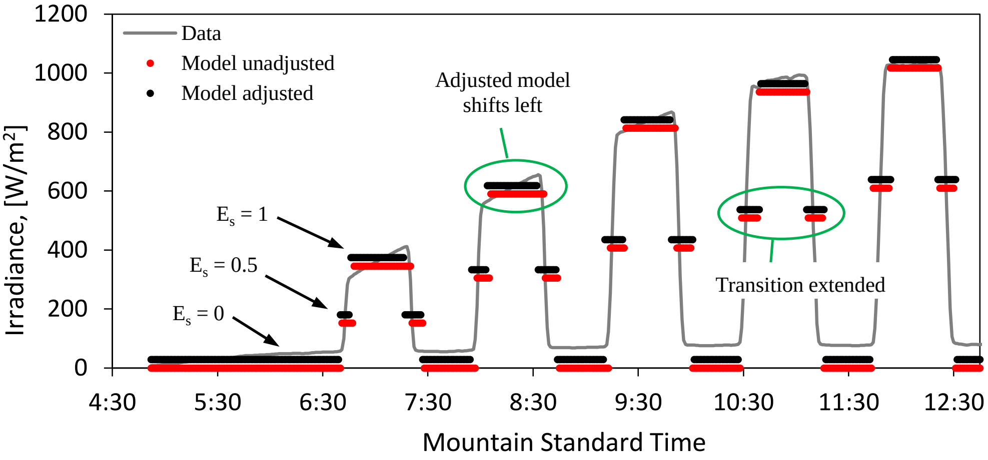

Figure 2.14: Correction of the predicted shading mask for NREL SRRL data sample (20 July 2012).

Structural distortion does not affect the band's capacity to split a composite signal into separate global and diffuse components under clear sky conditions, since a visual filtering technique can be applied. This approach is discussed in the next chapter.

Under cloudy conditions, the corrected ray trace model adequately identifies diffuse horizontal, global horizontal and transition data, albeit with the loss of a small number of measurement values as GHI and DHI patches are reduced in duration by 1 minute at their start and end. As a general principle of operation, it is important that a perforated band is carefully installed to replicate the geometry of the ray trace model and regularly checked for symmetry of the data about the solar noon position.

2.5.2 Shadow band blockage

All shadow bands cause a reduction in the measured diffuse horizontal irradiance by occluding a portion of the sky within the field of view of the pyranometer sensor. This increases the measurement uncertainty and requires a correction factor, f_{sb}, to reverse the effect, applied as follows:

$$E_{d\_corrected} = f_{sb} E_d \qquad (2.10)$$

For a solid band, f_{sb} typically ranges between 1.05 and 1.30 (Ineichen et al., 1983) and several approaches have been used to derive it. Drummond (1956) proposed the "Pretoria method" in which an isotropic sky is assumed and the band is modelled geometrically. The correction factor is derived as a function of solar position and the band parameters of width and radius. LeBaron et al. (1990) proposed a more sophisticated approach in which band geometric effects are combined with empirical data to yield a correction factor that accounts for the anisotropic nature of diffuse irradiance. Kudish and Evseev (2008) compared the above methods with two more approaches by Batlles et al. (1995) and Muneer and Zhang (2002) and found the latter to be the best overall performer.

The methodologies described above cannot be applied to the perforated shadow band since they rely at least partly on the solid band geometry. An alternate approach is to derive an empirical factor by comparing output from the PB system with an unshaded, collocated reference pyranometer under overcast conditions. Although an unshaded pyranometer normally registers GHI, the overcast sky ensures that the reference instrument measures diffuse horizontal irradiance with low uncertainty. The minute-based experimental values of f_{sb} were obtained by dividing the reference DHI by the diffuse output from the PB sensor at each 1-minute interval on a series of overcast days:

$$f_{sb} = \frac{E_{d\_ref}}{E_{fd}} \tag{2.11}$$

The daily correction factor was then obtained by averaging the resulting factors between 09:00 and 15:00. This was repeated for multiple days across a calendar year to yield f_{sb} as a function of day number, as given by the discrete markers in Figure 2.15 for both NREL and the UKZN ground stations. A regression curve was then fitted to the data to provide the final continuous functions describing f_{sb} at both sites. For the NREL data, the coefficient of determination (R^2) is 0.89, indicating a good fit with the data. The UKZN curve returned an R^2 value of 0.91.

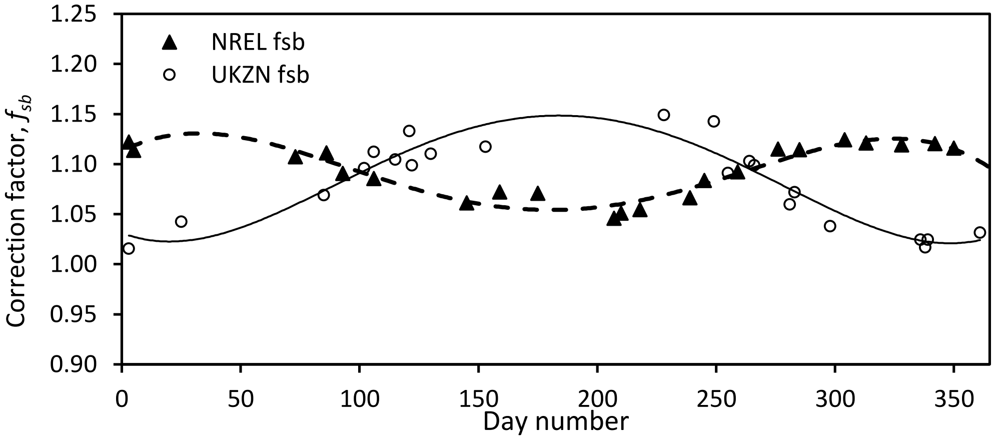

Figure 2.15: Empirically derived shadow band correction functions for the NREL SRRL and UKZN ground stations.

In Figure 2.16 a data sample from NREL SRRL on 12 September 2011 is given to illustrate the application of f_{sb} to experimental data. When measuring DHI, the uncorrected perforated band trace (grey) exhibits a visible deficit in magnitude versus the expected reference DHI curve (red). The corrected trace (black) coincides with the reference data, indicating that the blocking effect of the band has been properly accounted for.

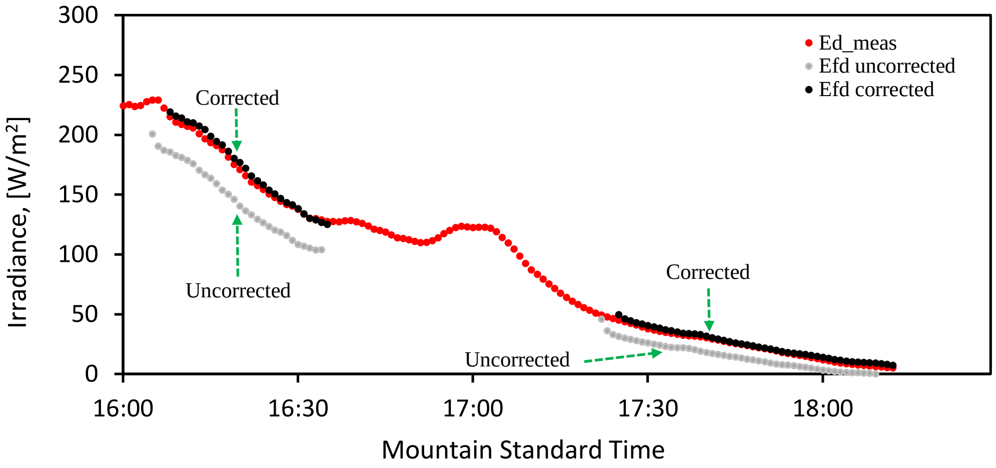

Figure 2.16: Application of a correction factor to amplify perforated band irradiance and reverse the blocking effect of the band structure (NREL SRRL data from 12 September 2011).

2.6 Summary

This chapter introduced the perforated shadow band as a device to decompose an aggregate pyranometric signal into separate GHI and DHI traces. The principle of operation was explained through a geometrical analysis of the interaction between the solar disc, the band and the pyranometer sensor.

A ray trace model of pyranometer exposure was developed to predict the time-dependent shading regime at the radiometer sensor as a function of hour angle. Other than minor variations at sunrise and sunset, the model is location-independent due to the polar mount of the band. The ray trace model permits the use of the band under partly cloudy and overcast conditions, and therefore removes any reliance on clear-sky conditions in order to process data from the radiometer. This transforms the system into an all-weather radiometric tool. Chapter 3 addresses the performance of the PB system under clear sky conditions, following which Chapter 4 uses the ray trace model developed here to formulate a cloudy sky processing methodology.

3. PERFORMANCE UNDER CLEAR SKY CONDITIONS

3.1 Introduction

The methodology used to process data from a perforated band depends on the sky conditions under which measurements are generated. Under clear skies, the PB trace is sufficiently coherent (see Figure 2.13) that a visual filtering technique can be employed to separate the diffuse and global horizontal values, before reconstructing the fragmented DHI and GHI traces. Under partly cloudy or overcast conditions, there may be limited differentiation between components and the ray trace model of pyranometer exposure must be used. The techniques employed to reconstruct fragmentary DHI and GHI curves are also more complex in the presence of trace stochasticity.

This chapter, which is drawn partly from the journal article by Brooks (2010), addresses the processing of data from a PB system under cloud-free conditions. The clear sky processing methodology (CrSPM) is introduced and applied to a set of NREL data gathered between 2008 and 2010. Results describe the statistical performance of the band under clear sky conditions versus collocated reference radiometers independently measuring global horizontal, diffuse and direct normal irradiance. In addition, PB uncertainty is compared to that of DNI predictions from radiative transfer models, since these offer an alternate method of generating irradiance estimates at ground stations.

3.2 NREL and the data gathering program

3.2.1 The Solar Radiation Research Laboratory

NREL's Solar Radiation Research Laboratory in the town of Golden, Colorado, was the primary test-site for the perforated shadow band system. The facility is located atop the South Table Mountain mesa, west of the city of Denver at 39.74°N 105.18°W and at 1829 m AMSL. Gueymard and Myers (2009) categorise SRRL as a major United States radiometric installation. It is active both in calibrating instruments and in developing better calibration techniques for implementation by organisations such as the ARM network and BSRN. Due to its elevation and location, the laboratory experiences lower pollution and atmospheric moisture levels than at sea level sites.

A prototype version of the perforated band, with the dimensions described in Figure 2.6, was shipped to SRRL in 2007 and mounted on a standard Eppley shadow band stand, over an Eppley Precision Spectral Pyranometer. The system was positioned on an outdoor instrument platform (Figure 3.1) where it was run continuously for over 7 years until early 2015. During this time it received regular maintenance alongside approximately 50 other radiometric instruments that were either undergoing tests or providing reference data for laboratory operations.

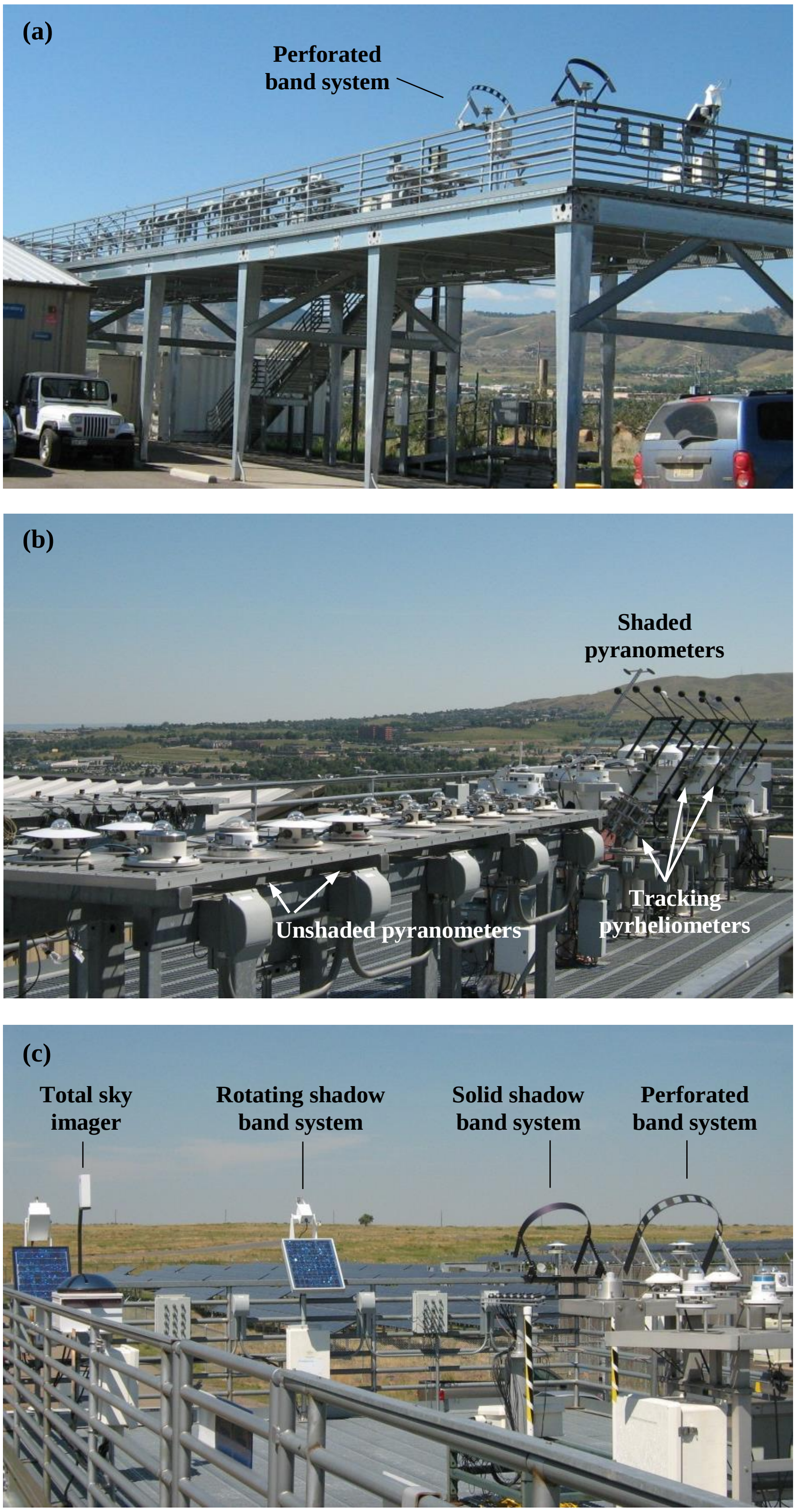

Figure 3.1: (a) The NREL Solar Radiation Research Laboratory instrument platform, (b) collocated research and reference radiometers, and (c) the PB system alongside a solid shadow band.

Data from most of SRRL's instruments, including the perforated shadow band pyranometer and the reference radiometers used in this study, are publicly available through the online Baseline Measurement System (BMS) (NREL, 2014). The website enables users to download measurements for a selected date range from the NREL archive and provides a solar calendar that makes preliminary filtering of data possible according to trace structure. A sample of the calendar is given in Figure 3.2 which covers August 2009, including the cloud-free day used to illustrate the operation of the ray trace model in Figure 2.13.

The Baseline Measurement System also provides solar vector information from the implementation of the NREL Solar Position Algorithm (Reda and Andreas, 2008). Data include the sun's hour, zenith, and declination angles at 1-minute increments, and extraterrestrial global and direct irradiance estimates.

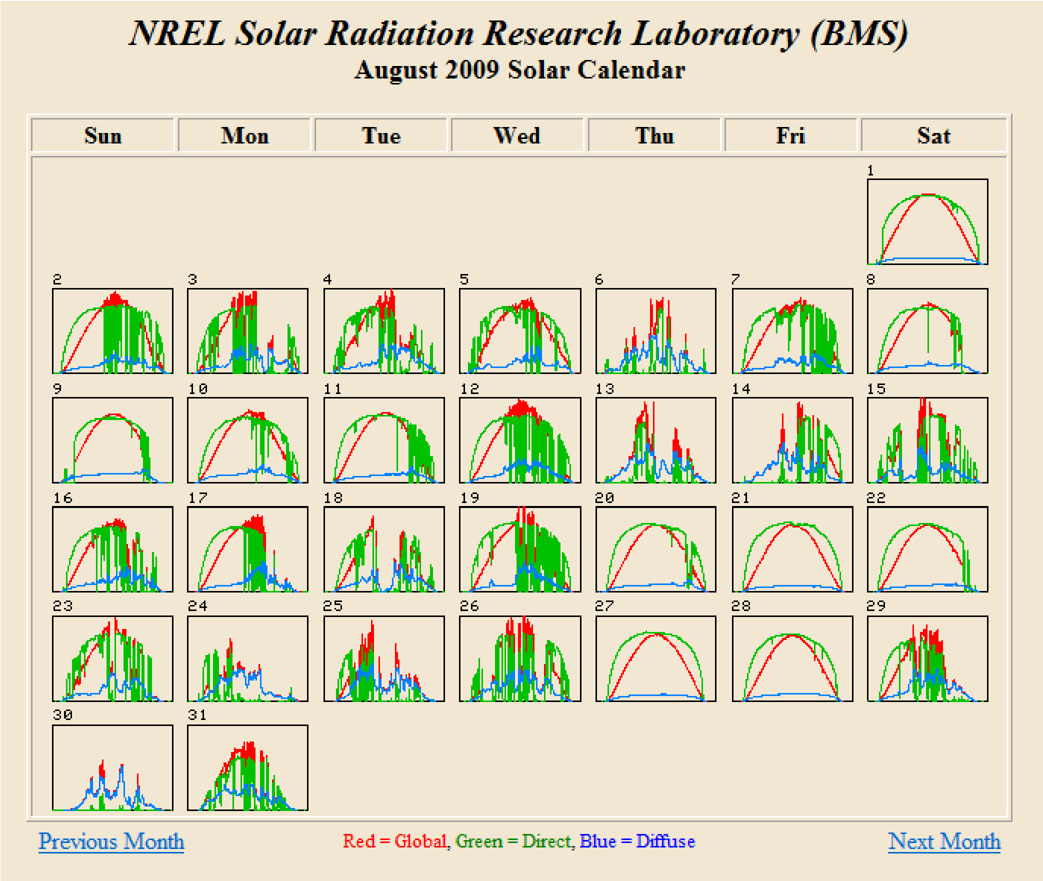

Figure 3.2: Sample NREL solar calendar showing GHI, DNI and DHI traces for August 2009 (NREL, 2014).

3.2.2 SRRL instruments

The perforated band was operated in conjunction with an Eppley PSP radiometer that was exchanged periodically as part of the NREL calibration process. Measurement scans were conducted by the laboratory's BMS every few seconds and averaged to provide data at 1-minute resolution.

The reference data used to establish perforated band performance in this study were obtained from two collocated, research-grade secondary standard Kipp & Zonen pyranometers and a first class pyrheliometer (Table 3.1). Table 3.2 gives the serial numbers, sensitivity coefficients and periods of operation for the Eppley pyranometers used with the perforated band in this study. In this case, sensitivity is defined as the inverse of the instrument responsivity, given in [W/m^2/mV]. Appendix A gives similar information for the reference sensors. A comprehensive maintenance log was kept for the PB system, a sample of which is given in Appendix B. The log remains publicly available through the Baseline Measurement System at www.nrel.gov/midc/srrl_bms/ (NREL, 2014).

Table 3.1: Instruments used at NREL SRRL to characterise PB performance.

Component	Instrument configuration	Manufacturer/type
Perforated shadow band	Pyranometer	Eppley PSP
GHI (reference)	Ventilated, unshaded pyranometer	Kipp & Zonen CM22
DHI (reference)	Ventilated, shaded pyranometer with occulting ball	Kipp & Zonen CM22
DNI (reference)	Tracking pyrheliometer	Kipp & Zonen CH1
Net infrared irradiance	Pyrgeometer	Eppley Precision Infrared Radiometer

Table 3.2: Instrument history of the perforated band PSP at NREL SRRL.

Eppley PSP serial number	Sensitivity [W/m^2/mV]	Date installed	Date removed
29668F3	121.30	25 May 2007	28 Jul 2008
25818F3	115.25	28 Jul 2008	22 Jul 2009
25765F3	116.68	22 Jul 2009	02 Jul 2010
25818F3	115.26	02 Jul 2010	26 May 2011
25765F3	117.20	26 May 2011	07 Jun 2012
25818F3	115.05	07 Jun 2012	20 Jun 2014
25765F3	116.59	20 Jun 2014	11 Dec 2014

3.2.3 Measurement uncertainty

SRRL radiometers are subject to rigorous maintenance, including cleaning of their optical windows multiple times each week. Importantly, they are calibrated on an annual or biennial basis to negate instrument drift and ensure that quality standards are maintained with respect to measurement uncertainty. The facility uses the Broadband Outdoor Radiometer Calibration (BORCAL) procedure, described in detail by Reda et al. (2003). This employs a component-sum technique to generate a pyranometer's responsivity, measured in [μV/W/m^2], that is divided into the radiometer output signal, measured in [μV], to generate an irradiance value in [W/m^2].

Despite careful maintenance, all radiometers exhibit some form of measurement uncertainty, or dispersion of measurand values about the true radiometric result (Joint Committee for Guides in Metrology, 2008). This is determined from the known behaviour of a radiometer (commonly referred to as 'type-B' errors) and from a statistical analysis of the instrument's performance against a class I instrument traceable to the World Group of Radiometers. The uncertainty for each radiometer is obtained by ascribing uncertainties to functional parameters such as the radiometer output voltage, net infrared responsivity, net infrared irradiance, direct normal irradiance measured by an absolute cavity pyrheliometer, and the reference diffuse irradiance measured by a shaded pyranometer (Reda et al., 2008). SRRL reports expanded uncertainties for each instrument to a 95% level of confidence.

Table 3.3 gives the overall instrumental uncertainties provided by NREL for GHI, DHI and DNI measurements in this study. These were obtained by combining the calibration uncertainties in the test PSP with those of the reference instruments as the root sum of squares (RSS).

Table 3.3: Average expanded measurement uncertainties for the radiometers used in the study, and RSS instrument uncertainties applicable to the measurement of E_g, E_d and E_{bn} (Brooks, 2010).

	Eppley PSP under band (%)	**K&Z CM22 E (%)**	**K&Z CM22 E_d (%)**	**K&Z CH1 E_{bn} (%)**
Average expanded uncertainty	± 4.7	± 1.7	± 1.6	± 0.6
RSS instrument uncertainty for combined PSP and reference data	± 5.0	combined with CM22 (E) for global horizontal irradiance		
	± 5.0	combined with CM22 (E_d) for diffuse horizontal irradiance		
	± 3.9	combined with CH1 (E_{bn}) for DNI		

The RSS values reflected in Table 3.3 include the PSP error as well as that from the comparative reference instrument. Because direct normal irradiance obtained using the PB system is a composite measurement, the uncertainty is scaled to include 80% global horizontal irradiance and 20% diffuse horizontal irradiance from the PSP, in combination with CH1 uncertainty. The radiometer serial numbers used to establish these metrics were #29668F3, #25818F3 and #25765F3 (PSP), #10046 and #10034 (CM22) and #10256 (CH1 for E_{bn}).

The combined overall measurement uncertainties applicable to this study are thus ±5% for global horizontal and diffuse horizontal irradiance, and ±3.9% for DNI (Gueymard and Myers, 2009; Joint Committee for Guides in Metrology, 2008; Myers, 2005; Myers et al., 2002; Reda et al., 2008). For full-range limits of 1100 W/m^2 (GHI), 250 W/m^2 (DHI) and 1100 W/m^2 (DNI), the true values of E_g, E_d and E_{bn} therefore lie within approximately ±55.0 W/m^2, ±12.4 W/m^2 and ±43.1 W/m^2 respectively of the reported values from the study, with a 95% confidence level. It is important to note that the values in Table 3.3 quantify measurement uncertainty only and do not permit direct comparison of the perforated band approach with the schemes listed in Table 1.2. For that purpose, it is necessary to quantify model uncertainty, or the difference between the PB system predictions of each solar component and the outputs from collocated reference instruments. Section 3.3 gives the results of such an analysis.

3.3 The clear sky processing methodology (CrSPM)

3.3.1 The clear sky dataset

This study focuses on high-resolution data at 1-minute intervals which are generally more useful in radiometric studies than hourly averages. The clear sky dataset consisted of 30 days drawn from the NREL Baseline Measurement System between March 2008 and January 2010. The days were selected by visual inspection of the solar calendar to ensure clean, cloud-free traces and as even a distribution as possible throughout the year.

The maximum zenith angle at which SRRL radiometers are calibrated is 60° therefore it is preferable to restrict the analysis of PB performance to the same limit. An expanded range up to 70° was permitted, however, to include the mid-winter period when zenith angles increase. In total, the dataset spans 14 002 minutes, with the early morning and late afternoon data ($Z \geq 70°$) excluded from the analysis to minimise the uncertainty associated with high incident angle measurements.

Table 3.4 provides metadata for the clear sky set, including the daily clearness index (K_{T_day}) that varies between 0.74 and 0.82, with an average of 0.78. The intermittency of measurements caused by the band apertures and zones means that the dataset contains only 5361 readings of diffuse horizontal irradiance, and 5789 readings of global horizontal irradiance. These constitute the input to the clear sky processing methodology for generation of DHI, GHI and DNI continuous curves.

Table 3.4: The NREL radiometric dataset for clear sky conditions.

Date	Day number	K_{T_day}	Number of data N	PB DHI		PB GHI	
				Measured (Z<70°)	Missing (Z<70°)	Measured (Z<70°)	Missing (Z<70°)
20080318	78	0.81	505	184	321	217	288
20080413	104	0.79	574	240	334	222	352
20080414	105	0.81	577	240	337	223	354
20080613	165	0.80	663	234	429	292	371
20080629	181	0.77	662	243	419	292	370
20080712	194	0.74	653	245	408	287	366
20080819	232	0.77	594	237	357	239	355
20080829	242	0.74	572	244	328	221	351
20080915	258	0.77	528	203	325	220	308
20080929	273	0.74	488	175	313	219	269
20081007	281	0.77	463	172	291	197	266
20081015	289	0.76	437	174	263	173	264
20081017	291	0.76	430	170	260	164	266
20081028	302	0.75	393	160	233	151	242
20090120	20	0.80	314	106	208	138	176
20090204	35	0.79	365	131	234	152	213
20090305	64	0.81	464	168	296	200	264
20090314	73	0.82	492	171	321	216	276
20090406	96	0.81	556	234	322	219	337
20090827	239	0.77	577	239	338	221	356
20090926	269	0.77	498	175	323	221	277
20090928	271	0.76	491	172	319	219	272
20091002	275	0.79	480	176	304	209	271
20091017	290	0.77	431	175	256	163	268
20091117	321	0.77	326	114	212	145	181
20091118	322	0.77	322	115	207	140	182
20091124	328	0.76	304	117	187	124	180
20091127	331	0.78	295	115	180	114	181
20091210	344	0.78	268	117	151	92	176
20100108	8	0.77	280	115	165	99	181

3.3.2 Process flow

The CrSPM algorithm for obtaining direct normal, diffuse and global components comprises five steps (Brooks, 2010):

1) Filtering: intermittent upper global and lower diffuse data are separated out from the composite PSP output signal. This is achieved using a statistical filtering approach in which the ramp rate of the PB trace is monitored so as to

detect the presence of a transition sequence, as illustrated in Figure 2.13 (c). The ramp rate, ΔE_i, is defined as:

$$\Delta E_i = \frac{E_i - E_{i-1}}{E_{i-1}} \times 100\% \qquad\qquad i = 2, \ldots, N \tag{3.1}$$

Since diffuse irradiance curves are flatter than their global irradiance counterparts under clear sky conditions, the threshold rates for identifying transition in the statistical filtering schema are set at 2% and 3% for DHI and GHI respectively. Early morning and late afternoon measurements are subject to additional visual inspection to ensure the quality of the filtering step.

2) Curve-fitting: following the removal of transition data and the separation of the composite trace into fragmented DHI and GHI traces, a fourth-order polynomial curve is applied to reconstitute the data as independent, continuous curves. Irradiance curves are expressed as a function of time, where time is defined as the normalised fraction of a 24-hour period. The curve-fitting technique differs from a previous method demonstrated in Brooks et al. (2007), where irradiance was correlated with the cosine of Z. The approach used here is simpler to employ and gives acceptable results.

3) Thermal offset correction: data from the perforated band PSP are corrected for thermal offset by subtracting the product of PSP net long wave responsivity and net radiation, as measured by SRRL pyrgeometers, from the pyranometer output, as described in equation (1.3). Positive thermal offset effects caused by the geometry of the perforated band are estimated to be on the order of 1 W/m^2 (Reda, 2010) and are disregarded in calculations of overall performance.

4) Shadow band correction: diffuse horizontal irradiance data are corrected for that portion of the sky obscured by the perforated band, according to the empirically derived function given in Figure 2.15.

5) Calculation of DNI: reformed functions representing E_g and E_d are used to calculate E_{bn} from equation (1.2).

3.4 Clear sky results

3.4.1 Uncertainty analysis

Measurement uncertainty (Table 3.3) describes the difference between an instrument’s output and the ‘true’ value of the solar component which is sought, and thus quantifies sensor error. Model uncertainty, on the other hand, refers to the difference between reference data and the predicted radiometric data from the perforated band processing methodology. The former is based on instrument calibration, but gives no insight to the effectiveness of the shadow band algorithm. The latter idealises the reference data as true, even though they are not, to characterise differences between competing measurement schemes.

This study is principally concerned with model uncertainty since the decision to implement a perforated band in preference to a competing radiometric scheme would rest on the relative performance of the two. In effect, the model uncertainties given in this study benchmark perforated band performance against a number of the reference schemes given in Table 1.2.

Model uncertainty

Perforated band performance is quantified through the metrics of mean bias difference (MBD) and root mean square difference (RMSD). These are the most commonly used measures of uncertainty in radiometric analysis and are cited in numerous modelling studies (Batlles et al., 2000; Dazhi et al., 2012; Erbs et al., 1982; Gueymard, 2009; Ineichen, 2006; Jacovides et al., 2006; Kudish and Evseev, 2008; Muneer and Younes, 2006; Perez et al., 1990a; Perez et al., 1990c; Singh et al., 1996; Skartveit et al., 1998; Zawilska and Brooks, 2011).

MBD quantifies the systematic difference between predicted values and their reference measurements, while RMSD indicates random error. Although both are important, RMSD may be considered the primary metric in assessing model performance since it captures the dispersion of predicted values, and is sensitive to poorly performing models. MBD and RMSD are calculated using equations (3.2) and (3.3) to yield values in [W/m^2] or using equations (3.4) and (3.5) to give equivalent percentages, where the divisor, $\bar{E}_{meas}$, is the average measured irradiance from the reference dataset (Gueymard and Myers, 2008b):

$$\text{MBD} = \frac{1}{N}\sum_{i=1}^{N}[E_{mod} - E_{meas}] \tag{3.2}$$

$$\text{RMSD} = \sqrt{\frac{1}{N}\sum_{i=1}^{N}[E_{mod} - E_{meas}]^2} \tag{3.3}$$

$$\%\text{MBD} = \frac{\text{MBD}}{\bar{E}_{meas}} \times 100\% \tag{3.4}$$

$$\%\text{RMSD} = \frac{\text{RMSD}}{\bar{E}_{meas}} \times 100\% \tag{3.5}$$

In the above equations, E_{mod} is the modelled (interpolated) value of irradiance, E_{meas} is the measured reference value and the population size is N.

3.4.2 Perforated band model uncertainty versus reference data

The application of the CrSPM is illustrated in Figure 3.3 for sample data from October 28, 2008 (n = 302). Unprocessed values from the PSP are shown in (a), following which transition data are removed and polynomial functions are used to reform the global and diffuse curves in (b). In (c) the final predicted irradiance curves are plotted along with reference data. For the given day (n = 302), the shadow band correction factor is 1.05 and the number of transition data equals 128 out of 633 minute values ($Z < 90°$). Measured data in (c) are shown in black and model values in grey. For $Z < 70°$, the MBD and RMSD values are –1.9% and 2.3% (global), 0.05% and 3.5% (diffuse), and –0.8% and 1.4% (direct). The R^2 coefficients applicable to the polynomial curves in (b) are 1.000 and 0.994 for global and diffuse irradiance respectively.

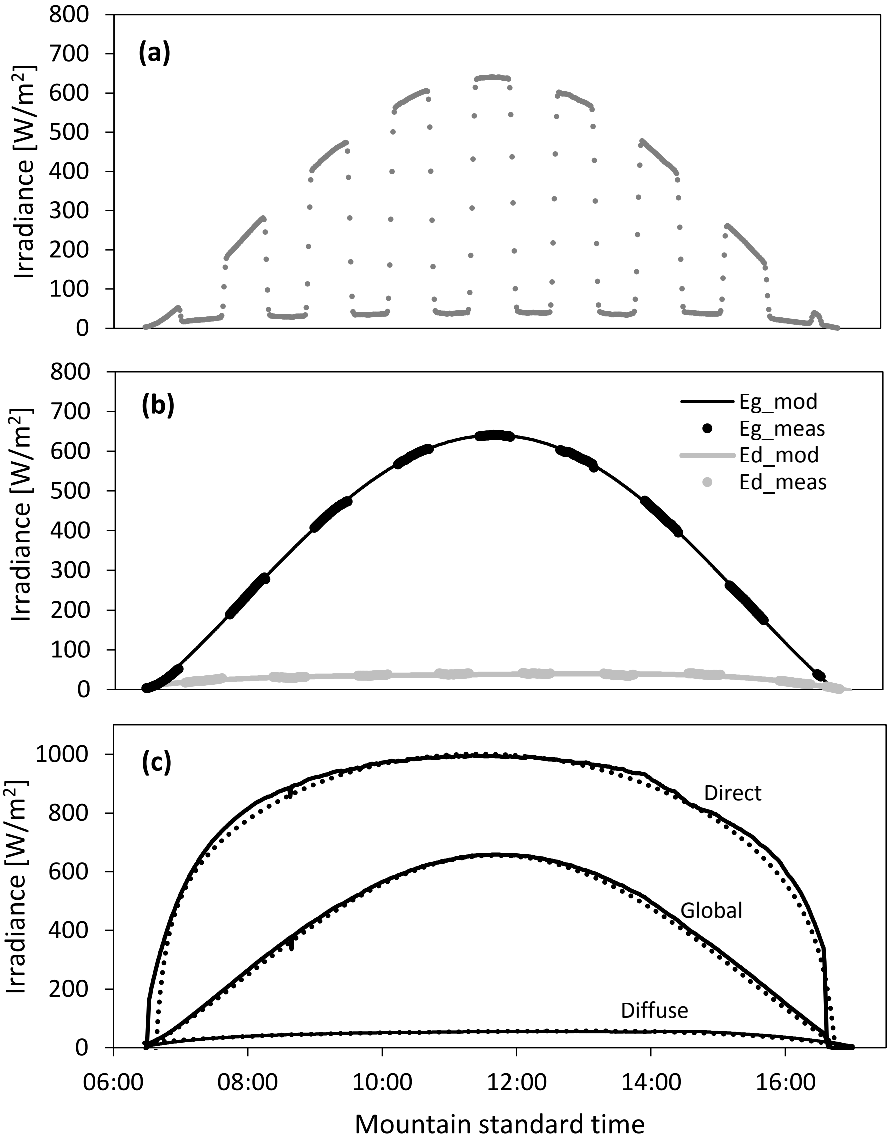

Figure 3.3: Application of the CrSPM to SRRL data on 28 October 2008 with (a) raw data, (b) separated DHI and GHI fragments and (c) model values shown as dashed lines and reference data as solid lines (Brooks, 2010).

The overall performance of the system under clear sky conditions is summarised in Table 3.5, which gives statistics for the full dataset of 14 002 minute-average values. The statistics are generated from mean measured irradiance values of 654.3 W/m^2 (global), 71.2 W/m^2 (diffuse) and 944.9 W/m^2 (direct). The perforated band system under-predicts DNI versus the reference data by 2.6 W/m^2 on average, or 0.3%. Random error for the direct component is 2.0%. The perforated band is effective at predicting global horizontal irradiance under clear sky conditions, returning a root mean square difference of just 2.7% and negligible bias. The RMSD and MBD values for diffuse horizontal irradiance are 13.6% and 7.9%, respectively. Diffuse and direct normal irradiance are both normally distributed for the full dataset, while the global distribution indicates a positive skewness. Kurtosis is close to zero for all three components.

Table 3.5: Clear sky performance of the perforated shadow band (Brooks, 2010).

	MBD (W/m^2)	**MBD (%)**	**RMSD (W/m^2)**	**RMSD (%)**
***Z* < 70°, *N* = 14002**				
Global, E_g	0.3	0.1	17.3	2.7
Diffuse, E_d	5.6	7.9	9.7	13.6
Direct normal, E_{bd}	-2.6	-0.3	19.0	2.0

3.4.3 Seasonal effects

As a check on seasonal dependence, daily averages of RMSD and MBD are plotted against the day number in Figure 3.4 (a) to (c). Some variation is evident suggesting that the bias difference, and to a lesser extent the random difference, is affected by changes in declination angle. Whether this is caused by seasonal adjustment of the band's position relative to the pyranometer sensor, by seasonal variation in sun strength or by other declination-related factors is not clear. Neither the curve-fitting procedure nor the location and number of apertures in the perforated band are thought to be the cause, however, since the R^2 values for GHI are consistently close to 1.00 throughout the year. Similarly, there is no obvious pattern in the deviation of the coefficient for DHI.

Since the data in Figure 3.4 represent differences between predicted and reference irradiances, it is possible that any seasonally-related variation is due to inaccuracies in the reference measurements and the PSP resulting from cosine response errors. The calibration factor for the reference pyranometer (CM22) is a fixed value obtained from the inverse of responsivity at Z = 45°, however responsivity decreases at higher zenith angles. In winter when high zenith angles prevail and the output voltage of the CM22 is multiplied by a fixed calibration factor, slightly lower readings are produced. The effect is more pronounced for the PSP (Myers, 2010a), thus MBD reflects an underestimation by the perforated band system relative to the reference data when zenith angles exceed 45°.

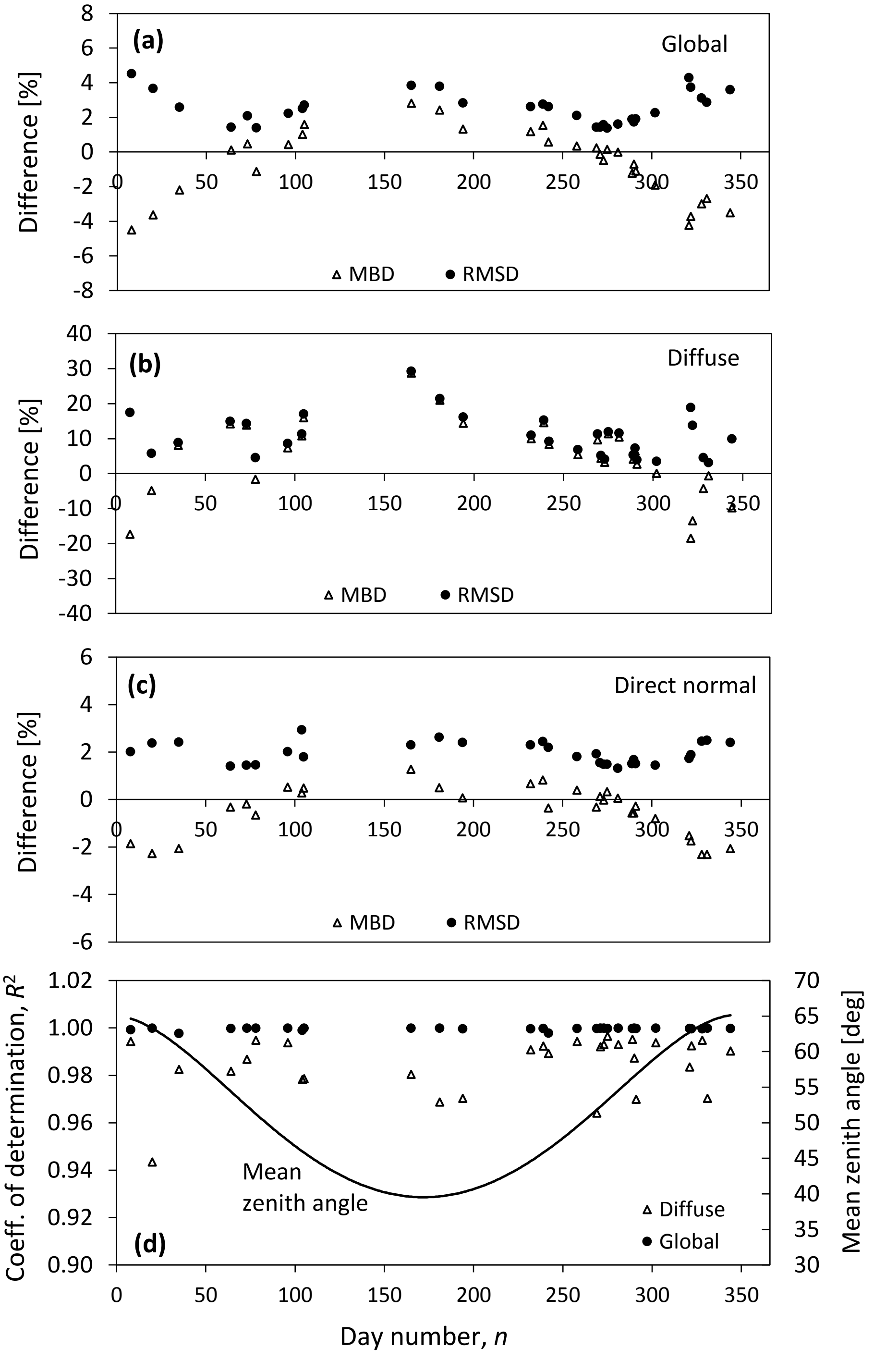

Figure 3.4: Mean bias and root mean square differences for (a) GHI, (b) DHI and (c) DNI versus day number at NREL SRRL, including R^2 coefficients for diffuse and global regression curves (d) (Brooks, 2010).

For low zenith angles the reverse is true and the model overestimates global irradiance, as shown in Figure 3.4 (a). Interestingly, bias difference for global irradiance is close to zero around $n = 100$ and $n = 250$ when the mean daily zenith angles are in the region of 45°.

3.5 Band performance compared with radiative transfer models

Radiative transfer models can estimate sun strength without direct measurement of solar flux and thus represent a potential alternative to the deployment of radiometers. They operate through the measurement and manipulation of indirect parameters such as geographic location, zenith angle, aerosol optical depth (AOD), barometric pressure and turbidity. They may be simple formulations based on empirically-derived coefficients, for example the ASHRAE model (ASHRAE, 1972), or complex models that require multiple inputs, for example the REST2 transmittance model of Gueymard (2008), described in equation (1.1).

Table 3.6 compares the statistical performance of eighteen clear-sky radiative models with that of the perforated shadow band system. The radiative models were not tested concurrently with the PB system but were implemented by Gueymard (2012) using 1-minute averaged NREL data gathered from June to July 2002 and from March to May 2005. Datasets were checked to eliminate the presence of cloud. The PB uncertainties listed for comparison are those reported in Table 3.5 using the 4th order curve-fitting methodology of the CrSPM applied to cloud-free data. Additionally, uncertainties are given for a ramp interpolation function applied to PB data on days for which $K_{T\_Day} \geq 0.75$, as described in Chapter 4. The latter were generated under predominantly clear skies in which some cloud may have been present, and are included here for comparison. Processing was carried out using the cloudy sky processing methodology that relies on the ray trace model of pyranometer exposure as a filtering mechanism, rather than the statistical filtering described in section 3.3.2.

In Table 3.6 the number of input parameters to each model, other than the date, zenith angle and solar constant, is indicated in column 2. In general the uncertainty is inversely proportional to the number of input parameters to the model. The REST2 model, for example, requires surface albedo, barometric pressure, total ozone abundance, total nitrogen dioxide abundance, precipitable water, the Angström wavelength exponent, Angström turbidity coefficient and aerosol single-scattering albedo. Some of these must be obtained using sensors such as the sunphotometer that are complex or expensive to operate. Thus, although the better models perform as well as conventional radiometric sensors, it is not practical to employ them across networks with large numbers of remotely distributed ground stations.

Other than REST2, the perforated band system utilising the CrSPM for data processing outperforms the radiative models under cloud-free conditions. It does so with two inputs: the PSP sensor data and infrared measurements for thermal offset correction. This is compared to the multiple inputs required by the better transfer models in the table. Importantly, the models cannot function in the presence of opaque cloud and are thus quite restricted in their application, while the PB system can decompose global horizontal irradiance to obtain the diffuse and direct normal components under the full spectrum of sky conditions, albeit with differing levels of uncertainty. Chapters 4 and 5 address the operation of the PB system under partly cloudy and overcast conditions.

Table 3.6: Radiative transfer models tested by Gueymard (2012) at NREL SRRL under cloud-free conditions compared with PB performance.

Radiative Transfer Model	No. of model inputs	DNI RMSD [%]	DHI RMSD [%]	GHI RMSD [%]	DNI MBD [%]	DHI MBD [%]	GHI MBD [%]
REST2	8	1.3	11.9	1.6	0.2	-1.7	0.0
Ineichen	3	2.1	26.7	2.5	1.1	-18.4	-1.6
METSTAT	5	2.8	26.0	2.1	2.2	-25.4	-1.6
Iqbal-C	6	3.6	18.4	1.6	2.7	-15.5	0.1
Yang	4	4.0	27.6	1.3	3.4	-21.2	0.0
Bird and Hulstrom	6	4.7	19.5	2.5	-3.3	5.2	-2.1
Hoyt	5	4.8	24.0	4.1	0.9	-19.8	-1.9
MRM-5	5	5.2	35.5	1.2	3.8	-26.1	-0.4
CSR	5	6.9	26.0	2.6	6.8	-25.4	2.4
ESRA	2	8.5	21.3	5.6	7.8	-11.3	5.3
Heliosat-1	2	8.5	26.6	4.6	7.8	-19.2	4.2
Hottel Liu and Jordan	1	14.1	68.0	4.3	5.5	-44.7	-1.1
ASHRAE	0	14.3	49.6	7.3	-6.7	-3.3	-5.9
NRCC	4	14.4	60.9	4.9	3.4	-12.4	1.4
McMaster	5	14.8	52.3	5.9	7.3	-14.6	4.3
Heliosat-2	2	15.7	40.0	8.9	15.1	-31.9	8.6
Kumar	1	21.2	85.1	7.6	16.5	-66.1	5.8
Fu and Rich	1	32.1	122.1	12.5	-28.5	100.1	-9.6
[*]Perforated Band – 4th order	2	**2.0**	**13.6**	**2.7**	**-0.3**	**7.9**	**0.1**
[**]Perforated Band - Ramp	2	**8.7**	**18.9**	**7.4**	**-1.9**	**5.8**	**-1.6**

[*] Applied to cloud-free data as per the clear sky processing methodology.

[**] Applied to data for which $K_{T\_Day} \geq 0.75$, using cloudy sky processing methodology.

3.6 Summary

Clear sky performance of the perforated shadow band was quantified using a clear sky processing methodology implemented on test data gathered at the NREL SRRL facility in Golden, Colorado, between March 2008 and January 2010. The test protocol utilised calibrated sensors for the PB system and the collocated reference instruments. The measurement uncertainty of the sensors was estimated at ± 5% for GHI and DHI, and ±3.9% for DNI.

Predictions of GHI, DHI and DNI obtained from perforated band system were compared with data from research-grade Kipp & Zonen instruments to quantify performance. Thermal correction of the PSP data was carried out.

A statistical evaluation of PB uncertainty versus reference measurements at zenith angles up to 70° indicated mean bias differences of 0.3 W/m^2 for GHI, 5.6 W/m^2 for DHI and –2.6 W/m^2 for DNI. These correspond to MBD percentages of the mean measured values equal to 0.1%, 7.9% and –0.3% respectively. Root mean square differences relative to the reference values were 17.3 W/m^2 or 2.7% for GHI, 9.7 W/m^2 or 13.6% for DHI and 19.0 W/m^2 or 2.0% for DNI. By comparison, most radiative transfer models utilising a similar number of input parameters deliver RMSD and MBD percentages several times higher. Only minor seasonal variation in PB performance was noted, and this was likely due to exaggeration of the radiometer’s cosine effect during winter, rather than the perforated band itself.

Under cloud-free conditions, the perforated shadow band is an effective tool for decomposing global horizontal irradiance so as to obtain the diffuse and direct normal components. Considering the relative inexpense of the system versus alternate schemes in Table 1.2, the retrofitting of an existing pyranometer with the perforated band may be considered a worthwhile option for operators wishing to measure more than a single solar component at a ground station. The system offers particular benefits for stations in arid regions measuring only diffuse irradiance with a single pyranometer and a conventional shadow band. In such cases, replacing the solid band with a perforated version enables the determination of all three solar components at little additional cost.

The question that must be addressed is how well the perforated band functions when skies are not cloud-free. When cloud intermittently obscures the PB sensor the coherent data traces from the pyranometer become chaotic, rendering the clear sky processing methodology ineffective. Under such conditions, irradiance ramp rates fluctuate excessively, the statistical filtering technique employed in the CrSPM does not work and the stochasticity of the fragmented traces precludes curve-fitting as an effective regeneration technique. Chapter 4 thus considers several alternate approaches to dealing with perforated band data under cloudy conditions and formalises the cloudy sky processing methodology.

4. CLOUDY SKY CONDITIONS: METHODOLOGY

4.1 Introduction

In this chapter a method is proposed for processing data generated by the perforated shadow band under partly cloudy and overcast conditions. The cloudy sky processing methodology (CdSPM) enables the generation of separate diffuse and global irradiance curves from a single PB pyranometer output trace despite the lack of structural coherency in the data.

A number of techniques are described for replacing missing values from the perforated band trace, including mathematical averaging methods, numerical interpolation, polynomial curve-fitting, statistical methods and radiometric modelling. In addition, an adaptive interpolation scheme is proposed that monitors clearness index and deploys specific interpolation models to minimise uncertainty.

The performance of the PB system under partly cloudy conditions was first addressed in a preliminary paper by Brooks and Roberts (2010), presented at the 2010 Optics and Photonics Conference of the Society of Photo-Optical Instrumentation Engineers (SPIE) in San Diego. Parts of this chapter are drawn from that paper and from a second article by Brooks et al. (2014) on the replacement of missing data in radiometric time series, presented at the 2nd Southern African Solar Energy Conference (SASEC) in Port Elizabeth.

4.2 Cloud effects in broadband radiometry

The World Meteorological Organisation defines cloud as a hydrometeor consisting of minute particles of liquid water or ice, suspended in the free air (World Meteorological Organization, 1987). Clouds may be classified according to ten primary genera (eg. *cirrus*, *stratos* and *cumulus*), fourteen species (defining form, structure and dimension, eg. *congestus*, *floccus* and *lenticularis*) and nine varieties (eg. *radiatus* and *translucidus*). Classification is done visually and with several types of instrumentation, including radiometers, sky spectral cameras, LIDAR, radiosondes and satellite imagery (Tapakis and Charalambides, 2013).

Clouds affect the magnitude of measured irradiance in two ways: first, they may obstruct the solar disc and either reduce or eliminate DNI, and second, they may reflect, dampen or amplify diffuse irradiance. When the solar disc is not obstructed, clouds tend to enhance DHI by scattering and reflection. When DNI is reduced, the overall effect on DHI can be enhancement or dampening, depending on the type of cloud and its degree of opacity (Tapakis and Charalambides, 2013).

In the absence of direct normal irradiance, the DHI and GHI measurements recorded by a pyranometer will be identical, as illustrated in Figure 4.1, which shows changing conditions from clear to cloudy for the UKZN Howard College ground station on 15 May 2011. The global irradiance is shown in blue (E_g), the diffuse irradiance is green (E_d) and the perforated band pyranometer output in black (E_f). As cloud occludes the radiometric station in the mid-afternoon, DNI is largely extinguished and DHI is enhanced, tracking the global value. After shading occurs, the coherent data curves evident throughout the morning become stochastic.

In a number of studies the effect of cloud on pyranometer output has been exploited to predict sky conditions, although with limited success. Duchon and O'Malley (1998) correlated the ratio of measured irradiance over modelled clear sky irradiance, with standard deviation of the observed measurements. The former represents a version of the clearness index and the latter captures the traverse of clouds through the portion of the sky where the sun is located. The results enabled correct prediction of five cloud types about 45% of the time, as measured against human observations.

Using a similar method on Antarctic data, Orsini et al. (2002) reported the successful prediction of cloud type at rates of 94% for cirrus, 67% for *cirrostratus*/*altostratus* and 33% for *cumulus*/*altocumulus*. The success rate is therefore higher under clearer conditions. Attempting to correlate specific forms of cloudiness with irradiance measurements taken by a single pyranometer is thus difficult because of the numerous ways in which clouds interact with the sun, and each other, to produce a range of radiometric conditions.

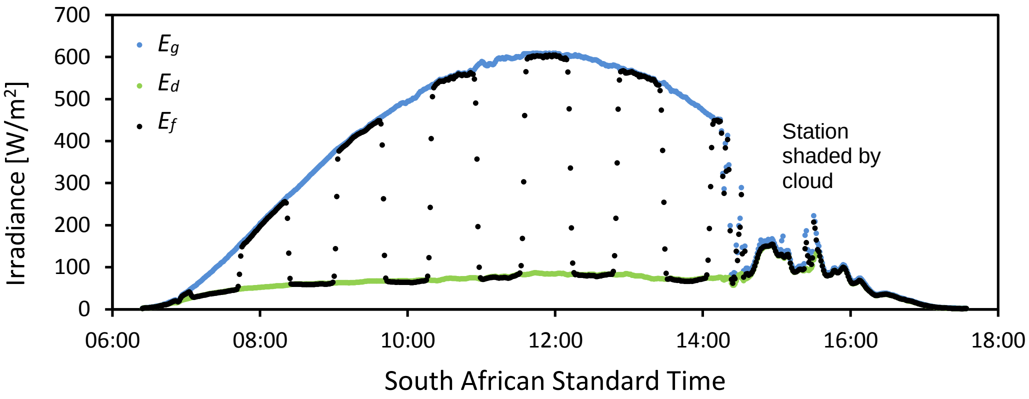

Figure 4.1: Typical interplay between GHI and DHI components logged at 1-minute intervals, as conditions change from clear to cloudy (UKZN data from 15 May 2011).

In general, clouds introduce an unstable element to the measurement record and disrupt the smooth data curves produced under clear conditions. This stochasticity is related to the nature of the cloud field. Tomson et al. (2008) define unstable radiation as successive measurements of global irradiance that vary by more than 50 W/m^2. They note that the most unstable time-series are produced by *cumulus*, *stratocumulus translucidus* and *altocumulus translucidus* clouds.

Mathematically, a solar radiation time-series comprises of a deterministic component, caused by astronomical effects, and the stochastic element caused by meteorological effects (Tovar-Pescador, 2008). Stochasticity is also affected by the frequency with which readings are sampled; at 1-minute intervals (applicable to this study) the potential for chaotic data structures to arise is high, while 30-minute or hourly values benefit somewhat from the smoothing effect of averaging.

4.3 Perforated band sensor output in the presence of cloud

In the presence of cloud, the sensor under a perforated band may be subject to varying degrees of shading from the direct normal component of sunlight, over and above that caused by the perforated band itself. This occurs as clouds drift into and out of the sensor's line of sight to the solar disc. Since the PB system is only capable of measuring DHI or GHI at any given moment, the reduction in DNI is not recorded directly, but is expressed through fluctuations in the two measured components.

The degree of sensor occlusion and the frequency with which an irregular shading regime is imposed by cloud on the PB data trace vary considerably. This variability yields a range of trace morphologies from near-clear sky curves with minimal disruption (high clearness index conditions) to stochastic structures in which the DNI is heavily attenuated for all or part of the day.

The disruption of the perforated band trace is illustrated in Figure 4.2. This includes the PB sensor trace (in black), reference irradiances in blue (GHI), red (DNI) and green (DHI), and the associated cloud patterns as photographed by a Total Sky Imager (TSI) at the NREL site on 3 May 2011. The daily clearness index was 0.58. Clear sky conditions prevail up until 10:00 during which the structure of the diffuse and global curves is strongly coherent and the PB values cycle unambiguously between the two, to an overcast period between 12:00 and 14:00 when both the PB sensor DHI and GHI traces continuously track the reference diffuse irradiance. A partly cloudy period follows between 14:00 and 15:30 during which no relationship can be visually determined between the output from the PB sensor and the reference data.

To illustrate the range of data structures produced under increasingly cloudy conditions, Figure 4.3 shows eight sample days from the NREL site, with the daily clearness index decreasing from high (a) to low (h). Clearness index typically varies between about 0.1 and 0.8, although extreme values occasionally occur outside this range.

The sequence of eight graphs illustrates how increasing cloudiness and decreasing clearness index are associated with a breakdown in structural coherency of the PB sensor output. Under cloud-free conditions (a), there is no ambiguity between diffuse and global irradiance measurements from the PB sensor, making visual sorting and processing possible. As K_{T_day} decreases in panes (b) through (f), it becomes difficult and in some cases impossible to determine the difference between the two components visually. Furthermore, the transition data cannot always be distinguished which adds to the complexity of the processing task. In panes (g) and (h) there is little difference between the DHI and GHI measurements since the DNI component is absent. It should be noted that short-term breakouts of sunshine can still occur for very low clearness index days, although they are not present in the data of Figure 4.3.

Figure 4.3 illustrates why the visual processing methodology of Chapter 3 cannot be used under partly cloudy conditions. A more sophisticated approach is required to enable sorting and processing of the PB data in the presence of cloud. Whether cloudy or clear, the following logic applies to the operation of the system:

1. When sunlight is admitted through an aperture in the band, the pyranometer is unshaded and records global irradiance
2. When the band occludes the sensor, the pyranometer records diffuse irradiance
3. When the sun is part-hidden by the band, whether emerging from behind the band or moving into a shading position, the resulting data are indeterminate and are classified as transition values.

As with clear sky operation, when the PB system is recording GHI, the DHI values are unknown and vice versa. This fact can be used to improve the CdSPM, as described in Section 4.8.

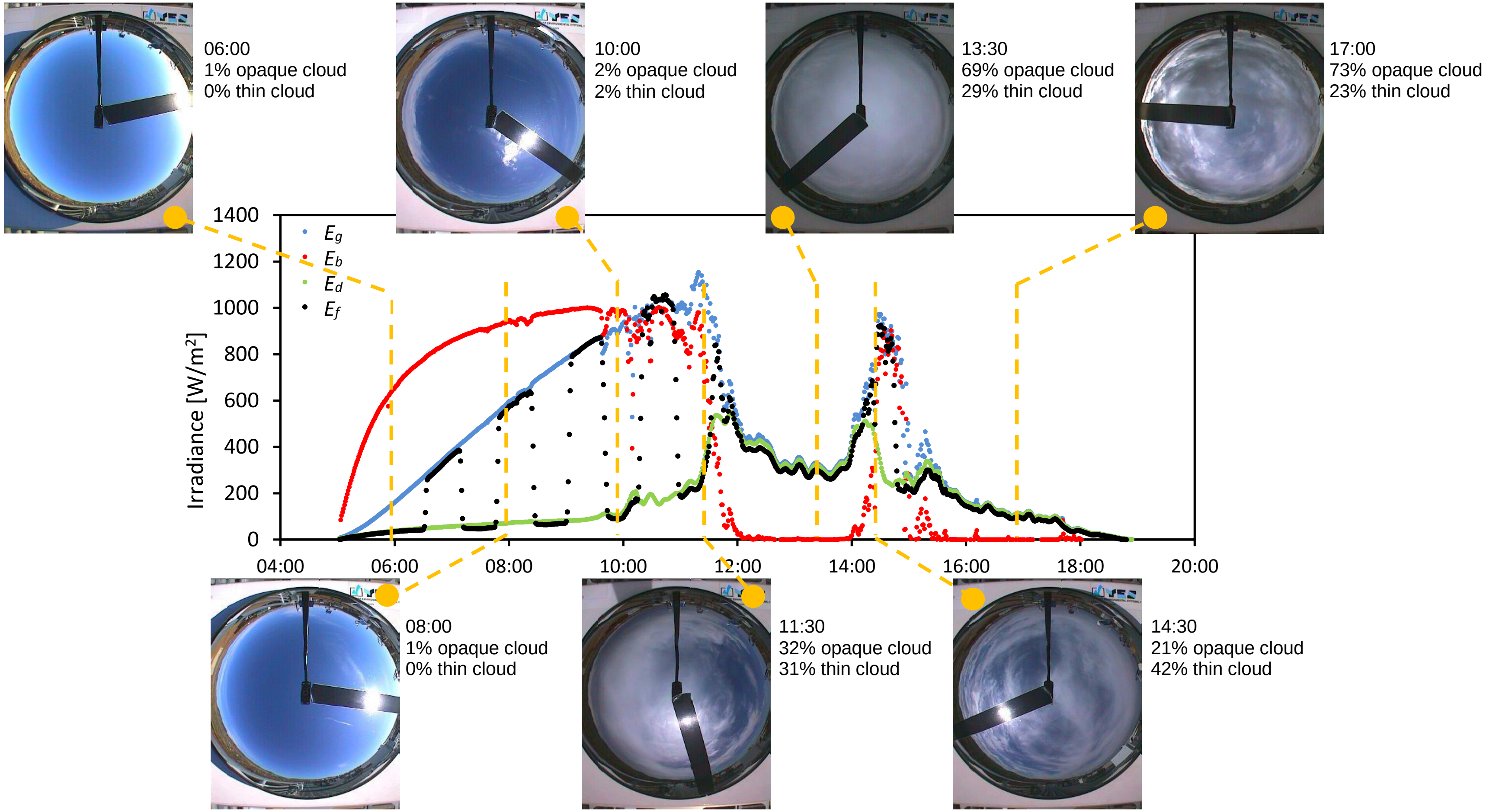

06:00
1% opaque cloud
0% thin cloud

10:00
2% opaque cloud
2% thin cloud

13:30
69% opaque cloud
29% thin cloud

17:00
73% opaque cloud
23% thin cloud

08:00
1% opaque cloud
0% thin cloud

11:30
32% opaque cloud
31% thin cloud

14:30
21% opaque cloud
42% thin cloud

Figure 4.2: Perforated band output and corresponding cloud cover under variable weather conditions on 23 May 2011 at NREL SRRL.

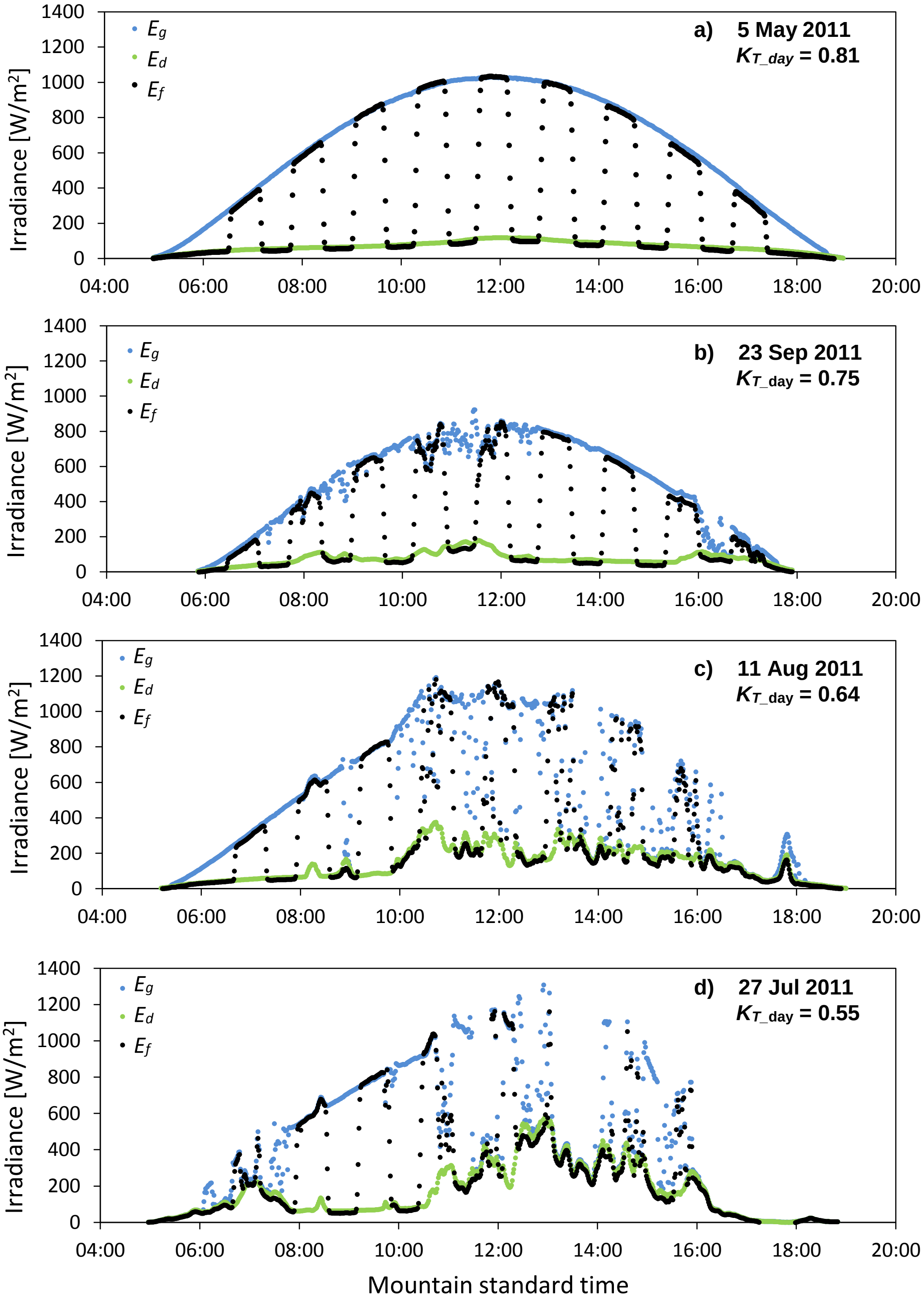

Figure 4.3: Deterioration in the coherency of perforated band data structures with decreasing daily clearness index, K_{T_day} (data from NREL SRRL).

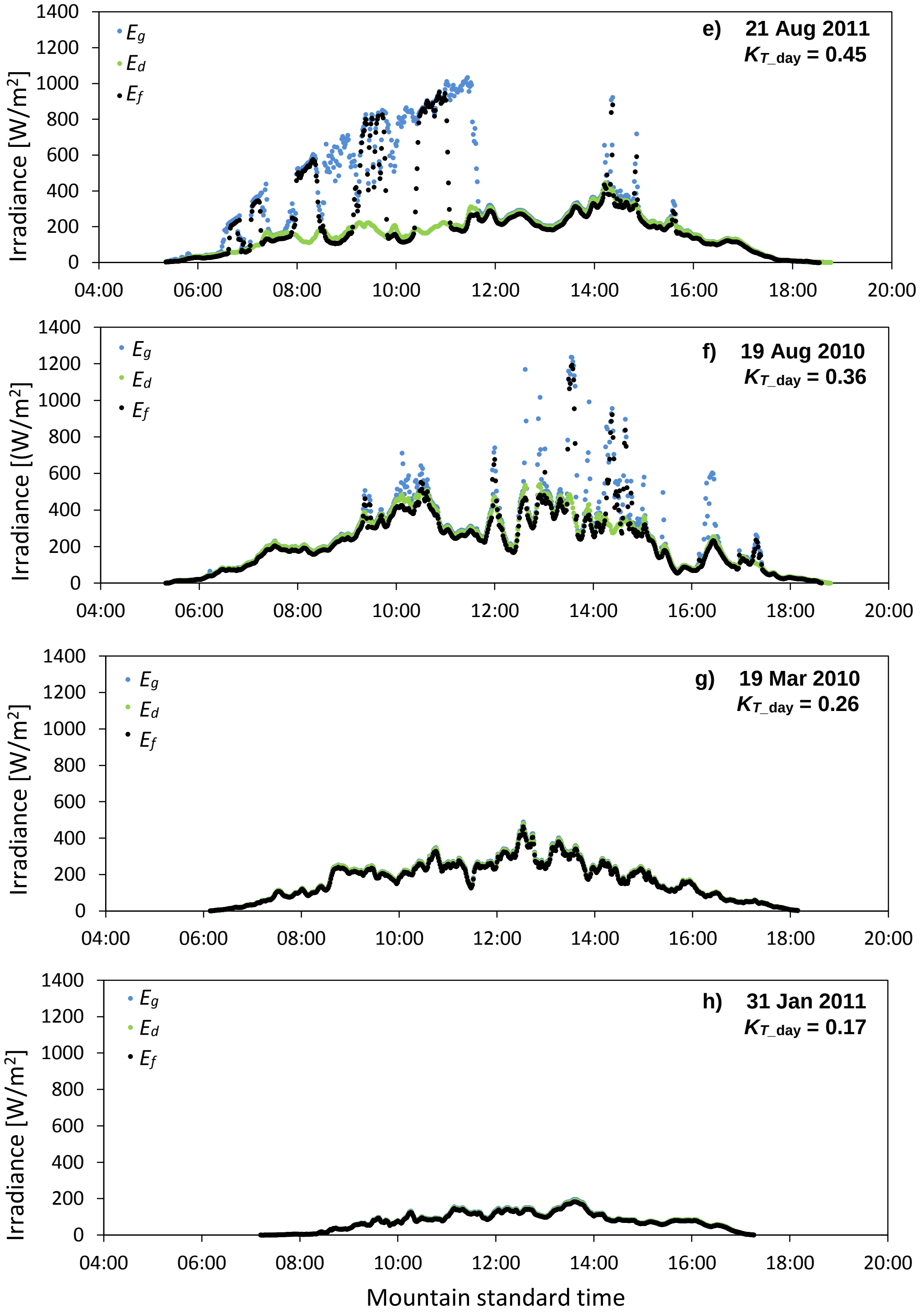

Figure 4.3 (continued): Deterioration in the coherency of perforated band data structures with decreasing daily clearness index, K_{T_day} (data from NREL SRRL).

4.4 The cloudy sky processing methodology (CdSPM)

4.4.1 Inputs

The cloudy sky processing methodology disaggregates the output signal from a PB pyranometer at 1-minute resolution into separate data for DHI and GHI, replaces missing data from the resulting fragmented traces and generates separate, continuous curves for the diffuse and global components. These are used to derive DNI by combining the resulting data through equation (1.2). It is required that the methodology be repeatable and sound, so as to minimise statistical uncertainty between the modelled irradiance and the measured reference values.

Although NREL reference data are used in this study to quantify CdSPM uncertainty, the final methodology is implementable without recourse to any measurement other than the output from a pyranometer located under a perforated shadow band. The following inputs were used to develop the CdSPM, and are described in the sections that follow:

1. Two temporally independent datasets; the first for development of the methodology and the second for its validation.
2. A filtering algorithm to eliminate errant data
3. The ray trace model of pyranometer exposure described in Chapter 3
4. Mathematical, numerical and statistical models for replacement of missing data
5. Radiometric decomposition models
6. Statistical metrics for the analysis of model uncertainty
7. An adaptive interpolation scheme to deploy interpolation methods optimally and in response to clearness index
8. Two MATLAB software programmes to implement the methodology

4.4.2 Process flow

The CdSPM is implemented in five stages as described in Figure 4.4. In stage 1 raw radiometric data at 1-minute intervals from the NREL ground station are combined with solar position information to yield the 18-column, daily spread sheet files making up dataset #1. The measurement data are filtered to screen out instrumentation errors and weather-related problems. The files for dataset #2 are configured the same way but held over for use later in the sequence. Sections 4.5 and 4.6 describe stage 1 in detail.

In stage 2, the daily data files are read by a MATLAB application that applies the ray trace model of pyranometer exposure to isolate GHI and DHI data as separate traces. The software then applies a range of interpolation schemes, described in Sections 4.8 and 4.9, to generate artificial values for the missing measurements.

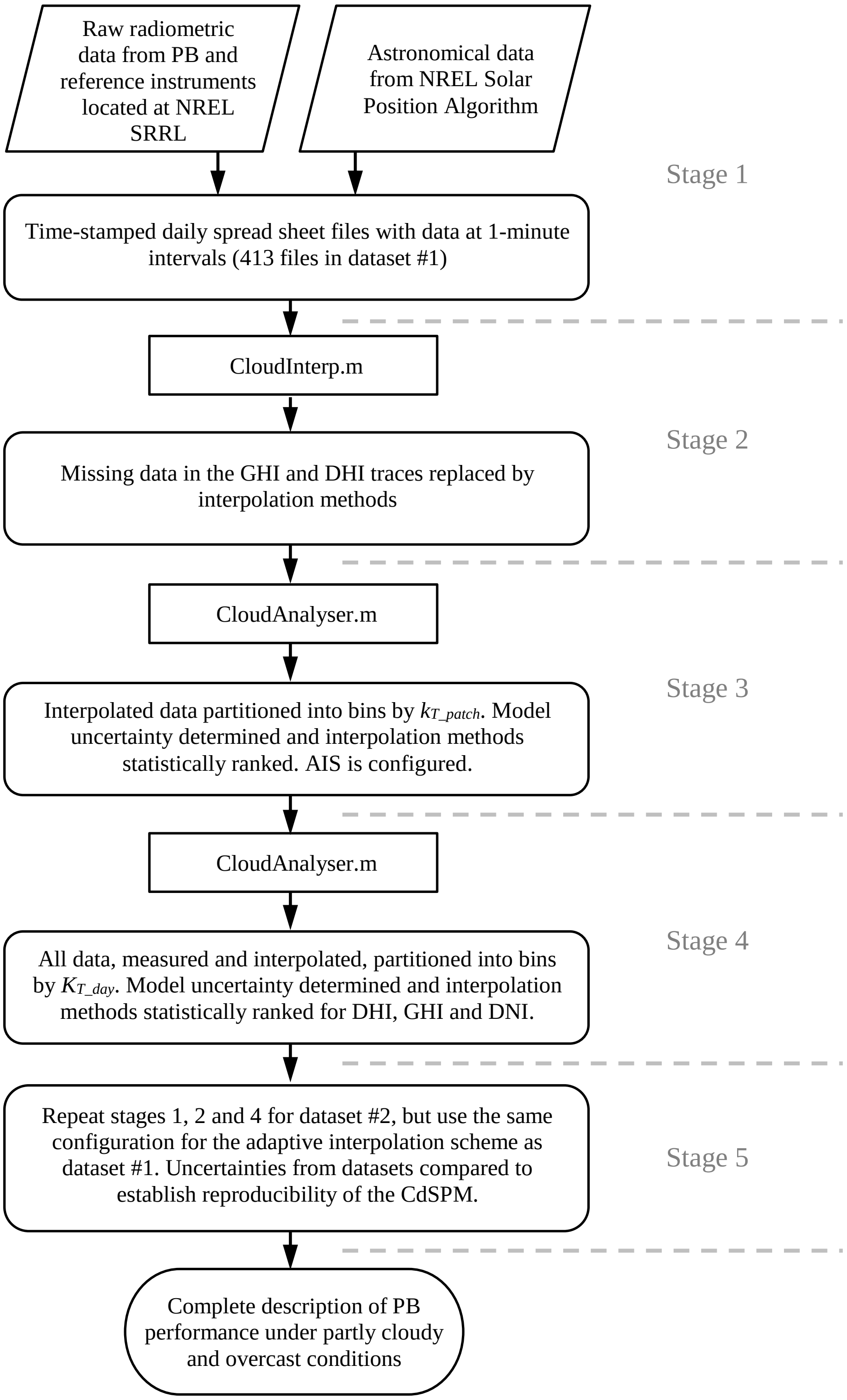

Figure 4.4: Stages of the cloudy sky processing methodology.

Stage 3 classifies the interpolated data for each scheme into bins using the patch-wise clearness index, k_{T_patch}, as the controlling parameter. There are eight bins covering the spectrum of possible values from 0 to 1. The patch-wise data in each bin are then concatenated to quantify overall statistical uncertainty through parameters such as the root mean square difference and mean bias difference. These metrics permit the ranking of interpolation methods as a function of k_{T_patch}. The adaptive interpolation scheme (AIS), which represents a formula for distributing the most effective interpolation scheme to each gap as a function of that gap's clearness index, is then configured. Stage 3 is executed by the MATLAB application "CloudAnalyser" and described in Section 4.11.

The uncertainty analysis conducted in stage 3 of the CdSPM applies only to interpolated values and therefore does not describe overall PB performance. In stage 4, the analysis is expanded to include all the data generated by the system, both measured as well as interpolated. This is achieved by concatenating the data for the full set and partitioning them into bins based on daily clearness index, K_{T_day}. An uncertainty analysis is conducted by comparing the concatenated data with reference values at 1-minute intervals.

The use of K_{T_day} as the partitioning parameter in the uncertainty analysis of stage 4, and not k_{T_patch}, is necessary to inform decisions about deployment. The perforated band offers a potential improvement over the standard shadow band, but this may not be true in all geographic regions or for all sky conditions. The decision to deploy the band must be made quantitatively, using available radiometric data, but this is contingent on linking system performance to an easily understood and readily available metric. One of the more commonly available metrics is average daily clearness index, which can be obtained from ground-based data, satellite imagery and maps such as that provided by Diabate et al. (2004). The final description of PB performance (uncertainty) is therefore given in terms of daily clearness index.

A comparison between results from the temporally independent datasets #1 and #2 is conducted in stage 5 of the CdSPM. This is necessary to confirm reproducibility of the method and to ensure that the uncertainty values determined in stage 4 are a true representation of the system's performance. Inputs to the CdSPM are described in detail in the sections that follow.

4.5 Development and validation datasets

The use of two datasets is a standard approach in the development of radiometric models (Gueymard and Myers, 2008b) and is intended to confirm repeatability and temporal independence of the methodology under investigation. In this study the development and validation datasets (#1 and #2 respectively hereafter), each contain a series of identically formatted spread sheet files, covering different periods. Dataset #1 (413 days) runs from August 2009 to December 2011, with the majority of data from the 2011 year (339 days) and the remainder from 2009 and 2010. The total number of data rows (N) for which $Z < 70°$ is 201 454.

Dataset #2 comprises of 341 days taken exclusively from 2012 and contains 167 681 rows. Metadata for sets #1 and #2 are given in Table 4.

Table 4.1: NREL radiometric datasets #1 and #2 used in the development of the CdSPM.

	Dataset #1 (Development)	**Dataset #2 (Validation)**
No. of daily files	413	341
Time span	August 2009 to December 2011	January 2012 to December 2012
Total number of data rows for $Z < 70°$, N	201 454	167 681
No. of DHI data interpolated	72 756 (36.1%)	60 581 (36.1%)
No. of GHI data interpolated	128 698 (63.9%)	107 100 (63.9%)
Average daily clearness index, K_{T_day}	0.59	0.61

Structurally, each daily file contains 18 columns and between 560 and 897, rows depending on the time of year. The full period from sunrise to sunset is included, from which a subset of measurements are analysed for $Z < 70°$. Table C-1 in Appendix C contains an extract from one of the files (26 November 2011), presented as it appears in spread sheet form. Table C-2 describes the contents of the file, in addition to which further samples of NREL data may be requested from the author.

4.6 Data filtering algorithm

All files were filtered using an algorithm adapted from standards set by the European Commission on Daylight, as reported by Jacovides et al. (2006). This eliminates data that meet the following criteria:

Reference DHI: $E_d > 1.1E_g$ (4.1)

Reference DHI: $E_d > 0.8E_o$ (4.2)

Reference GHI: $E_g > 1.2E_o$ (4.3)

Reference DNI: $E_{bn} > E_{on}$ (4.4)

Perforated band PSP: $E_f > 1.2E_o$ (4.5)

All radiometers: Output signal < –100 W/m^2 (check for disconnection) (4.6)

The exclusion criteria remove non-physical readings from the dataset. For example, equation (4.3) ensures that the global horizontal irradiance from the reference instrument does not exceed the global extra-terrestrial irradiance by more than 20%. Equation (4.6) eliminates egregious errors due to electrical disconnection, which typically produces a “-9999” output signal.

4.7 The ray trace model as disaggregation tool

The ray trace model is incorporated in the CdSPM software to distinguish between data types under cloudy conditions. The hour angle value for each measurement is assessed (column R in Table C-1) from which the associated PB value is designated as diffuse (E_{fd}), global (E_{fg}) or transitional (E_{ft}). This is illustrated in the upper pane of Figure 4.5 which shows the result for 27 July 2011. Reference GHI and DHI data are given in blue and green respectively. Patches of measured diffuse irradiance (P_{d1} to P_{d10}) are indicated with light red shading and measured global patches (P_{g1} to P_{g9}) are in grey. Transitional gaps are left unshaded. The trace begins with the PB sensor fully occluded, thus the exposure transition sequence for this file is designated Sq_1. Three other sequences are possible throughout the year depending on the initial exposure state of the sensor: initially exposed, partially exposed becoming occluded, and partially exposed becoming fully exposed.

Transitional data are stripped from the trace, leaving separate curves for global horizontal irradiance and diffuse horizontal irradiance, shown in the middle and lower panes of Figure 4.5 respectively. Once fully separated, the DHI and GHI traces each represent a fragmented irradiance time-series comprising patches of known values interspersed with gaps of missing data (G_d and G_g) that must be filled. In the sections that follow, various techniques are described for replacing missing data, some of which are common to both the DHI and GHI traces.

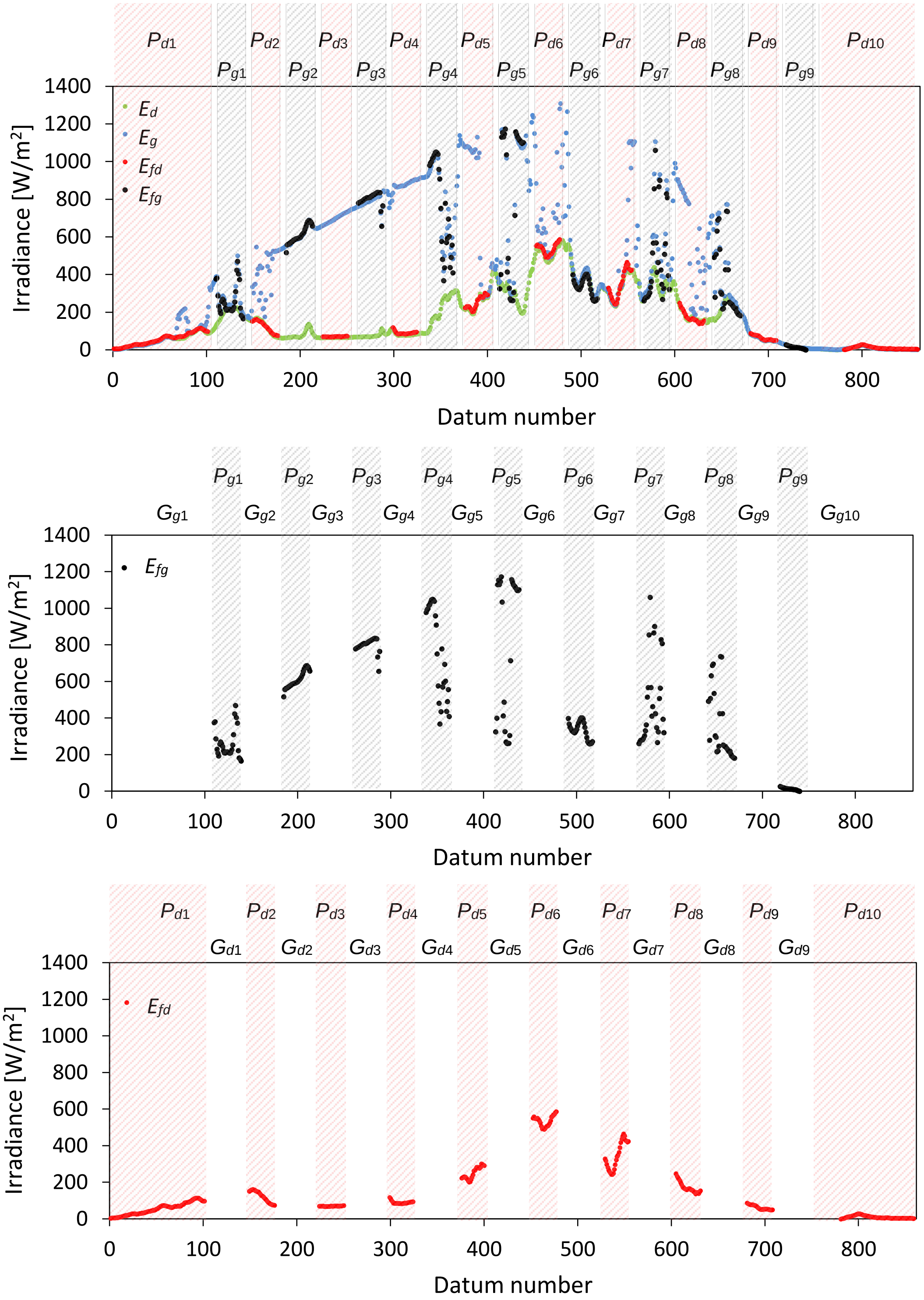

Figure 4.5: Application of the ray trace model to a sample NREL daily file showing measured diffuse data (red) and global data (black).

4.8 Numerical techniques for the replacement of missing data

In the strict definition of mathematical interpolation, a continuous function assumes specified values at discrete points in a field permitting prediction of field values between the known points. When predictions outside of the known values are made, the process is extrapolation (Kreyszig, 1988). In this work interpolation includes any technique that uses known radiometric data from the left and/or right patch of a PB trace, to generate irradiance values in the adjacent gap. Techniques such as curve-fitting and averaging are therefore included.

Although it may not describe the underlying physics governing changes in flux, artificial data generation through interpolation can capture patterns in the trace of a PB system with some accuracy. Some interpolation techniques perform better than others, requiring that different approaches be tested. Table 4.2 lists the techniques used in this study to replace missing radiometric data, some of which are applicable to both the GHI and DHI gaps and others of which are exclusive to one only, as indicated.

Table 4.2: Interpolation methods used in the CdSPM.

Interpolation method	Abbreviation	Type	Applicability
Ramp function	Ramp	Numerical	GHI/DHI
1-minute averaging	1 min	Numerical	GHI/DHI
10-minute averaging	10 min	Numerical	GHI/DHI
20-minute averaging	20 min	Numerical	GHI/DHI
Spline	Spline	Numerical	GHI/DHI
Piecewise cubic Hermite interpolating polynomial	PCHIP	Numerical	GHI/DHI
3rd order polynomial	3OP	Least squares regression	GHI/DHI
4th order polynomial	4OP	Least squares regression	GHI/DHI
5th order polynomial	5OP	Least squares regression	GHI/DHI
ARIMA(1,0,1)	A101	Statistical/numerical	GHI/DHI
ARIMA(1,0,0)	A100	Statistical/numerical	GHI/DHI
ARIMA(0,0,1)	A001	Statistical/numerical	GHI/DHI
ARIMA(0,1,1)	A011	Statistical/numerical	GHI/DHI
ARIMA(1,1,1)	A111	Statistical/numerical	GHI/DHI
Orgill and Hollands	O&H	Decomposition model	DHI
Erbs, Klein and Duffie	Erbs	Decomposition model	DHI
Boland, Ridley and Brown	BRB	Decomposition model	DHI
Boland, Ridley and Lauret	BRL	Decomposition model	DHI
Reindl, Beckman and Duffie	Reindl	Decomposition model	DHI
GHI equals DHI	GeD	Numerical	GHI
Bird and Hulstrom	Bird	Clear sky transmittance model	GHI/DHI/DNI

The interpolation methods in Table 4.2 span a range of techniques. There are relatively simple numerical techniques, such as averaging values from the left and right patches as well as more complex polynomial expressions. Advanced statistical techniques such as the autoregressive integrated moving average (ARIMA) models are included because researchers are now using them in radiometric analyses. The various methods are described in detail in the sections that follow.

A unique feature of the PB system is that for those gaps in the data trace where diffuse irradiance is not known, the contemporaneous global horizontal component is measured. In addition to purely numerical or statistical techniques, this permits another approach to data generation using decomposition models. A decomposition model relates diffuse irradiance to global irradiance via a correlating equation, permitting the prediction of DHI when GHI is the only known component. Details of this data generation method are given in Section 4.9.

Figure 4.6 gives a schema by which the mathematics of some of the techniques in Table 4.2 is formalised (Brooks et al., 2014). In the general case there are N_L 1-minute measurements in the patch to the left of the gap for which $j = 1, ..., N_L$ and N_R 1-minute measurements in the patch to the right of the gap such that $k = 1, \dots, N_R$. The missing data in the gap, which must be artificially generated and are denoted as $E_{int,i}$, comprise of N_G values where $i = 1, \dots, N_G$.

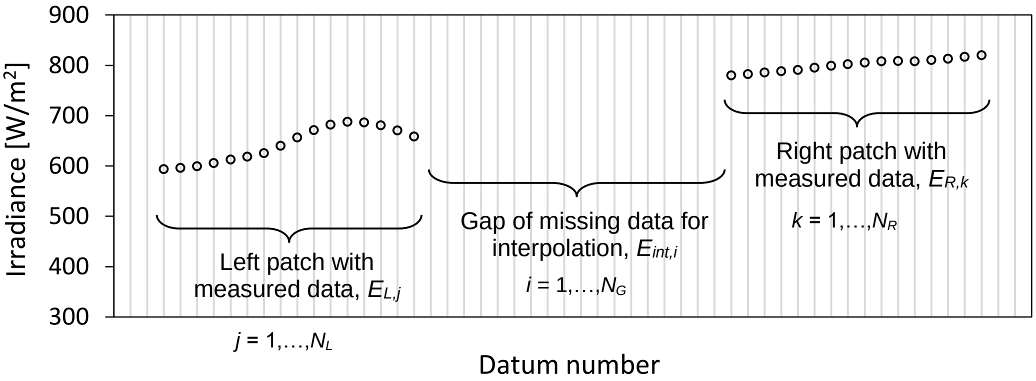

Figure 4.6: Schema used to formalise interpolation methodologies (Brooks et al., 2014).

4.8.1 The ramp function

The ramp function is a type of linear interpolation in which the generated data form a bridge, or ramp, to span the gap between the last measurement in the preceding patch to the left, and the first value in the succeeding patch to the right. For a gap-length of N_G 1-minute values, the i^{th} interpolated value, $E_{int,i}$, is given by equation (4.7).

$$E_{int,i} = E_{int,i-1} + \frac{E_{R,1} - E_{L,N_L}}{N_G + 1} \qquad i = 2, \dots, N_G \tag{4.7}$$

For $i = 1$, the first term on the right becomes E_{L,N_L}. An example is given in Figure 4.7.

4.8.2 1-minute, 10-minute and 20-minute averaging

The 1-minute average interpolation scheme is weighted in favour of the measured irradiance values immediately preceding and succeeding the data gap. All interpolated data assume the same value, generated from the last measurement in the patch to the left of the gap, and the first value in the patch to the right.

$$E_{int,i} = \frac{E_{L,N_L} + E_{R,1}}{2} \qquad i = 1, \dots, N_G \tag{4.8}$$

Where the left or right patch is missing at the start or end of the day, the average is calculated by setting E_{L,N_L} or $E_{R,1}$ equal to zero.

The 10-minute averaging scheme uses ten measured values either side of the gap. Results will be similar to the 1-minute scheme unless the irradiance trace is highly variable in the adjacent patches, in which case the widened range over which sampling occurs will bias the result accordingly. All interpolated data assume the same value, $E_{int,i}$, calculated as follows:

$$E_{int,i} = \frac{\sum_{j=0}^{9} E_{L,N_L-j} + \sum_{k=1}^{10} E_{R,k}}{20} \qquad i = 1, \dots, N_G \tag{4.9}$$

Where the left or right patch contains fewer than ten values at the start or end of the day, the average is calculated from the available data.

The 20-minute averaging scheme uses twenty measured values either side of the gap to calculate an average, further widening the sampling range as compared with the 10-minute scheme. All interpolated data assume the same value, $E_{int,i}$, calculated as follows:

$$E_{int,i} = \frac{\sum_{j=0}^{19} E_{L,N_L-j} + \sum_{k=1}^{20} E_{R,k}}{40} \qquad i = 1, \dots, N_G \tag{4.10}$$

The average is calculated from the available data when the left or right patches contain fewer than twenty values. Graphical examples of the 1-, 10- and 20-minute averaging schemes are given in Figure 4.7 for the 7th diffuse irradiance gap on 27 July 2011 (NREL data). Measured DHI values are represented by black markers and the corresponding reference data are presented as a blue line. The interpolated data are shown as discrete markers in red, green, purple and yellow.

Since the adjacent patches (P_{d7} and P_{d8}) contain variable data, there is a clear difference in the performance of the 1-, 10- and 20-minute averaging schemes. Although none of the schemes capture the variability of the reference DHI within the gap, the 1-minute scheme appears to provide the best visual performance.

Determining the relative effectiveness of each interpolation scheme is a statistical exercise in which the results for each gap, across all days in the datasets, are analysed using appropriate metrics. The overall statistical performance of all schemes is described in Section 4.11.2.

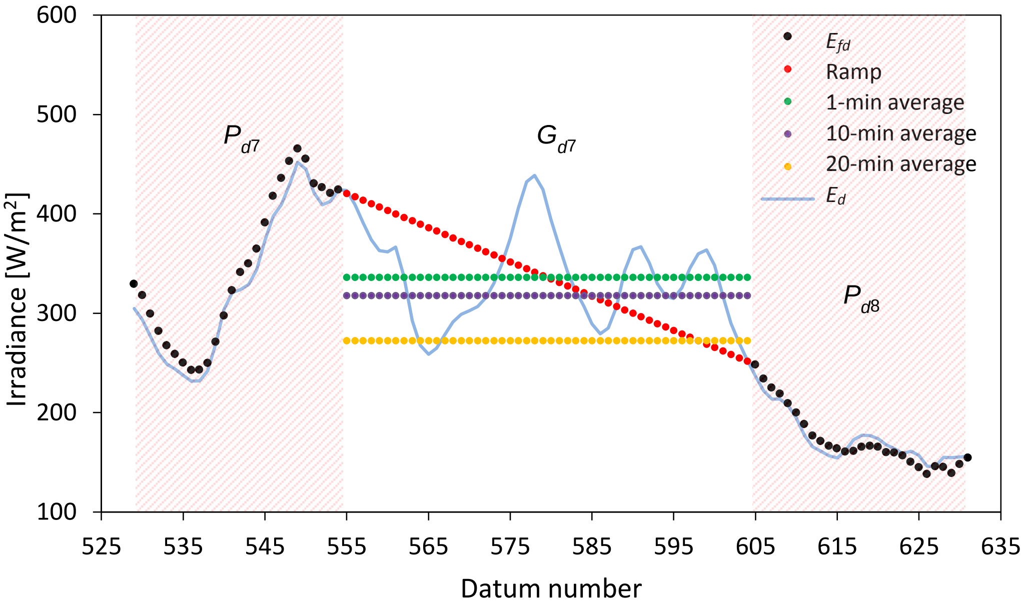

Figure 4.7: Comparison of the Ramp, 1-minute averaging, 10-minute averaging and 20-minute-averaging interpolation schemes applied to a diffuse gap.

4.8.3 Spline interpolation

In the general case, an interpolating polynomial is a unique function, $f_{int}(x)$, passing exactly through n known points in a plane, given by (x_q, y_q), with $q = 1, \ldots, n$. The Lagrangian form of $f_{int}(x)$ is given as follows (Moler, 2004):

$$f_{int}(x) = \sum_{q=1}^{n} \left(\prod_{\substack{r=1 \\ r \neq q}}^{n} \frac{x - x_r}{x_q - x_r} \right) y_q \tag{4.11}$$

Equation (4.11) is an n^{th} order polynomial of n terms. At each known point x_q, (n–1) terms vanish, reducing the expression to y_q and ensuring that the polynomial passes through the given data.

In the case of spline interpolation, constraints are imposed on the slope of the interpolating polynomial. A smooth function is generated by partitioning the domain into subintervals defined by common endpoints, called nodes (Kreyszig, 1988). In this work, the resulting spline function $E_{int,i}$ is made up of one cubic polynomial per subinterval such that the first and second derivatives, $E_{int,i}'$ and $E_{int,i}''$, are continuous everywhere. This ensures that the slopes of adjacent polynomials are equal at the nodes, and that the resulting spline is smooth.

The spline scheme is implemented using MATLAB's "interp1" 1-dimensional interpolation function, together with the "spline" option. All measured data from the patches to the left and the right of a gap are stored as a column vector along with their respective time values. When "interp1" is invoked, $E_{int,i}$ is generated for the interval, along with newly created values for the missing data. These are saved to file as the spline interpolants for the given gap.

When either the left or right patches of measured data are absent at the start or end of a day, gap values are extrapolated. A complete description of the governing mathematics for MATLAB splines is given by De Boor (1978) and Moler (2004).

4.8.4 Piecewise cubic Hermite interpolation

The cubic spline may produce unwanted gradient reversals within a subinterval. This is overcome by the piecewise cubic Hermite interpolating polynomial (PCHIP), based on the work of Fritsch and Carlson (1980), who imposed a condition of monotonicity between nodes. They proposed that the resultant function represents physical reality more accurately than a pure spline.

The spline and PCHIP polynomials are both cubic, but the second derivative of the spline, $E_{int,i}''$, is continuous at each node, while the PCHIP derivative exhibits discontinuities, or jumps. This is illustrated for sample data in Figure 4.8 (Moler, 2004). The requirement of monotonicity is visible between nodes 1 and 2 where the spline function yields a change in gradient sign, while the PCHIP function is monotone.

Piecewise cubic Hermite interpolation is carried out using the MATLAB "interp1" function paired with the "PCHIP" option. An example is given in Figure 4.9, which shows interpolation data for the 7th diffuse irradiance gap, taken from the daily file of 27 July 2011 (dataset #1). For comparison, this is given together with data obtained using the spline method and three least-squares polynomials of order 3, 4 and 5. The monotone nature of the PCHIP function in G_{d7} is clear, as opposed to the spline which undergoes a change in gradient sign from positive to negative.

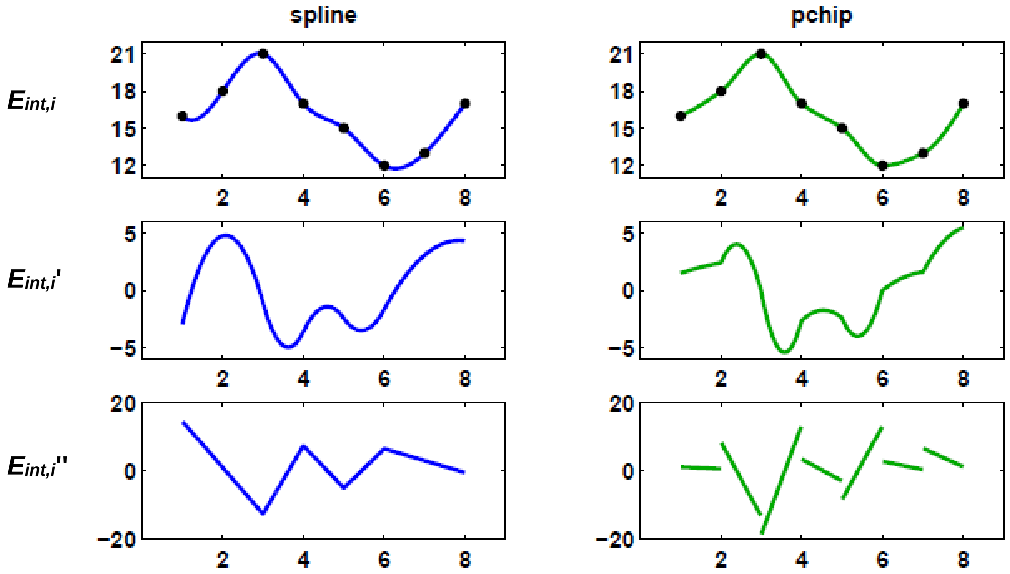

Figure 4.8: MATLAB interpolating functions for spline and PCHIP applied to sample data with first and second derivatives, adapted from Moler (2004).

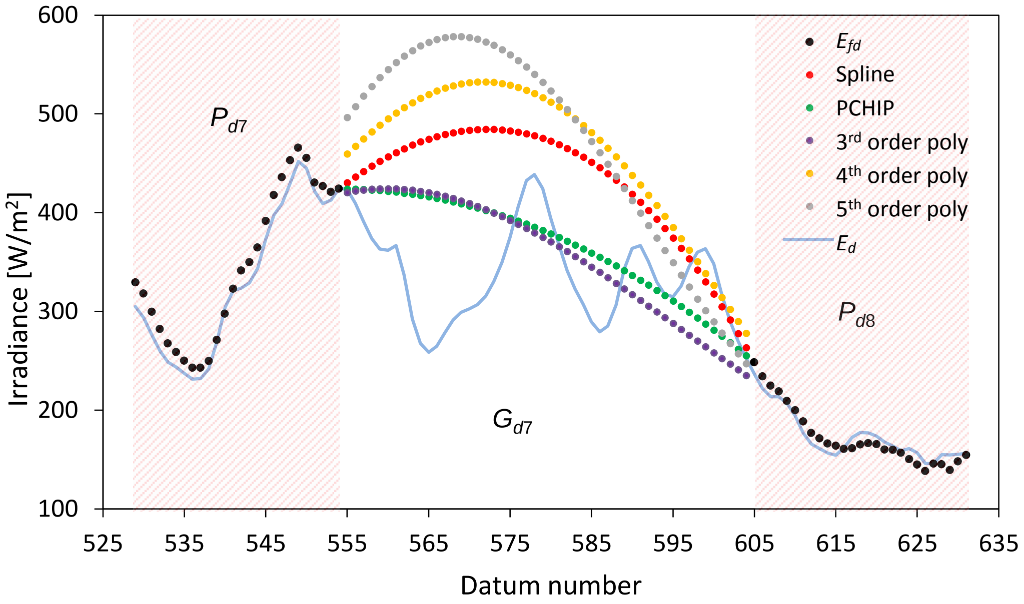

Figure 4.9: Comparison of the spline, PCHIP, 3rd order polynomial, 4th order polynomial and 5th order polynomial interpolation schemes applied to a diffuse gap.

4.8.5 3rd, 4th and 5th order polynomial curve-fitting

For a set of known data, given by (x_q, y_q), with $q = 1, \ldots, n$, made up of the measured patch-wise irradiance measurements left and right of the gap, curve fitting seeks a function $f_{int}(x)$ such that $f_{int}(x_q) \approx y_q$ (Kreyszig, 1988). A number of different functions can be used, but in this work $f_{int}(x)$ is given by a polynomial of degree $m = 3, 4, 5$:

$$f_{int}(x) = b_0 + b_1 x + \cdots + b_m x^m \qquad \text{where } m \leq n - 1 \tag{4.12}$$

Unlike the spline and PCHIP schemes, $f_{int}(x)$ need not pass exactly through all the known points. Rather, the sum of the squares of the distances of all y_q from $f_{int}(x)$, given by SS, must be a minimum, where:

$$SS = \sum_{q=1}^{n} \left(y_q - f_{int}(x_q)\right)^2 \tag{4.13}$$

It can be shown that the necessary condition for SS to be a minimum is given by the following set of (m + 1) conditions (Kreyszig, 1988):

$$\frac{\partial SS}{\partial b_0} = 0, \ldots, \frac{\partial SS}{\partial b_m} = 0 \tag{4.14}$$

These yield a set of (m + 1) normal equations which are solved for the unknowns $b_0, \ldots, b_m$, giving the final form of the function. The 3rd, 4th and 5th order polynomials used in this work were generated by MATLAB's "polyfit" function. As can be seen in Figure 4.9, the generated data do not transition smoothly to measurements in the adjacent patches because there is no requirement for the polynomials to pass through the patch values.

4.8.6 Autoregressive integrated moving average (ARIMA)

ARIMA models are commonly used in time-series analysis across a wide range of fields, including econometrics, environmental science, energy studies, agriculture and the social sciences. They can be applied whenever a process of discrete time-based events occurs at regular intervals, and their primary use is forecasting future values of a univariate series based on its past data history. They are particularly well-suited to short-term forecasting in stochastic systems that defy conventional analytical methods, such as the stock market, and have also been used by several authors in solar radiometric studies (Craggs et al., 1999; Dazhi et al., 2012; Paoli et al., 2010; Reikard, 2009; Santos et al., 2003).

The generalised algebraic statement of an ARIMA model links a variable at a moment in time (z_t) with its own past values (z_{t-1}, z_{t-2}, z_{t-3},…) (Pankratz, 1983), The authoritative text by Box and Jenkins (1976) develops the final form of the model by considering three components: an autoregressive (AR) term, a moving average (MA) term and a differencing or integrative (I) term, as follows:

The autoregressive process, AR(*p*)

In an autoregressive process, the value (z_t) at time t is the linear sum of p previous z-values and a probabilistic shock, or random white noise, component, a_t:

$$z_t = \varphi_1 z_{t-1} + \varphi_2 z_{t-2} + \cdots + \varphi_p z_{t-p} + a_t \tag{4.15}$$

where φ_1 , …, φ_p are fixed coefficients. Equation (4.15) represents an AR process of order p, or AR(p), to indicate the longest time-lag active in the series.

The moving average process, MA(*q*)

A moving average process relates the value, z_t, to q previous, time-lagged random components, a, also as a linear sum, as follows:

$$z_t = a_t - \theta_1 a_{t-1} - \theta_2 a_{t-2} - \cdots - \theta_q a_{t-q} \tag{4.16}$$

where θ_1 , …, θ_q are fixed weightings. By convention, equation (4.16) is given purely as a function of a, although it can also be written with z values on the right hand side, through manipulation. The given series represents an MA process of order q, or MA(q).

Stationarity and the differencing term (*D*)

A series that is stationary has a constant mean, variance and auto-correlation function (ACF) with time. When a series is nonstationary, it is possible to introduce a differencing term, D, of first order or higher, to transform the series from z_t to w_t, such that:

$$w_t = \nabla^D z_t \tag{4.17}$$

where ∇^D is a differencing operator. For example, the differencing schemes for $D = 1$ and $D = 2$ are given by:

$$w_t = \nabla^1 z_t = z_t - z_{t-1} \qquad t = 2, 3, \ldots, n \tag{4.18}$$

$$w_t = \nabla^2 z_t = (z_t - z_{t-1}) - (z_{t-1} - z_{t-2}) \quad t = 3, 4, \ldots, n \tag{4.19}$$

In most cases the first difference is sufficient to eliminate nonstationarity, and in many cases no differencing is required at all ($D = 0$). Generally, unnecessary differencing results in artificial patterns in the data and reduces the accuracy of the forecast (Pankratz, 1983).

The ARIMA(*p*,*D*,*q*) model

The “I” in ARIMA is a reference to the integrative, or summation process that is followed to generate an ARIMA series, inversely, from a white noise signal, a_t.

The model is properly described as ARIMA(p,D,q) and is extrapolative, that is, it forecasts ahead based on a user-defined number of previous values. Using the notation from equations (4.17) to (4.19), the final form of the model is as follows:

$$w_t = \varphi_1 w_{t-1} + \cdots + \varphi_p w_{t-p} + a_t - \theta_1 a_{t-1} - \cdots - \theta_q a_{t-q} \tag{4.20}$$

Given the range of values that can be assigned to p, D, and q, and the resulting combinations, ARIMA(p,D,q) represents a family of models that must be tailored to each case for the best results. Although there are many possible combinations, high-order ARIMA models are rare and seldom effective. Pankratz (1983) suggests that superior results are usually obtained with simpler, low-order models.

As with the numerical interpolation methods described previously, an ARIMA model used to forecast solar irradiance does not explain the underlying physics governing variability, but is purely a statistical description of the time-series.

Conventional modelling procedure

The development cycle of an ARIMA model comprises of several stages. A rigorous description is given by Box and Jenkins (1976), but may be summarised thus:

1. Identification of an appropriate model based on the ACF and partial autocorrelation function (PACF) of the series
2. Estimation of the model coefficients
3. Diagnostic checking by means of statistics to refine the model
4. Forecasting of future values

Both the ACF and PACF are statistical descriptors of autocorrelation; that is, they define the relationship between observations separated by a set number of time periods, or lags. The degree of autocorrelation is indicated graphically for each lag. By estimating the ACF and PACF, it is possible to intuit the most appropriate ARIMA(p,D,q) model for the time-series. For example, a single, pronounced spike at lag 1 for the ACF would suggest an MA(1) process; that is, $q = 1$.

A disadvantage of ARIMA modelling is that the procedure is iterative and requires visual inspection of the ACF and PACF. It therefore contains an element of subjectivity and is difficult to implement in a fully automated way. Pankratz (1983) describes the formulation of a proper ARIMA model as an “art” requiring judgement and experience.

Application of the ARIMA(p,D,q) model to PB data

With several thousand gaps in datasets #1 and #2, the conventional ARIMA procedure, as an iterative approach utilising visual inspection, is not feasible for PB data analysis. In this study the visual inspection of autocorrelation functions is replaced by a pre-screening exercise aimed at identifying a subset of ARIMA models that produce better results for the type of data encountered in the study. The approach consists of the following steps:

1. Ranking of 25 ARIMA(p,D,q) models, as applied to a subset of PB daily data files, graded by clearness index
2. Selection of five candidate models from the larger group for use with datasets #1 and #2
3. Development of a blended forecasting/backcasting technique to ensure smooth transition between gap and patch data
4. Forecasting by the selected models and analysis of results

Box and Jenkins (1976) suggest that 50 or more observations should be used to generate an ARIMA model, although fewer data can be used if caution is exercised. In this work, most of the data patches contain between 25 and 28 readings; the ranking exercise and selection of candidate models is intended to screen out poorly performing options.

Ranking methodology

The ranking exercise assumes that ARIMA models perform differently depending on the sky condition under which data are generated. This is because cloudiness dictates, to a large extent, the type of trace structures that result; whether they are smooth and coherent (mainly clear skies) or disrupted and stochastic (overcast or partly cloudy).

Eighty patches of global horizontal irradiance data (N = 2060) were selected randomly from files in dataset #1. These were graded such that each patch-wise clearness index, k_{T_patch}, fell into one of eight bins covering all possible sky conditions, with each bin containing ten patches for even distribution. The bin divisions are defined in Table 4.3. Bins 1 and 8 span larger ranges because data for $0 \leq k_{T\_patch} < 0.1$ and $0.9 \leq k_{T\_patch} < 1.0$ rarely occur in practice.

Table 4.3: Bin divisions for analysis of ARIMA(p,D,q) model performance.

Bin	Clearness index limits
1	$0.0 \leq k_{T\_patch} < 0.2$
2	$0.2 \leq k_{T\_patch} < 0.3$
3	$0.3 \leq k_{T\_patch} < 0.4$
4	$0.4 \leq k_{T\_patch} < 0.5$
5	$0.5 \leq k_{T\_patch} < 0.6$
6	$0.6 \leq k_{T\_patch} < 0.7$
7	$0.7 \leq k_{T\_patch} < 0.8$
8	$0.8 \leq k_{T\_patch} \leq 1.0$

The raw data were prepared in Excel spread sheet format and processed using MATLAB’s ARIMA modelling capability, available in the Econometrics toolbox.

The ARIMA(p,D,q) models were implemented using the function "arima" to specify values for p, D, and q , "estimate" to create the model vector and "forecast" to generate data for the gap.

A spectrum of ARIMA models was investigated by varying each of the parameters p, D, and q from 0 to 2 inclusive. The ARIMA(2,0,2) and ARIMA(0,0,2) models were excluded because of matrix non-invertability during processing, giving a total of 25 different sets of ARIMA forecast data, each covering all 80 patches and spread across 8 clearness index bins.

The percentage root mean square difference (%RMSD) between the forecast values at 1-minute intervals and the reference GHI data was used to rank the models for each bin, from which a hierarchy of ARIMA performers for the full dataset was selected. A subset of five candidate models was chosen for use in the CdSPM processing software. The results of the ranking exercise are shown in Table 4.4.

The differencing term (D) plays a dominant role in determining the uncertainty of the various models. The ARIMA(p,0,q) variants perform best and all return mean %RMSD values within 1% of each other, this being nearly 10% lower than the best performing ARIMA(p,1,q) variants. Models with two orders of differencing return high uncertainties, which may be explained by the relatively short lengths of patch-wise data and lack of nonstationarity.

Bins for which a model was within the top performing group are listed in Table 4.4. Given the measurement uncertainty of the instruments, any model that realises a %RMSD within 5% of the top performer is statistically also in the "best" category. It should be noted that the ARIMA(0,0,0) model yields the statistically determined constant, a_t, from equation (4.15).

Selection of five ARIMA models for use with datasets #1 and #2

Implementing all 25 ARIMA models on datasets #1 and #2 was neither feasible nor warranted. A subset of five ARIMA variants was selected for inclusion in the CdSPM processing software: the (1,0,1), (1,0,0), (0,0,1), (0,1,1) and (1,1,1) models, highlighted in grey in Table 4.4. The last two did not return especially low uncertainties, however they were included for interest; the ARIMA(0,1,1) variant is the best performing moving average model that includes differencing, and the ARIMA(1,1,1) variant was included because it contains non-zero parameters.

Importantly, the suite of models selected for use in the CdSPM software provides at least one top performing option in all eight bins of clearness index. This gives the ARIMA models a fair chance to compete against the other interpolation methods tested in the study, regardless of sky conditions.

Table 4.4: Performance of twenty-five ARIMA(p,D,q) models on a subset of NREL GHI data, ranked by decreasing %RMSD.

ARIMA parameters *p*	*D*	*q*	Bins where the model is within 5% of top performer	Mean RMSD (%)	Motivation for use in the CdSPM software
1	**0**	**1**	1, 2, 3, 5, 6, 8	49.9	Best overall performer
1	**0**	**0**	1, 3, 5, 6, 7, 8	50.0	Best AR(1) model
2	**0**	**0**	2, 3, 7, 8	50.3	
2	**0**	**1**	2, 3, 5, 7, 8	50.4	
0	**0**	**0**	2, 3, 4, 6, 7, 8	50.6	
1	**0**	**2**	3, 5, 6, 7, 8	50.7	
0	**0**	**1**	2, 3, 4, 6, 7, 8	50.9	Best MA(1) model
0	**1**	**0**	8	60.5	
0	**1**	**1**	2, 8	61.3	Best MA model with $D = 1$
0	**1**	**2**	2, 8	62.7	
1	**1**	**0**	8	78.2	
2	**1**	**0**	8	78.7	
1	**1**	**1**		79.5	Best model with non-zero terms
2	**1**	**1**	8	85.4	
1	**1**	**2**	2	91.7	
2	**1**	**2**	1, 8	92.2	
1	**2**	**2**		275.1	
2	**2**	**1**		328.3	
2	**2**	**2**		341.0	
2	**2**	**0**		358.4	
0	**2**	**2**		375.8	
1	**2**	**1**		384.2	
0	**2**	**1**		391.7	
1	**2**	**0**		418.5	
0	**2**	**0**		617.8	

Adaption for transition between ARIMA data and adjacent patches

ARIMA forecasting is extrapolative. For the PB data, this means that a preceding patch of known measurements is used to forecast into the following gap without reference to the subsequent patch. In most cases, this creates a mismatch between the modelled values at the end of the gap, and the known data that follow it. To improve the accuracy of the method, a blended forecasting/backcasting technique is employed in this study. In the general case of a centrally located gap of missing data, flanked by left and right patches of measured values, the procedure is as follows:

1. Generate ARIMA model values by forecasting ahead into the gap using the left patch of known data

2. Reverse the order of measurements in the right patch and forecast ahead by the same number of time steps using the ARIMA function
3. Reverse the model values from the right patch so that they represent a series of backcast data correctly positioned in the gap
4. Blend the forecast and backcast sets of data using a weighting factor, f_w

The weighting factor constrains the interpolated values as follows: 1) predicted values close to the left patch are dominated by the forecast from the left side, 2) values on the right side of the gap are dominated by the backcast values, and 3) at the midpoint of the gap, the blended value consists of 50% forecast and 50% backcast data. This approach is prudent since ARIMA forecasts grow in uncertainty the further forward they are projected.

Given a projected series of N_G values forecast from the left patch ($E_{int\_L,i}$) and a second series generated by backcasting the right patch ($E_{int\_R,i}$), the final blended ARIMA interpolant, $E_{int,i}$, is given by:

$$E_{int,i} = f_w E_{int_{L,i}} + (1 - f_w) E_{int_{R,i}} \qquad i = 1, \dots, N_G \tag{4.21}$$

where the weighting factor, f_w, is a cosine function such that $0 \leq f_w \leq 1$:

$$f_w = \frac{1}{2}\left(1 + \cos\left(\frac{\pi(i-1)}{N_G - 1}\right)\right) \tag{4.22}$$

Application of the blending procedure is illustrated in Figure 4.10 for an 11-point gap. The upper straight line represents the ARIMA forecast series ($E_{int\_L,i}$) and the lower dashed line is the backcast series ($E_{int\_R,i}$). The resulting blended function ($E_{int,i}$) transitions smoothly from the first to the second.

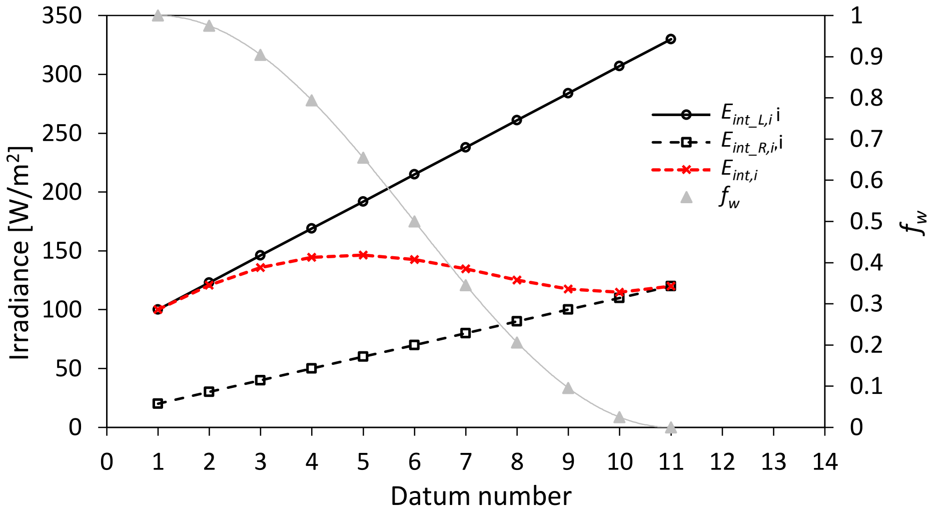

Figure 4.10: Blended interpolation function (in red) for ARIMA models.

Forecasting with the ARIMA models and blending function

The ARIMA modelling procedure can be applied to GHI and DHI data. Figure 4.11 shows interpolation data for the 7th diffuse irradiance gap, taken from the NREL daily file of 27 July 2011 (dataset #1). It is important to note that the data are not the raw ARIMA output, but a blend of the forecast and backcast models, combined according to equations (4.21) and (4.22). The blending function, together with the underlying statistical nature of ARIMA modelling technique, can yield identical results for different variants as evident in Figure 4.11 with the (1,0,1) and (0,1,1) models. In the case of the (0,0,1) model, the resulting blended function is offset because it is generated from averages of the preceding and succeeding data patches.

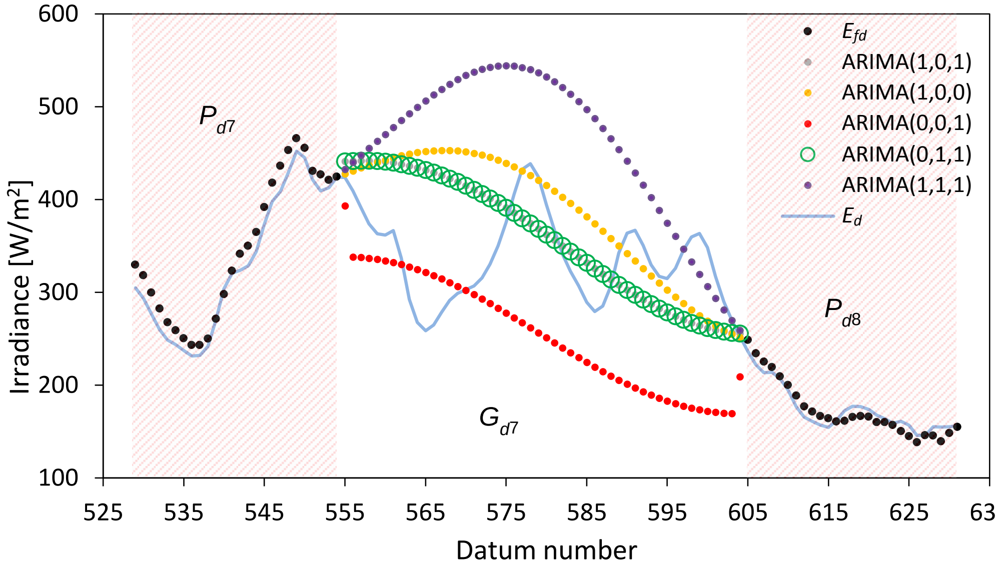

Figure 4.11: Comparison of the ARIMA (1,0,1), (1,0,0), (0,0,1), (0,1,1) and (1,1,1) models applied to a diffuse gap.

4.9 Data replacement via radiometric modelling

4.9.1 Clear and cloudy sky models

Model typology

Radiometric models can be employed when all or some of the physical sun strength measurements are unavailable at a site. Gueymard and Myers (2008b) propose a typology of models based on nine classification criteria. These include the types of output and input data, the spatial, temporal and spectral resolutions, the type of methodology (deterministic or stochastic), the type of algorithm (physical or empirical), the surface geometry (horizontal surface or tilted plane) and the sky type (clear or cloudy).

Using this approach, the models relevant to this study are those that: 1) enable prediction of DHI, GHI and DNI time series, 2) use only solar position data and the input from a single pyranometer, 3) offer reasonable uncertainties for the NREL and UKZN sites, 4) can be used at 1-minute resolution, 5) are broadband in nature, 6) are either deterministic or stochastic, 7) are either physical or empirical, 8) are concerned with the horizontal plane for DHI and GHI and 9) can cover the spectrum of cloud conditions from overcast to clear.

Clear sky models in perforated band analysis

Considerable effort has gone into modelling irradiance under clear sky conditions, covering both the spectral and broadband regimes. The aim is to predict sun strength, usually DNI, with the assumption that attenuation is caused by scattering and absorption of sunlight by water vapour, gases and particles, and not by cloud. Notable examples are the Hottel model (Hottel, 1976), the Bird model (Bird and Hulstrom, 1981), SMARTS2 (Gueymard, 2001), REST2 (Gueymard, 2008) as given in equation (1.1) and the Yang model (Yang et al., 2001). In most cases, an extinction function is proposed that scales extra-terrestrial DNI through a series of transmittances, each tuned to a specific scattering or absorption process in the atmosphere. The Bird model for calculating broadband DNI, appears thus:

$$E_{bn} = 0.9662\, E_{on}\tau_R\tau_o\tau_{UM}\tau_w\tau_A \tag{4.23}$$

where E_{on} is the extraterrestrial direct normal irradiance, and τ_R, τ_o, τ_{UM}, τ_w and τ_A are the atmospheric transmittances associated with Rayleigh scattering and absorption by ozone, uniformly mixed gases, water vapour and aerosols respectively. A number of articles have compared the relative performance of clear sky models, including comprehensive studies by Ineichen (2006) and Gueymard (2003a; 2003b).

In this work, the clear sky model of Bird and Hulstrom (1981) is used as a check on the results obtained for DNI under high clearness index conditions, as described by Gueymard and Myers (2008a). Aside from this, clear sky models have a limited role to play in processing PB measurements since most of the data are obtained under partly cloudy or overcast conditions and, in any event, the clean data curves from clear sky conditions are easily reformed into separate traces for DHI and GHI without the need for physical modelling techniques.

Importantly, clear sky models do not work under partly cloudy conditions because there is no accurate way to model cloud transmittance, which is highly variable with respect to time (Myers, 2013). Instead, other means must be used to predict global, diffuse and direct normal irradiance when the available instrumentation at a site is unable to provide these components individually.

Decomposition models for cloudy sky conditions

A decomposition model (DM) can be exploited to replace missing diffuse horizontal irradiance values in the output from a perforated band system (Brooks and Roberts, 2010). This is achieved by applying the DM to contemporaneous GHI measurements, thereby generating predictions for the missing DHI as an alternative to conventional interpolation methods.

Decomposition models are the most common method of modelling irradiance in the presence of cloud and are typically empirical in nature. Their underlying premise is that the fraction of global solar irradiance due to diffuse sunlight (called the diffuse fraction, k) is correlated with the sky clearness index k_T. The 1-minute averaged diffuse fraction at the i^{th} datum is calculated as:

$$k_i = E_{fd,i}/E_{fg,i} \tag{4.24}$$

$E_{fg,i}$ is a measured value drawn from the contemporaneous patch of GHI values, occurring at the same instant as the unknown quantity $E_{fd,i}$. The minute-based clearness index, k_T, can therefore be calculated using $E_{fg,i}$. This alone is insufficient to obtain DHI, but if an independent correlation exists between k_i and k_T, then the artificial diffuse irradiance arising from the perforated band system, $E_{fd,i}$, can be determined as follows:

$$E_{fd,i} = E_{fg,i}.f(k_T)|_i \qquad\qquad i = 1, \ldots, N_G \tag{4.25}$$

where $f(k_T)|_i$ represents k_i, the predicted diffuse fraction obtained via the decomposition model and evaluated over a 1-minute time interval for a specific datum point (i) in the gap of a PB trace. Once the diffuse irradiance is known, DNI can be calculated through the closure equation (1.2). The empirical relationship between k and k_T is shown in Figure 4.12(a), using hourly data collected by Kunene et al. (2012) at the UKZN Howard College ground station.

Developers of a DM fit curves to the data, most of which are simple functions of k_T and others of which involve additional parameters, such as solar altitude angle. The curves are usually split into three separate regimes, each based on the sky condition: overcast, mid-range k_T and clear skies. Although clearness index and diffuse fraction are quite well correlated at very low k_T values (for overcast conditions DHI is approximately equal to GHI) and under clear skies, the dispersion of data points around the mid-clearness index range is problematic and leads to high uncertainties in the calculation of diffuse irradiance.

Decomposition models have two further shortcomings. They can be used to derive diffuse irradiance when global irradiance is measured, but are not intended for use in the reverse order. They also tend to be location-dependent, therefore a number should be tested at a site before one is adopted as a standard processing tool. Figure 4.12(b) shows several DM applied to the data in Figure 4.12(a). The Reindl

(Reindl et al., 1990) and S&O (Skartveit and Olseth, 1987) models are functions of both k_T and solar altitude, hence the dispersion of predicted values for a given clearness index. The HC model shown in Figure 4.12(b) is a piecewise variant developed from UKZN data.

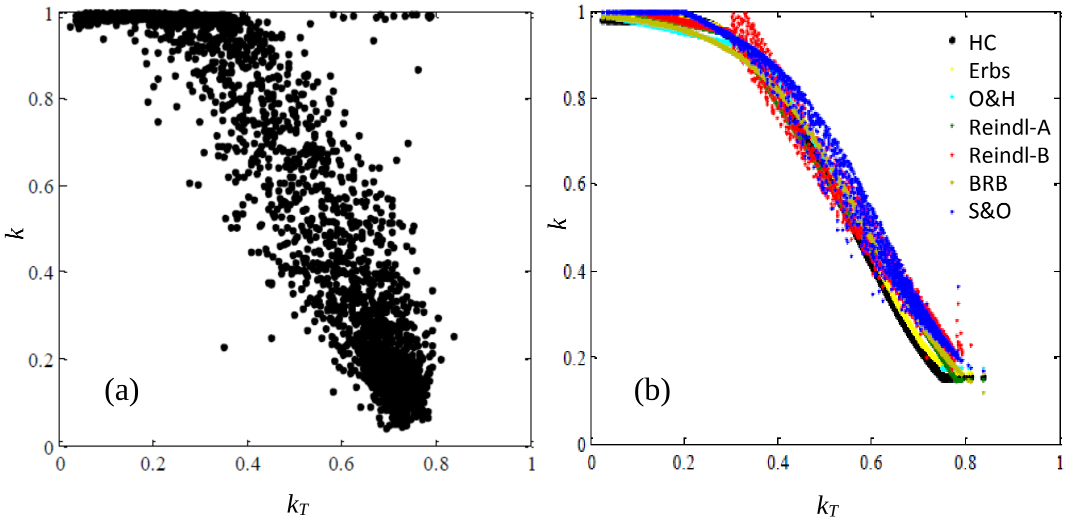

Figure 4.12: (a) The relationship between diffuse fraction and clearness index as measured by Kunene et al. (2012), and (b) application of decomposition models to the data.

The variable dispersion of data in Figure 4.12(a) suggests that the uncertainties associated with DM-derived data are dependent on the sky condition. This implies that there is scope for tailoring the models to different sky conditions as determined by the clearness index, whether applied over an entire day or over shorter time-scales, such as the individual patches resulting from PB operation.

Numerous decomposition models have been proposed, five of which are used in this study. Named after their originators, they are: 1) Orgill and Hollands (Orgill and Hollands, 1977), 2) Erbs, Klein and Duffie (Erbs et al., 1982), 3) Boland, Ridley and Brown (Boland et al., 2008), 4) Boland, Ridley and Lauret (Ridley et al., 2010) and 5) Reindl, Beckman and Duffie (Reindl et al., 1990). Their selection for use in this study was based on factors such as popularity, number of inputs, performance and suitability with respect to the perforated band system. For conciseness the five models are hereafter referred to as O&H, Erbs, BRB, BRL and Reindl, respectively, and are described in detail in the sections that follow.

Decomposition models are frequently compared to determine relative performance. Gueymard (2009) describes the O&H, Erbs and Reindl models as widely used and “relatively universal”. Torres et al. (2010) studied 17 models using 1-hour averaged data for a 20 month period in Pamplona, Spain. These included the O&H, Reindl, Erbs and BRL variants used in this study. Of this subset, BRL was the best performer with a percentage RMSD of 31.4% in converting GHI to DHI. The overall best performer was the DirInt model of Perez et al. (1992), with uncertainty of 29.4%. DirInt is an adaptation of Maxwell's DISC model (Maxwell, 1987), but requires dew point temperature as an input and was omitted from the DM group used here.

Jacovides et al. (2006) used hourly data from a ground station in Cyprus to compare 10 established models, including O&H, Reindl and Erbs. They found little difference in performance, with the percentage RMSD for all variants within 1.7% of the top performer.

Batlles et al. (2000) tested 7 models, including O&H, Erbs, Reindl and Maxwell (1987) on data from six Spanish locations. They do not give uncertainties for the resulting DHI, but rather calculate the DNI using predicted diffuse irradiance and then report uncertainties for the resulting DNI. Very little difference is noted between the percentage RMSD values for all 7 models, although the mean bias difference percentage is lower for Reindl than for O&H or Erbs. It is clear from these studies that of the models selected for use with the PB system, none stands out under all conditions, although the BRL variant, which was not included in Figure 4.12, and the Reindl model offer some promise for lowering uncertainty.

Application of decomposition models to high-resolution data

As a novel application of decomposition models, this study exploits the availability of GHI data when DHI readings are unknown to fill the artificially generated gaps in a PB trace. Consideration must be given to the time period over which a DM was derived, versus the interval over which it is used in practice, which in this case is 1-minute steps.

Most DM were developed using hourly averaged data and consequently provide correlations between the diffuse fraction and K_{T_hour} rather than the minute-based index, k_T. Their intended output is therefore hourly DHI. Some early models were developed using daily values (Orgill and Hollands, 1977). Nevertheless, the use of models over shorter time steps is not without precedent and is becoming necessary as the need grows for high-resolution data.

Lanini (2010) compared the diffuse fraction obtained using six decomposition models against measured reference data, over time periods of 1, 10, 15 and 60 minutes. The models included those of Skartveit and Olseth (1987), Ridley et al. (2010), Maxwell (1987), Perez et al. (1992) and Reindl et al. (1990). Root mean square differences between the model and reference data are not given, however the mean bias differences for 1-minute data are only slightly higher than for the longer periods. In general, there is little difference in the uncertainties for short time steps compared to longer intervals.

Ineichen (2008) used sub-hourly data at 5-, 10-, 15-, 30- and 60-minute intervals with global-to-beam decomposition models, and concluded that they can be used on short time-step data without a serious loss in bias or precision. He nevertheless argues for adapting models derived from hourly data when used over shorter time periods.

Gueymard (2009) assessed various transposition models for converting GHI to irradiance on a tilted surface using 12 months' of data from NREL's Solar Radiation Research Laboratory (the same data source as this study). He included an analysis of the Erbs and O&H decomposition models. Interestingly, the more sophisticated models performed no better than Erbs and O&H. Although the transposition models had been developed from hourly averaged data, they functioned well at 1-minute resolution.

The studies referred to above support the use of hourly-derived models at 1-minute time steps. Details of the decomposition models used in this study are given below. In all cases they are described in terms of 1-minute values of diffuse fraction and clearness index.

The use of DM to replace missing data is restricted to those intervals where GHI is measured. Since there are zones of transition data interspersed between DHI and GHI patches (shown as unshaded regions in the upper pane of Figure 4.5), it remains necessary, even when applying a decomposition model, to interpolate for the missing transition data. This is done using a simple linear interpolation method, similar to that described in 4.8.1. The number of data typically lost during transition is about 10 to 12.

4.9.2 Orgill and Hollands (O&H)

Based on data from Toronto, this model partitions the curve correlating diffuse fraction, k, with the hourly clearness index, K_{T_hour} into three sections for predominantly clear, partly cloudy and overcast conditions (Orgill and Hollands, 1977). The hourly parameters are replaced with minute-based values to yield the following:

$$k = 1.0 - 0.249k_T \qquad 0 \leq k_T < 0.35 \tag{4.26a}$$

$$k = 1.557 - 1.84k_T \qquad 0.35 \leq k_T \leq 0.75 \tag{4.26b}$$

$$k = 0.177 \qquad k_T > 0.75 \tag{4.26c}$$

Under high clearness index conditions, k becomes a constant as given in equation (4.26c). This is partly to suppress spikes in irradiance that result through amplification of DHI.

4.9.3 Erbs, Klein and Duffie (Erbs)

The Erbs model was developed using hourly data from four United States cities and is similar to O&H in that the k-K_{T_hour} curve is partitioned into three divisions (Erbs et al., 1982). Unlike O&H, the central curve is a 4th order polynomial:

$$k = 1.0 - 0.09k_T \qquad 0 \leq k_T \leq 0.22 \tag{4.27a}$$

$$k = 0.9511 - 0.1604k_T + 4.388{k_T}^2 - 16.638{k_T}^3 + 12.336{k_T}^4 \tag{4.27b}$$

$$0.22 < k_T \leq 0.80$$

$$k = 0.165 \qquad k_T > 0.80 \tag{4.27c}$$

In addition to U.S. measurements, Erbs et al. (1982) tested the model against hourly reference data from Highett in the Australian state of Victoria. The model hourly values were found to be within 3% of the reference data for measurements in the central partition ($0.22 < K_{T\_hour} \leq 0.80$). Overall, the model displayed some seasonal bias and tended to overpredict DHI in autumn and winter.

4.9.4 Boland, Ridley and Brown (BRB)

Concerned for the lack of generic decomposition models applicable globally, Boland et al. (2008) proposed a logistic model developed with hourly data from seven cities: Adelaide, Darwin, Maputo, Bracknell, Lisbon, Uccle and Macao. Unlike the piecewise models of O&H and Erbs, the BRB model (equation (4.28)) is continuous and does not require partitioning of the data into clearness index bins making it easier to work with. In 1-minute form, the BRB model is given as:

$$k = 1/\left(1 + e^{-5.00+8.60k_T}\right) \tag{4.28}$$

4.9.5 Boland, Ridley and Lauret (BRL)

Although effective, BRB is a single-predictor model, referencing only the clearness index. Building on the work of Boland et al. (2008), Ridley et al. (2010) expanded BRB into a multi-predictor variant to improve its performance. In addition to hourly clearness index, they included parameters for solar altitude angle (α), daily clearness index (K_{T_day}), apparent solar time (AST) and a persistence factor (ψ). Replacing the hourly clearness index term with the 1-minute equivalent value gives equation (4.29).

$$k = 1/\left(1 + e^{-5.38\,+\,6.63k_T\,+\,0.006AST\,-\,0.007\alpha\,+\,1.75K_{T\_day}\,+\,1.31\psi}\right) \tag{4.29}$$

The apparent solar time is calculated from the hour angle, ω:

$$AST = \omega/15 + 12 \tag{4.30}$$

The solar altitude angle, α, is the complement of the zenith angle, as given in equation (2.8). The persistence factor reflects the influence of the clearness index values to the left and right of the present value. In the BRL model, which was developed for hour-based measurements, ψ is given in terms K_{T_hour} however it has been adapted here to reflect the influence of the adjacent minute-based clearness index values, immediately prior to and after the i^{th} datum point:

$$\psi = \begin{cases} \left(k_{T,i-1} + k_{T,i+1}\right)/2 & 1 < i < N_G \\ k_{T,i+1} & i = 1 \\ k_{T,i-1} & i = N_G \end{cases} \tag{4.31}$$

Ridley et al. (2010) validated the BRL model against data from Camborne in the United Kingdom and Gillot on the Indian Ocean island of Reunion, and found that it performs well in both hemispheres. Furthermore, the model is noted for its relative simplicity in terms of required inputs and computational expense.

4.9.6 Reindl, Beckman and Duffie (Reindl)

Reindl et al. (1990) developed a correlation based on four predictors: clearness index, solar altitude angle, ambient temperature and relative humidity. The model was developed from hourly data gathered at two U.S. stations (Albany and Cape Canaveral) and three European sites (Copenhagen, Hamburg and Valencia). In places where temperature and humidity data are not available, a simplified version can be used. This is a function of clearness index and altitude angle only, and is applied in this study.

$$k = 1.020 - 0.254k_T + 0.0123\sin(\alpha) \qquad 0 \le k_T \le 0.3 \qquad (4.32a)$$

$$k = 1.400 - 1.749k_T + 0.177\sin(\alpha) \qquad 0.3 < k_T < 0.78 \qquad (4.32b)$$

$$k = 0.486k_T - 0.182\sin(\alpha) \qquad k_T \ge 0.78 \qquad (4.32c)$$

The Reindl model was validated against an independent dataset from Oslo, Norway, and found to perform better than the Erbs model. Some seasonality and location dependence were noted (Reindl et al., 1990). The application of the O&H, Erbs, BRB, BRL and Reindl models is illustrated in Figure 4.13, which shows interpolated data in diffuse gap 7 of the NREL daily file for 27 July 2011. The interpolated values include 22 minutes of transition data (12 on the left side of the gap and 10 on the right), which are generated using a simple linear interpolation scheme. Transition data cannot be replaced using the DM approach because the contemporaneous GHI values are absent.

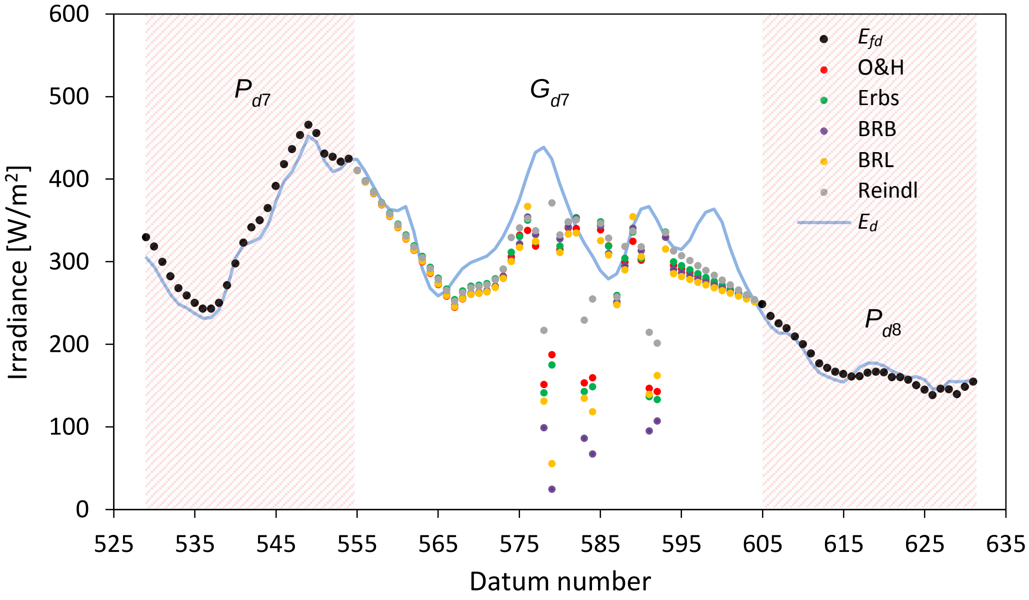

Figure 4.13: Comparison of the O&H, Erbs, BRB, BRL and Reindl decomposition models applied to a diffuse gap.

4.9.7 Global equals diffuse (GeD)

Decomposition models have not been developed to calculate GHI when DHI is known. Although it is mathematically possible to invert a conventional DM so as to obtain GHI, this is computationally expensive because of their piecewise nature and the generation of multiple roots that must be subjected to validation checks (Journée and Bertrand, 2011).

Intuitively, a case can be made for introducing a simplified "reverse" decomposition model in this study to enable the generation of GHI when DHI values are known. This can be done without recourse to curve-fitting or regression analysis; instead, it is proposed to equate GHI with DHI on the understanding that the two are equal when direct normal irradiance is zero. This is effectively what decomposition models do, as shown in equations (4.26a) and (4.27a), where k reduces to unity when k_T is zero. The model is designated here as "global equals diffuse", or GeD, and is given as:

$$E_{fg,i} = E_{fd,i} \qquad\qquad i = 1, \dots, N_G \qquad\qquad (4.33)$$

The GeD model is not a function of clearness index and will perform poorly under clear and partly cloudy conditions, however it will generate accurate values of GHI when the clearness index is low. This is useful because the GHI data trace exhibits a measure of stochasticity under overcast conditions and therefore resists accurate interpolation by conventional numerical methods. The GeD model is applied to NREL data in Figure 4.14 for global gap 7 on 27 July 2011.

The interpolated data are shown in red and divided into four zones for explanation. Zones I and IV contain transition values generated using a simple linear interpolation scheme. The values in zones II and III are generated using GeD and illustrate both the success and failure of the model to replicate the reference trace, shown in blue. In zone II the sensor is largely occluded by cloud, DNI is zero, and the model performs well, tracking the reference GHI trace. In zone III the DNI component is non-zero and the GHI trace separates from DHI, resulting in poor GeD performance.

In the absence of k_T-dependence, the deployment of GeD must be controlled by logic built into the CdSPM software. By limiting the application of the model to those gaps where the clearness index is estimated to be low, the resulting uncertainties are likely to be reduced. This is achieved with the adaptive interpolation scheme, described in 4.11.

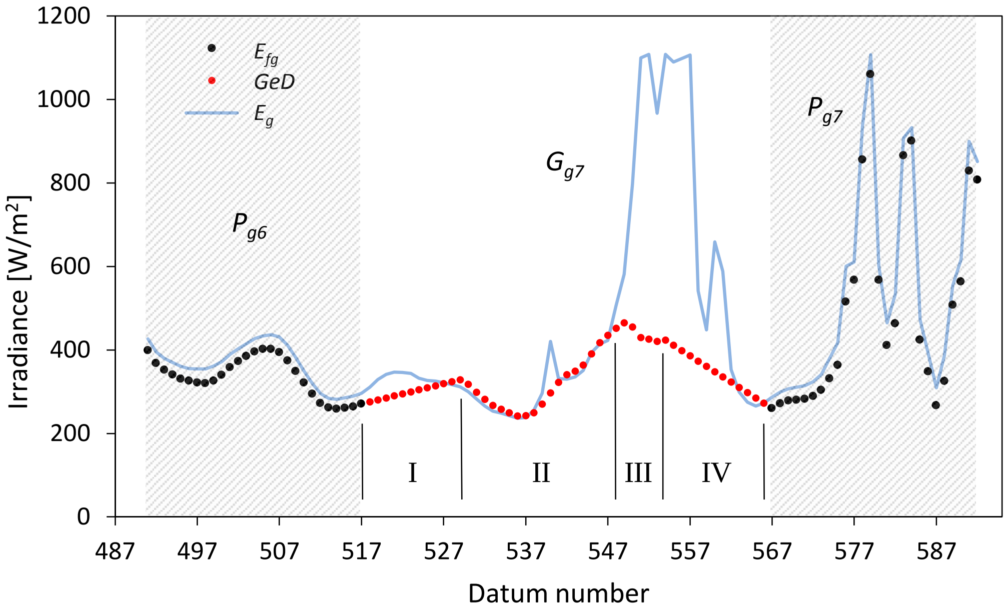

Figure 4.14: Application of the GeD model to a global irradiance gap.

4.10 Statistical metrics and ranking method

The effectiveness of individual interpolation methods and the overall performance of the CdSPM are determined statistically. This work follows the guidelines of Gueymard and Myers (2008b) who proposed several conditions that should be satisfied for a radiometric model to be validated convincingly:

1. The development and validation datasets should be independent
2. An uncertainty analysis should be carried out on the reference dataset
3. Datasets should be filtered for errors
4. Model inputs should possess the same time resolution as the validation data and should be obtained at the same site
5. The best possible ancillary data should be used
6. Inputs to the model should be measured independently with co-located instruments at the necessary frequency and with limited uncertainty

Root mean square difference and mean bias difference were used to validate the interpolation schemes, with formulations as given in section 3.4.1. In this chapter, E_{mod} represents the interpolated value of irradiance and E_{meas} the measured reference value for a population size of N. When determining the uncertainty of individual interpolation methods in stage 3 of the CdSPM, N becomes N_G.

Percentage root mean square difference is used to rank competing interpolation schemes for the purpose of configuring the AIS in stage 3 of the CdSPM. The ranking produces clusters rather than a continuous list because the reference measurements carry their own uncertainties, which are estimated to be 5% (Table

3.3). The method adopted here is similar to that of Gueymard (2012), where schemes with uncertainties within a certain percentage of each other receive the same ranking, since they are statistically similar to each other.

In this study, the top cluster is obtained by grouping all schemes that produce a percentage RMSD result within 5% of the best performing model. The second cluster consists of all schemes within 5% of the top model in the second-best group, and so on. A maximum of five clusters is used per bin, with the 5th cluster containing all schemes not classified in the first four, regardless of uncertainty.

In stage 4 of the cloudy sky methodology, %RMSD and %MBD are used to characterise PB performance. For completeness, standard deviation and expanded uncertainty (U_{95}) are also reported, with definitions given in Appendix D.

4.11 The adaptive interpolation schemes for DHI and GHI

4.11.1 Clearness index as functional parameter

Interpolation techniques are not equally effective under all sky conditions. Their success in replacing lost values depends on the structure of the data trace, which in turn is influenced by cloud patterns that lead to complex interplay between the irradiance components. Conditions can also change over short time intervals leading to ineffective interpolation when a single-scheme approach is used over an entire day.

It is therefore proposed to refine the use of interpolation techniques by linking their deployment to the prevailing cloud condition. The resulting adaptive interpolation scheme, or AIS, seeks to reduce model uncertainty by using the best scheme, as determined statistically, on a gap-wise basis for both GHI and DHI traces. That is, a daily file with nine DHI gaps may end up with a different interpolation scheme in each gap if the conditions so dictate. No attempt is made here to apply more than one scheme within a specific gap, since many of the interpolation methods are defined over the entire span of missing data.

Clearness index is the parameter by which the deployment of interpolation schemes is controlled in this study. It is a recognised metric in characterising solar climate (Gueymard and Myers, 2008a) and provides a convenient, if imperfect, method of classifying DHI and GHI data. Importantly, it is one of the few metrics available at ground stations operating a single pyranometer. It therefore represents a sound choice for interpreting data generated by the PB system and for selecting the best interpolation technique for a given gap.

Within each of the daily files, clearness index is calculated for individual DHI gaps from the contemporaneous GHI measurements. This is called the patch-wise clearness index, k_{T_patch}, since it is obtained from a patch of known GHI measurements coinciding with the missing data. The patch-wise index is then used to direct deployment of interpolation schemes in an optimal manner, using statistical performance as a guide. The same approach is used for GHI gaps except that it is not possible to calculate a clearness index directly since global data are absent. Therefore k_{T_patch} is obtained from the average of the two adjacent DHI patches and used to apply the appropriate scheme in a given gap of the GHI trace.

By using the clearness index, the CdSPM achieves two aims. First, the deployment of different interpolation schemes is optimised within individual gaps generated by the band. This requires the calculation of clearness index at 1-minute or patch-wise intervals, as described above, to service the high-resolution requirements of the system.

Secondly, the statistical uncertainty for a full day's worth of data can be reported as a function of daily clearness index, K_{T_day} from which deployment of the system may be determined. This enables potential operators of the perforated band to base their decision on quantitative data available at a given site. The clearness index limits of each bin division are identical to those described in Table 4.3. Overall performance of the PB system is therefore reported as uncertainty classified according to daily clearness index.

4.11.2 Configuration of the AIS for DHI and GHI

Statistical performance of interpolation schemes

The interpolation schemes listed in Table 4.2 are tested on datasets #1 and #2 in two ways. First, the schemes are applied in blanket fashion without any attempt to tailor them to the radiometric condition. This is the 'single-model' approach in which each interpolation method is applied regardless of patch-wise clearness index. There are 15 interpolation schemes applicable to global irradiance data and 19 applicable to diffuse measurements. Second, the schemes are deployed selectively and in combination with each other, according to the configurations of the diffuse adaptive interpolation scheme and its global counterpart.

The diffuse and global adaptive interpolation schemes are referred to as D_AIS and G_AIS respectively. They are generated using the results in Tables 4.5 and 4.6, which indicate the cluster rankings by percentage RMSD in each clearness index bin. Light blue denotes cluster 1; these are all schemes that perform within 5% of the best individual performer in each bin. The remaining clusters are light orange, purple, green and brown, in ascending uncertainty.

Some bins contain fewer than five clusters because of the reduced spread in %RMSD values, which is indicative of more consistent performance under the given sky conditions. This can be seen in bin 4 for DHI and bin 8 for GHI.

Certain trends are evident in Tables 4.5 and 4.6. For DHI interpolation, the decomposition models easily outperform other schemes for low patch-wise clearness index (bins 1 to 3), where they are the sole occupiers of cluster 1. Their uncertainties increase relative to other schemes from bin 4 onward, however, and they steadily become ineffective as conditions improve from partly cloudy to clear. Under clear conditions they are among the worst performers.

From bin 4 onward, the Ramp and PCHIP schemes are best performers within cluster 1, although a number of alternatives yield statistically similar results, including the averaging methods and a number of ARIMA models. Of the least squares regression techniques, only the 3rd order polynomial (3OP) consistently appears in the top cluster. Spline interpolation is a poor performer throughout.

It is worth noting that the percentage RMSD values given in Table 4.5 refer only to interpolated data. The overall daily uncertainty of the perforated band system is much lower since it includes measured values from PB patches, which closely track the reference data.

For GHI interpolation (Table 4.6), the “reverse” decomposition model, GeD, performs well under heavily overcast and cloudy conditions (bins 1 to 3), as expected. Its performance falls off rapidly as conditions improve. Unlike Table 4.5, the number of schemes in cluster 1 increases steadily as cloud diminishes, with all but three of the fifteen options yielding statistically similar results for bin 8. The Ramp function once again does well at higher clearness indices, but the PCHIP scheme is only effective in bin 8.

The uncertainty results hold significance beyond the scope of this study. Aside from their influence on the way the CdSPM is implemented, Tables 4.5 and 4.6 give useful insight into the more general problem of lost measurements in radiometric datasets – the so-called ‘missing data’ problem.

Almost all sources of radiometric data, regardless of their origin, suffer from gaps in the record due to power outages, equipment failures, maintenance issues and a host of other technical problems. There remains no definitive method of replacing such measurements and most authors use a simple linear interpolation approach (Marion and George, 2001; Muzathik et al., 2010; Zawilska and Brooks, 2011). Journée and Bertrand (2011) investigated techniques for replacing missing solar measurements at 10-minute time steps, although they limited their analysis to four radiometric models, including the Erbs variant. They did not consider numerical techniques other than to mention linear interpolation as an option for gaps of only a ‘few’ missing measurements.

The results in Table 4.5 suggest that linear interpolation is indeed a statistically good choice for filling in gaps of missing DHI data at high time resolution, but only when the clearness index is above 0.4. Below that level, the application of a decomposition model yields substantially lower RMSD uncertainties, and linear interpolation should be avoided.

The PCHIP scheme also outperforms linear interpolation in some of the higher clearness index bins, although the difference is within the uncertainty of the measuring sensor. The 1-minute averaging scheme is equally effective. Decomposition models should not be applied for clearness indices exceeding 0.5.

The results in Table 4.6 for replacing GHI produce a similar result. The GeD model reduces RMSD uncertainty compared with linear interpolation at low clearness indices under 0.4, but above this level the Ramp function, which is identical to linear interpolation, is a safe choice. The 1- and 10-minute averaging schemes, 3rd order polynomial and some of the ARIMA variants are equally effective throughout bins 3 to 8.

Table 4.5: Performance of 19 interpolation schemes applied to missing diffuse horizontal irradiance data (dataset #1).

Bin 1		**Bin 2**		**Bin 3**		**Bin 4**		**Bin 5**		**Bin 6**		**Bin 7**		**Bin 8**	
$0 \le k_{T\_patch} < 0.2$		$0.2 \le k_{T\_patch} < 0.3$		$0.3 \le k_{T\_patch} < 0.4$		$0.4 \le k_{T\_patch} < 0.5$		$0.5 \le k_{T\_patch} < 0.6$		$0.6 \le k_{T\_patch} < 0.7$		$0.7 \le k_{T\_patch} < 0.8$		$0.8 \le k_{T\_patch} \le 1.0$	
Scheme	**RMSD (%)**	**Scheme**	**RMSD (%)**	**Scheme**	**RMSD (%)**	**Scheme**	**RMSD (%)**	**Scheme**	**RMSD (%)**	**Scheme**	**RMSD (%)**	**Scheme**	**RMSD (%)**	**Scheme**	**RMSD (%)**
Reindl	11.2	Reindl	14.1	Reindl	16.8	Ramp	22.6	PCHIP	22.9	PCHIP	24.8	PCHIP	31.3	Ramp	34.0
Erbs	11.6	Erbs	14.5	Erbs	18.1	PCHIP	22.7	Ramp	23.2	Ramp	25.5	Ramp	31.5	PCHIP	34.1
BRL	12.0	BRL	15.4	BRL	18.4	1 min	23.2	1 min	23.7	1 min	26.4	1 min	32.5	1 min	36.1
BRB	12.6	O&H	16.2	O&H	18.8	10 min	23.5	A100	24.8	A101	26.8	A101	33.7	10 min	37.5
O&H	13.4	BRB	16.4	BRB	20.5	20 min	24.8	A101	25.2	10 min	28.1	3OP	33.8	3OP	38.4
PCHIP	60.2	Ramp	34.3	Ramp	23.6	3OP	25.0	10 min	25.6	A011	28.4	10 min	34.1	A001	39.2
Ramp	62.2	PCHIP	34.8	PCHIP	24.4	A101	25.3	3OP	25.8	3OP	29.3	A011	34.9	20 min	39.4
1 min	63.3	20 min	34.9	1 min	24.6	Reindl	25.4	20 min	26.8	20 min	30.0	A100	35.0	A101	39.8
10 min	67.0	A001	35.0	20 min	25.1	A001	26.0	A011	27.0	A100	30.5	20 min	36.1	A011	41.3
20 min	67.6	10 min	35.5	A001	25.2	BRL	26.2	A001	28.4	A001	31.2	A001	37.8	A100	42.2
A001	69.3	1 min	35.7	10 min	25.2	A100	26.7	4OP	32.0	5OP	33.1	4OP	42.9	4OP	48.0
A101	70.1	3OP	40.4	A101	28.9	Erbs	27.6	5OP	32.7	4OP	33.1	5OP	43.9	5OP	48.9
A011	70.8	A101	40.5	3OP	29.3	O&H	27.9	Reindl	33.0	Reindl	40.5	Erbs	58.8	Erbs	62.8
3OP	72.7	A011	43.8	A100	30.5	A011	28.6	O&H	37.0	O&H	45.1	BRL	59.1	O&H	65.8
A100	74.8	A100	44.5	A011	31.6	BRB	30.1	BRL	37.0	Spline	46.2	O&H	59.4	BRL	67.0
Spline	82.3	4OP	58.6	4OP	35.9	4OP	30.8	Erbs	37.4	BRL	46.3	BRB	65.4	BRB	70.4
4OP	96.5	5OP	59.5	5OP	36.6	5OP	31.3	BRB	41.6	Erbs	46.6	Reindl	71.7	Spline	75.1
5OP	97.2	A111	65.1	Spline	48.4	A111	40.0	Spline	42.3	A111	50.8	Spline	72.9	Reindl	107.3
A111	111.9	Spline	68.5	A111	64.5	Spline	40.1	A111	70.0	BRB	52.2	A111	157.7	A111	133.4

Table 4.6: Performance of 15 interpolation schemes applied to missing global horizontal irradiance data (dataset #1).

Bin 1		**Bin 2**		**Bin 3**		**Bin 4**		**Bin 5**		**Bin 6**		**Bin 7**		**Bin 8**	
$0 \leq k_{T\_patch} < 0.2$		**$0.2 \leq k_{T\_patch} < 0.3$**		**$0.3 \leq k_{T\_patch} < 0.4$**		**$0.4 \leq k_{T\_patch} < 0.5$**		**$0.5 \leq k_{T\_patch} < 0.6$**		**$0.6 \leq k_{T\_patch} < 0.7$**		**$0.7 \leq k_{T\_patch} < 0.8$**		**$0.8 \leq k_{T\_patch} \leq 1.0$**	
Scheme	**RMSD (%)**	**Scheme**	**RMSD (%)**	**Scheme**	**RMSD (%)**	**Scheme**	**RMSD (%)**	**Scheme**	**RMSD (%)**	**Scheme**	**RMSD (%)**	**Scheme**	**RMSD (%)**	**Scheme**	**RMSD (%)**
GeD	51.5	GeD	39.7	GeD	52.1	Ramp	47.6	Ramp	37.5	A100	32.4	A101	15.8	A001	11.5
A101	66.1	Ramp	52.6	A100	53.8	A100	50.4	A100	39.0	A101	32.5	20 min	16.2	10 min	11.5
A011	67.8	A101	54.3	Ramp	54.3	1 min	50.8	A101	40.0	20 min	33.0	10 min	16.3	20 min	11.7
Ramp	68.5	A100	54.5	A101	55.5	A101	51.0	1 min	40.8	10 min	33.3	A100	16.3	Ramp	11.7
PCHIP	69.6	1 min	56.0	1 min	57.2	10 min	51.8	A001	42.3	A001	33.6	A001	16.5	A100	11.9
4OP	69.6	A001	57.3	10 min	57.7	3OP	52.0	10 min	42.3	Ramp	33.7	Ramp	16.8	PCHIP	11.9
1 min	70.8	10 min	59.5	A001	58.2	20 min	53.7	20 min	43.1	1 min	34.9	3OP	17.0	3OP	11.9
5OP	71.6	20 min	60.1	20 min	58.5	A001	54.4	3OP	44.4	3OP	36.7	1 min	17.7	A101	12.2
A100	71.7	A011	62.3	3OP	59.6	GeD	56.4	A011	47.4	A011	43.8	A011	21.9	1 min	12.3
10 min	75.9	3OP	62.9	A011	64.1	A011	59.0	GeD	59.3	4OP	55.0	4OP	24.8	4OP	13.6
A001	77.4	4OP	71.7	PCHIP	72.9	4OP	68.4	4OP	59.6	5OP	58.7	5OP	28.3	5OP	13.6
20 min	78.3	5OP	80.1	A111	84.5	5OP	123.3	5OP	70.3	A111	61.1	PCHIP	58.6	A011	14.6
3OP	78.6	PCHIP	94.1	4OP	86.6	A111	158.6	A111	103.5	GeD	64.2	A111	60.2	Spline	69.9
A111	80.3	A111	127.3	5OP	104.6	PCHIP	814.2	PCHIP	276.0	PCHIP	98.5	GeD	73.3	GeD	72.9
Spline	120.9	Spline	314.7	Spline	270.8	Spline	1431.0	Spline	331.1	Spline	170.7	Spline	361.5	A111	84.8

Formulation of the G_AIS and D_AIS

The results in Tables 4.5 and 4.6 present two challenges. First, it is not possible to identify a single scheme in every bin that outperforms the others, therefore multiple AIS configurations are possible. Secondly, the AIS is configured using the *patch-wise* clearness index, which is a good but imperfect descriptor of sky conditions. It cannot be assumed that an AIS configured with the best statistical performers will necessarily give the lowest uncertainty when tested across days with different *daily* clearness indices. There are three reasons for this:

1) Clearness index is usually calculated as an average, therefore a day may contain periods for which k_{T_patch} differs substantially from the average daily clearness index, K_{T_day}. For example, a daily clearness index of 0.5 may result from consistent, partly cloudy conditions with a repetitive trace structure, or it may result from a day with a cloudless morning (high k_{T_patch} values) and a sudden switch to heavily overcast conditions in the afternoon (low k_{T_patch} values).

2) Interpolation schemes are sensitive not only to the bulk value of clearness index, but also to high-resolution features of the underlying trace structure, such as stochasticity, which depend on cloud type and distribution.

3) Data trace structures are not evenly distributed with daily clearness index. Therefore, when days are classified in bins according to K_{T_day}, a weaker secondary grading also takes place related to the structural morphology of the irradiance graph. That is, data with a patch-wise index of 0.2 from a day with K_{T_day} of 0.3 may, on average, appear structurally different to data with the same patch-wise index, but for which K_{T_day} is 0.7.

Because high-resolution structural features are not well captured by k_{T_patch}, and given that interpolation schemes do not work equally well for all trace morphologies, it is possible that a single AIS will not be the top performer on days with different daily clearness indices. This is true even though the AIS can allocate schemes within individual gaps at short time intervals. This result seems counter-intuitive since the intention of the AIS, in theory, is to respond to local conditions, and therefore any variation should be accounted for. In practice though, structural effects such as stochasticity are imperfectly correlated with k_{T_patch} and so the deployment of interpolation schemes may well be sub-optimal.

A solution to these challenges is to configure a number of AISs in the development dataset using Tables 4.5 and 4.6, test them and confirm their effectiveness in the validation dataset. If the results are consistent, then the best performing adaptive schemes can be adopted with confidence. It is likely that more than one AIS will be specified for use, depending on the daily clearness index. The formulations of the diffuse and global adaptive schemes are given in Tables 4.7 and 4.8, which can be read horizontally for each variant. There are 21 variants in the diffuse scheme and 18 in the global scheme. Colour-coding has been retained from Tables 4.5 and 4.6.

Table 4.7: Configuration of 21 diffuse adaptive interpolation schemes (D_AIS) by patch-wise clearness index.

D_AIS	Bin 1	Bin 2	Bin 3	Bin 4	Bin 5	Bin 6	Bin 7	Bin 8
1	Reindl	Reindl	Reindl	Ramp	PCHIP	PCHIP	PCHIP	Ramp
2	Erbs	Erbs	Erbs	PCHIP	Ramp	Ramp	Ramp	PCHIP
3	BRL	BRL	BRL	1 min	1 min	1 min	1 min	1 min
4	O&H	BRB	BRB	Erbs	A011	3OP	20 min	3OP
5	Reindl	Reindl	Reindl	Ramp	Ramp	Ramp	Ramp	Ramp
6	Reindl	Reindl	Reindl	PCHIP	PCHIP	PCHIP	PCHIP	PCHIP
7	Erbs	Erbs	Erbs	Ramp	PCHIP	PCHIP	PCHIP	Ramp
8	BRL	BRL	BRL	Ramp	PCHIP	PCHIP	PCHIP	Ramp
9	O&H	O&H	O&H	Ramp	PCHIP	PCHIP	PCHIP	Ramp
10	BRB	BRB	BRB	Ramp	PCHIP	PCHIP	PCHIP	Ramp
11	Reindl	Reindl	Reindl	1 min	1 min	1 min	1 min	1 min
12	Reindl	Reindl	Reindl	10 min	10 min	10 min	10 min	10 min
13	Reindl	Reindl	Reindl	20 min	20 min	20 min	20 min	20 min
14	BRL	BRL	BRL	Ramp	Ramp	Ramp	Ramp	Ramp
15	Erbs	Erbs	Erbs	Ramp	Ramp	Ramp	Ramp	Ramp
16	PCHIP	Ramp	Ramp	O&H	A001	20 min	A001	A001
17	1 min	1 min	10 min	5OP	Reindl	4OP	A001	A100
18	10 min	3OP	A101	A111	O&H	Reindl	4OP	4OP
19	A011	A100	A011	Spline	BRB	O&H	5OP	5OP
20	3OP	4OP	4OP	Spline	Spline	Spline	Erbs	Erbs
21	BRL	BRL	BRL	BRL	BRL	BRL	BRL	BRL

Table 4.8: Configuration of 18 global adaptive interpolation schemes (G_AIS) by patch-wise clearness index.

G_AIS	Bin 1	Bin 2	Bin 3	Bin 4	Bin 5	Bin 6	Bin 7	Bin 8
1	GeD	GeD	GeD	Ramp	Ramp	A100	A101	A001
2	GeD	GeD	A100	A100	A100	A101	20 min	10 min
3	GeD	GeD	Ramp	1 min	A101	20 min	10 min	20 min
4	GeD	GeD	A101	3OP	10 min	3OP	1 min	A011
5	GeD	GeD	Ramp	Ramp	Ramp	Ramp	Ramp	Ramp
6	GeD	GeD	GeD	A101	A101	A101	A101	A101
7	GeD	GeD	GeD	A100	A100	A100	A100	A100
8	GeD	GeD	GeD	A001	A001	A001	A001	A001
9	GeD	GeD	GeD	1 min	1 min	1 min	1 min	1 min
10	GeD	GeD	GeD	10 min	10 min	10 min	10 min	10 min
11	GeD	GeD	GeD	20 min	20 min	20 min	20 min	20 min
12	GeD	GeD	GeD	3OP	3OP	3OP	3OP	3OP
13	GeD	GeD	GeD	4OP	4OP	4OP	4OP	4OP
14	A101	Ramp	1 min	20 min	20 min	A011	A011	Spline
15	1 min	A001	3OP	GeD	A011	A011	4OP	GeD
16	5OP	10 min	A011	A011	GeD	4OP	5OP	A111
17	10 min	3OP	A011	A011	4OP	5OP	5OP	A111
18	A001	4OP	PCHIP	4OP	5OP	A111	PCHIP	A111

The diffuse and global adaptive schemes are configured to cover as wide a range of combinations without being exhaustive. In the diffuse case, the first three variants (D_AIS 1 to 3) represent the top three combinations of interpolation methods, taken directly from the rankings in Table 4.5. The fourth variant represents the worst combination from the top cluster.

D_AIS 5 and 6 represent the best DM but with Ramp and PCHIP schemes dominating the higher clearness index bins. A reason for testing these variants is that some schemes are computationally easier to apply and yet may still give good overall results. D_AIS 7 to 10 maintain the best combinations for the higher order bins, but investigate the use of different decomposition models for cloudier conditions. These test the relative performance of one DM versus the others.

D_AIS 11 to 13 utilise the averaging schemes for higher clearness indices. These are of interest since averaging is sometimes used for replacing missing data in radiometric studies and is simple to apply. D_AIS 16 to 20 represent the best and worst combinations from their respective clusters in Table 4.5. They are included to test for an increase in uncertainty that is expected from sub-optimal interpolation techniques. D_AIS 21 is a test scheme used to confirm that the MATLAB coding functions correctly. The results for scheme 21 should be identical to those for the single-model BRL scheme.

In total there are 39 diffuse irradiance interpolation schemes tested, comprising 19 single-model variants and 20 adaptive schemes. In the G_AIS variants, the GeD model is unchallenged in bins 1 and 2 and is used throughout G_AIS 1 to 13. G_AIS 1 to 3 represent the top three combinations from Table 4.6 and the fourth variant represents the worst combination from the top cluster.

G_AIS 5 tests the use of the computationally simpler Ramp function in combination with GeD. G_AIS 6 to 13 retain GeD for the lower clearness index bins but test the uniform application of ARIMA, averaging and polynomial schemes for the higher clearness index bins. Schemes 14 to 17 represent the best and worst of clusters 2 and 3, and G_AIS 18 is the best combination from the fourth cluster in Table 4.6. There are 33 GHI interpolation schemes tested in this study, comprising 15 single-model variants and 18 adaptive schemes.

4.12 Implementation of the CdSPM: MATLAB code

The processing architecture of the CdSPM makes use of MATLAB for all data manipulation and Microsoft Excel spread sheets for displaying results. This enabled visual inspection of the outputs as the code was developed and helped with debugging. In studies of this nature the datasets are very large and rigorous checking is necessary as new models or analytical features are added.

The cloudy sky processing methodology is implemented through two custom-written MATLAB programmes. “CloudInterp” creates daily files from the unprocessed NREL radiometric data according to the format described in Tables

C-1 and C-2. Each daily file is written in Excel spreadsheet format to facilitate inspection of the data for errors.

The bulk of data processing occurs in CdSPM stages 3 to 5 using a second MATLAB programme called “CloudAnalyser”. This concatenates data from the individual daily files into cumulative analysis matrices (CAM), segregated according to radiometric component (DHI, GHI or DNI), interpolation scheme and clearness index bin. A statistical analysis can then be carried out to characterise performance of the perforated band system in each category.

There are 23 CAM files, each addressing a different aspect of PB performance. CAMs 3 to 6 deal only with interpolated data for DHI, while CAMs 7 to 11 do the same for GHI. CAMs 12 to 20 assess the performance of pure decomposition models at different time intervals. CAM 21 analyses the ability of the system to measure diffuse horizontal irradiance on a daily basis and so includes all PB data, both measured and interpolated. This includes a further subdivision according to the daily clearness index. CAM 22 does the same for GHI and CAM 23 combines the results and gives overall performance results for the DNI component. Concatenation of the daily data is necessary because statistical metrics, such as RMSD and MBD, must be determined from the full dataset.

4.13 Summary

A five-stage methodology has been presented to enable the processing of data generated by the PB system under partly cloudy and overcast conditions. The CdSPM uses the ray trace model of pyranometer exposure to separate DHI and GHI data fragments for each daily trace, from which two reconstituted curves can be obtained. The methodology proceeds by comparing the curves with radiometric measurements from collocated reference instruments. Performance can then be described in terms of %RMSD, %MBD and other metrics.

The CdSPM considers a wide range of numerical and model-based techniques for filling gaps generated by the band. The required inputs to the methodology are discussed, including two independent datasets comprising more than 268 000 rows of information gathered at 1-minute intervals, and spanning 3 years.

Cloud structure and distribution have a strong effect on the signal output from a pyranometer under a perforated band, therefore clearness index has been adopted as a means of classifying data. The chapter introduces a novel, adaptive interpolation scheme to direct the deployment of different data-generation techniques, using the statistical uncertainty (RMSD) and the clearness index as governing parameters. The configuration of the AIS is described for both the DHI and GHI components.

The CdSPM is instituted via two MATLAB programmes and generates a series of spreadsheet files to enable visual inspection of the results.

The results of the CdSPM are given in Chapter 5, including a description of the overall performance of the PB system.

5. CLOUDY SKY CONDITIONS: RESULTS

5.1 Introduction

This chapter describes the performance of the perforated shadow band system in measuring DHI, GHI and DNI under partly cloudy and overcast conditions. Results are given from the application of the cloudy sky processing methodology to two temporally independent datasets using the methods described in Chapter 4.

Performance is expressed mainly in terms of root mean square difference between the PB output and collocated reference instruments, as well as the mean bias difference, standard deviation and an expanded uncertainty parameter. The daily clearness index parameter is used to classify performance throughout the analysis.

This work focuses on high temporal resolution data with measurements at 1-minute intervals. Compared to more commonly used protocols that utilise hourly or daily interval values, this produces substantially greater variability in data structures making the processing task more complex. Importantly, the high-resolution analysis subjects the perforated band system to a rigorous test. This is necessary to establish its baseline performance against which alternate measurement schemes, such as the SPN1 and silicon diode radiometer, can be compared.

5.2 Perforated band uncertainty in the modelling of DHI

The accuracy of the perforated band system was determined separately for DHI and GHI as described in Stages 4 and 5 of the CdSPM flow chart (Figure 4.4). Direct normal irradiance was then obtained by combination of the modelled DHI and GHI components. For brevity, this section contains the key graphs and tables quantifying CdSPM performance, with Appendix E containing additional uncertainty information per bin for all schemes in graph form. For consistency, all results given in sections 5.2, 5.3 and 5.4 are for zenith angles less than 70°.

5.2.1 DHI: Dataset #1

For dataset #1, the perforated band was able to generate continuous DHI traces with RMSD uncertainties that varied between 19.4 and 43.0 W/m^2 (Table 5.1). The equivalent percentage uncertainties were relatively constant at 16 to 23% of the mean reference DHI in each K_{T_day} bin. The values in Table 5.1 represent the best interpolation schemes for each bin and were obtained by ranking the techniques in order according to the following criteria: percentage RMSD, percentage MBD, percentage standard deviation and expanded uncertainty.

Mean bias differences, which are indicative of systematic error in prediction, varied between –4.6% and 7.8% for dataset #1. These are negative under cloudier conditions (PB underestimates the reference DHI), becoming positive as skies clear (PB overestimates the DHI). The expanded uncertainties were between 44.8% and 62.1%.

Table 5.1: Statistical parameters for best performing DHI interpolation schemes by daily clearness index (NREL, $Z < 70°$).

Bin	Ave. K_{T_day}	Scheme	RMSD [W/m^2]	 [%]	MBD [W/m^2]	 [%]	SD [W/m^2]	 [%]	U_{95} [%]	|MBD| [%]
1	0.14	BRL	27.6	22.6	-5.6	-4.6	27.0	22.2	62.1	4.6
2	0.25	D_AIS_14	32.9	16.5	-8.4	-4.2	31.8	15.9	44.9	4.2
3	0.36	D_AIS_8	43.0	17.4	-6.0	-2.4	42.5	17.2	48.0	2.4
4	0.45	D_AIS_6	40.9	16.2	-2.9	-1.2	40.8	16.2	44.8	1.2
5	0.55	D_AIS_1	37.2	18.1	1.6	0.8	37.2	18.0	50.0	0.8
6	0.65	D_AIS_6	32.2	17.7	4.9	2.7	31.8	17.5	48.8	2.7
7	0.75	Ramp	19.6	20.6	4.2	4.4	19.1	20.1	56.3	4.4
8	0.81	D_AIS_1	19.4	21.2	7.2	7.8	18.1	19.8	56.8	7.8

It is important to note that although several adaptive schemes appear as best performers, many of them are configured similarly. For example, D_AIS_1 and D_AIS_6 both deploy the same interpolation techniques for $0 \leq k_{T\_patch} < 0.4$ and $0.5 \leq k_{T\_patch} < 0.7$, with the only differences appearing in bins 4 and 8 where D_AIS_1 uses the Ramp function and not PCHIP. D_AIS_8 is identical to D_AIS_1 except for the type of decomposition model used in bins 1 to 3 (see Table 4.7). The success of the decomposition models under cloudy skies is evident, while the Ramp function is clearly effective under clear skies.

The statistics in Table 5.1 include all PB data for which $Z < 70°$, both interpolated and measured. It is evident that the performance of the perforated band system is a function of clearness index, and thus should not be reduced to a single uncertainty measurement, either RMSD or MBD. In this respect Table 5.1 represents an expanded but appropriate description of how well the CdSPM performs in generating DHI from a broken PB system trace at the NREL site.

Figures 5.1 and 5.2 enable comparison of the AISs with single-scheme interpolation methods in dataset #1 and decomposition models. In most bins the adaptive interpolation scheme outperforms a single-method approach with respect to RMSD and MBD. Interestingly, the single-scheme BRL model performs best in bin 1, probably because decomposition models handle short-lived spikes in irradiance under overcast conditions better than Ramp or PCHIP methods that are normally invoked by the AIS for gaps with mid-range clearness indices.

The blue markers in Figures 5.1 and 5.2 represent the uncertainty of the best performing decomposition model per bin, obtained primarily with NREL reference data gathered from a ventilated Kipp and Zonen CM22 radiometer. These permit comparison of the PB-generated DHI with that obtained using a single unshaded pyranometer together with the models described in sections 4.9.2 to 4.9.6. As an alternate measurement approach, the DM technique is less expensive than the perforated band because it relies only on a single unshaded pyranometer, however the RMSD uncertainties of the best performing models grow considerably under partly cloudy and clear skies, making them less accurate for all conditions except heavily overcast. A similar trend is evident for the MBD uncertainty (Figure 5.2). Further details on the implementation of the decomposition models are given in section 5.6.

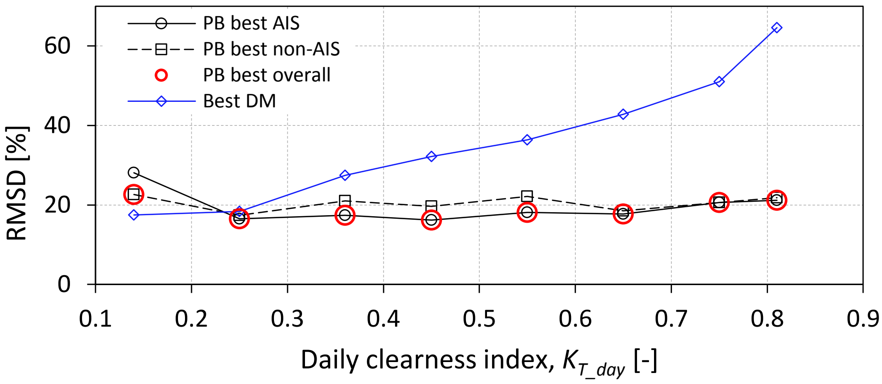

Figure 5.1: Root mean square difference for best adaptive, best non-adaptive and best overall DHI interpolation schemes in dataset #1 by daily clearness index, including best decomposition model performance (*Z* < 70°).

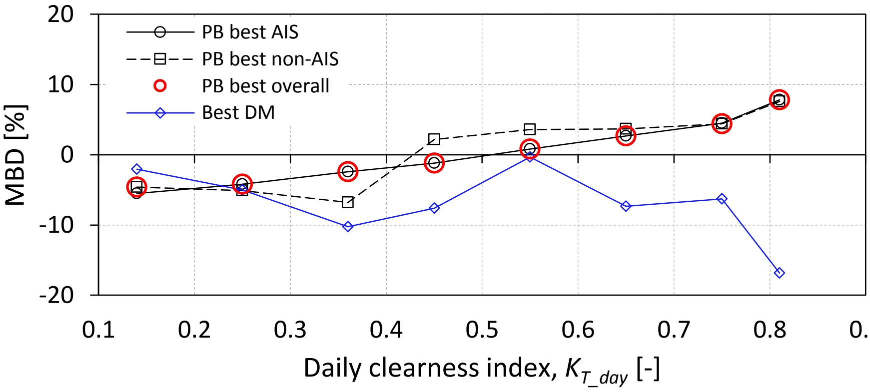

Figure 5.2: Mean bias difference for best adaptive, best non-adaptive and best overall DHI interpolation schemes in dataset #1 by daily clearness index, including best decomposition model performance (*Z* < 70°).

5.2.2 DHI: Dataset #2

The reproducibility of the CdSPM was tested using a second, independent dataset (#2). Three analyses of the RMSD and MBD metrics were conducted:

1. The best performing schemes from dataset #1, as given in Table 5.1, were compared with the best schemes from dataset #2 on a bin-by-bin basis. In three of the bins the same schemes were top performers for both #1 and

#2, otherwise they differed. This aimed to establish whether the overall magnitudes of RMSD and MBD statistics changed appreciably and addresses the fundamental effectiveness of the PB system, rather than the consistency of specific interpolation methods. Results can be seen in Figures 5.3 and 5.4 where the circular black markers (best in #2) and circular red markers (best in #1) track each other reasonably well. The average difference between the RMSD values across all bins is 2.5% and –0.3% for MBD.

2. The best performing schemes in dataset #1 were compared with results for the same schemes in #2. This aimed to establish inconsistencies in the performance of those specific interpolation methods across independent datasets. Results can be seen by comparing the red markers in Figures 5.3 and 5.4 with the green circles (best of #1 in #2). The average difference between the RMSD values across all bins is 2.3% and –0.2% for MBD.
3. The best performers in dataset #2 were compared with the best performing schemes from #1 in dataset #2. This aimed to establish the overall effectiveness and reproducibility of the CdSPM by examining whether the differences in the types of schemes making up the top performers in each dataset set made any appreciable difference to the statistical uncertainty in modelling DHI. This is illustrated by comparing the black markers (best in #2) in Figures 5.3 and 5.4 with the green circles (best of #1 in #2).

   This is arguably the most important test of the CdSPM. It matters less that the identical schemes perform best across different datasets however it is crucial that the CdSPM should yield similar uncertainties regardless of the exact mix of schemes that provide them. In this case, the best performing schemes from dataset #1 give almost identical uncertainties to the best performers in dataset #2 when transferred to dataset #2, with an average difference in RMSD across all bins of just 0.2% and MBD of 0.1%.

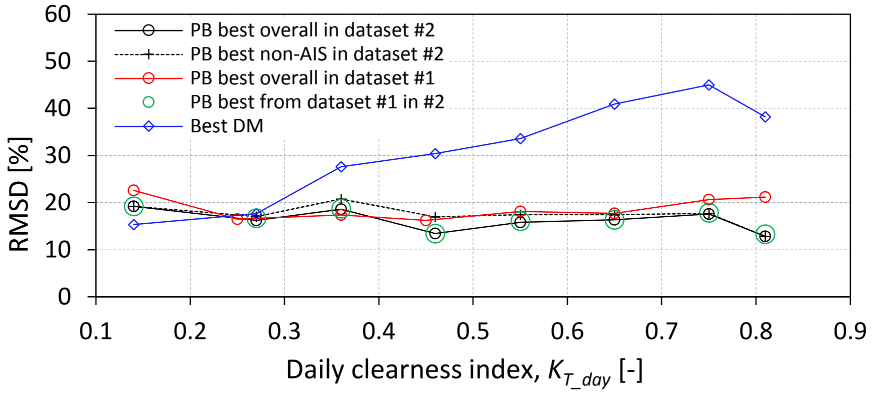

Figure 5.3: Comparative root mean square difference of best overall and best non-AIS schemes for DHI in datasets #1 and #2, by daily clearness index, including best decomposition model performance (*Z* < 70°).

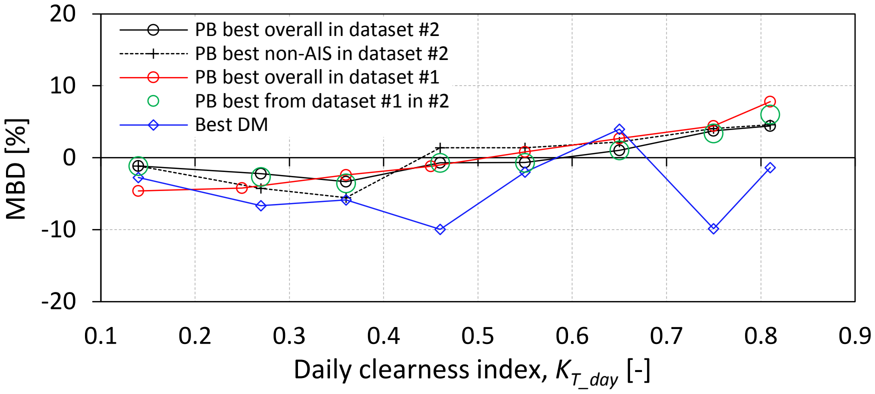

Figure 5.4: Comparative mean bias difference of best overall and best non-AIS schemes for DHI in datasets #1 and #2, by daily clearness index, including best decomposition model performance ($Z < 70°$).

These results confirm that the CdSPM is a robust and statistically reproducible processing methodology for generating DHI from a perforated band system at the NREL SRRL site.

5.3 Perforated band uncertainty in the modelling of GHI

The GHI analysis follows a similar approach to the diffuse, with uncertainties calculated against reference values for all PB data, interpolated and measured. The number of interpolation schemes is reduced due to the absence of decomposition models (Table 4.8).

5.3.1 GHI: Dataset #1

As Table 5.2 indicates, the magnitude and variability of the RMSD uncertainties for GHI across most bins were higher than for DHI. The CdSPM returned a minimum RMSD of 6.7% (bin 8) and a maximum of 35.2% (bin 3), with G_AIS_1 dominating in half of the bins. Unlike the DHI results which were relatively constant regardless of the sky condition, Figure 5.5 shows a pronounced rise in uncertainty over the mid-clearness index range, which may be explained by the greater sensitivity of global irradiance to fluctuations in DNI.

Under partly cloudy conditions DNI is ‘switched’ on and off frequently by the cloud field and the stochasticity of the GHI trace increases, registering greater extremes than the DHI. Under these conditions, the gaps in the perforated band output trace are more difficult to fill accurately by interpolation. Under clear sky conditions (bins 7 and 8) the data trace cleans up considerably and the PB values track the reference measurements closely.

The mean bias difference is negative throughout all bins, meaning that the PB system underestimates global irradiance. MBD values range between –1.2% and –6.7%, with the greatest variance in the mid-K_{T_day} range.

The adaptive schemes once again outperform the best single-scheme interpolation techniques for RMSD and MBD in most bins, although there is little difference between the two approaches under clear conditions (Figures 5.5 and 5.6). In bin 7, for example, G_AIS_6 returns identical uncertainties for RMSD, MBD, SD and U_{95} as the A101 scheme, which is expected given the composition of G_AIS_6.

Decomposition models do not apply to the calculation of GHI from DHI, therefore no graphical comparison is made as in Figures 5.5 and 5.6.

Table 5.2: Best performing GHI interpolation schemes by bin (NREL, *Z* < 70°).

Bin	**Ave.**	**Scheme**	**RMSD**		**MBD**		**SD**		**U_{95}**	**|MBD|**
	K_{T_day}		**[W/m^2]**	**[%]**	**[W/m^2]**	**[%]**	**[W/m^2)\]**	**[%]**	**[%]**	**[%]**
1	0.14	G_AIS_1	29.0	22.9	-6.2	-4.9	28.3	22.3	62.7	4.9
2	0.25	G_AIS_9	49.1	22.6	-13.2	-6.1	47.3	21.8	61.6	6.1
3	0.36	G_AIS_1	113.4	35.2	-21.2	-6.6	111.4	34.6	96.7	6.6
4	0.45	G_AIS_1	128.6	31.7	-27.0	-6.7	125.7	31.0	87.0	6.7
5	0.55	G_AIS_1	145.2	29.1	-25.3	-5.1	143.0	28.7	80.1	5.1
6	0.65	G_AIS_2	129.5	22.0	-15.9	-2.7	128.5	21.8	60.7	2.7
7	0.75	G_AIS_6	74.7	11.9	-10.8	-1.7	73.9	11.8	32.8	1.7
8	0.81	G_AIS_5	46.0	6.7	-8.4	-1.2	45.3	6.6	18.5	1.2

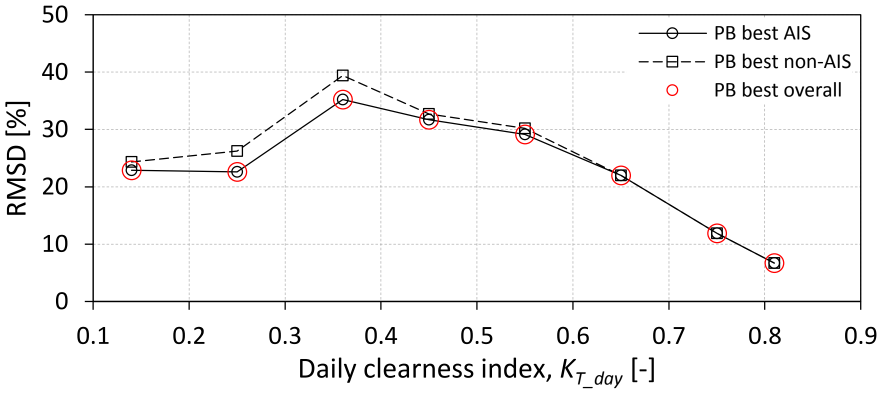

Figure 5.5: Root mean square difference for best adaptive, best non-adaptive and best overall GHI interpolation schemes in dataset #1 by daily clearness index (*Z* < 70°).

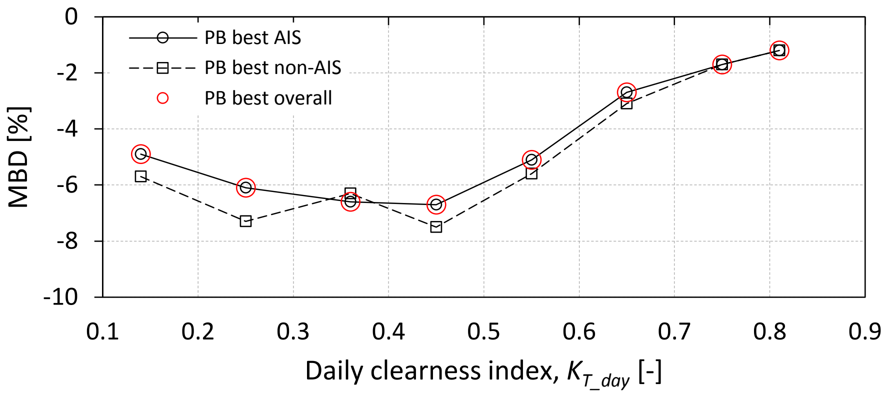

Figure 5.6: Mean bias difference for best adaptive, best non-adaptive and best overall GHI interpolation schemes in dataset #1 by daily clearness index ($Z < 70°$).

5.3.2 GHI: Dataset #2

Reproducibility of the CdSPM was demonstrated as follows, with respect to the generation of GHI in datasets #1 and #2:

1. The best performing schemes from dataset #1, given in Table 5.2, were compared with the best schemes from dataset #2. Results are shown in Figures 5.7 and 5.8 where the circular black markers (best in #2) and circular red markers (best in #1) are closely aligned, although a difference exists under overcast conditions for MBD. The average difference between the RMSD values across all bins is 2.3% and for MBD the difference is 1.1%. Interestingly, in bins 1, 2, 6 and 8 the same schemes were top performers for both datasets.
2. The uncertainties of the best performing schemes in dataset #1 (red markers) were compared with those generated by the same schemes in #2 (green circles). This would highlight inconsistencies in the performance of those specific interpolation methods. The average difference between the RMSD values across all bins in the two datasets is 1.8% and 0.9% for MBD.
3. A comparison of the best performing schemes from dataset #2 (black markers) with the set of best performing schemes from dataset #1 operating in #2 (green circles), was undertaken. As with the DHI analysis, very little difference in results was observed, with an average difference in RMSD across all bins of just 0.4% and –0.1% for MBD.

A similar conclusion can be drawn for GHI as for DHI, namely that the uncertainties change very little across independent datasets and consequently the CdSPM is confirmed as a reproducible processing methodology for generating GHI using the perforated band.

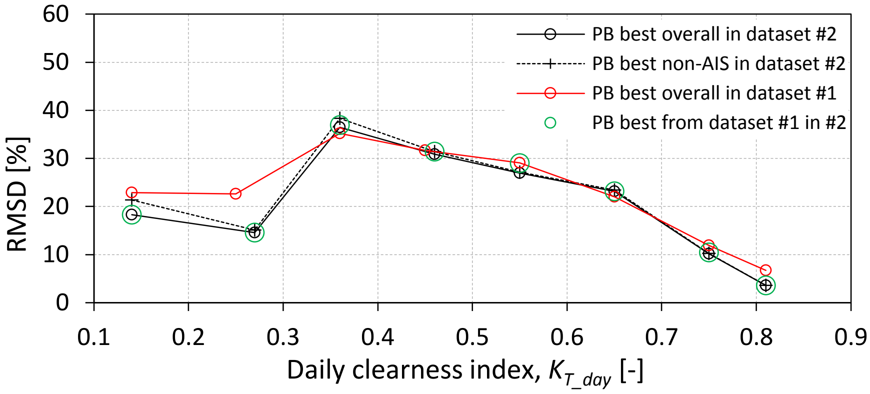

Figure 5.7: Comparative root mean square difference of best overall and best non-AIS schemes for GHI in datasets #1 and #2, by daily clearness index (Z < 70°).

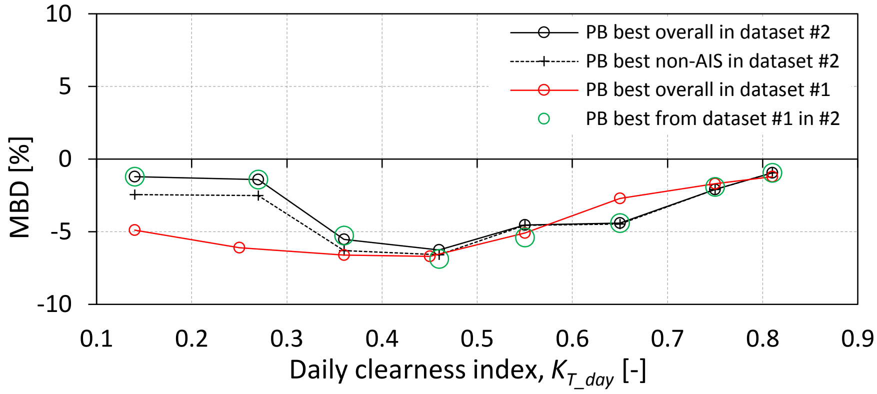

Figure 5.8: Comparative mean bias difference of best overall and best non-AIS schemes for GHI in datasets #1 and #2, by daily clearness index (Z < 70°).

5.4 Calculation of the DNI component and its uncertainty

Direct normal irradiance cannot be measured directly by a perforated band system however DNI can be calculated at 1-minute intervals by combining contemporaneous data from DHI and GHI interpolation schemes, using equation (1.2). This was done for measured and interpolated data in each daily clearness index bin, to yield a set of K_{T_day}–dependant uncertainties representing the modelling performance of the perforated band for DNI.

When two identical single-scheme methods were combined (eg. Ramp DHI with Ramp GHI) the same name was given to the resulting DNI output. If different single-scheme methods were combined, or if either of the components was an adaptive scheme drawn from Tables 4.9 or 4.10, the resulting combination was referred to as B_AIS_*x*, where *x* is a designation from 1 to 38. Table 5.3 gives the components for each of the B_AIS variants.

A total of 36 DNI variants were tested in each of the eight daily clearness index bins of datasets #1, consisting of the following:

- 14 matched single-scheme methods, derived from the DHI and GHI components listed in Table 4.2. These are the non-AIS methods pairing like with like.
- 20 adaptive combinations (B_AIS_1 to 20) from Table 5.3. B_AIS_1 to 6 combine a selection of the best DHI performers on a gap-wise basis with the best gap-wise performer for GHI (G_AIS_1). This is repeated for B_AIS_7 to 12 using G_AIS_2 as the global component, and again for schemes B_AIS_13 to 18 using G_AIS_3.
- B_AIS_19 and 20 are identical to B_AIS_1 except that the adaptive scheme for DHI is suspended on days when K_{T_day} is less than 0.2, and the BRL and Reindl decomposition models are applied instead regardless of the intraday patch-wise index. This was done because results for DHI indicated that under heavily overcast conditions the decomposition models yielded lower RMSD uncertainties than the adaptive approach (Table 5.1).
- B_AIS_ 21 to 28 combine the best performing DHI schemes from Table 5.1 with the best performing GHI schemes from Table 5.2. These are determined according to their performance in dataset #1, after classification according to the daily clearness index, and not the patch-wise index. B_AIS_29 to 36 are determined the same way, but apply to results for dataset #2 and are necessary to enable a comparison between the datasets. Since schemes 21 to 36 are determined from specific bins, they are not applied universally for all daily clearness index conditions, but only for the bin in which they excelled. Thus B_AIS_21 was tested only for $K_{T\_day} < 0.2$, B_AIS_22 was tested for $0.2 < K_{T\_day} \leq 0.3$, and so on. These schemes were expected to give low uncertainties since they combine the best performers for diffuse and global irradiance.
- B_AIS_37 was tested for interest, and represented the combination of best DHI and GHI performers by ABS(%MBD) as found for dataset #1 ($Z < 70°$) across all clearness index bins and without segregation according to K_{T_day}. B_AIS_38 does the same for dataset #2. These schemes were expected to perform poorly because the resulting DNI was determined from DHI and GHI components that do not exploit the advantage provided by classifying data according to K_{T_day}.

The total number of DNI schemes tested therefore rose to 38 in dataset #2 as B_AIS 29 and B_AIS_38 were added to the existing group, for comparison purposes.

Table 5.3: Configuration of direct normal irradiance adaptive interpolation schemes (B_AIS).

B_AIS	DHI Scheme	GHI Scheme	B_AIS	DHI Scheme	GHI Scheme
1	D_AIS_1	G_AIS_1	**21**	BRL	G_AIS_1
2	D_AIS_5	G_AIS_1	**22**	D_AIS_14	G_AIS_9
3	D_AIS_6	G_AIS_1	**23**	D_AIS_8	G_AIS_1
4	D_AIS_7	G_AIS_1	**24**	D_AIS_6	G_AIS_1
5	D_AIS_8	G_AIS_1	**25**	D_AIS_1	G_AIS_1
6	D_AIS_14	G_AIS_1	**26**	D_AIS_6	G_AIS_2
7	D_AIS_1	G_AIS_2	**27**	Ramp	A101
8	D_AIS_5	G_AIS_2	**28**	D_AIS_1	Ramp
9	D_AIS_6	G_AIS_2	**29**	BRL	G_AIS_1
10	D_AIS_7	G_AIS_2	**30**	D_AIS_2	G_AIS_9
11	D_AIS_8	G_AIS_2	**31**	D_AIS_6	G_AIS_8
12	D_AIS_14	G_AIS_2	**32**	D_AIS_6	G_AIS_5
13	D_AIS_1	G_AIS_3	**33**	D_AIS_6	G_AIS_5
14	D_AIS_5	G_AIS_3	**34**	D_AIS_6	G_AIS_2
15	D_AIS_6	G_AIS_3	**35**	D_AIS_1	G_AIS_5
16	D_AIS_7	G_AIS_3	**36**	D_AIS_4	Ramp
17	D_AIS_8	G_AIS_3	**37**	O&H	G_AIS_12
18	D_AIS_14	G_AIS_3	**38**	D_AIS_3	G_AIS_12
19	D_AIS_1*	G_AIS_1	**C**	Denotes corrected by Bird	
20	D_AIS_1**	G_AIS_1			

* suspension of AIS for $K_{T\_day} < 0.2$ and use of BRL for DHI regardless of k_{T_patch}

** suspension of AIS for $K_{T\_day} < 0.2$ and use of Reindl for DHI regardless of k_{T_patch}

In theory, B_AIS schemes 19, 20 and 21 might be expected to give the same uncertainties for days in bin 1, since the BRL model is implemented uniformly whenever $K_{T\_day} < 0.2$. In practice the uncertainties are different because the PB system measures daily clearness index using only patches of known GHI values and not the full day’s record, as done for the NREL reference instruments. Therefore, a misclassification of daily data can occur if, for example, the PB system determines that the K_{T_day} exceeds 0.2 but the reference data determines that it does not. This is rare but possible because in the calculation of statistical uncertainty, data are necessarily classified according to reference-derived K_{T_day} values, while the internal processing of data is done using only output from the PB system.

The DNI outputs produced by equation (1.2) can exceed physical limits and even become negative because of inaccuracies in the component DHI and GHI values. As a quality-control measure, the Bird clear sky model (Bird and Hulstrom, 1981) was used to monitor each DNI value produced by the PB system, E_{fbn}, and impose limits to prevent non-physical results, as follows:

$$E_{fbn} = \begin{cases} E_{bn\_Bird} & E_{fbn} > 1.3E_{bn\_Bird} \\ 0 & E_{fbn} < 0 \end{cases} \tag{5.1}$$

Schemes subjected to the correction procedure were given the same names as their unrestricted counterparts, however the letter ‘C’ was appended to indicate correction by the Bird model. The number of variants tested in datasets #1 and #2 thus doubled from 36 and 38 to 72 and 76 respectively.

Setting the upper DNI limit at 130% of the predicted Bird value allowed for possible underprediction of DNI by the clear sky model. No attempt was made to optimise this value, however it can be seen from the results that the implementation of the limit improves performance in most of the bins.

5.4.1 DNI: Dataset #1

Table 5.4 gives bin-based results for DNI obtained by the combination of DHI and GHI, according to Table 5.3. These results should be interpreted with care since the percentage RMSD values become amplified under overcast conditions when the reference DNI drops close to zero. For this reason, additional graphs are provided for RMSD and MBD showing the absolute values in [W/m^2].

Several trends are evident in Table 5.4. The CdSPM returns absolute uncertainties that balloon noticeably in the mid-clearness index range, similar to the GHI results. Under partly cloudy conditions ($0.3 \leq K_{T\_day} < 0.7$) the PB system performs poorly, with RMSD values of between 142.9% and 31.1%. Bias is consistently negative at values between –3.5 and –5.0%, meaning that the direct normal component is underestimated by the CdSPM.

The adaptive schemes composed of the best performing DHI and GHI components generally returned the lowest, or close to the lowest uncertainties. The Ramp function (pairing Ramp DHI with Ramp GHI) generally performed well. It is also clear that the application of the Bird model to restrict the direct normal component at its upper and lower limits gives better results than the uncorrected schemes, except in bin 8. This is most likely because the data in bin 8 are nearly cloud-free, thus the advantage provided by the Bird model in dealing with extreme values is neutralised for data traces that are structurally coherent.

Under the clearer conditions of bins 7 and 8, considerably lower RMSD uncertainties in the region of 10% are obtained. This confirms that the perforated band is best deployed in areas where the daily clearness index exceeds 0.7, if DNI is the component of interest.

The adaptive interpolation schemes generally perform better than non-AIS variants, although there is little difference under clearer conditions (Figures 5.9 to 5.12). This was to be expected given that similar trends were observed for each of the constituent GHI and DHI components.

Table 5.4: Best performing DNI interpolation schemes per bin (NREL, $Z < 70°$).

Bin	**Ave.**	**Scheme**	**RMSD**		**MBD**		**SD**		**U_{95}**	**|MBD|**
	K_{T_day}		**[W/m^2]**	**[%]**	**[W/m^2]**	**[%]**	**[W/m^2]**	**[%]**	**[%]**	**[%]**
1	0.14	B_AIS_21C	28.0	516.2	1.7	31.5	27.9	515.2	1429.4	31.5
2	0.25	B_AIS_6C	63.9	244.5	-0.3	-1.2	63.9	244.5	677.8	1.2
3	0.36	B_AIS_23C	145.8	142.9	-3.6	-3.5	145.8	142.9	396.0	3.5
4	0.45	RampC	172.0	78.4	-10.9	-5.0	171.6	78.2	217.0	5.0
5	0.55	RampC	193.2	45.4	-20.4	-4.8	192.1	45.2	125.5	4.8
6	0.65	A100C	182.7	31.1	-20.6	-3.5	181.5	30.9	85.9	3.5
7	0.75	B_AIS_27C	119.4	13.7	-16.1	-1.8	118.3	13.6	37.9	1.8
8	0.81	Ramp	89.4	9.4	-13.5	-1.4	88.4	9.3	25.9	1.4

Figures 5.9 to 5.12 permit comparison of the CdSPM data with output from decomposition models implemented mainly with reference GHI measurements. The decomposition models return lower RMSD uncertainties throughout, although the difference becomes small for bins 7 and 8.

Interestingly, the decomposition models perform quite poorly in terms of mean bias difference, as compared to the perforated shadow band system. Other than in bins 5 and 7, the PB system yields lower bias differences for the top performing schemes listed in Table 5.4. The DM bias difference is consistently positive up to bin 7, indicating that the decomposition models overestimate DNI.

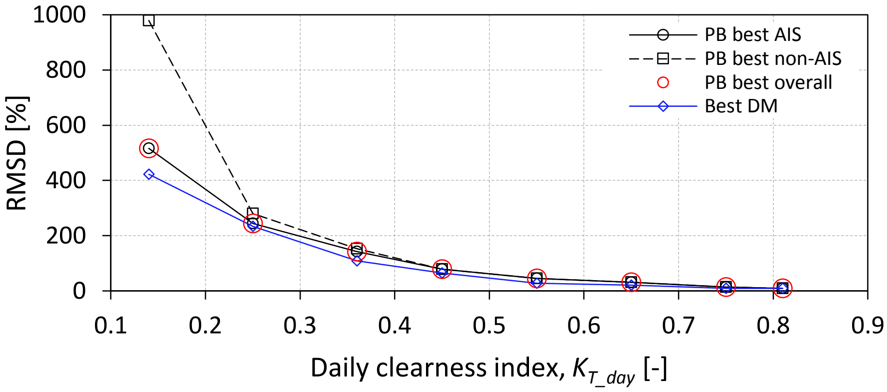

Figure 5.9: Percentage root mean square difference for best adaptive and non-adaptive schemes in dataset #1 by daily clearness index ($Z < 70°$).

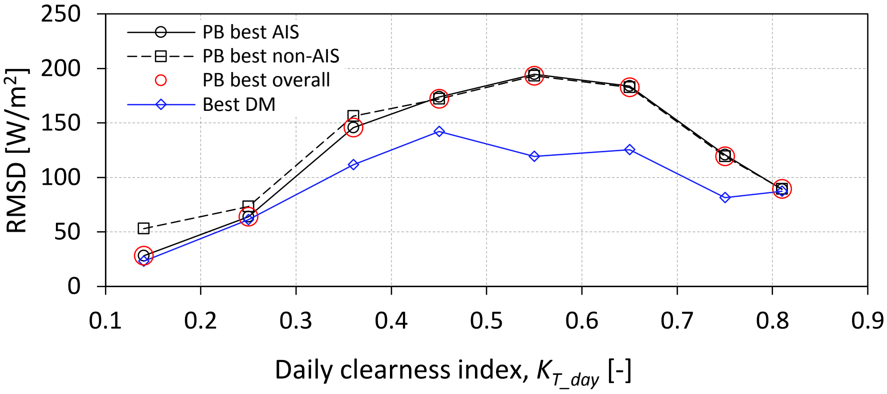

Figure 5.10: Root mean square difference in [W/m^2] for best adaptive and non-adaptive schemes in dataset #1 by daily clearness index (Z < 70°).

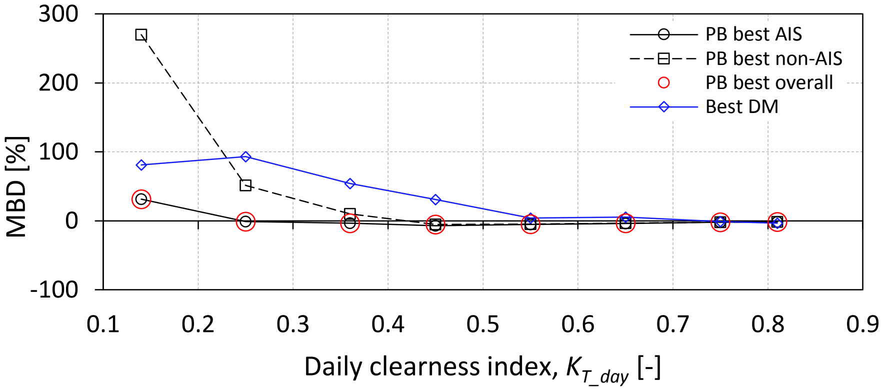

Figure 5.11: Percentage mean bias difference for best adaptive and non-adaptive schemes in dataset #1 by daily clearness index (Z < 70°).

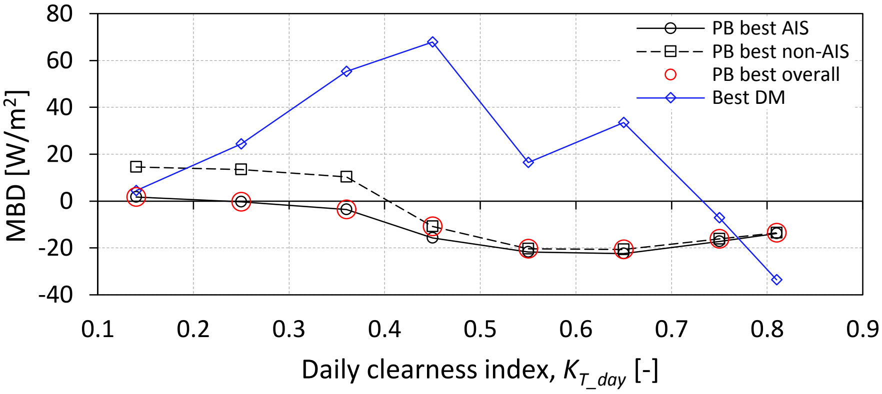

Figure 5.12: Mean bias difference in [W/m^2] for best adaptive and non-adaptive schemes in dataset #1 by daily clearness index (Z < 70°).

A more detailed discussion of decomposition model performance versus that of the perforated band is provided in section 5.6. Appendix E provides additional RMSD uncertainty results for dataset #1, comprising a graphical comparison between the best performing schemes described here and those that performed poorly. The comparison covers DHI, GHI and DNI interpolation results.

5.4.2 DNI: Dataset #2

The implementation of the CdSPM in dataset #2 confirmed the reproducibility of the results with regard to DNI. For readability, the DNI uncertainties in Figures 5.13 and 5.14 are given in [W/m^2] rather than percentages.

As with dataset #1, the top performing schemes in dataset #2 were generally those combining the best performing DHI and GHI components and, in two bins, the Ramp interpolation function. The best performing schemes from dataset #1 and the best schemes from dataset #2 (black markers and red markers respectively) follow a similar trend and return very similar root mean square differences.

As before, RMSD uncertainties are pronounced in the mid-range of clearness index. As in dataset #1, the decomposition models yield lower uncertainties, although the mean bias difference for the models is higher in half of the bins. There is little to choose between the AIS and non-AIS schemes at higher clearness indices, however the adaptive schemes tend to perform better in bins 1 and 2.

Significantly, the interpolation methodologies that performed best in dataset #1 also returned low RMSD uncertainties when instituted in dataset #2. The average difference in RMSD across all bins between the transferred list of schemes from dataset #1 and the best schemes in #2 is 1.8%. This is shown graphically in Figures 5.13 and 5.14, where the black markers and the green circles are largely coincident.

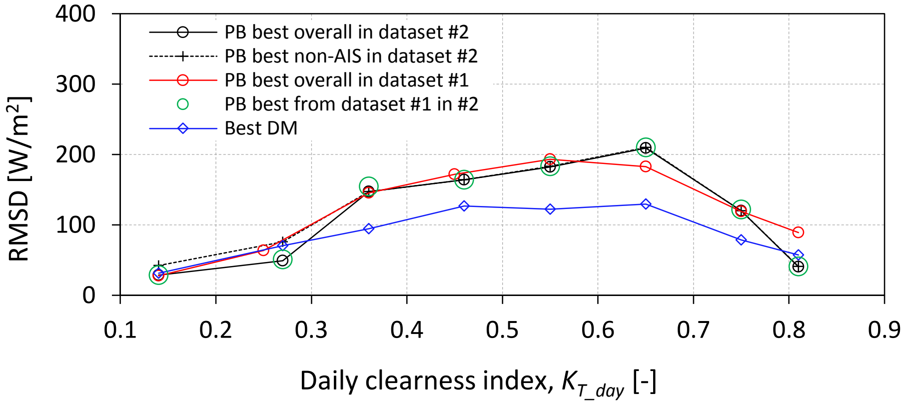

Figure 5.13: Comparative root mean square difference of best overall and best non-AIS schemes for DNI in datasets #1 and #2, by daily clearness index (Z < 70°).

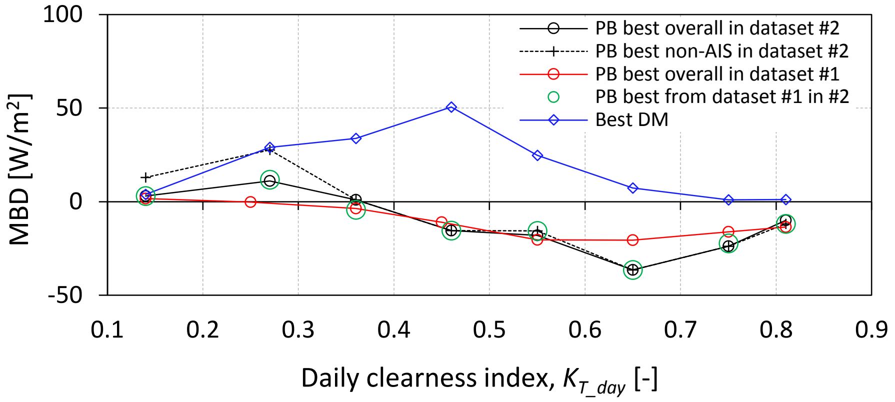

Figure 5.14: Comparative mean bias difference of best overall and best non-AIS schemes for DNI in datasets #1 and #2, by daily clearness index (Z < 70°).

These results confirm that the schemes identified in dataset #1 as most effective in reducing uncertainty, do so consistently across independent datasets. Therefore, the CdSPM itself may be assumed robust and capable of reproducing similar DNI results at the NREL site.

5.5 Visualisation of CdSPM results for daily data

The statistical analyses of the preceding sections identified superior interpolation schemes based on two substantial datasets. In this section, the CdSPM is applied to three daily data files as an example of how the methodology produces irradiance curves in practice. The resulting traces are presented graphically.

The days reflect three different average daily clearness indices of 0.14 (heavily overcast), 0.33 and 0.49 (mixed conditions). In each case, irradiance traces from a selection of the interpolation schemes are provided along with the reference measurements for comparison. Since the CdSPM was shown to perform in a robust, reproducible manner across different datasets, it should be expected to yield RMSD and MBD uncertainties approaching those described in Tables 5.1, 5.2 and 5.4, when applied to individual daily files from the two datasets.

5.5.1 Mixed conditions

Figures 5.15, 5.16 and 5.17 show the CdSPM's attempts to reproduce a reference trace for DHI, GHI and DNI curves, respectively, using data recorded at NREL SRRL on 2 June 2012. The day represents an interesting test case since it transitions from a cloudless morning to an overcast afternoon, and therefore contains intraday extremes in the clearness index. The average daily clearness index was 0.33 with the transition to overcast occurring just after 10:00 hours.

Figure 5.15 gives the results for DHI reconstruction, with the uppermost pane showing the reference diffuse irradiance in grey (E_d) and the measured DHI from the PB system in red (E_{fd}). Gaps in the trace for which no DHI measurements were recorded, are clearly visible and include periods with high irradiance ramp rates, which represent a challenge for the interpolation process.

The second, third and fourth panes contain a selection of interpolation schemes together with the percentage RMSD for each technique. It should be noted that the uncertainties are calculated for the entire day and not for a subset of the data for which $Z < 70°$. This is done to illustrate the actual %RMSD that would result for a PB system run under these conditions. The lowest pane contains the most successful scheme for the given data (D_AIS_14), as well as the scheme identified by the CdSPM as the best statistical option for the given clearness index (D_AIS_8), taken from Table 5.1. In this case, D_AIS_8 performs slightly worse than D_AIS_14 by 0.5%.

Importantly, Figure 5.15 shows that the adaptive scheme works very well in dealing with highly variable conditions. Had a pure Ramp interpolation approach been used throughout the day, the resulting RMSD percentage would have risen to 29.9% as shown in the lowest pane. Conversely, the use of a decomposition model such as BRL throughout to deal with the overcast patches would have returned an uncertainty of 40.1%. The adaptive schemes successfully deploy both of these techniques in a selective manner to reduce the uncertainty.

The results for GHI can be seen in Figure 5.16. The Spline and PCHIP schemes are configured to pass only through the measured data and therefore deviate considerably from the reference trace at high zenith angles (second pane). The reverse decomposition model (GeD) works well under overcast conditions, but is a poor performer in the absence of cloud, giving the saw-tooth waveform typical of PB output under clear skies (pane 3). G_AIS_1 utilises both GeD and other schemes, as dictated by the patch-wise clearness indices, returning a daily RMSD uncertainty of 39.5%. G_AIS_9 makes use of 1 minute average interpolation for the clearer part of the day and does marginally better. This is mainly due to its superior performance in the 4th gap around 10:00, where the difference between the reference trace and the interpolated data becomes large. RMSD is particularly sensitive to such differences because of the exponential nature of its formulation.

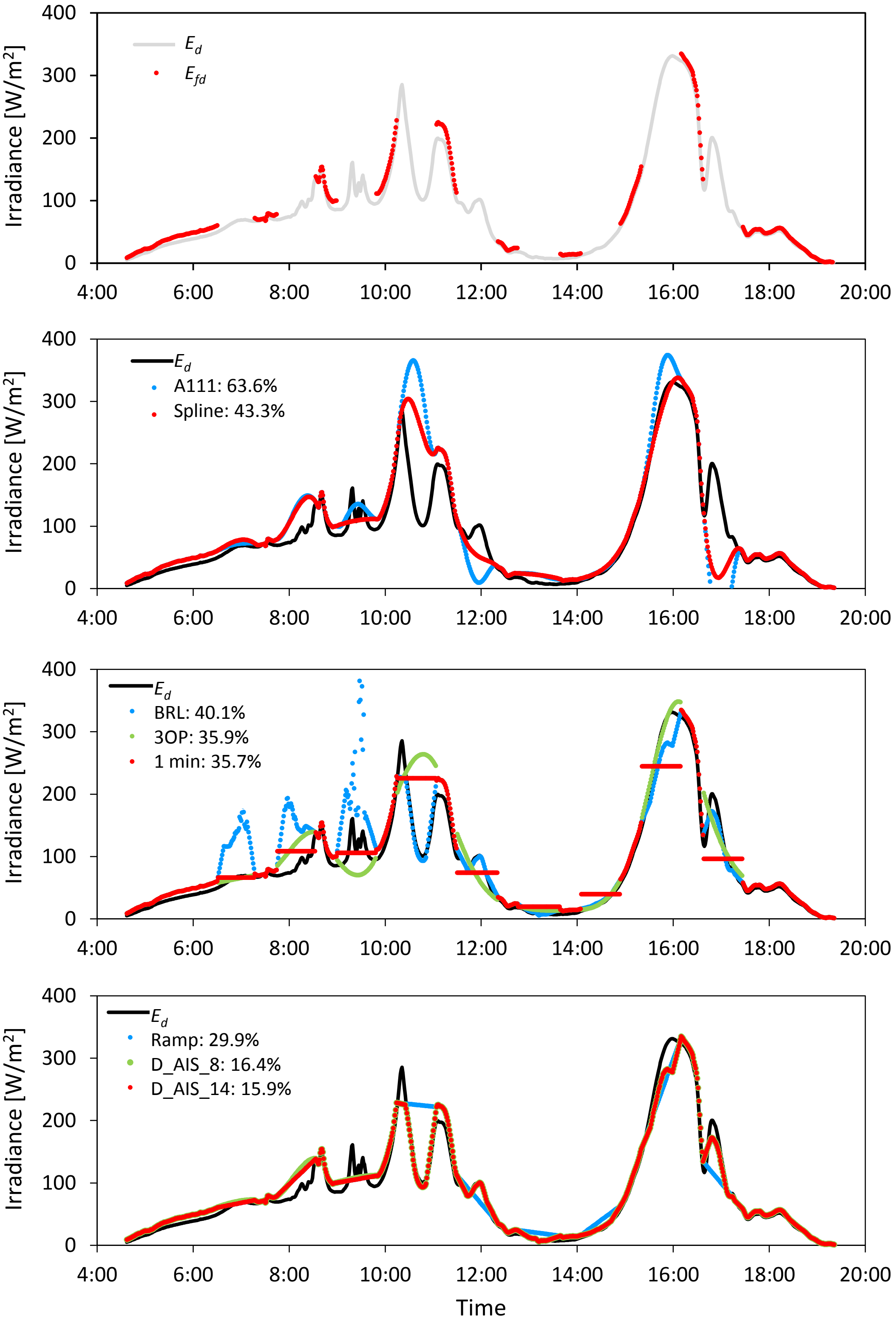

Figure 5.15: Application of the CdSPM to DHI data on 2 June 2012 for mixed cloud conditions and K_{T_day} = 0.33. Uncertainties are given in %RMSD.

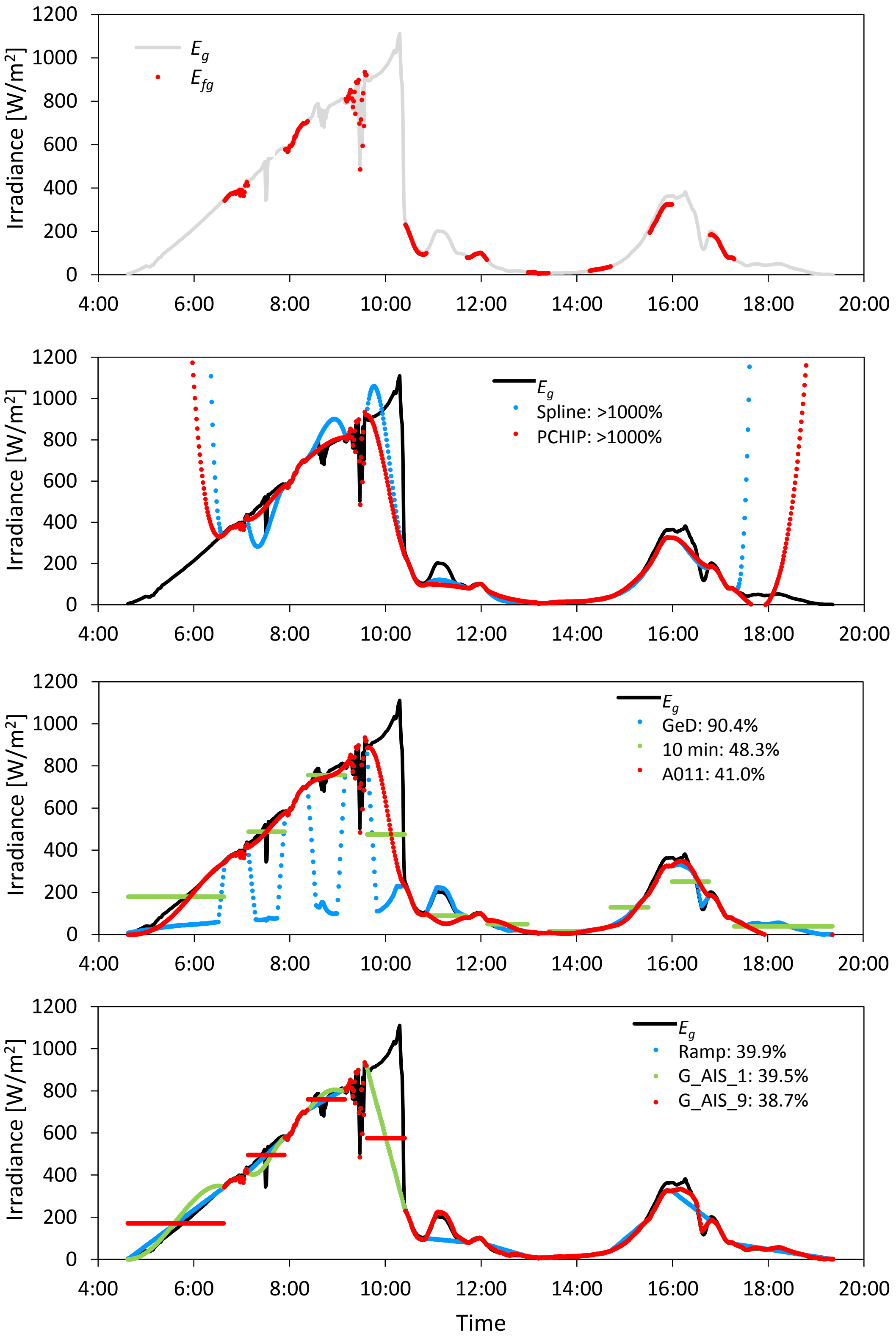

Figure 5.16: Application of the CdSPM to GHI data on 2 June 2012 for mixed cloud conditions and K_{T_day} = 0.33. Uncertainties are given in %RMSD.

The DNI results for 2 June 2012 are given in Figure 5.17. The top pane includes both the global irradiance (E_{fg}) and the diffuse component (E_{fd}) from the PB pyranometer, together which must recreate the reference DNI trace.

The effectiveness of the Bird model as a correction tool is evident in the early hours of the day up to about 06:30 where non-physical results are obtained for the 3rd order polynomial, PCHIP and Spline schemes. In this case a reasonable clear-sky curve is created by imposing the Bird correction on the data. Overall, the B_AIS_23C adaptive scheme returns the lowest uncertainty for the day.

Figures 5.18 to 5.20 show the CdSPM at work for 7 July 2011, for which the average clearness index is 0.49. Once again the morning is relatively clear however the afternoon reflects a partly cloudy sky with considerable stochasticity in the data traces. In fact, the day contains DHI gaps with clearness index values that fall into seven different bins.

In the four panes of Figure 5.18 a selection of interpolation schemes and their associated uncertainties are given. The Spline scheme over- and undershoots the reference DHI as the mathematics enforces continuity of the first and second derivatives at the nodes. The model uncertainties improve with the 1-minute average scheme in pane 3, although averaging generates plateaus that appear highly non-physical.

The application of a pure linear interpolation approach (Ramp) produces a daily RMSD uncertainty of 24.4%, but the Ramp function misses the short-lived spike in DHI that occurs at 16:00. The Reindl decomposition model detects and tracks the spike because the clearness index within that gap drops to 0.16, the diffuse fraction approaches unity and the DHI is set approximately equal to the contemporaneously measured global data. The Reindl model shows its weakness between 06:30 and 09:00 where there are two gaps in the trace whose clearness indices are 0.64 and 0.73, representing almost clear conditions. In the absence of cloud the DM yields a series of irregular bumps in the trace.

The effectiveness of the D_AIS_6 adaptive scheme can be seen as it selectively deploys interpolation methods according to the local, patch-wise clearness index, making use of both the decomposition model and other techniques. In this way the uncertainty is reduced to 17.5%.

In Figure 5.19, the GHI reference trace exhibits considerable high-frequency fluctuation and represents a particular challenge for data regeneration efforts. Schemes G_AIS_1 and 2 do better than the Ramp function and return uncertainties of 34.2% and 32.6% respectively, but much of the afternoon trace volatility defies accurate tracking. This illustrates the weakness of the perforated band system and underscores its suitability for clearer sky conditions.

In Figure 5.20 the most successful DNI interpolation approach is the B_AIS_8C scheme, which gives an RMSD uncertainty of 45.1% for the day. None of the schemes performs particularly well, although the morning period is more effectively dealt with since the DNI reference trace is largely coherent between sunrise and 10:00 hours.

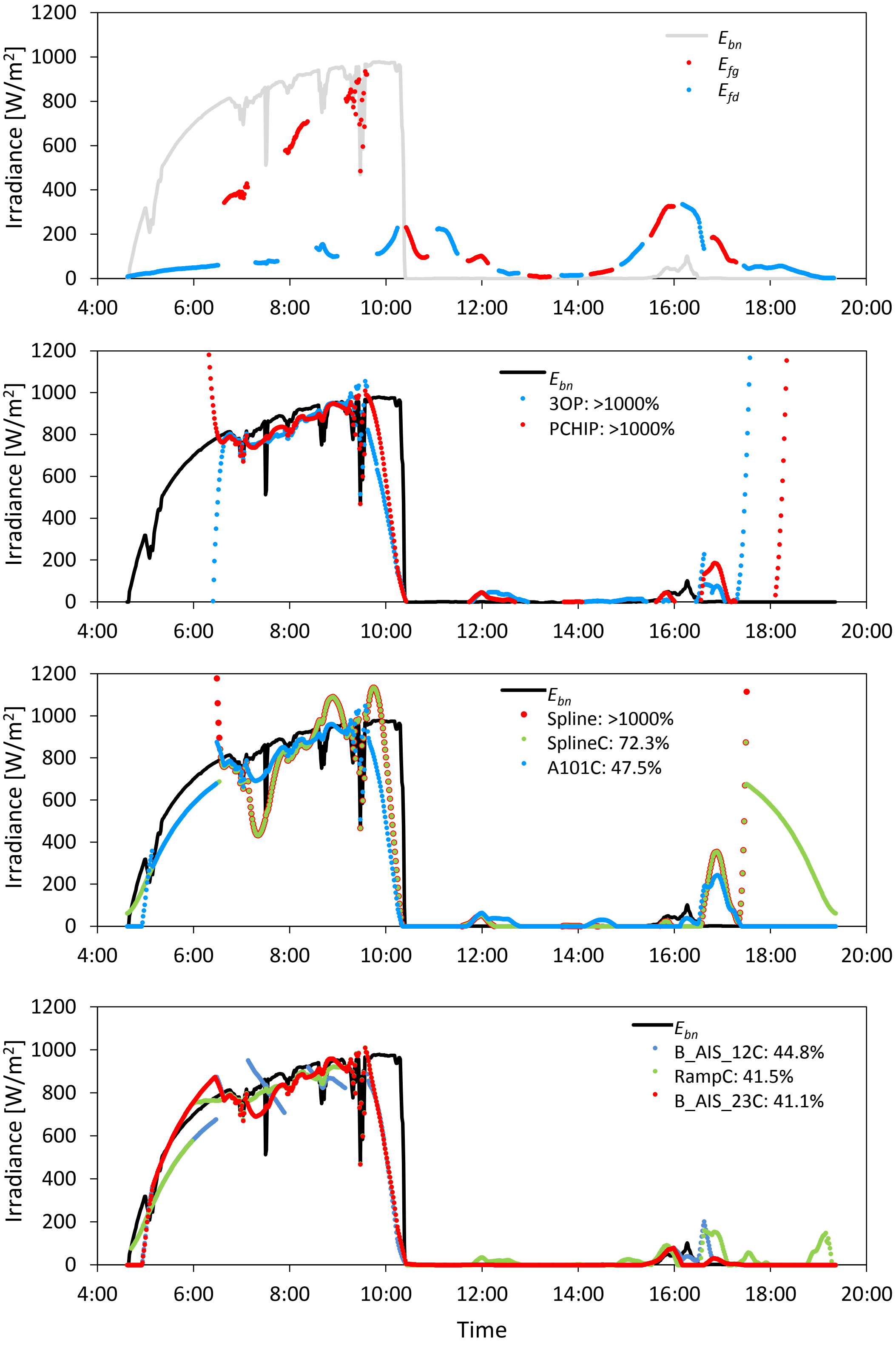

Figure 5.17: DNI resulting from the application of the CdSPM to DHI and GHI data on 2 June 2012 for mixed cloud conditions and K_{T_day} = 0.33.

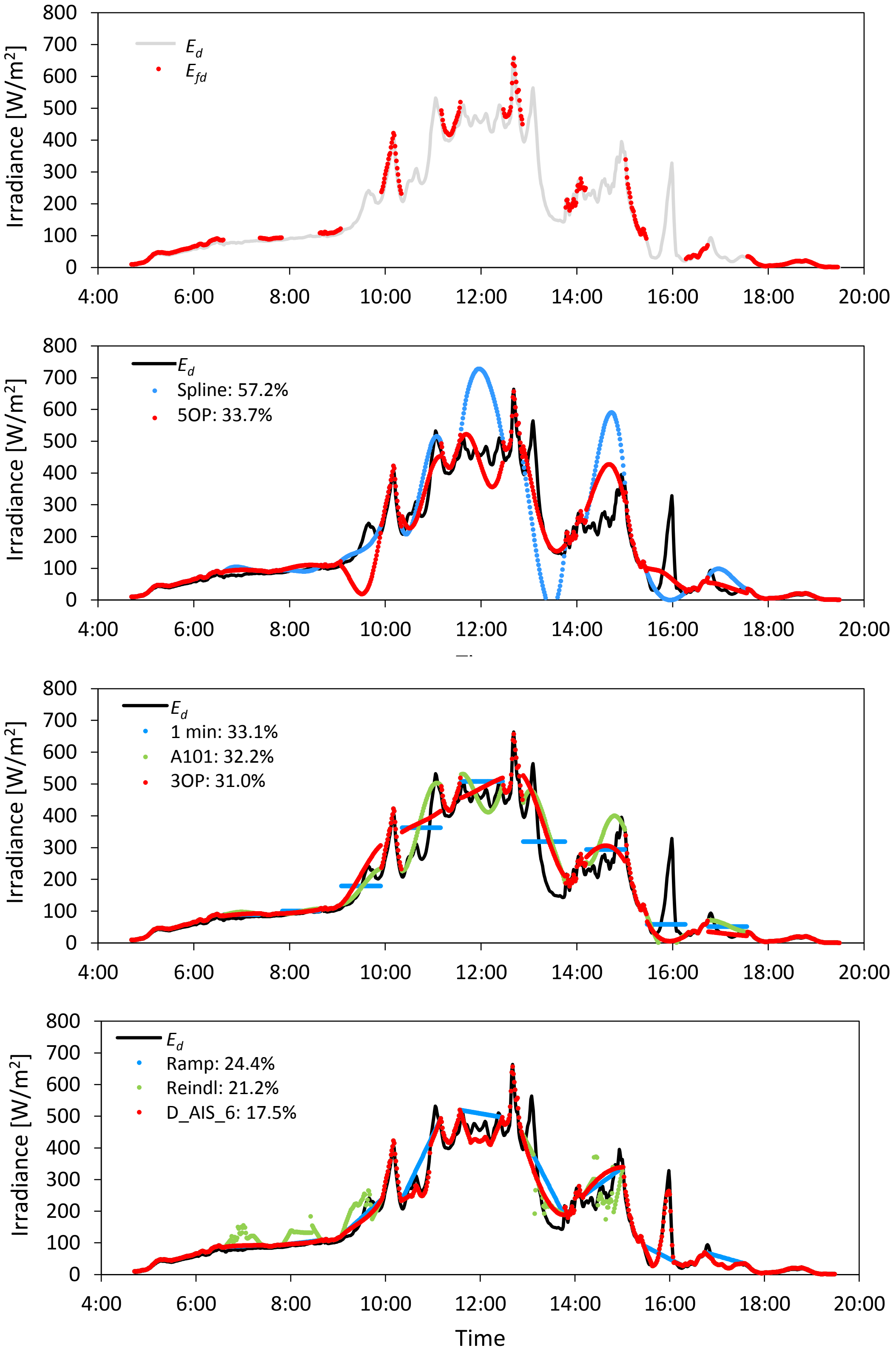

Figure 5.18: Application of the CdSPM to DHI data on 7 July 2011 for mixed cloud conditions and K_{T_day} = 0.49. Uncertainties are given in %RMSD.

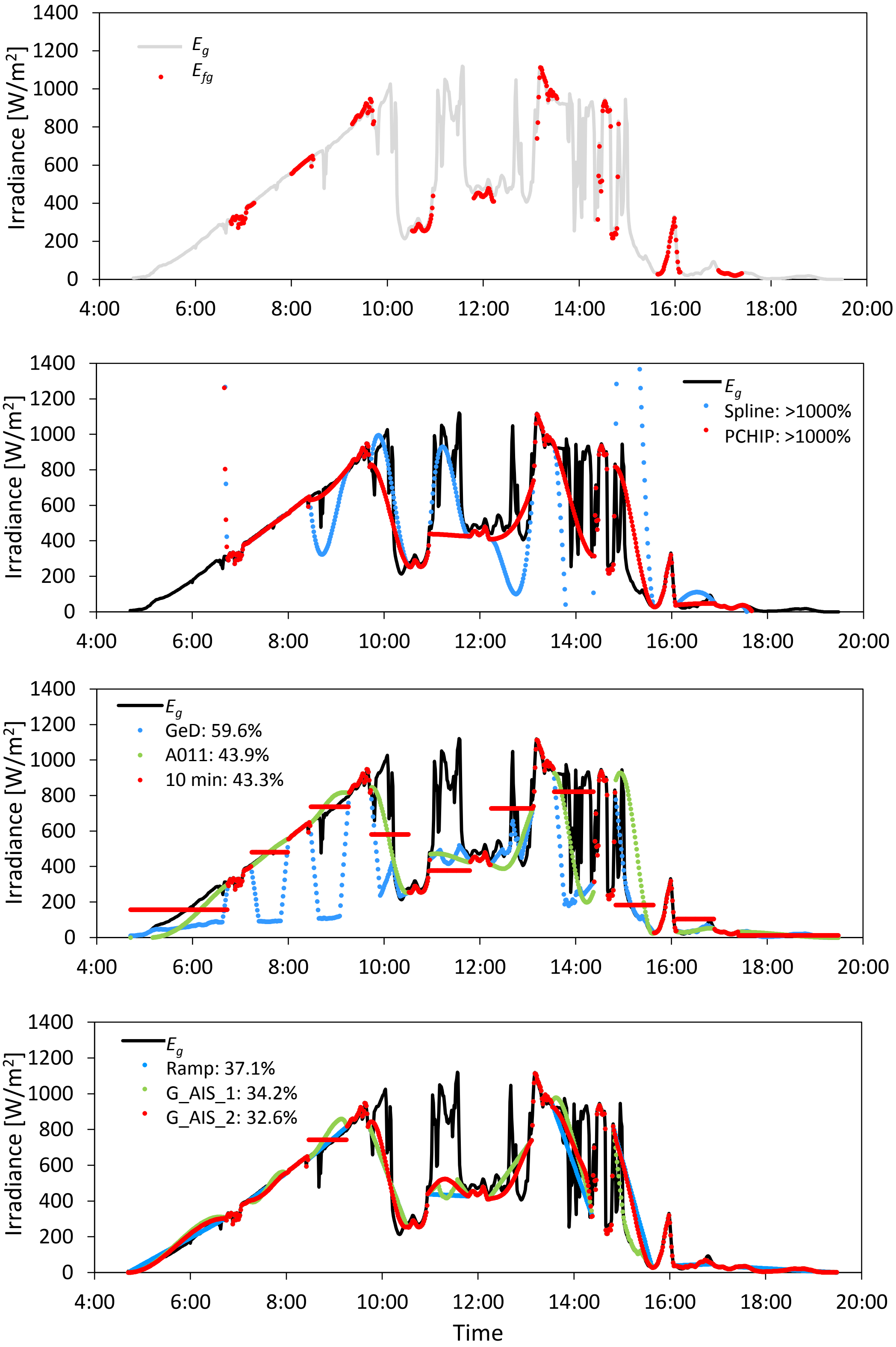

Figure 5.19: Application of the CdSPM to GHI data on 7 July 2011 for mixed cloud conditions and K_{T_day} = 0.49. Uncertainties are given in %RMSD.

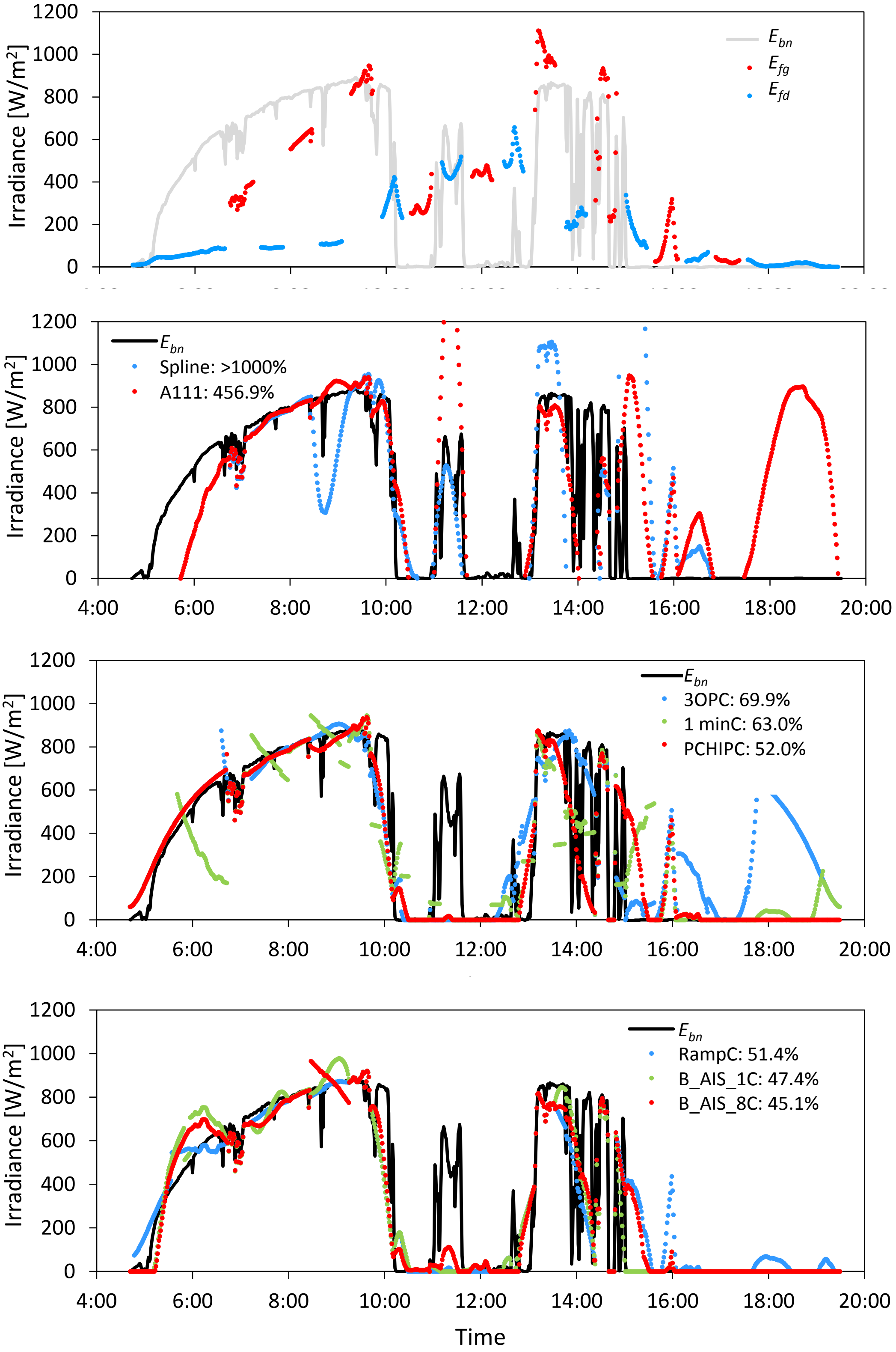

Figure 5.20: DNI resulting from the application of the CdSPM to DHI and GHI data on 7 July 2011 for mixed cloud conditions and K_{T_day} = 0.49.

5.5.2 Overcast conditions

The application of the CdSPM to an overcast day is shown in Figures 5.21 to 5.23. On 12 September 2012 there was considerable stochasticity in the DHI and GHI traces which are largely identical due to the complete absence of direct normal irradiance. The average daily clearness index was 0.14.

The top pane of Figure 5.21 shows DHI output data from the perforated band system together with the reference trace. Within most of the DHI gaps, there are high ramp rates and data fluctuations to which the PB system is blind. The use of curve-fitting techniques, such as the Spline, polynomial and PCHIP methods, yields relatively poor results with uncertainties ranging from 21.3 to 63.1%. The Ramp function returns an RMSD uncertainty of 20.5%.

The use of decomposition models to interpolate under overcast conditions reduces uncertainty by half compared with the Ramp approach on the given day. Two examples are given in the lowest pane of Figure 5.21, namely the BRL and Erbs models which yield uncertainties of 11.4% and 11.2% respectively. The adaptive schemes making use of DM techniques (not shown) also return similar uncertainties.

Figure 5.22 gives results for GHI interpolation. Since the trace is almost identical to the diffuse data, similar uncertainties result for the polynomial, Spline and Ramp functions. In this case there is no applicable decomposition model, but the GeD function is deployed by adaptive scheme G_AIS_1 with excellent effect, reducing the RMSD uncertainty for the day to 10.4%.

The direct normal irradiance results are shown in Figure 5.23, with uncertainties given in [W/m^2] fore readability rather than percentages. In this case the reference DNI trace is a flat line on the zero axis. As shown in the second, third and fourth panes, some of the interpolation schemes generate false DNI values by combining DHI and GHI data for the day, even when data are corrected by the Bird model. The adaptive schemes that deploy decomposition models and the GeD function operate correctly and produce very low uncertainties on the order of a few watts per square metre.

The visualisation of the CdSPM in Figures 5.15 to 5.23 illustrates an important point: the interpolation problem for 1-minute resolution data is complex because it varies in nature depending on the sky conditions under which the measurements are generated. Under clear conditions ordinary linear or polynomial functions perform well, but not so under cloudy or overcast skies. An adaptive approach in which clearness index is continuously monitored and alternate strategies such as decomposition modelling employed, is therefore crucial to reducing RMSD uncertainty for the perforated shadow band system.

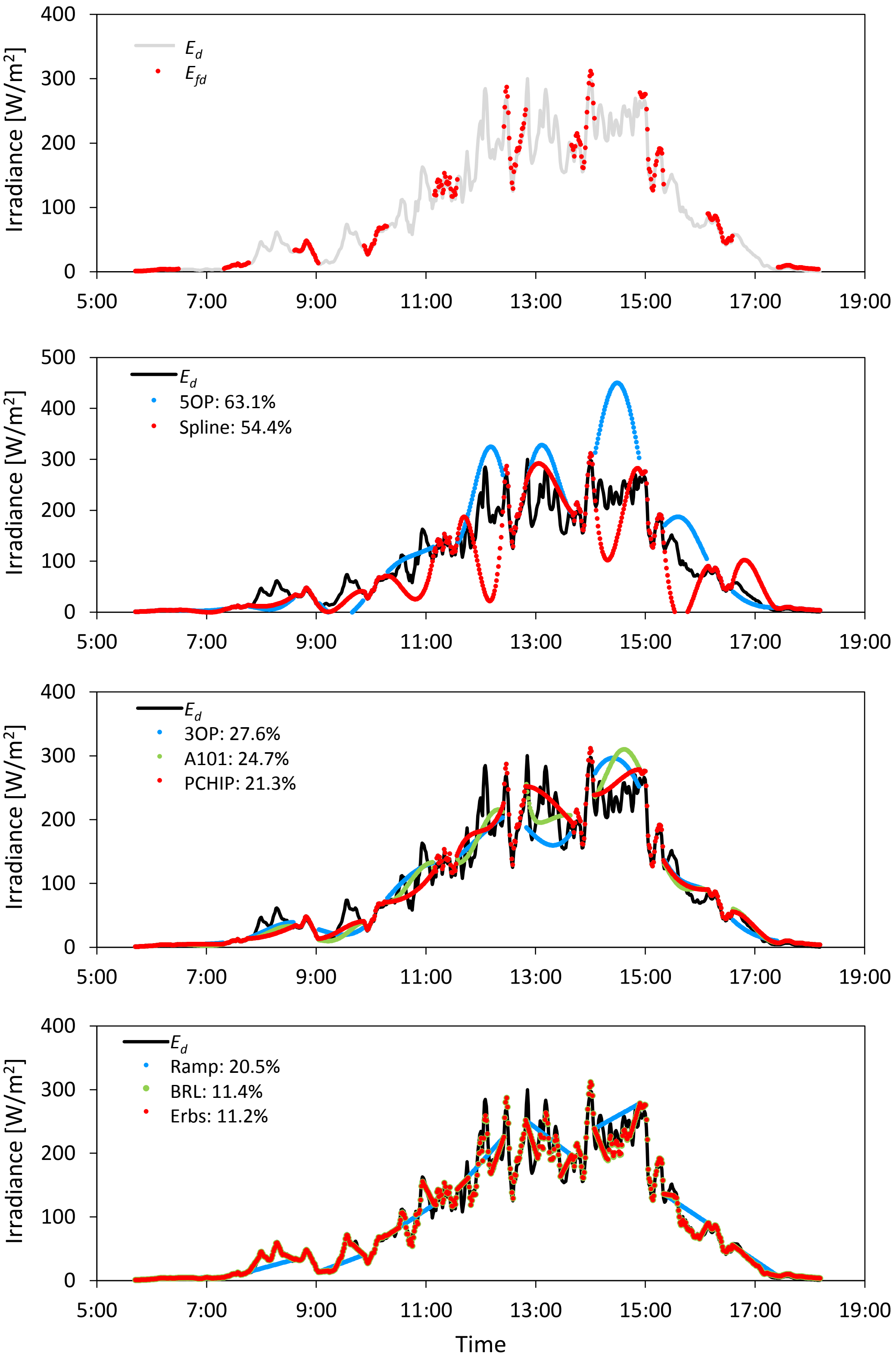

Figure 5.21: Application of the CdSPM to DHI data on 12 September 2012 for overcast conditions and K_{T_day} = 0.14. Uncertainties are given in %RMSD.

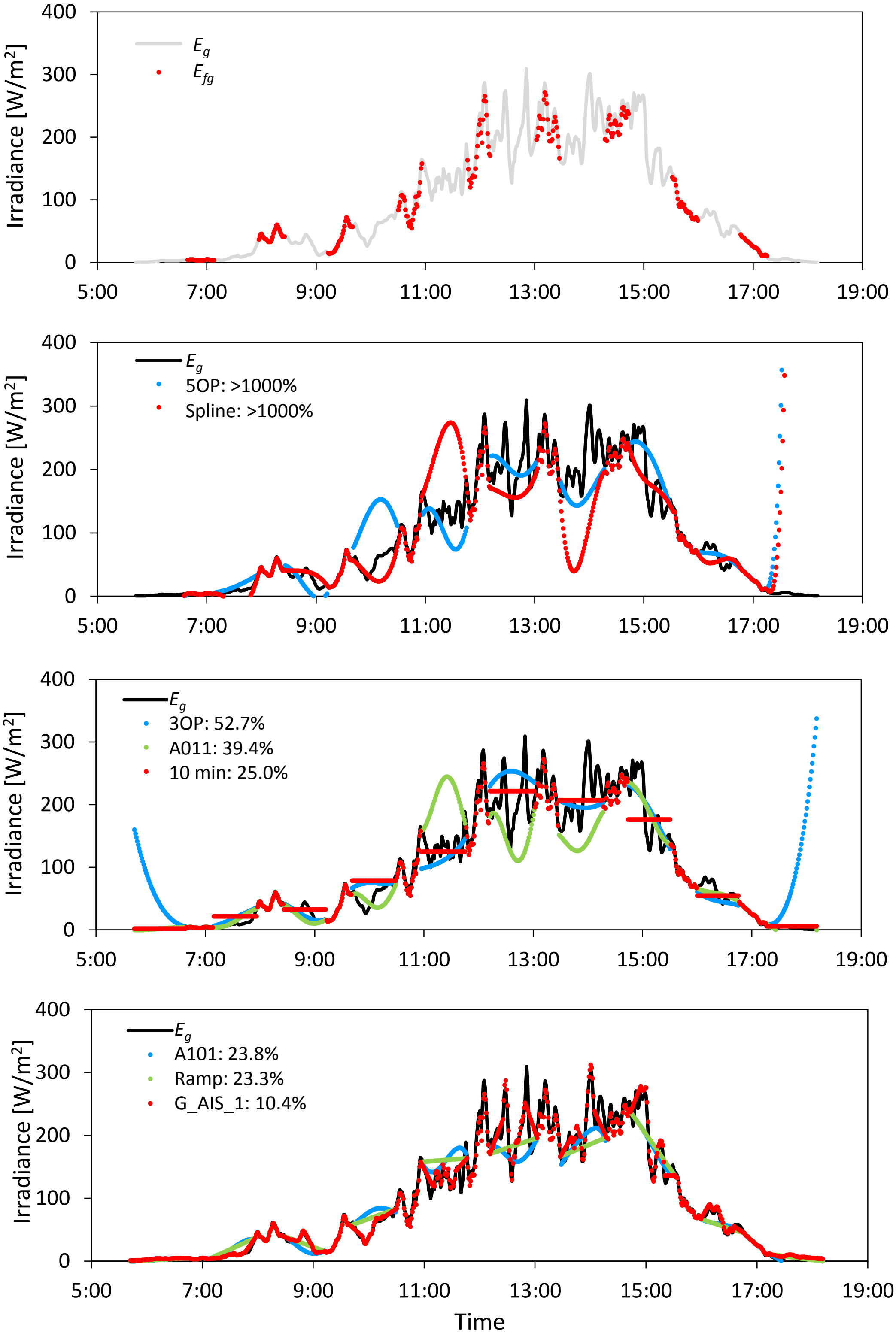

Figure 5.22: Application of the CdSPM to GHI data on 12 September 2012 for overcast conditions and K_{T_day} = 0.14. Uncertainties are given in %RMSD.

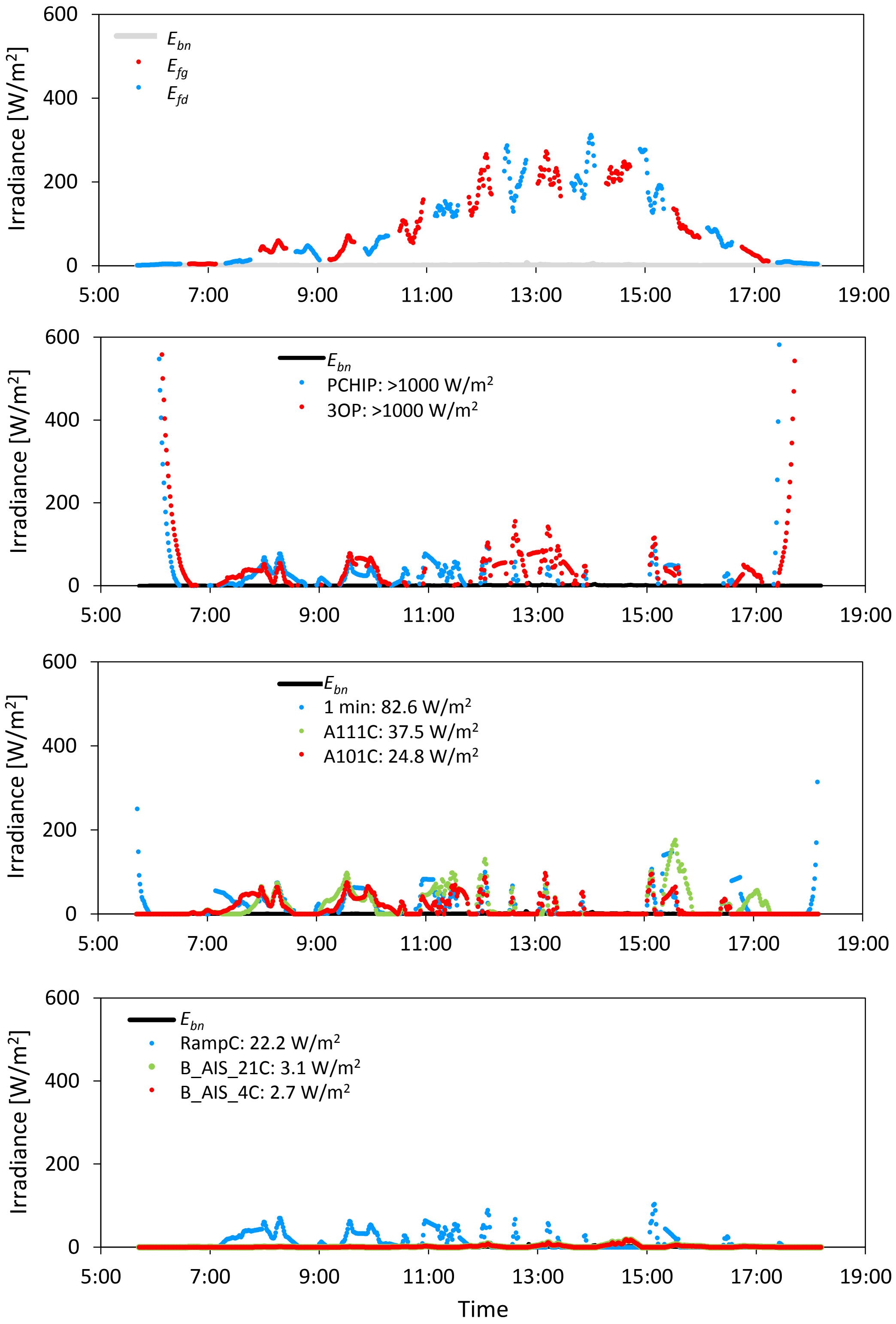

Figure 5.23: DNI resulting from the application of the CdSPM to DHI and GHI data on 12 September 2012 for overcast conditions and $K_{T\_day} = 0.14$. Uncertainties are given in [W/m^2].

5.6 Perforated band performance versus decomposition models

The use of a single, unshaded pyranometer measuring GHI in conjunction with radiometric decomposition models to derive DHI represents an alternative to the perforated band system for ground station operators. In order to quantify the difference between these two approaches, uncertainty data from the decomposition models of sections 4.9.2 to 4.9.6 were shown graphically in Figures 5.1 to 5.4 for DHI and Figures 5.9 to 5.14 for DNI. (Data for GHI were omitted because an unshaded pyranometer measures the global component directly, and therefore the model uncertainty is zero.) This section expands on the methods used to generate the decomposition model data against which PB performance was compared.

5.6.1 Diffuse horizontal irradiance

To assess the decomposition models as alternatives to the PB system, 1-minute GHI and clearness index values were obtained from the collocated reference pyranometer used in datasets #1 and #2. For the BRL model, the daily clearness index parameter (K_{T_day}) was taken from the perforated band algorithm in the CdSPM, together with the solar altitude angle, where required. The models were then implemented to yield DHI values for comparison.

It is worth noting that models are typically derived using hour-averaged input data, as discussed in section 4.9.1. In this study the decomposition models were run using input data with averaging periods of 10, 30 and 60 minutes in addition to the standard 1-minute interval. The input irradiance thus remained constant for the averaging period as did the output values.

In all cases the uncertainty was calculated by comparing the modelled irradiance with the contemporaneous 1-minute reference measurement of DHI. This was done to ensure a fair comparison between the DM approach and the PB system, whose performance is determined against 1-minute reference values throughout this study.

Table 5.5 gives the uncertainties of the best performing models for converting GHI to DHI in both datasets. These data are represented in Figures 5.1 to 5.4 as blue markers. The naming convention includes the time period over which model input irradiance was averaged. For example, the DM in bin 3 with the lowest RMSD uncertainty was BRL10, indicating that the model values were averaged over 10 minutes rather than 1 minute.

The BRL model is the top performer in most bins for both datasets. The Reindl model also does well for mid-range clearness indices. Interestingly, there is a mix of averaging periods in the top performers ranging from 1-minute intervals mainly in the cloudier categories to 60 minutes under clearer sky conditions. This is significant and confirms that decomposition models do not necessarily yield their lowest uncertainties when used over hourly periods. They may indeed be used over shorter periods and in some cases perform better at higher temporal resolutions.

Table 5.5: Statistical parameters for best performing decomposition models in generating DHI from GHI in datasets #1 and #2 ($Z < 70°$).

Dataset #1				Dataset #2			
Bin	**Scheme**	**RMSD [%]**	**MBD [%]**	**Bin**	**Scheme**	**RMSD [%]**	**MBD [%]**
1	BRL1	17.5	-2.0	**1**	BRL1	15.3	-2.8
2	BRL10	18.4	-5.0	**2**	BRL10	17.6	-6.7
3	BRL10	27.4	-10.2	**3**	BRL10	27.6	-5.9
4	BRL30	32.2	-7.6	**4**	Reindl1	30.4	-10.0
5	Reindl1	36.4	-0.3	**5**	Reindl1	33.6	-2.0
6	O&H1	42.8	-7.3	**6**	Reindl1	40.9	4.0
7	BRL60	51.0	-6.3	**7**	BRL60	45.0	-9.9
8	BRB60	64.6	-16.9	**8**	BRB10	38.2	-1.4

5.6.2 Direct normal irradiance

Direct normal irradiance was calculated by combining GHI values from the reference pyranometer with DHI values obtained from decomposition models. The Bird model was again used to limit extreme values arising during the calculation. Uncertainties were determined by comparing the model-derived DNI with 1-minute measurements from NREL's collocated Kipp and Zonen CH1 pyrheliometer. The results in Table 5.6 are given in [W/m^2], and are shown in Figures 5.9 to 5.14 with blue markers. Although decomposition models perform poorly compared with the perforated band in estimating DHI, they return lower uncertainties for DNI because the direct normal component is a combination of DHI and GHI, which has a zero error. Under clear sky conditions there is little difference between the PB and decomposition model approach.

Table 5.6: Statistical parameters for best performing decomposition models in generating DNI from GHI in datasets #1 and #2 ($Z < 70°$).

Dataset #1				Dataset #2			
Bin	**Scheme**	**RMSD [W/m^2]**	**MBD [W/m^2]**	**Bin**	**Scheme**	**RMSD [W/m^2]**	**MBD [W/m^2]**
1	BRL10C	22.9	4.4	**1**	BRL30	31.5	3.9
2	BRL1C	61.3	24.4	**2**	BRL10	70.8	29.0
3	BRL1C	111.6	55.3	**3**	BRL1C	94.5	33.7
4	BRL1C	142.2	67.9	**4**	BRL1C	126.9	50.5
5	RnB1C	119.4	16.5	**5**	RnB1C	122.5	24.8
6	OH1C	125.6	33.5	**6**	RnB1	129.7	7.2
7	BRB1C	81.3	-7.1	**7**	BRB1C	78.7	1.0
8	E1C	87.2	-33.7	**8**	BRB1C	57.3	1.2

5.7 Perforated band performance versus other radiometric methods

Apart from the use of an unshaded pyranometer, other measurement options represent competitive alternatives to the perforated shadow band system. These include the use of satellite data and alternate radiometer configurations.

5.7.1 Satellite data

Satellite-derived solar data can be obtained from a number of providers, including the National Aeronautics and Space Administration (NASA), the Solar Radiation Data Service (SoDa), SOLEMI and GeoModel Solar. Most of the measurements come from instruments on the METEOSAT and Geostationary Operational Environmental Satellite (GOES) spacecraft, operated by a European consortium and the United States National Oceanic and Atmospheric Administration (NOAA) respectively (Myers, 2013).

A direct comparison of PB uncertainty versus satellite-derived predictions is not possible because satellite providers do not offer 1-minute time-series. Furthermore, the uncertainties for satellite-based data are not classified according to clearness index, as in this study, but are generally reported as a single value, either RMSD in [W/m^2] or as a percentage of the mean recorded irradiance. Therefore, to enable meaningful comparison three subsets of PB measurements were randomly selected from dataset #1 (2011) and used to generate hourly averages for DHI, GHI and DNI components. The subsets each comprise 80 days worth of measurements for which $Z < 70°$, distributed between all eight clearness index bins, with ten days per bin.

The effect of integrating 1-minute readings over longer periods is to reduce the RMSD uncertainty, as shown in Figure 5.24. The DHI data comprised 39 014 minute-averaged values for the D_AIS_1 scheme, generated by the perforated band and reintegrated over successively longer periods from 15 minutes to 1 hour.

The reduction in uncertainty between 1-minute and hourly periods varies from 4% to 8.2%, depending on the clearness index bin. The overall RMSD average for the hourly period, as determined from the full data subset, is 11.3% which may be used when comparing PB uncertainty with that of satellite-based measurements. A similar reduction in uncertainty occurs for other interpolation schemes like the Ramp function.

These results are consistent with trends reported by Zelenka (1999) where reductions in the uncertainty of GHI occurred for integrating periods increasing from 10 minutes to one month. Mean bias differences remain largely unchanged with averaging period.

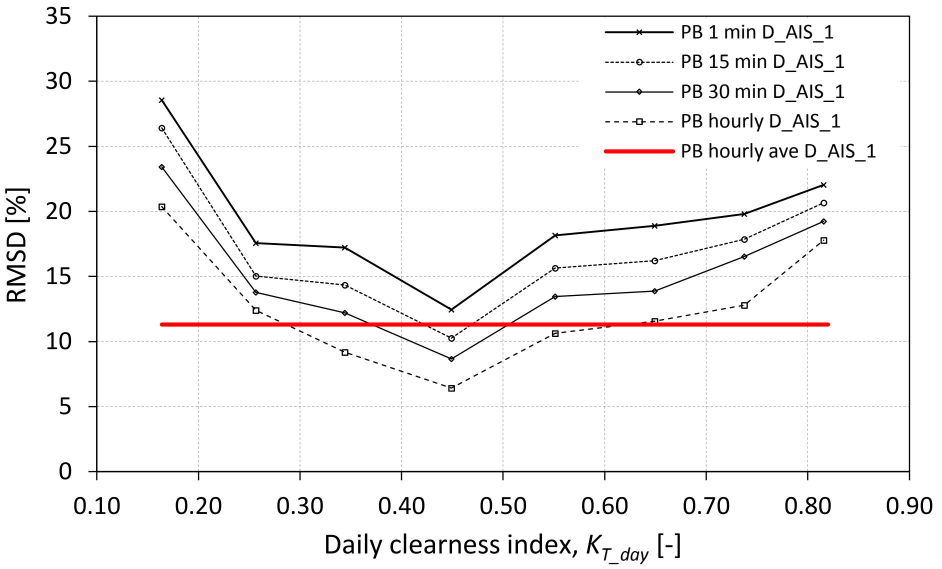

Figure 5.24: Reduction in %RMSD for DHI adaptive scheme D_AIS_1 generated by the perforated band, with increasing period of integration.

GHI and DNI uncertainties are published for the HelioClim-3 database (SoDa) and for the SolarGIS database version 1.8 from GeoModel Solar (SolarGIS, 2013). When compared against these products, the perforated band RMSD uncertainties compare favourably for hourly intervals, which is the most commonly reported, sub-daily interval, as shown in Figures 5.25 and 5.26.

For global horizontal irradiance, the perforated band system yields an average hourly RMSD of 12.3% using the G_AIS_1 adaptive scheme. The equivalent uncertainty for the Ramp scheme is 12.7%. The averaged hourly satellite-derived uncertainty for SolarGIS version 1.8, compared to ground station measurements where the mean GHI values are given, is approximately 19% (SolarGIS, 2013). The RMSD for HelioClim-3 is 22.0% based on a minimum threshold value of 10 W/m^2, although this figure drops to 16.3% when the threshold is raised to 200 W/m^2 (SoDa, 2013). The uncertainty quoted for HelioClim-3 by Espinar et al. (2012) is “around 20%”.

The mean bias difference for PB hourly data, based on the G_AIS_1 scheme, is –3.5%, compared with –1.1% for HelioClim-3 and a value of 1.1% reported by SolarGIS for European stations.

It should be noted that the satellite uncertainties are averages derived from a comparison with ground station data. They are represented in Figures 5.25 and 5.26 as constants because variability as a function of K_{T_day} is not provided in the HelioClim-3 or SolarGIS specifications. Nevertheless, both SoDa and GeoModel Solar list the stations against which their databases are compared and it appears that uncertainty is generally lower in arid regions. For example, the HelioClim-3

RMSD for GHI is lowest over Tamanrasset (10.3%), De Aar (11.4%) and Sede-Boqer (11.5%). Conversely, the European stations in cloudier regions produce higher uncertainties, for example 18.2% (Geneva) and 27.8% (Bergen). The same trend applies to the SolarGIS database. This variability in RMSD and MBD arises from factors such as the cloud condition, topography and vegetation. It suggests a need for the publication of uncertainty as a function of clearness index to clarify the applicability of satellite-based measurements and to permit greater confidence in the results.

The mean measured GHI at stations used by HelioClim-3 for their analysis is 326 W/m^2 with a 10 W/m^2 minimum threshold (SoDa, 2013). The measured GHI at SolarGIS ground stations, where available, averages to approximately 353 W/m^2 (SolarGIS, 2013). The mean measured GHI for the PB subset of data is 433.5 W/m^2 and the data are drawn from NREL's SRRL site in Colorado.

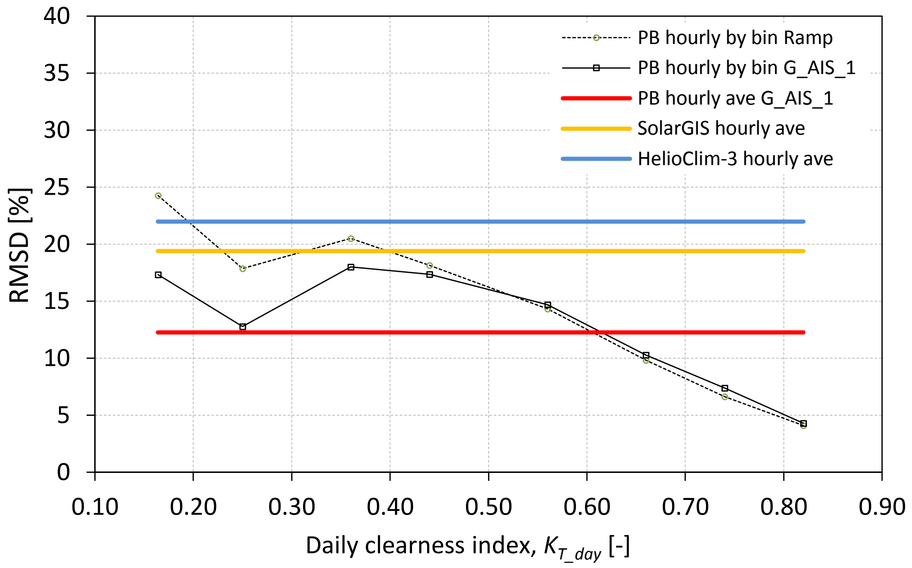

Figure 5.25: Hourly RMSD uncertainty of PB-derived global irradiance using the G_AIS_1 and Ramp schemes, with reported uncertainties for the HelioClim-3 and SolarGIS databases.

For direct normal irradiance, the perforated band system yields an average hourly RMSD of 84.1 W/m^2, or 21.3% of the mean measured DNI, using the RampC scheme (Figure 5.26). The equivalent averaged hourly uncertainty for the B_AIS_1C scheme is almost identical. Uncertainties are given in [W/m^2] rather than percentages for readibility.

The averaged hourly satellite-derived uncertainty for SolarGIS version 1.8, where the mean DNI values are given, is approximately 123 W/m^2, or 33.8% of the mean irradiance (SolarGIS, 2013). This figure is highly variable and drops to between 16% and 22% for six South African ground stations. Data from the UKZN Howard College ground station were provided to GeoModel Solar by the author of this study to validate the SolarGIS database. The RMSD for Durban is 32.2% (SolarGIS, 2013). No classification of DNI uncertainty is given versus clearness index in the SolarGIS specification. SoDa does not provide DNI uncertainty values for HelioClim-3 in their specifications, nor do they give uncertainties pertaining to diffuse horizontal irradiance.

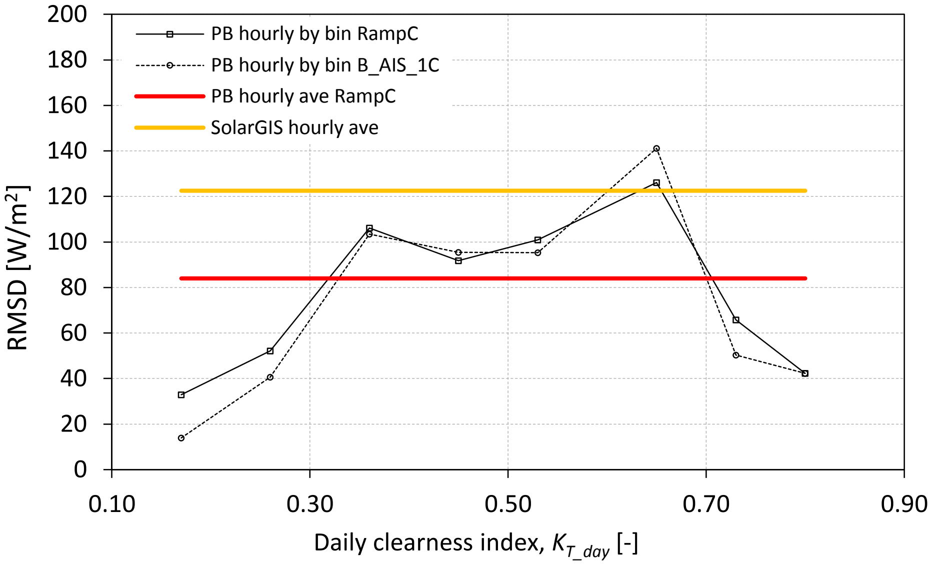

Figure 5.26: Hourly RMSD uncertainty of PB-derived direct normal irradiance using the RampC and B_AIS_1C schemes, with reported uncertainty for the SolarGIS database.

5.7.2 Commercial radiometers

Commercial instrument manufacturers typically provide a basic indication of sensor accuracy limited to percentage uncertainty over daily, monthly or annual intervals. Minute-averaged statistics are rare, and the general lack of detailed data, or of a standard reporting method, makes it difficult to compare instruments. Furthermore, sensors exhibit seasonal, spatial and temporal variations in uncertainty that are not usually reported on technical data sheets. Drawing definitive conclusions about comparative sensor performance is therefore dependent on measurement campaigns in which multiple instruments are tested simultaneously at a common location.

Wilcox and Myers (2008) conducted one of the few studies detailing run-off trials at high temporal resolution between different, collocated sensors. They report performance results for 12 global horizontal radiometers, three direct beam pyrheliometers, and two diffuse pyranometers from a 12-month monitoring programme at NREL SRRL. Data have been drawn from their study to compare the PB system's performance against alternate, commercial radiometers. An exhaustive description of all commercially available instruments is beyond the scope of this work, but the following sections serve to contextualise the PB system's performance against two popular types of instrument: the Delta-T SPN1 radiometer and the Rotating Shadowband Radiometer (RSR) by Irradiance Inc.

Delta-T Devices Ltd. describes the overall accuracy of GHI and DHI outputs as ±5% for daily totals, ±5% ± 10 W/m^2 for hourly averages and ±8% ± 10 W/m^2 for individual readings. The figures are given for 95% confidence limits but it is not clear whether they represent measurement uncertainty, or model uncertainty derived from comparison with reference radiometers. No uncertainties are quoted for DNI.

Table 5.7 gives bias and standard deviation uncertainties for SPN1, RSR2 and LI-200 instruments tested at NREL SRRL in a separate trial over periods of 4 months, 12 months and 11 months respectively (Wilcox and Myers, 2008). Both the SPN1 and the RSR2 instruments contain correction algorithms in their software to mitigate spectral selectivity and cosine error.

Table 5.7: Uncertainty results of Wilcox and Myers (2008) for SPN1, RSR2 and LI-200 instruments at 1-minute time intervals and zenith angles of up to 80°.

Instrument	**Bias max/min [%]**	**Standard deviation [%]**
SPN1 (GHI)	-0.3 to -3.7	4 to 7
SPN1 (DNI)	+8.1 to +3.0	19 to 24
SPN1 (DHI)	-13.8 to -4.3	7 to 11
LI-200 (GHI)	+2.8 to -2.0	3 to 8
RSR2 (GHI)	+1.0 to -1.2	4 to 6
RSR2 (DNI)	-3.5 to -7.5	16 to 19
RSR2 (DHI)	-0.2 to +3.0	5 to 6

Measurements from an RSR2 were not available from NREL during this study, however SPN1 and LI-200 instruments were generating 1-minute data over the same time period as dataset #1, permitting comparison with the PB system. Figures 5.27 to 5.29 illustrate comparative uncertainties for DHI, GHI and DNI respectively, determined for zenith angles less than 70°. The LI-200 device provides GHI only, while the SPN1 provides DHI and GHI from which DNI has been calculated without correction of the resulting data.

The PB system produces higher percentage RMSD uncertainties than the SPN1 for all components and across all clearness index bins. In the case of DHI, the difference is approximately constant at around 10%, while the difference is considerably higher for GHI and DNI in the mid-clearness index range. Under very clear conditions the differences are smaller. Standard deviations for the LI-200 and SPN1 instruments obtained in this study are consistent with the results given in Table 5.7 by Wilcox and Myers (2008). Interestingly, the inexpensive LI-200 sensor produces the lowest %RMSD of all three systems for GHI, from mid-range clearness index through to clear sky conditions.

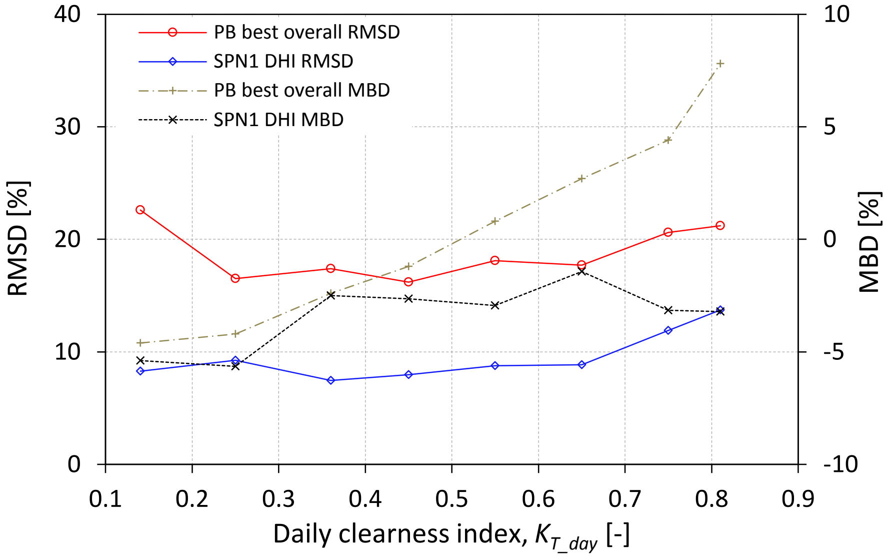

Figure 5.27: DHI uncertainties of the PB system and collocated SPN1 sensor, classified by daily clearness index for dataset #1 and Z < 70°.

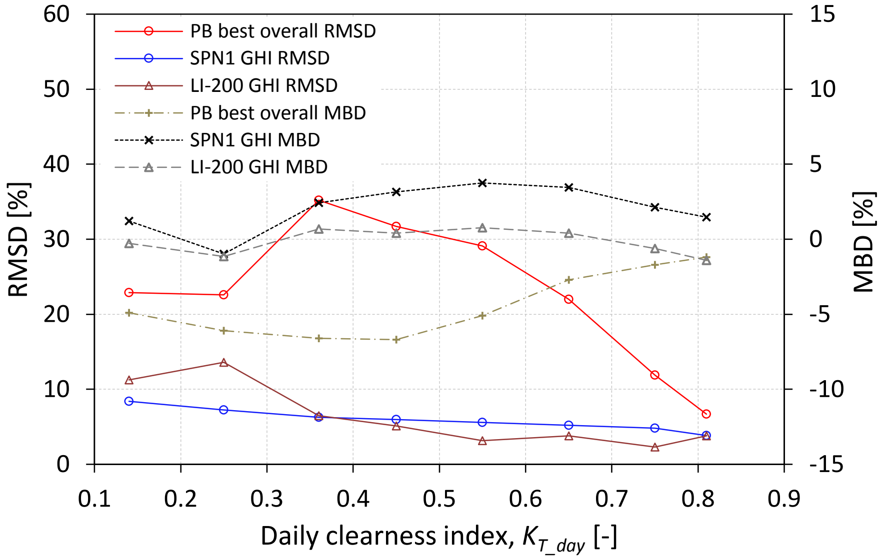

Figure 5.28: GHI uncertainties of the PB system and collocated SPN1 and LI-200 sensors, classified by daily clearness index for dataset #1 and Z < 70°.

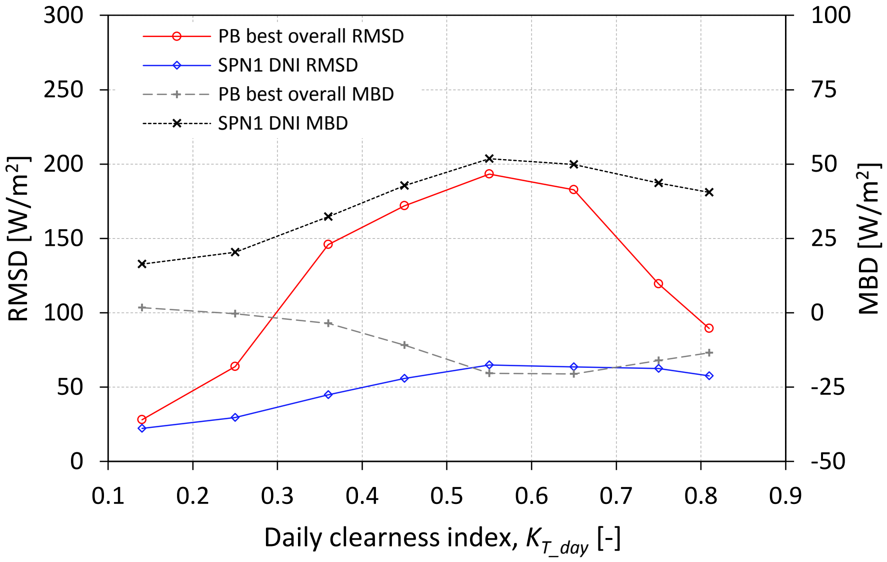

Figure 5.29: DNI uncertainties of the PB system and collocated SPN1 sensor, classified by daily clearness index for dataset #1 and $Z < 70°$.

The PB system produces a lower mean bias difference than the SPN1 for DHI measurements up to a clearness index of about 0.6. Thereafter the PB system performs worse, recording a MBD percentage above 7% under the clearest conditions. The SPN1 consistently under-predicts DHI across all sky conditions but generally over-predicts GHI. The LI-COR sensor exhibits very low bias versus the reference data for global horizontal irradiance. Mean bias differences for DNI are considerably higher for the SPN1 than for the PB system across all sky conditions.

In general, the random uncertainty of the SPN1 and LI-200 sensors is considerably lower than for the perforated band system, however the PB setup shows less bias than the SPN1 in predicting DHI and DNI.

5.8 The effect of non-classification by clearness index

The performance of the perforated band in predicting GHI and DNI is strongly related to cloud conditions, with increased uncertainty in the mid-K_{T_day} range. When the analysis is done without classifying data by K_{T_day}, the result provides a useful indication of the device's accuracy over time versus reference data for the location at which measurements were taken, in this case Golden, Colorado.

Table 5.8 gives MBD, RMSD and SD percentages for selected perforated band interpolation schemes when applied to datasets #1 and #2 without consideration of the cloud conditions. The results are average statistical uncertainties for all 1-minute data ($Z < 70°$) and are obtained by concatenating data to form a continuous record, irrespective of K_{T_day}, from which statistical parameters are determined.

Table 5.8: PB performance disregarding classification according to clearness index, including data for collocated SPN1 and LI-200.

	MBD		RMSD		SD	
	[%]	[%]	[%]	[%]	[%]	[%]
Dataset	**#1**	**#2**	**#1**	**#2**	**#1**	**#2**
PB Diffuse horizontal irradiance						
D_AIS_1	1.0	0.5	19.4	17.2	19.3	17.2
D_AIS_6	1.1	0.6	19.4	17.1	19.3	17.1
D_AIS_8	0.7	0.3	19.5	17.4	19.5	17.3
D_AIS_14	0.4	0.1	19.7	17.5	19.7	17.5
Ramp	3.2	2.3	22.9	20.3	22.7	20.1
A101	4.1	2.7	25.3	21.9	25.0	21.7
1 min	3.0	2.1	26.0	23.1	25.8	23.0
BRL	-6.1	-6.3	29.9	29.1	29.3	28.4
4OP	4.0	3.2	32.7	28.6	32.4	28.4
SPN1	-2.8		9.5		9.0	
PB Global horizontal irradiance						
G_AIS_1	-3.4	-3.8	21.0	20.3	20.7	20.0
G_AIS_2	-2.9	-3.3	21.6	20.2	21.4	19.9
G_AIS_5	-3.4	-3.6	21.6	19.9	21.3	19.6
G_AIS_6	-3.1	-3.1	21.7	20.4	21.4	20.1
Ramp	-3.6	-3.7	21.9	20.2	21.6	19.9
A101	-3.0	-3.3	22.2	20.8	22.0	20.6
G_AIS_9	-3.8	-4.0	22.5	21.2	22.1	20.8
1 min	-3.9	-4.0	23.1	21.8	22.8	21.4
4OP	-3.6	-3.7	32.7	28.8	32.5	28.5
SPN1	2.7		5.3		4.6	
LI-200	-0.1		3.7		3.7	
PB Direct normal irradiance						
B_AIS_1C	-3.2	-4.6	28.2	29.2	28.0	28.8
RampC	-2.4	-3.8	28.5	28.6	28.3	28.3
B_AIS_1	-3.6	-4.9	28.8	29.7	28.6	29.3
A101C	-1.8	-3.3	29.3	29.5	29.3	29.3
Ramp	-5.0	-5.7	30.2	29.9	29.8	29.3
1 min C	-2.8	-4.1	31.2	31.5	31.0	31.2
1 min	-5.2	-6.1	32.9	32.9	32.5	32.3
4OPC	-1.6	-3.1	34.8	34.2	34.8	34.1
SPN1	7.9		10.9		7.5	

The uncertainties necessarily reflect the weighting of the clearness conditions making up the archive. In other words, they are representative of conditions at NREL between 2009 and the end of 2012, but are likely to vary at other sites.

For comparison, the measured average uncertainties for the SPN1 and the LI-200, as determined from dataset #1, are also given in Table 5.8. These are consistent with results from the study by Wilcox and Myers (2008), given in Table 5.7 and the superior performance of the alternate measurement sensors is again evident. There is little difference between the perforated band results for datasets #1 and #2, although mean bias difference is higher for DNI predictions in dataset #2. Aside from this, there is consistency of the PB interpolation methods across independent datasets.

5.9 The effect of zenith angle on performance

For most interpolation schemes, relaxing the upper zenith angle limit of 70° so as to include data for $Z < 90°$ has a relatively small effect on the RMSD and MBD metrics. Figures 5.30 and 5.31 illustrate this by comparing the percentage RMSD and MBD uncertainties for DHI, GHI and DNI across a range of schemes.

The uncertainties were calculated for the entire dataset #1 without segregation according to clearness index. For the schemes shown, the average increase in RMSD uncertainty when the upper limit is extended from 70° to 80° is 1.4%. It increases by 4.2% when the zenith angle limit is extended to 90°. The average changes in percentage mean bias difference are –0.4% and –0.5% when extending the limits to 80° and 90° respectively.

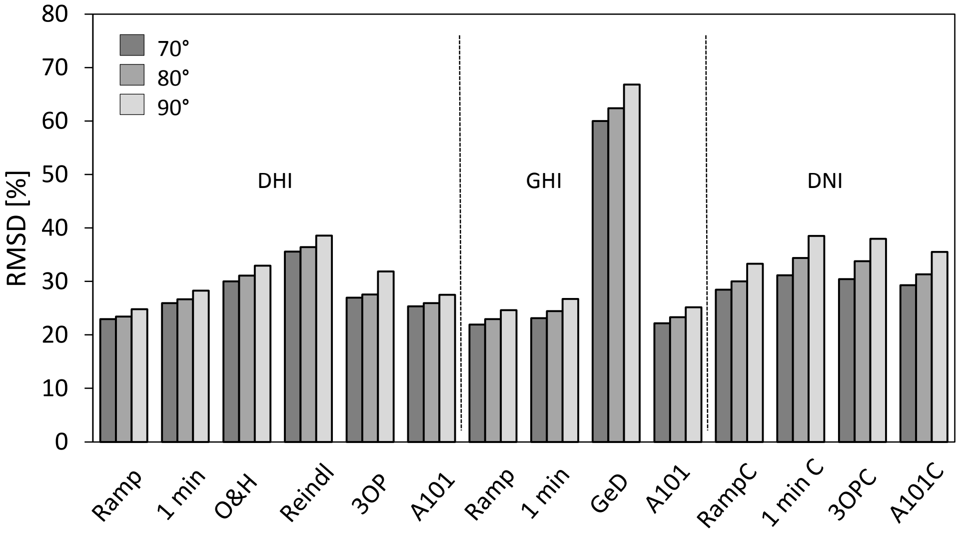

Figure 5.30: Comparative %RMSD uncertainty of selected interpolation schemes from dataset #1 as a function of upper zenith angle limit.

In the case of schemes which are not anchored to the horizontal axis at sunrise and sunset, such as the spline and PCHIP, the uncertainties can increase dramatically for data close to $Z = 90°$ although this is purely an artefact of the mathematics. Generally, high zenith angle pyranometric data are disregarded in radiometric studies because of inaccuracies arising from the instrument cosine effect. It should also be noted that the uncertainties of the GeD scheme in Figures 5.30 and 5.31 are high because it functions effectively under overcast conditions only, while the graph data cover all conditions, including clear sky measurements.

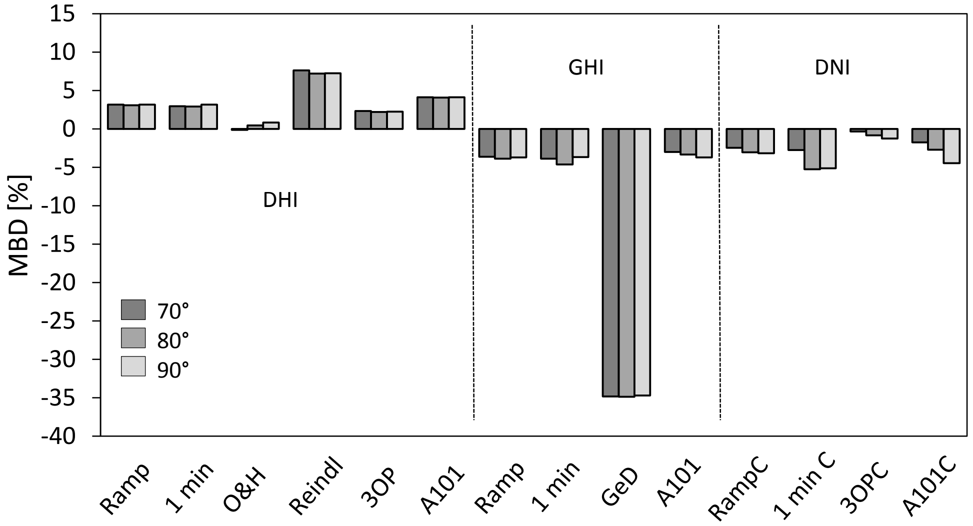

Figure 5.31: Comparative %MBD uncertainty of selected interpolation schemes from dataset #1 as a function of upper zenith angle limit.

5.10 The CdSPM applied to clear sky data

The CdSPM is intended for cloudy conditions but may also be used with cloud-free data. This is important as it enables operators of the perforated band to use a single processing methodology for all conditions.

Table 5.9 gives uncertainty metrics for a selected group of interpolation schemes as applied to a subset of 11 cloud-free days ($N = 4272$) in dataset #1, processed using the CdSPM software. The average daily clearness index for the data subset is 0.77. The methodology is able to generate DNI values with RMSD uncertainties of just a few per cent, similar to those obtained by manual processing and reported in Table 3.5 of Chapter 3. The percentage DHI uncertainties are somewhat higher because of the low level of diffuse irradiance prevalent on clear days. The general performance of the PB system is very good in the absence of clouds, mainly because of the structurally coherent data traces that result for all three components of sun strength.

Table 5.9: Performance of selected CdSPM schemes under cloud-free conditions for 11-day subset from dataset #1 ($Z < 70°$).

Scheme	RMSD		MBD		SD		U_{95}
	[W/m^2]	[%]	[W/m^2]	[%]	[W/m^2]	[%]	[%]
PB Diffuse horizontal irradiance							
4OP	8.8	13.4	2.7	4.2	8.4	12.8	36.3
Ramp	8.2	12.6	1.7	2.6	8.1	12.3	34.5
PCHIP	8.4	12.9	2.1	3.2	8.2	12.5	35.2
A101	8.6	13.0	2.3	3.5	8.2	12.6	35.5
D_AIS_1	8.4	12.9	2.1	3.2	8.2	12.5	35.2
1 min	8.4	12.7	1.6	2.4	8.2	12.5	35.0
Spline	10.3	15.8	4.0	6.2	9.5	14.5	42.0
PB Global horizontal irradiance							
4OP	15.4	2.6	-7.2	-1.2	13.6	2.3	6.9
Ramp	16.5	2.8	-8.7	-1.5	14.0	2.4	7.3
PCHIP	17.3	3.0	-9.1	-1.5	14.7	2.5	7.6
A101	16.2	2.8	-4.6	-0.8	15.5	2.7	7.5
G_AIS_1	18.6	3.2	-7.5	-1.3	17.0	2.9	8.4
1 min	27.2	4.6	-9.3	-1.6	25.6	4.4	12.5
Spline	30.0	5.1	-12.1	-2.1	27.5	4.7	13.6
PB Direct normal irradiance							
4OP	20.0	2.1	-11.5	-1.2	16.4	1.7	5.3
Ramp	21.8	2.3	-12.6	-1.3	17.8	1.9	5.8
PCHIP	25.3	2.7	-14.1	-1.5	21.0	2.2	6.8
A101	24.4	2.6	-6.0	-0.6	23.7	2.5	7.0
B_AIS_1	28.6	3.0	-10.9	-1.2	26.4	2.8	8.0
1 min	53.2	5.6	-12.1	-1.3	51.8	5.4	15.3
Spline	60.2	6.3	-24.4	-2.6	55.1	5.8	16.8

5.11 Summary

The cloudy sky processing methodology was applied to two independent radiometric datasets to characterise the performance of the perforated shadow band system. Performance was defined primarily in terms of the root mean square difference and the mean bias difference between the modelled irradiance from the PB system and data from collocated reference radiometers. The uncertainties were presented as a function of the average daily clearness index parameter since the system is heavily influenced by the cloud condition under which it operates. This approach allows potential operators of the perforated band to judge the suitability of installing the instrument, based on known conditions at a given site.

The CdSPM was first applied to the primary dataset (#1) and yielded a set of optimal interpolation schemes for disaggregating a composite PB trace into separate DHI, GHI and DNI curves. When repeated with the validation dataset

(#2), results were similar, both with respect to the magnitude of the uncertainties and the types of schemes that yielded the best results. Although an exact match between the best performing schemes in datasets #1 and #2 was not achieved in every clearness index bin, the optimal schemes from #1 yielded almost identical statistical results in dataset #2. It can be concluded that the CdSPM is a robust and reproducible means of generating separate diffuse, global and direct normal irradiance curves from the single output trace of an Eppley PSP pyranometer operated under a perforated band. The recommended configuration of the CdSPM is given in Table 5.10 together with expected statistical uncertainties for each average daily clearness index bin.

Table 5.10: Summary of recommended interpolation methods for processing data from a PB system and expected uncertainties by average daily clearness index.

Bin	**Average** K_{T_day}	**Scheme**	**RMSD** [W/m^2]	[%]	**MBD** [W/m^2]	[%]	**Ramp RMSD** [W/m^2]	[%]
Diffuse horizontal irradiance								
1	$0 \le K_{T\_day} < 0.2$	BRL	27.6	22.6	-5.6	-4.6	46.3	38.0
2	$0.2 \le K_{T\_day} < 0.3$	D_AIS_14	32.9	16.5	-8.4	-4.2	44.2	22.1
3	$0.3 \le K_{T\_day} < 0.4$	D_AIS_8	43.0	17.4	-6.0	-2.4	56.8	23.0
4	$0.4 \le K_{T\_day} < 0.5$	D_AIS_6	40.9	16.2	-2.9	-1.2	49.9	19.8
5	$0.5 \le K_{T\_day} < 0.6$	D_AIS_1	37.2	18.1	1.6	0.8	46.1	22.4
6	$0.6 \le K_{T\_day} < 0.7$	D_AIS_6	32.2	17.7	4.9	2.7	34.2	18.9
7	$0.7 \le K_{T\_day} < 0.8$	Ramp	19.6	20.6	4.2	4.4	19.6	20.6
8	$0.8 \le K_{T\_day} \le 1.0$	D_AIS_1	19.4	21.2	7.2	7.8	20.0	21.8
Global horizontal irradiance								
1	$0 \le K_{T\_day} < 0.2$	G_AIS_1	29.0	22.9	-6.2	-4.9	47.8	37.7
2	$0.2 \le K_{T\_day} < 0.3$	G_AIS_9	49.1	22.6	-13.2	-6.1	63.8	29.4
3	$0.3 \le K_{T\_day} < 0.4$	G_AIS_1	113.4	35.2	-21.2	-6.6	127.1	39.4
4	$0.4 \le K_{T\_day} < 0.5$	G_AIS_1	128.6	31.7	-27.0	-6.7	132.6	32.7
5	$0.5 \le K_{T\_day} < 0.6$	G_AIS_1	145.2	29.1	-25.3	-5.1	150.7	30.2
6	$0.6 \le K_{T\_day} < 0.7$	G_AIS_2	129.5	22.0	-15.9	-2.7	132.5	22.5
7	$0.7 \le K_{T\_day} < 0.8$	G_AIS_6	74.7	11.9	-10.8	-1.7	78.0	12.4
8	$0.8 \le K_{T\_day} \le 1.0$	G_AIS_5	46.0	6.7	-8.4	-1.2	46.0	6.7
Direct normal irradiance								
1	$0 \le K_{T\_day} < 0.2$	B_AIS_21C	28.0	516.2	1.7	31.5	78.9	>1000
2	$0.2 \le K_{T\_day} < 0.3$	B_AIS_6C	63.9	244.5	-0.3	-1.2	102.8	393.2
3	$0.3 \le K_{T\_day} < 0.4$	B_AIS_23C	145.8	142.9	-3.6	-3.5	181.3	177.6
4	$0.4 \le K_{T\_day} < 0.5$	RampC	172.0	78.4	-10.9	-5.0	190.1	86.6
5	$0.5 \le K_{T\_day} < 0.6$	RampC	193.2	45.4	-20.4	-4.8	206.2	48.5
6	$0.6 \le K_{T\_day} < 0.7$	A100C	182.7	31.1	-20.6	-3.5	189.3	32.2
7	$0.7 \le K_{T\_day} < 0.8$	B_AIS_27C	119.4	13.7	-16.1	-1.8	124.0	14.3
8	$0.8 \le K_{T\_day} \le 1.0$	Ramp	89.4	9.4	-13.5	-1.4	89.4	9.4

In general, the adaptive interpolation schemes yielded lower uncertainties than the single-scheme techniques, validating their use. Nevertheless, in many of the bins the simple linear interpolation function (Ramp) performed well and operators of the perforated band may therefore opt to simplify the processing methodology by reverting to Ramp interpolation throughout. In that case the expected RMSD uncertainties increase according to the data given in the last two columns of Table 5.10, which are provided for comparison. Under heavily cloudy and overcast conditions ($0 \leq K_{T\_day} < 0.4$) a linear interpolation approach is not recommended.

In comparison with alternate radiometric measurement approaches, the perforated band delivered mixed results. Against satellite data it returned lower hourly average RMSD and MBD uncertainties for global horizontal and direct normal irradiance.

When compared to alternate commercial radiometers such as the SPN1, the PB system generally produced higher RMSD uncertainties for DHI and GHI measurement across all sky conditions. Under clear skies the perforated band system was competitive with the SPN1 for the generation of direct normal irradiance. The PB system yielded lower mean bias differences across all sky conditions than the SPN1 in this study.

No performance assessment of the RSR2 radiometer was done in this study, however a comparison with published data suggests that it yields lower RMSD and MBD uncertainties than the perforated band system. The LI-200 sensor, which is used with the RSR2, was assessed and returned an RMSD lower than that of the PB system in the measurement of global horizontal irradiance. The same is true of MBD values except under clear sky conditions.

The use of decomposition models in conjunction with an unshaded pyranometer measuring GHI offers an inexpensive alternative to multi-instrument measurement schemes. Compared to the perforated band system, decomposition models generally yielded higher RMSD and MBD uncertainties when measuring DHI in this study, except under heavily overcast skies. The PB system is thus a better candidate for measuring diffuse irradiance than an unshaded pyranometer used with a model.

With respect to DNI, the PB system was less accurate than an unshaded pyranometer paired with a decomposition model, except under clear skies where the difference between the approaches was negligible. In general, the CdSPM results indicate that the perforated shadow band system performs best in conditions where the average daily clearness index is greater than 0.7.

6. LOCATION DEPENDENCE AND DEPLOYABILITY

6.1 Introduction

Solar radiometric schemes may require modification depending on their geographic location. For example, many radiometric models contain location-specific parameters such as geographic latitude or elevation.

In the case of the perforated band, several features of the physical setup and data processing methodology must be adjusted when the latitude, φ, changes:

1. The polar mount of a shadow band in the southern hemisphere is inclined upwards to the north, rather than the south, affecting the way in which the equipment is installed.
2. In the ray trace model of Chapter 2, the sensor exposure state, E_s, is a function of hour angle, ω, but not of the day number, n, or latitude (Figure 2.11). The only exception is for apertures 1 and 9, and zones 1 and 10, at high zenith angles. Limited location dependence is therefore expected with respect to the hour angle values of the ray trace model in Table 2.1. However, the zenith angle itself is a function of latitude, therefore the graphs of Z versus n in Figure 2.12 must be recalculated by location. This can be done using equation (2.9) without recourse to the ray tracing software itself.
3. At high zenith angles (applicable to apertures 1 and 9 and shading zones 1 and 10) the exposure state of the pyranometer sensor varies as a function of n and φ (Figures 2.11 and 2.12). If *a priori* knowledge of these changes is required at a site, the ray tracing model must be rerun to determine the limits of sensor exposure. Alternately, the band can be operated for a period and the limits can be obtained experimentally from clear sky data, avoiding the ray trace analysis.
4. The correction factor for structural deformation of the band will vary by location and must be updated on a regular basis. This can be done by post-processing experimental data from clear sky days.
5. The shadow band correction factor is latitude dependent and must be adjusted accordingly.
6. The CdSPM utilises radiometric models that are location dependent and must therefore also be adjusted.

This chapter, which is drawn partly from the conference paper by Brooks and Roberts (2009) addresses the location-dependence of the PB system by assessing its performance at a southern hemisphere ground station. The cloudy sky processing methodology is adjusted accordingly and applied to data generated by a perforated band installed at the University of KwaZulu-Natal in Durban, South Africa. Results are compared to those generated at NREL SRRL. Recommendations are then made regarding the geographic deployment of the band, with particular reference to the African continent.

6.2 Southern hemisphere test results

6.2.1 The UKZN HC ground station and dataset

Radiometric measurements have been recorded at the University of KwaZulu-Natal's Howard College (HC) campus in Durban since 2009, when the author established a solar monitoring capability (Brooks and Roberts, 2009). The UKZN HC station is now part of a cluster of three ground stations in the greater Durban area that includes Mangosuthu University of Technology's STARlab facility (Brooks and Harms, 2005) and the UKZN Westville campus. The stations are located within 18 km of each other, deliver high temporal resolution measurements of DNI, GHI and DHI at 1-minute intervals with thermopile sensors, and all belong to the SAURAN network.

UKZN HC is located at 29.87°S 30.98°E, 151 m above sea level on the roof of a university building with largely clear horizons and excellent exposure. The original instrument suite, comprising Eppley PSP and NIP radiometers, was upgraded in 2013 to include Kipp & Zonen sensors (a CH1 and two CMP11 pyranometers) on a SOLYS tracker, as illustrated in Figures 1.6 and 1.7.

At commissioning, the facility was equipped with a perforated shadow band operating under an Eppley PSP to provide research data for this study. Table 6.1 gives the instrument serial numbers and sensitivity factors for the radiometers used in deriving PB test data for this study. For budgetary reasons, there are no pyrgeometers installed at UKZN HC therefore it is not possible to apply a correction for thermal offset to data from the PSP sensor as was done for the NREL PSP.

The UKZN instruments were calibrated in January 2009 before installation and the measurement uncertainties applicable to this study are on the order of 5 to 10% for the PSP (Gueymard and Myers, 2009) and under 1% for the NIP (Wilcox and Myers, 2008). With higher uncertainties and unventilated radiometers, the measurement scheme at UKZN HC is inferior to that at NREL SRRL. To some extent this hampers a direct comparison of PB performance between the two sites, but there is still value in analysing the trends in perforated band performance to see if they are repeated at the southern hemisphere location.

Table 6.1: Instruments used at UKZN HC to characterise PB performance.

Component	Instrument configuration	Serial number	Sensitivity [W/m^2/mV]	Date installed
Perforated band	Unventilated PSP	35663F3	108.93	30 Jan 2009
GHI (reference)	Unventilated, unshaded PSP	35622F3	113.75	30 Jan 2009
DHI (reference)	Unventilated, shaded PSP w/band	35662F3	114.55	16 Jan 2009
DNI (reference)	Tracking Eppley NIP	35649E6	123.15	30 Jan 2009

Table 6.2 provides metadata for the UKZN HC measurements, referred to as dataset #3. In the absence of calibration facilities at the UKZN ground station, a limited set of 114 days between August 2010 and April 2011 was used to ensure the quality of the measurements and limit the effect of instrument drift. All daily data files were filtered using the exclusion criteria given in equations (4.1) to (4.6). The average daily clearness index is 0.50, somewhat lower than the values for datasets #1 (0.59) and #2 (0.61) from NREL. This was caused in part by fewer winter months in the dataset than summer months when rainfall is generally higher in Durban. There is also a difference in elevation between Golden and Durban, which is an industrial city at sea level and therefore subject to a higher average air mass. One can expect the maximum clear index values to be lower for the UKZN station than NREL SRRL.

Table 6.2: Southern hemisphere radiometric dataset #3 used with the CdSPM (φ = –29.87°).

Description	UKZN HC dataset #3
No. of daily files	114
Time span	August 2010 to April 2011
Total number of data rows for $Z < 70°$, N	63 134
No. of DHI data interpolated	22 764 (36.1%)
No. of GHI and transition data interpolated	40 370 (63.9%)
Average daily clearness index, K_{T_day}	0.50

6.2.2 The ray trace model applied to a southern hemisphere site

Data relating ω, Z and n to the exposure state of a sensor in the southern hemisphere at φ = –29.87° are given in Figures 6.1 (a) and (b). These are analogous to the NREL ray trace model of Figures 2.11 (a) and (b). For each aperture or zone, the lower set of markers represents the values of ω at which full exposure or occlusion of the sensor first occurs and the upper markers represent the end of full exposure or occlusion. In the case of Figure 6.1 (a), the starting hour angles for apertures 1 and 9 do not apply for $122 \leq n \leq 220$ because the band is adjusted to where the lower edges lie beneath the horizon. Under these conditions, shading zones 1 and 10 fall below the level of the pyranometer and have no influence on the sensor exposure state (Figure 6.1 (b)). Apart from this anomaly, the hour angle remains constant for a given aperture or zone throughout the year. The linear regions of Figures 6.1 (a) and (b) are similar to the NREL model but the variable parts are reversed with respect to day number because of the inversion of seasons from the northern to southern hemispheres.

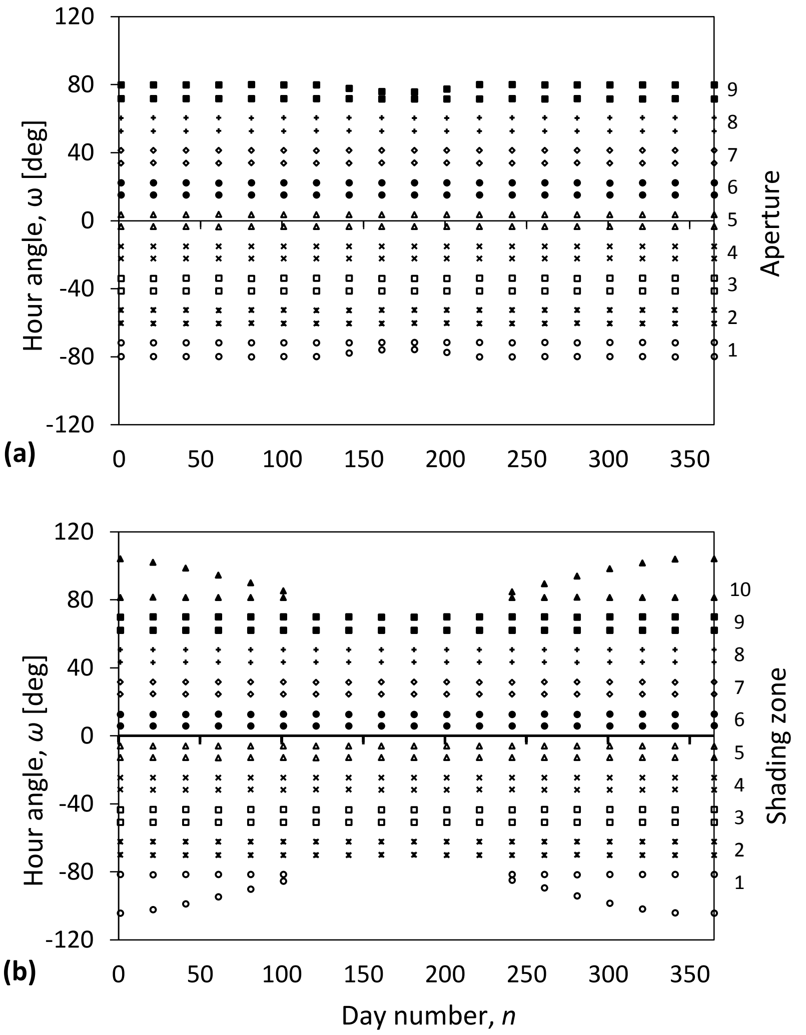

Figure 6.1: Ray tracing-derived hour angle limits for (a) full sensor exposure ($E_s = 1$), and (b) full sensor shading ($E_s = 0$) as a function of day number at $\varphi = -29.87°$ (Brooks and Roberts, 2009).

Table 6.3 gives average hour angle values applicable to the beginning and end of exposure and shading phases for the linear regions of Figure 6.1. These represent the ray trace model of pyranometer exposure for a perforated band in the southern hemisphere at $\varphi = -29.87°$.

As was done for the NREL version of the model, equivalent zenith angle values are calculated using equation (2.9) for each aperture and zone and represented in

Figures 6.2 (a) and (b). For UKZN HC, $K_1 = -0.498$ and K_2 is given in Table 6.3 as a function of hour angle. Both ω and K_2 vary for the start of shading zone 1 and the end of shading zone 10 as a result of seasonal changes in band height relative to the pyranometer.

Table 6.3: Annual hour angle limits for onset and completion of full pyranometer exposure ($E_s = 1$) and shading ($E_s = 0$) at UKZN HC (Brooks and Roberts, 2009).

$E_s = 1$ (Exposure)					$E_s = 0$ (Shading)				
Aper-ture	**Start ω**	**K_2**	**End ω**	**K_2**	**Shad. zone**	**Start ω**	**K_2**	**End ω**	**K_2**
1	-79.94*	0.15	-71.71	0.27	**1**	*Variable*		-81.45*	0.13
2	-60.43	0.43	-52.65	0.53	**2**	-70.06	0.30	-62.23	0.40
3	-41.27	0.65	-33.83	0.72	**3**	-50.71	0.55	-43.33	0.63
4	-22.30	0.80	-15.15	0.84	**4**	-31.64	0.74	-24.59	0.79
5	-3.49	0.87	3.49	0.87	**5**	-12.77	0.85	-5.94	0.86
6	15.15	0.84	22.30	0.80	**6**	5.94	0.86	12.77	0.85
7	33.83	0.72	41.27	0.65	**7**	24.59	0.79	31.64	0.74
8	52.65	0.53	60.43	0.43	**8**	43.33	0.63	50.71	0.55
9	71.71*	0.27	79.94	0.15	**9**	62.23	0.40	70.06	0.30
					10	81.45*	0.13	*Variable*	

Limits are valid approximately as: $^{*}122 \leq n \leq 220$

A comparison between Tables 2.1 and 6.3 permits a check on the location-dependence of the ray trace model. This shows a maximum absolute variation in the hour angle exposure start and end limits for any single aperture of 0.14° and an average absolute difference for all apertures of 0.05°.

For shading zones, the maximum difference in predicted hour angle limits between the sites is 0.23° and the average absolute difference is 0.07°. The results confirm that for latitudes in the 30° to 40° range (northern or southern hemisphere) the ray trace model is latitude-independent with respect to hour angle. This invariability is a useful feature of the perforated band's operation since no recalculation is required when deploying the system. The only difference between sites is the variation peculiar to the first and last apertures as they fall below the sensor level in winter. Since pyranometric data obtained at high zenith angles are generally treated with caution, or disregarded completely, the variability of the model at sunrise and sunset is of limited consequence.

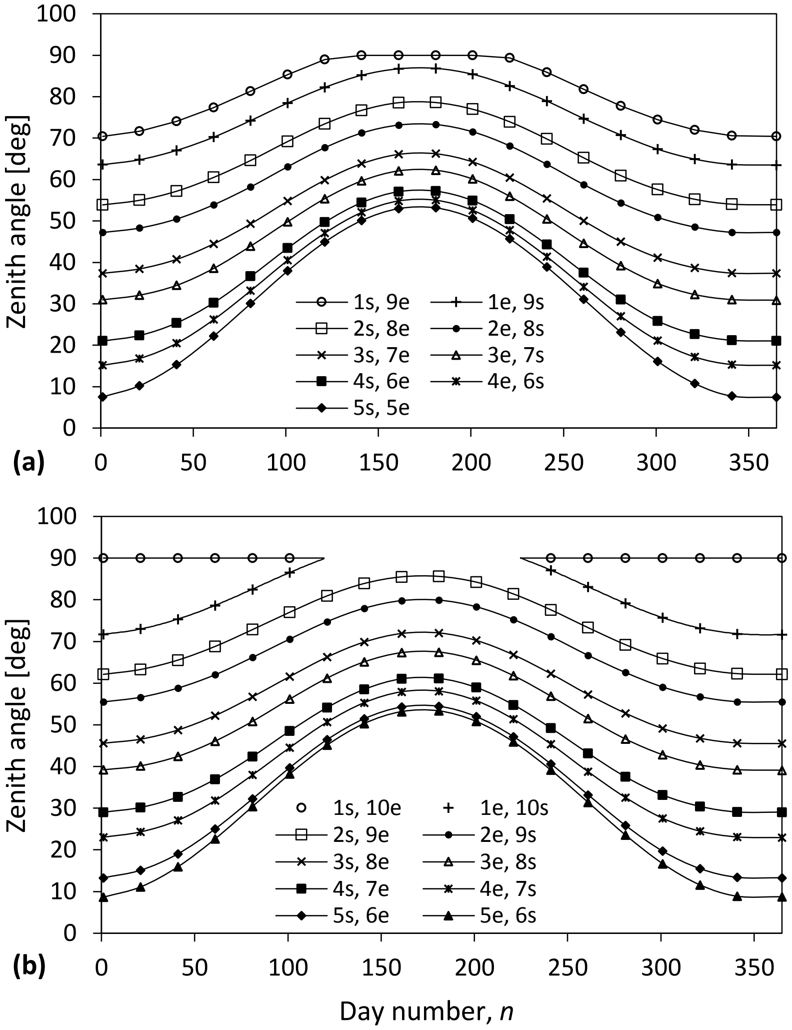

Figure 6.2: Annual zenith angle start (s) and end (e) limits at φ = –29.87°: (a) by band aperture for pyranometer exposure (E_s = 1) and (b) by shading zone (E_s = 0) (Brooks and Roberts, 2009).

As with the NREL test article, data from the UKZN HC station were corrected to account for structural deformation of the band and for the shadow band blocking effect, as described in section 2.5. The correction factor for structural deformation was determined empirically for the UKZN site, based on the difference between the ray trace model described in Table 6.3 and clear-sky data extracted from the dataset.

6.2.3 Dataset #3: PB uncertainties for GHI, DHI and DNI

Uncertainties for the southern hemisphere PB system are presented similarly to those for NREL SRRL. Performance is assessed via the RMSD and MBD, with some additional metrics provided including the SD and expanded uncertainty, U_{95}. These are calculated with reference to irradiance data from collocated sensors that independently record GHI, DHI and DNI. The adaptive interpolation schemes are numbered according to the same configuration as listed in Tables 4.7 and 4.8. As before, the root mean square difference is considered the primary metric for comparative purposes, followed by mean bias difference.

Diffuse horizontal irradiance

The statistical uncertainties of the PB system in recreating DHI are given in Table 6.4, partitioned by clearness index. Although dataset #3 contains several days in which little cloud is present, no data for bin 8 were available ($K_{T\_day} \geq 0.8$). This is due to the coastal sub-tropical climate of Durban and the limited period over which useable measurements were available. In addition, there is a higher average air mass above Durban and a consequent reduction in maximum clearness index for the site versus the high-altitude, clearer conditions at NREL. Root mean square differences for dataset #3 vary between 20.3 W/m^2 for bin 1 and 49.8 W/m^2 for bin 4. The RMSD percentage is consistent with that of NREL, except in bin 6 where it rises to 27.6%. Figure 6.3 enables comparison of the Durban results with those from NREL (datasets #1 and #2).

Table 6.4: Statistical parameters for best performing DHI interpolation schemes in dataset #3 by daily clearness index (φ = –29.87°, Z < 70°).

Bin	Ave. K_{T_day}	Scheme	RMSD [W/m^2]	RMSD [%]	MBD [W/m^2]	MBD [%]	SD [W/m^2]	SD [%]	U_{95} [%]	|MBD| [%]
1	0.15	BRL	20.3	16.1	9.1	7.2	18.1	14.4	42.3	7.2
2	0.25	RnB	30.6	15.6	11.6	5.9	28.3	14.4	41.6	5.9
3	0.35	RnB	43.8	19.0	13.9	6.0	41.6	18.0	51.2	6.0
4	0.45	D_AIS_9	49.8	21.7	27.2	11.9	41.8	18.2	55.5	11.9
5	0.55	D_AIS_9	47.1	23.7	28.0	14.1	37.8	19.1	59.7	14.1
6	0.64	D_AIS_5	39.4	27.6	23.8	16.6	31.4	22.0	69.1	16.6
7	0.71	PCHIP	20.5	20.6	10.4	10.4	17.7	17.7	53.2	10.4
8		No data								

Figures 6.3 and 6.4 permit a comparison of the southern hemisphere data with NREL SRRL results. In bins 1, 2 and 3 there is little difference in percentage RMSD between the three datasets, but under clearer skies the Durban data exhibit uncertainties somewhat higher than at NREL. In Figure 6.3, the best non-AIS uncertainties for Durban are mainly equivalent to those of the adaptive schemes,

except in bin 5 where they are slightly higher. Interestingly, there is little difference between the performance of the best schemes transferred from #1 into #3, and that of the best schemes in #3, meaning that the superior schemes identified using NREL data performed consistently well for DHI generation, even at a different location and latitude. The same can be said of the MBD uncertainties (Figure 6.4) where the better performing schemes from #1 continue to do well in #3 (green circles versus blue circles). Bias differences are, however, higher for the southern hemisphere site than for the NREL data. Given that the reference scheme at the UKZN station is inferior to NREL's sensors, it is likely that the bias values reported here are affected by the reference data at UKZN. The scheme used for this study employs a shadow band to generate DHI and not a tracking ball that yields lower measurement uncertainties.

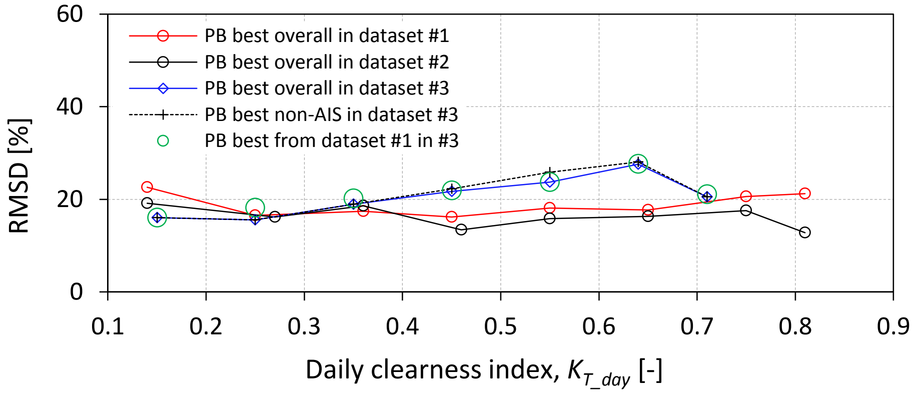

Figure 6.3: Root mean square difference for best DHI interpolation schemes in dataset #3 (φ = –29.87°, Z < 70°) by daily clearness index, with comparative results from datasets #1 and #2.

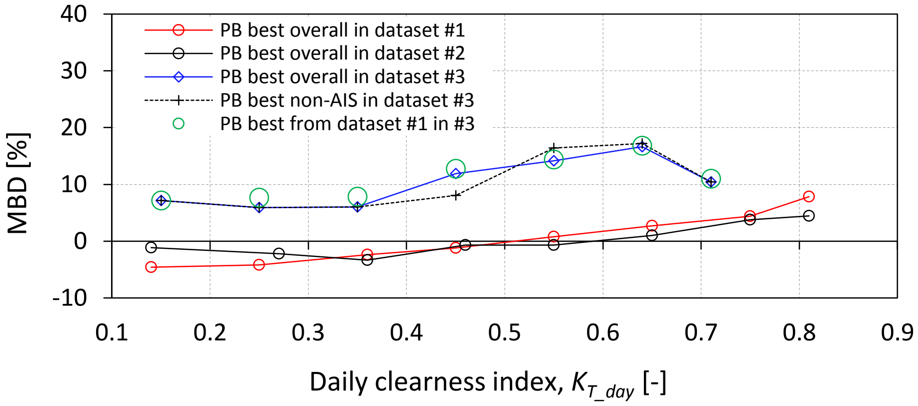

Figure 6.4: Mean bias difference for best DHI interpolation schemes in dataset #3 (φ = –29.87°, Z < 70°) by daily clearness index, with comparative results from datasets #1 and #2.

Global horizontal irradiance

Table 6.5 gives uncertainty data for GHI, while Figures 6.5 and 6.6 compare RMSD and MBD uncertainties for dataset #3 with those of #1 and #2. Four points are worth noting:

1. The trends in the percentage RMSD and MBD curves are very similar for datasets #1 and #3. Root mean square differences balloon in the mid-K_{T_day} range where partly cloudy conditions give rise to stochasticity in the GHI curves and interpolation becomes less effective. In the case of dataset #3, there is a compression of the RMSD curve towards the overcast side of the graph that is likely caused by differences in air mass and quality above the Durban station.
2. In absolute terms, the RMSD and MBD percentages are very similar for datasets #1 and #3. Biases are negative throughout the bins, indicating that the PB system underestimates GHI, regardless of location. A slight increase in MBD can be observed for partly cloudy conditions in all three sets and the PB system operates more effectively under clear conditions.
3. The best performing schemes from dataset #1 continue to perform well in dataset #3, as shown by the green circles tracking the blue. All but one of the best performing schemes in Table 6.5 utilise the GeD or Ramp functions for overcast or heavily cloudy conditions (bins 1 to 3). For the higher bins, adaptive schemes 6 and 11 deploy either ARIMA or averaging methods (Table 4.8).
4. The adaptive schemes generally perform better than their non-adaptive competitors throughout, except in bin 8. Although the differences between AIS and non-AIS results are quite small, there is enough consistency in the data to confirm the value of using adaptive interpolation.

Table 6.5: Statistical parameters for best performing GHI interpolation in dataset #3 ($\varphi = -29.87°$, $Z < 70°$).

Bin	**Ave.**	**Scheme**	**RMSD**		**MBD**		**SD**		**U_{95}**	**|MBD|**
	K_{T_day}		**[W/m^2]**	**[%]**	**[W/m^2]**	**[%]**	**[W/m^2)\]**	**[%]**	**[%]**	**[%]**
1	0.15	G_AIS_1	20.5	14.2	-7.1	-4.9	19.3	13.3	38.2	4.9
2	0.25	G_AIS_11	68.8	28.0	-16.5	-6.7	66.8	27.1	76.4	6.7
3	0.35	G_AIS_5	112.2	32.4	-33.2	-9.6	107.2	31.0	87.9	9.6
4	0.45	G_AIS_6	127.4	27.7	-42.1	-9.2	120.3	26.1	74.6	9.2
5	0.55	G_AIS_11	122.9	22.8	-29.0	-5.4	119.4	22.2	62.4	5.4
6	0.64	G_AIS_6	88.4	13.4	-25.1	-3.8	84.7	12.9	36.5	3.8
7	0.71	3rd OP	44.2	6.1	-12.0	-1.7	42.6	5.9	16.7	1.7
8		No data								

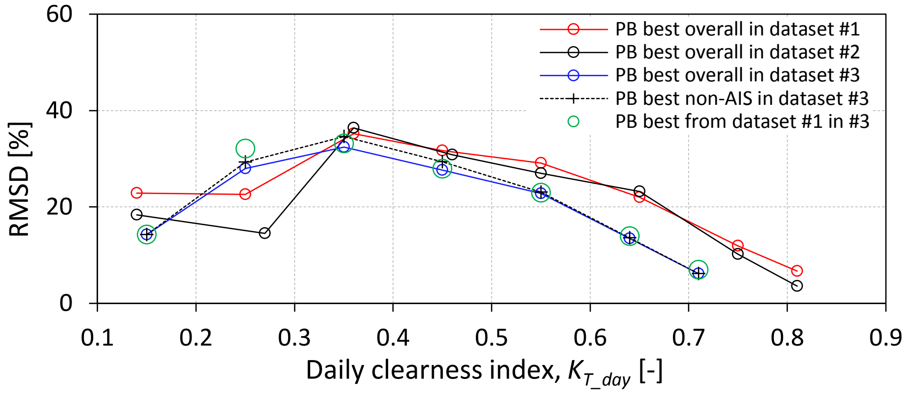

Figure 6.5: Root mean square difference for best GHI interpolation schemes in dataset #3 (φ = –29.87°, Z < 70°) by daily clearness index, with comparative results from datasets #1 and #2.

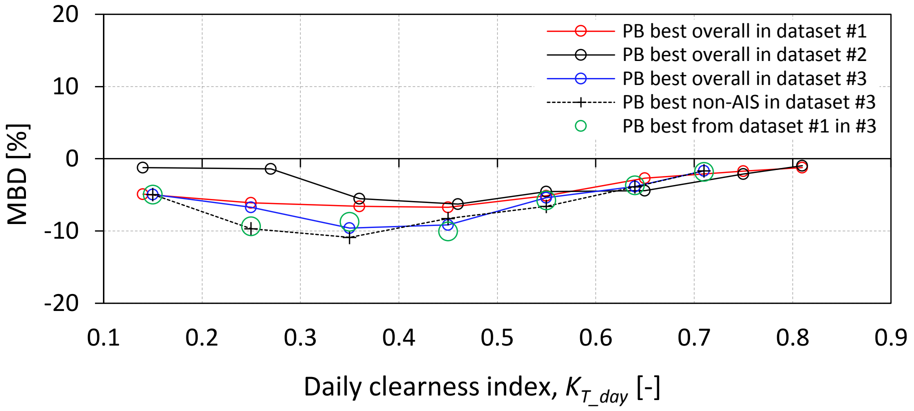

Figure 6.6: Mean bias difference for best GHI interpolation schemes in dataset #3 (φ = –29.87°, Z < 70°) by daily clearness index, with comparative results from datasets #1 and #2.

Direct normal irradiance

Table 6.6 provides the configuration of additional DNI schemes for dataset #3. These comprise the DHI and GHI components that yielded the lowest RMSD uncertainties for the UKZN HC ground station in each clearness index bin. For example, B_AIS_3_1 is comprised of BRL and G_AIS_1, since they were the best performers as shown in Tables 6.4 and 6.5. It should be noted that G_AIS_1 yielded identical uncertainty to the non-AIS GeD for bin 1, which is to be expected since the GeD scheme is deployed under overcast conditions for that adaptive approach (Table 4.8). By including these additional combinations, it is possible to compare the best schemes from dataset #3 with the top performers in sets #1 and #2, as shown in Figures 6.7 and 6.8. This enables the identification of differences in overall system performance, apart from differences in the performance of specific schemes carried over from the NREL site to UKZN Howard College.

Table 6.6: Configuration of direct normal irradiance adaptive interpolation schemes (B_AIS) for southern hemisphere dataset #3.

B_AIS	DHI Scheme	GHI Scheme
B_AIS_3_1	BRL	G_AIS_1
B_AIS_3_2	RnB	G_AIS_11
B_AIS_3_3	RnB	G_AIS_5
B_AIS_3_4	D_AIS_9	G_AIS_6
B_AIS_3_5	D_AIS_9	G_AIS_11
B_AIS_3_6	D_AIS_5	G_AIS_6
B_AIS_3_7	PCHIP	3OP

Table 6.7 provides the DNI performance results for the perforated shadow band system at UKZN HC. Because DNI levels drop close to zero in the lower bins, it is more useful to consider the uncertainties in units of [W/m^2] rather than percentages. Other than for overcast conditions (bin 1) and clear-sky days (bin 7), the schemes corrected using the Bird model performed best in each bin. As with the NREL results, this reflects the positive effect of 'damping' excessive fluctuations in DNI caused by the combination of the global and diffuse components.

Table 6.7: Statistical parameters for best performing DNI interpolation schemes per bin in dataset #3 (φ = –29.87°, Z < 70°).

Bin	Ave.	Scheme	RMSD		MBD		SD		U_{95}
	K_{T_day}		[W/m^2]	[%]	[W/m^2]	[%]	[W/m^2]	[%]	[%]
1	0.15	B_AIS_21	7.0	263.5	-0.1	-2.0	7.0	263.5	730.5
2	0.25	B_AIS_3_2C	81.6	282.0	1.8	6.2	81.6	282.0	781.6
3	0.35	B_AIS_3_3C	131.1	134.5	-1.5	-1.6	131.1	134.5	372.8
4	0.45	B_AIS_5C	149.4	61.4	-32.7	-13.5	145.8	59.9	168.1
5	0.55	RampC	159.2	39.8	-21.9	-5.5	157.7	39.4	109.8
6	0.64	RampC	128.7	19.7	-31.7	-4.9	124.8	19.1	53.8
7	0.71	Ramp	75.5	9.0	-28.6	-3.4	69.9	8.3	23.9
8		No data							

Figures 6.7 and 6.8 provide a graphical comparison of PB performance across the three datasets. As with the GHI data, the trend in root mean square difference for dataset #3 is similar to that of the northern hemisphere data, increasing in the mid-range bins where GHI uncertainties are also higher, and decreasing under overcast and clear-sky conditions. In bins 1 to 3, the mean bias difference is close to zero, becoming negative as skies clear and where the PB system tends to underestimate DNI. Again, the trend in dataset #3 is much the same as for the other two sets.

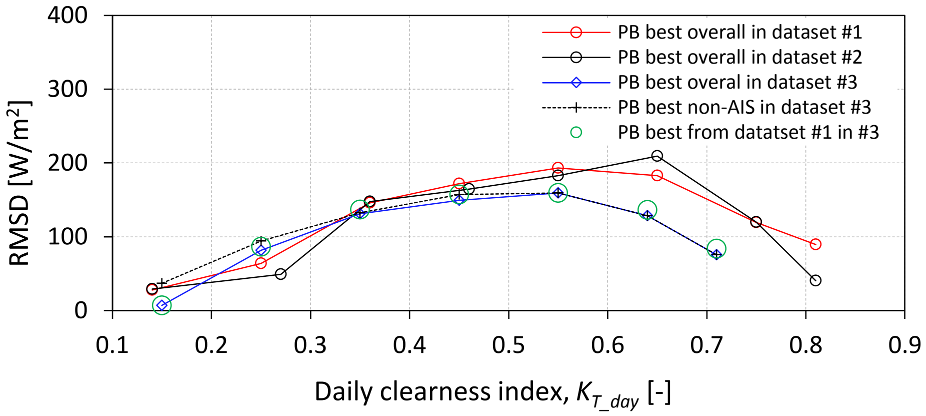

Figure 6.7: Root mean square difference for best DNI interpolation schemes in dataset #3 ($\varphi = -29.87°$, $Z < 70°$) by daily clearness index, with comparative results from datasets #1 and #2.

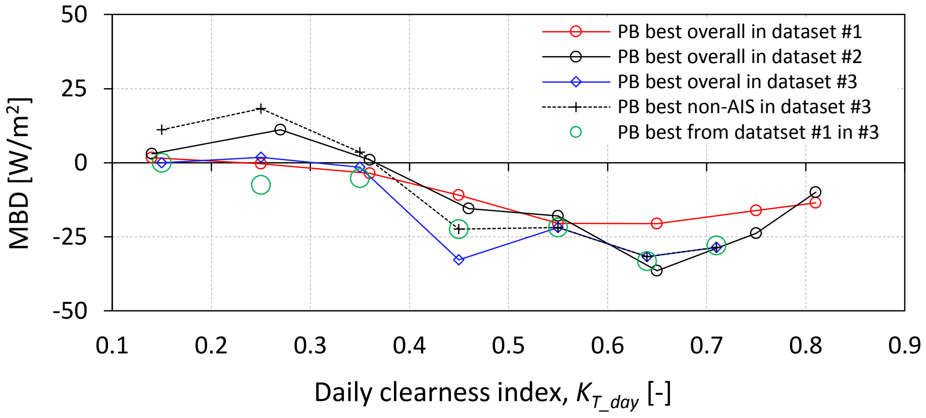

Figure 6.8: Mean bias difference for best DNI interpolation schemes in dataset #3 ($\varphi = -29.87°$, $Z < 70°$) by daily clearness index, with comparative results from datasets #1 and #2.

As before, the DNI uncertainty data for RMSD are somewhat compressed versus datasets #1 and #2, reflecting a reduction in maximum measured clearness index. This suggests that the results presented here are conservative with respect to clearness index, since NREL SRRL is known to possess an exceptionally clean atmosphere. At lower elevations or at sites where atmospheric conditions are poor due to non-cloud related turbidity, the uncertainty results will shift to the left with respect to K_{T_day} (as in Figure 6.7). The system will thus return similar uncertainties but at lower values of clearness index. Since the perforated band is more effective at higher values of K_{T_day} (that is, for clear skies), the threshold value of clearness index at which the system becomes attractive to station operators may be lower than the values reported here. In this sense, the uncertainties given in Chapter 5 are conservative with respect to K_{T_day}.

6.3 Deployment of the perforated shadow band

Having described the performance of the perforated shadow band in Chapters 3 and 5 (see Tables 3.5 and 5.10 for summaries) it remains to be established how these results influence the deployment of the system. A qualitative summary of PB performance is first provided and then two questions are addressed:

1. What advantages does the PB system offer over existing radiometric schemes?
2. Where should the PB system be deployed to exploit any advantages identified in its operation?

6.3.1 Characteristics of PB system performance

The general characteristics of the perforated band system, established in the previous chapters, can be summarised as follows:

1. The system decomposes GHI so as to obtain diffuse and direct normal components at 1-minute intervals, according to the statistical uncertainties reported in Chapters 2 and 5, and its performance is related to the daily average clearness index under which it operates.
2. Compared to optimal schemes and those making use of independent radiometers for the measurement of GHI, DHI and DNI, there is a penalty to be paid in using the PB system which returns higher RMSD and MBD uncertainties.
3. The system is most effective under clear sky conditions where occlusion of the pyranometer sensor due to transitory cloud fields is minimal.
4. Under overcast conditions the cloudy sky processing methodology is able to exploit the equivalence of global and diffuse irradiance to constrain RMSD and MBD uncertainties.
5. The system is least effective under partly cloudy conditions characterised by transitory cloud fields and intermittent occlusion of the sensor.
6. Tests at a southern hemisphere location show very similar performance trends to the primary NREL test site. As the system does not suffer from any terminal flaw in its operation within the 30° to 40° degree latitude

band, or between hemispheres, it is reasonable to assume that it will return similar uncertainties at latitudes bounded by the polar circles (between +66° and –66°). This has not been verified experimentally.

Advantages of the PB system

A broad range of solar radiometers exists for equipping stations, leading to a spectrum of possible measurement schemes varying in cost from a few hundred to many thousands of dollars. A small selection of these was given in Table 1.2. Within the cost-performance spectrum, measurement uncertainty is generally inversely proportional to cost, such that at one end there exist inexpensive but less accurate sensors, while at the opposite end one finds research-grade, optimal measurement schemes with multiple radiometers and full redundancy. The spectrum includes an extensive set of options varying as a function of sensor cost, accuracy and scheme complexity, with the perforated band system positioned closer to the inexpensive end. Before drawing conclusions about the deployment of the PB, a brief summary of its performance versus that of alternate configurations is appropriate:

Versus the optimal measurement scheme and those measuring three components independently (schemes 1 and 2 in Table 1.2):

There is a performance disadvantage compared to optimal radiometric schemes but the PB system is considerably less expensive than installations employing multiple radiometers for independent measurement of DHI, GHI and DNI. As possible candidates for deployment in a radiometric project, the two schemes are some distance apart on the spectrum.

Versus sub-optimal schemes measuring one component (DHI or GHI only):

Under predominantly cloud-free skies (bins 7 and 8 with average clearness index exceeding 0.7) the PB system returns RMSD uncertainties of around 12% or lower versus a single, unshaded secondary standard pyranometer measuring GHI only (Figure 5.5). Importantly, the perforated band can also measure DHI while the unshaded pyranometer must rely on decomposition models, the best of which returned RMSD uncertainties of 50% or higher for bins 7 and 8 in this study (Figure 5.1). At the NREL site, the PB system consistently measured DHI with an uncertainty of approximately 20%, regardless of the sky condition.

It can be argued that the perforated band offers an advantage over single unshaded pyranometers where more than one component is required and the clearness index is above 0.7. The capability of the system to measure GHI and DHI also represents an advantage over installations intended for moderate or low quality data generation where a single pyranometer is fitted with a solid shadow band to measure DHI only. This is especially true where a shaded pyranometer is already in operation and the scheme can be modified by replacing the solid band with its perforated counterpart for virtually no cost.

Versus the SPN1 and RSR2 sensors:
The SPN1 instrument is marginally more expensive than the PB system, but it returns substantially lower uncertainties for DHI and GHI (Figures 5.27 and 5.28). Experimental data for the RSR2 sensor were not available during this study, but the performance of the LI-200 sensor on which it is based suggests that the Rotating Shadowband Radiometer would perform better than the PB system, and it costs marginally less. The PB system is, however, mechanically simpler than the RSR2 which needs a constant power supply for its moving arm mechanism. The mechanical complexity of the RSR2 may represent a disadvantage at remote locations where monitoring of the arm mechanism is not possible.

6.3.2 Opportunities for PB deployment

The many options that exist for configuring a station makes it difficult to draw definitive conclusions about which sensor is best since much depends on the specifications and resources of a particular project. Nevertheless, Gueymard and Myers (2009) have identified three categories into which radiometric projects generally fall:

1. Installations with inexpensive sensors to provide local data at least cost;
2. Installations for provision of long-term data by organisations like weather services, where proven technology is used and innovation is avoided;
3. Installations utilising state-of-the-art sensors for research grade data generation (an example is the installation of a new BSRN station).

In practice, the perforated band does not occupy the same part of the cost-performance spectrum as optimal schemes and cannot compete with them where research-grade data are specified. It is therefore not a candidate for equipping high-quality stations of the third project type, where proportionally higher budgets are available. The question of sensor selection becomes more complex in project type 1 where budget constraints play a more significant role in the decision-making process.

For installations where higher uncertainties are tolerable, the PB system may represent better value than a single pyranometer measuring GHI, but only where skies are largely clear. Since this work has linked performance of the band to cloud conditions through the K_{T_day} parameter, the geographic deployment of the band may be informed by studies of clearness index. An advantage of this approach is that clearness index is a widely used and well-understood descriptor of cloudiness, and information exists about its variation globally. In this study, the variation of K_{T_day} across the African continent is considered.

Diabate et al. (2004) used data from 62 sites across Africa to generate a map of the continent's solar radiation climate. Using Ward's clustering method, they divided the continent into 20 zones based on the behaviour of the monthly average daily clearness index throughout the year (Figure 6.9). Within each zone, the average daily clearness index varies as a function of the month. Predictably, clearness index is generally higher in the Sahara desert regions (zones IV, XII, XIII, XIV and XVIII), in the horn of Africa (III) and in the south-western parts of the continent (XVI). According to their study no part of the continent experiences values of K_{T_day} that exceed 0.7 throughout the year, but there are regions where the clearness index exceeds this value or closely approaches it for part of the year. These include zones III, IV, XIII and XIV. The perforated band might therefore compete with alternate measurement schemes in these parts of the African continent.

Figure 6.9: Division of continental Africa into 20 solar radiation climate zones by Diabate et al. (2004).

For the purposes of this study, satellite-derived maps of the monthly average daily clearness index for Africa were commissioned from GeoModel Solar (2014). The variation in K_{T_day} is shown in Figures 6.10 and 6.11, with the yellow to red regions indicating a clearness index of 0.7 or greater. The colour maps were generated from raster data for zenith angles less than 70° to eliminate errors associated with high angles of incidence. Figures 6.10 and 6.11 indicate trends similar to those reported by Diabate et al. (2004).

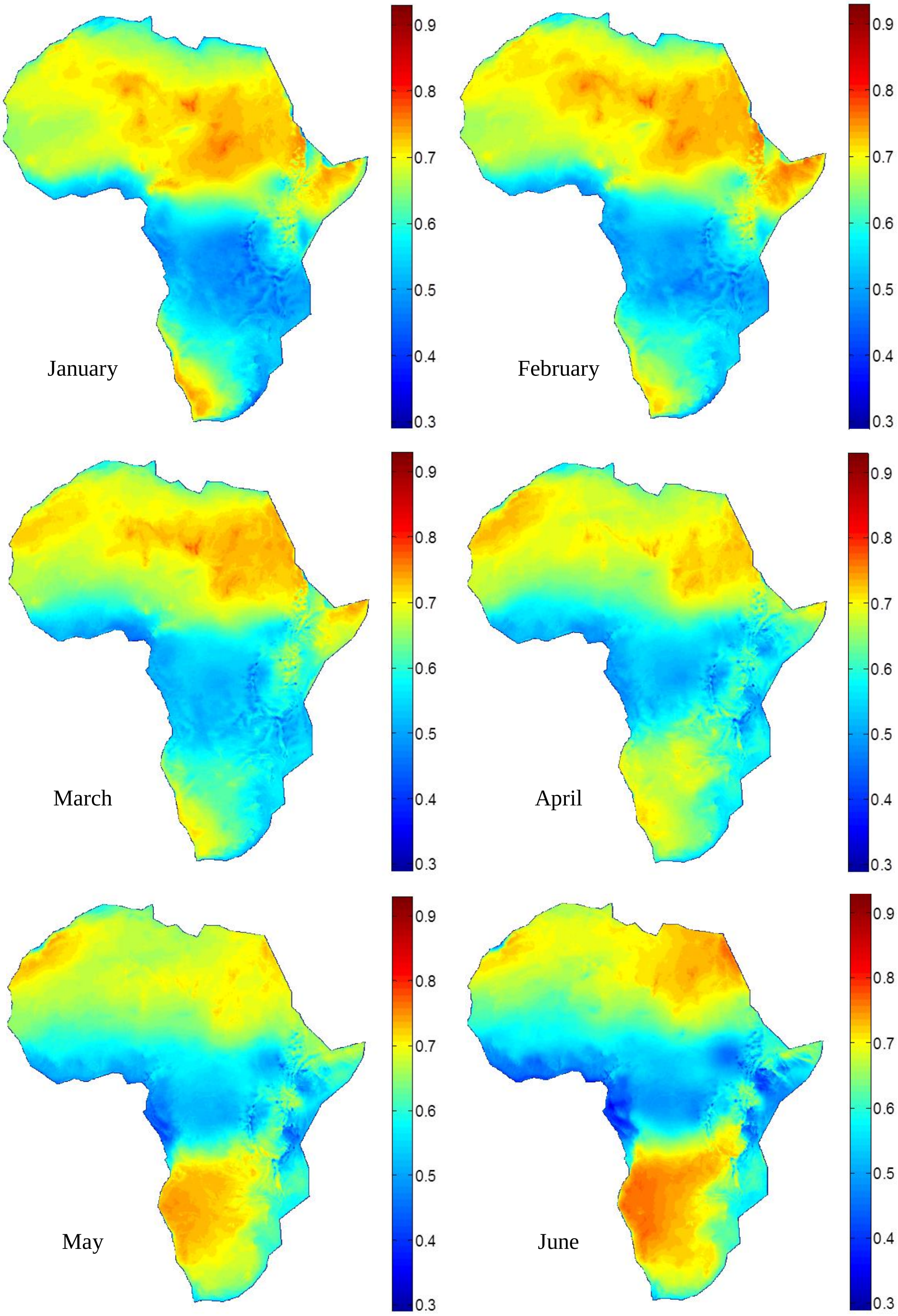

Figure 6.10: Satellite-derived monthly average daily clearness index for Africa from January to June (GeoModel Solar, 2014).

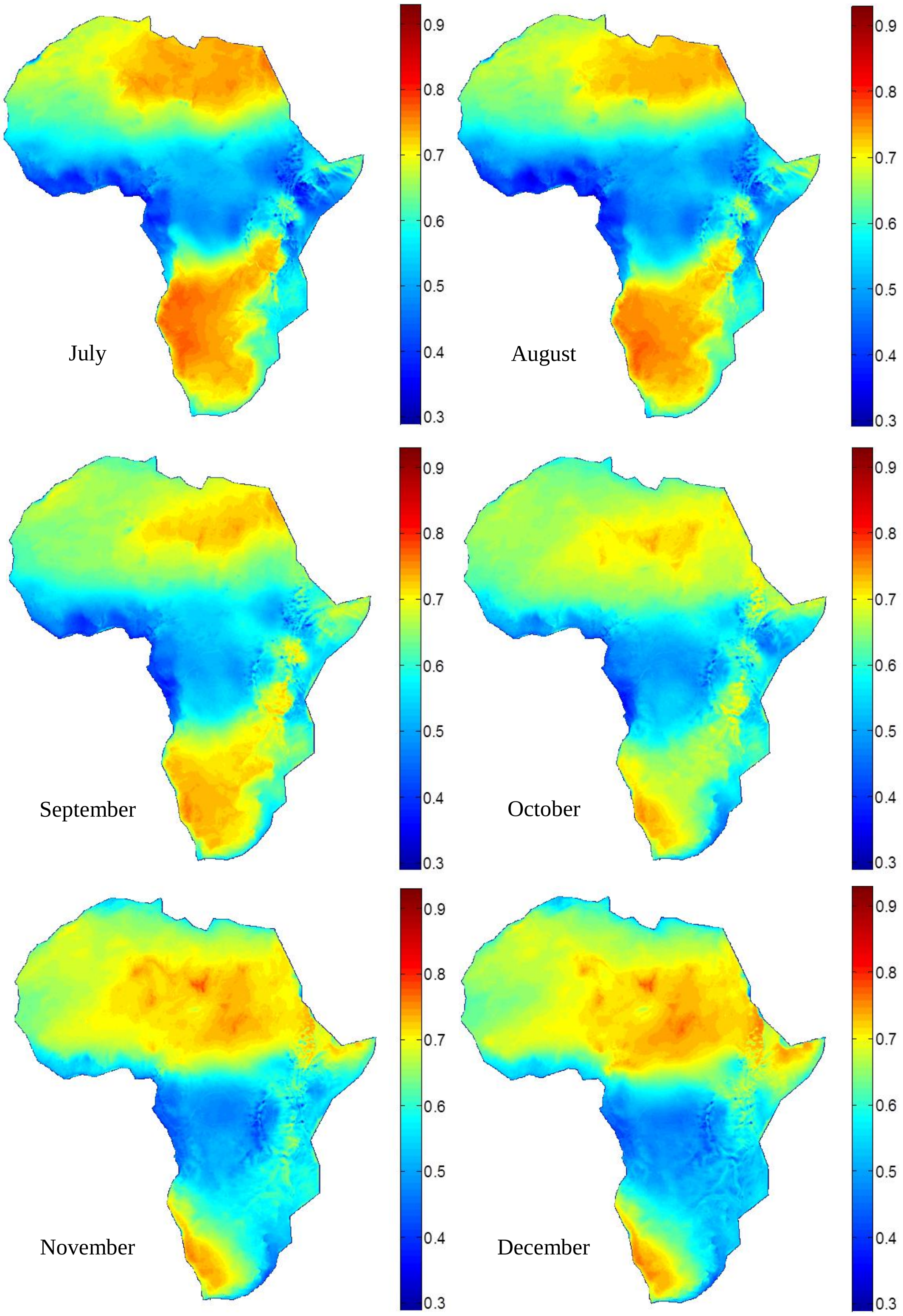

Figure 6.11: Satellite-derived monthly average daily clearness index for Africa from July to December (GeoModel Solar, 2014).

The central parts of Africa, represented in blue on the colour maps and characterised by a tropical climate and lush vegetation, typically experience lower values of clearness index year-round. The PB system would return relatively high uncertainties if used here and alternate radiometric schemes using an unshaded pyranometer, a rotating shadow band, or the SPN1 sensor should be preferred. The same applies to the eastern coastal regions down into Mozambique and South Africa. Of greater interest to this study are the yellow-to-red regions that vary in size through the year but which typically occupy substantial portions of north and south-western Africa. The potential for deploying the perforated shadow band in these parts is favourable since uncertainties are expected to be low.

Coupled to the above, there are two further considerations impacting the band's deployment. First, the daily clearness index is a bulk parameter averaged over each month. Therefore the data in Figures 6.10 and 6.11 comprise the average of some cloudy or overcast days and some that are cloud-free. Even in zones where the average daily values are closer to 0.7 than 0.75 there will be many days in any given month that are cloud-free. This means that a station operator can, if present on site, implement the perforated shadow band system in response to prevailing weather conditions. This is not ideal since the band must then be replaced or removed when periods of cloud prevail, however the approach does offer a potential method of improving the quality of data from a station already operating a solid band in high-K_{T_day} regions.

Second, the PB results for Durban (Figures 6.5 and 6.7) show that a small leftwards compression in the uncertainty curves occurs with K_{T_day} when a site is located at lower elevation than the primary test site at Golden, Colorado. This is because of higher air mass values that prevail as elevation drops, and not necessarily because of cloud. In a similar way, dry desert areas often experience dust that manifests as evenly distributed atmospheric particulates. Under such conditions, the suppression of clearness index will not be accompanied by the data stochasticity associated with transient cloud fields. In other words, if atmospheric turbidity increases as a result of evenly distributed dust then PB uncertainties are likely to remain low because the sky is still largely cloud-free, even if the clearness index is suppressed. It is therefore likely that the perforated band would find greater potential for deployment in the arid regions of Africa than is suggested even by the results of Diabate et al. (2004) and those presented in Figures 6.10 and 6.11. It should be noted that the augmentation of clearness index with other parameters, such as average sunshine hours, could assist in establishing patterns of deployment.

The data in Figures 6.10 and 6.11, taken together with the uncertainty results of Chapters 5 and 6, suggest favourable opportunity for PB deployment on the African continent. The system should compete well against alternate radiometric schemes at the lower end of the cost-performance spectrum across substantial parts of the arid south-western and northern regions. The PB system is therefore most likely to find application in the 1st and 2nd project categories mentioned above where moderate or low quality data are required at locations experiencing a high clearness index, either at new or existing ground stations. Although this analysis was confined to Africa, a similar approach can be applied to other regions globally where clearness index data are available.

6.4 Summary

Those aspects of the perforated band's operation that are affected by changes in location were addressed in this chapter. A revised ray trace model of pyranometer exposure for Durban, South Africa, was presented and discussed.

As part of a test on location-dependence, the PB system was evaluated at a ground station in Durban, South Africa, with the intention of characterising its performance under different conditions to NREL. The resulting dataset (#3) consists of 114 days of 1-minute averaged radiometric data from a PB system identical to that installed at the NREL SRRL site. Reference instruments are more limited at the Durban site and do not permit the application of a correction for thermal offset due to the absence of pyrgeometers.

With respect to diffuse horizontal irradiance, the southern hemisphere results show very similar RMSD percentages to the NREL data, with values of between 15% and 28%. Bias differences are somewhat higher for Durban than for NREL, rising as high as 16.6%. Importantly, when the best performing schemes from dataset #1 are transferred into dataset #3, they once again do well versus the other interpolation schemes. This is significant and suggests that performance of the PB system is consistent regardless of changes in location.

For the GHI results, dataset #3 once again gives similar percentage uncertainties to #1, and the trends in uncertainty variation are almost identical, with an increase in RMSD percentage in the mid-range clearness index range. Transferring the best processing schemes from dataset #1 into #3 again shows consistency in the performance of the best interpolation methodologies.

Direct normal irradiance uncertainties are similar for the southern hemisphere site as compared to those of the northern hemisphere site, increasing in the mid-range bins and declining under overcast and clear-sky conditions. All told, the outcome of the Durban-based test confirms that the performance of the PB system is universal and not tied to a specific location.

The deployment of the perforated band as an operational system was addressed by first considering its performance advantages over competing radiometric schemes. Based on this, the study addressed the practical question of where in Africa it might offer better value than sensors such as the SPN1 and the rotating shadow band system.

The PB system cannot compete with optimal measurement schemes requiring the highest quality data and redundancy. This would preclude its use in most bankability studies for large-scale CSP installations. For those projects where moderate to low data quality are tolerable, however, the system may offer an advantage provided that it is deployed where the daily average clearness index is around 0.7 or higher. As an illustration of the connection between PB performance and available clearness index data, a set of satellite-derived maps of the variation of K_{T_day} with month of the year for Africa was presented. These maps make it possible to identify areas of the continent where the perforated band system may be deployed to ensure that the resulting statistical uncertainties are constrained to the values presented in chapters 5 and 6. The areas of interest comprise large parts of northern African desert, portions within the horn of Africa and sections of south-western Africa, including areas within the Northern Cape province of South Africa and Namibia. Since clearness index is a function of climate, K_{T_day} varies seasonally and therefore the PB system may not be equally effective throughout the year at a given location, depending on the weather conditions experienced.

As perforated band performance is better understood with expanded deployment, it may be possible to refine the uncertainty analysis by accounting for air mass variation between sites. One possibility is the introduction of a normalised clearness index parameter so that differences in air mass are eliminated when the system is run at different elevations, as was done in this study.

In addition, it is worth considering the inclusion of other parameters such as the number of sunshine hours in future analyses of PB uncertainty. This may assist in clarifying the relationship between statistical uncertainty and the suppression of clearness index, which can be caused both by transient cloud fields, and by evenly distributed dust in the atmosphere. Since uncertainty is primarily a function of trace stochasticity, it would be helpful to distinguish between reductions in K_{T_day} that are caused by cloud, and those caused by dust or haze.

7. CONCLUSIONS AND RECOMMENDATIONS

7.1 Overview

The harnessing of solar energy is an increasingly popular alternative to conventional power sources as the world contends with environmental challenges and a growing appetite for energy. With the accelerated deployment of photovoltaics, solar water heaters and CSP systems the need for improved solar resource data has increased substantially. Numerous endeavours now rely on accurate radiometric measurements. Governments seek data to inform policy, developers require on-site measurements for the techno-economic analysis of power plant projects and environmental scientists need reliable solar data to model the earth's climate, to name a few.

In response to the growing need for ground-based measurements, the literature has expanded dramatically over the past few decades as researchers seek better ways of gathering, processing and interpreting sun strength data. A review of the global radiometric enterprise suggests three distinct priorities:

- to improve the quality of radiometric datasets by reducing statistical uncertainty and refining modelling techniques
- to improve the technical performance of radiometric sensors while reducing their cost
- to expand spatial coverage of stations and the resulting database of available sun strength information

This study potentially impacts all three of the above priorities, with particular emphasis on the second and third points. It proposes a novel adaptation of the shadow band method to generate estimates of global horizontal, diffuse horizontal and direct normal irradiance from a single pyranometer. The perforated shadow band is a low-cost radiometric measurement scheme that quantifies global horizontal and diffuse horizontal irradiance directly when paired with a thermopile pyranometer. Under clear sky conditions, it returns DHI, GHI and DNI uncertainties that are comparable to many commercially available, sub-optimal schemes especially those employing a single shaded or unshaded pyranometer. It therefore offers an inexpensive option to ground station operators with the *caveat* that it should be deployed in predominantly sunny regions where a high clearness index prevails.

7.2 Conclusions

Conclusions are presented with reference to the technical objectives of the study given in Chapter 1:

Objective 1: Define the geometry of a perforated shadow band

The geometry of a novel, perforated shadow band has been described to enable the decomposition of a composite radiometric trace into constituent GHI and DHI components. The interaction between the band’s geometry and key solar parameters such as azimuth, declination angle and zenith angle was described.

The band is installed on a polar mount over an Eppley Laboratory Precision Spectral Pyranometer, such that the thermopile sensor is intermittently shaded and exposed. The resulting shading pattern is described by means of a ray-trace derived model that associates the state of pyranometer exposure to the hour angle of the sun. A key finding of the study is that the model is location-independent aside from minor variations in the shading pattern at sunrise and sunset. The operation of the model was demonstrated using experimental data and a correction was included to account for structural deformation resulting from in situ distortion of the band. The system functions effectively in both the northern and southern hemispheres.

Objective 2: Establish a test programme in which the performance of the PB system is rigorously assessed

The performance of the perforated shadow band has been characterised through an extensive test programme conducted over five years at two sites, one in the United States and a second at the University of KwaZulu-Natal in South Africa.

The primary test site was NREL’s Solar Radiation Research Laboratory in Golden, Colorado where the system was maintained by laboratory staff who provided the data online through NREL’s publicly accessible website. Performance was assessed by comparing the PB-derived solar components with data from collocated, research grade reference instruments using recognised statistical metrics. A set of rigorous quality control checks was performed on all data files throughout the study.

Objective 3: Characterise the performance of a PB system under all sky conditions

This study has demonstrated that a perforated shadow band, used in conjunction with a thermopile pyranometer, can generate a composite output signal that may be decomposed into independent components of global horizontal and diffuse horizontal irradiance at 1-minute time steps. Furthermore, the resulting GHI and DHI fragments may be reconstituted using a variety of interpolation techniques to yield continuous traces of each component. Once separated and reformed, the DHI and GHI components may serve as inputs to calculate direct normal irradiance as an additional output of the system.

A key finding of this work is that the accuracy with which the fragmented data from the radiometer are reconstituted into continuous curves depends strongly on the underlying stochasticity of the data. This stochasticity is a direct function of the frequency and duration of occlusion of the pyranometer sensor due to cloud fields present during measurement. It may further be concluded that not all interpolation techniques function equally effectively in reconstituting the GHI and DHI traces. In this study over 21 approaches were tested and it was found that many techniques exhibit a functional dependence on the clearness index. It was concluded that an adaptive interpolation scheme that deploys specific techniques in response to the prevailing clearness index is generally more effective in filling data gaps than a single-scheme method. This approach is particularly useful when clearness index is moderate to low and the associated stochasticity increases.

It may be concluded that the PB band system is able to function under all sky conditions but this conclusion requires qualification. The statistical uncertainties of the irradiance measurements derived using the band are affected by the type of cloud present. Therefore the test programme was structured to consider both clear and cloudy sky conditions, and the performance of the system is reported in terms of clearness index, which served as a descriptor of cloud presence.

In the absence of cloud the pyranometer output signal may be decomposed by manual separation of the trace into GHI and DHI fragments and reconstitution of the fragments by curve-fitting. The PB system can be expected to return RMSD uncertainties versus research-grade reference data of approximately 3% for GHI, 14% for DHI and 2% for DNI.

Partly cloudy and overcast conditions present a greater challenge because of the aforementioned chaos in the data traces. Under these conditions, uncertainties must be reported as a function of clearness index, rather than as constants. These were provided in Chapter 5 of the study. For global irradiance, the RMSD uncertainties range between 6% for high clearness indices and around 36% for indices between 0.3 and 0.4. Bias is typically negative, indicating that the PB system underestimates GHI by between 1% (clear skies) and 7% (partly cloudy skies). Adaptive interpolation schemes generally perform best in reconstituting GHI curves under all sky conditions. For K_{T_day} values below 0.5, a highly effective approach is to equate GHI with DHI using the 'GeD' interpolation technique proposed in this work.

Diffuse horizontal irradiance shows less dependence on the clearness index than GHI and DNI. Generally speaking, the use of decomposition models is recommended for replacing missing diffuse data under heavily cloudy and overcast conditions. Root mean square differences of around 20% can be expected for DHI measurements obtained with the band. Bias varies between –5% for overcast conditions and +8% for clear skies versus reference data.

The DNI results are obtained by combining DHI and GHI values and therefore carry uncertainties through from the constituent measurements. Root mean square differences for DNI are highest in the middle of the clearness index range under partly cloudy skies, reaching a peak of about 200 W/m^2. They drop to around 30 W/m^2 under heavily overcast conditions and around 90 W/m^2 for K_{T_day} values of 0.8 or higher. This equates to about 10% of the mean measured DNI.

As part of the PB characterisation study, a second test campaign was run using data from a southern hemisphere ground station in Durban, South Africa. Similar trends were observed in the performance of the system, suggesting that the perforated band does not suffer any meaningful location-dependence. A significant finding is that the uncertainty curves generated as a function of clearness index may shift somewhat when the system operates at lower elevations than the primary test site in Colorado. This is due to the effects of a higher air mass located above sea-level ground stations.

Lastly, the study considered opportunities for deployment of the PB system. A number of conclusions may be drawn in this regard: first, the PB system is a low-cost alternative to optimal measurement schemes and cannot compete against sensors intended to provide research-grade data. Given the uncertainties reported here, one could not recommend the approach in commercial resource assessment studies for evaluating the location and predicted performance of large-scale concentrating solar power plants, for example. Second, there are categories of radiometric project in which higher uncertainties can be tolerated and budgets are constrained, such that alternate measurement schemes at the lower-cost end of the cost-performance continuum become viable.

Based on the uncertainty results of this study, the PB system should be seen as a niche option best suited to applications where single radiometers are required or are already in use. It provides lower uncertainties than hourly averaged satellite-derived measurements and may compete against instruments like the rotating shadow band radiometer and the SPN1 instrument provided that it is deployed in regions where the average daily clearness index is high and cloudy conditions do not predominate. Mostly though, it offers potential value to station owners already operating solid shadow bands in sunny regions, since the cost of retrofitting the perforated band is negligible, and the resulting uncertainties will be suppressed by a lack of stochasticity in the data.

The performance of the band is described in terms of the daily clearness index parameter, therefore a set of monthly averaged daily clearness index maps for the continent was commissioned from a European satellite data supplier. It may be concluded that there are substantial areas of Africa where the daily clearness index exceeds 0.7, and where the PB system might find application. Seasonal variation in the clearness index means that the system may not be deployable permanently in all such locations, but there is potential for it to be used over specific parts of the year to yield better quality radiometric data than would be obtainable from a single pyranometer and other low-cost radiometric schemes.

7.3 Recommendations for future work

As the inaugural study on a novel radiometric scheme, this work was intended to provide the first comprehensive analysis of the perforated shadow band system. It was also intended to lay the groundwork for future improvements to the data processing methodologies described in Chapters 2 to 5. In this regard, the following shortcomings and opportunities for further work have been identified:

Refining interpolation techniques

The extent to which the PB system is able to measure sun strength accurately rests largely on the effectiveness of the interpolation methods used to fill gaps in the fragmented DHI and GHI traces. Although many approaches were evaluated here, including numerical, regression, statistical and radiometric, there are other options that remain to be tested. Notably, the problem of PB data interpolation is similar to that experienced in short-term solar forecasting, which is a subject of growing interest mainly due to concerns about the impact of PV plants on electrical grid stability. In this regard, Voyant et al. (2013) provide a useful review of irradiance time-series modelling approaches. Methodologies such as Kalman filtering, artificial neural networks and Markov chains are gaining popularity in forecasting (Chaabene and Ben Ammar, 2008; Ngoko et al., 2014; Paoli et al., 2010) and could potentially reduce uncertainties in PB-generated data.

Clearness index as controlling parameter in the analysis

In this study clearness index was used as the fundamental parameter on which the uncertainty analysis was based, and for good reason. It is a recognised metric in characterising solar climate and can be calculated at ground stations where a single pyranometer is used, therefore it works well with the perforated band configuration. It has shortcomings, however, since it is a bulk average and therefore cannot characterise intraday variation in irradiance. For example, it may yield the same value for a day with consistent levels of sunshine as for one on which the morning is clear and the afternoon overcast.

Since adaptive interpolation has been shown to be effective, it would be helpful if the controlling parameter used in deploying interpolation schemes carried more information about the stochasticity present in the data before allocating a method. The clearness index parameter does this to some extent, but it is only weakly correlated with stochasticity and is therefore limited. Improvements to the AIS concept are likely through better definition of underlying data structural types, for example through correlation of stochasticity with additional parameters beyond K_{T_day}. The use of sunshine hours derived from Campbell-Stokes recorders offers potential but would require additional sensors on site. Better prospects include the morphological methods and structuring classification of Gastón-Romeo et al. (2011) that seek to characterise the intraday dynamics of irradiance, and the fractal analysis proposed by Harrouni (2008). If better characterisation of stochasticity is possible, it is likely that the interpolation results will improve and yield lower uncertainties for DHI and GHI data.

Lower cost sensor

The perforated band setup employs a PSP thermopile radiometer which is in common use, but far cheaper sensors are available. For example, a perforated shadow band could be paired with a LI-200 silicon sensor, lowering the cost of the installation. This would require a repeat of the ray-tracing analysis to update the model of pyranometer exposure, but is a worthwhile avenue of future research.

Cost versus performance analysis of radiometric schemes

This study emphasised the technical performance of the PB system, but there is scope for further investigation of the economics of broadband radiometry and the role of low-cost schemes, like the perforated band system. More generally, work is needed to systematise the selection and configuration of radiometric sensors available on the cost-versus-performance spectrum. What is required by developers of ground stations is a robust methodology that accounts for data quality, budgetary constraints, the range of data required, temporal resolution, spatial coverage and integration with existing networks.

REFERENCES

Alados-Arboledas, L., Batlles, F.J. and Olmo, F.J. 1995. Solar radiation resource assessment by means of silicon cells. *Solar Energy*, 54, 183-191.

Alados, I. and Alados-Arboledas, L. 1999. Direct and diffuse photosynthetically active radiation: measurements and modelling. *Agricultural and Forest Meteorology*, 93, 27-38.

Ammonit. 2014. *Specification of solar irradiance sensors*. http://www.ammonit.com/en/products/sensors/solar-sensors-pyranometers (accessed on 14 March 2014).

ASHRAE. 1972. Handbook of Fundamentals. American Society of Heating, Refrigerating and Air-Conditioning Engineers, Inc, Atlanta, GA.

Batlles, F.J., Olmo, F.J. and Alados-Arboledas, L. 1995. On shadowband correction methods for diffuse irradiance measurements. *Solar Energy*, 54, 105-114.

Batlles, F.J., Rubio, M.A., Tovar, J., Olmo, F.J. and Alados-Arboledas, L. 2000. Empirical modeling of hourly direct irradiance by means of hourly global irradiance. *Energy*, 25, 675-688.

Bird, R.E. and Hulstrom, R.L. 1981. A simplified clear sky model for direct and diffuse insolation on horizontal surfaces. SERI/TR-642-761, Solar Energy Research Institute, Golden.

Boland, J., Ridley, B. and Brown, B. 2008. Models of diffuse solar radiation. *Renewable Energy*, 33, 575-584.

Bosch, J.L., Batlles, F.J., Zarzalejo, L.F. and López, G. 2010. Solar resources estimation combining digital terrain models and satellite images techniques. *Renewable Energy*, 35, 2853-2861.

Box, G.E.P. and Jenkins, G.M. 1976. *Time series analysis: forecasting and control*. Holden-Day.

British Petroleum. 2013. *Energy outlook.* http://www.bp.com/en/global/corporate/about-bp/energy-economics/energy-outlook.html (accessed on 13 March 2014).

Brooks, M.J. 2010. Performance characteristics of a perforated shadow band under clear sky conditions. *Solar Energy*, 84, 2179-2194.

Brooks, M.J., Braden, S. and Myers, D.R. 2007. Passive separation of global irradiance into direct normal and diffuse components. In: *SPIE Optics and Photonics*. D.R. Myers (ed). SPIE, San Diego.

Brooks, M.J., du Clou, S., van Niekerk, J.L., Gauche, P., Leonard, C., Mouzouris, M.J., Meyer, A.J., van der Westhuizen, N., van Dyk, E.E. and Vorster, F. 2015. SAURAN: A new resource for solar radiometric data in Southern Africa. *Journal of Energy in Southern Africa*, 26, 2-10.

Brooks, M.J. and Harms, T.M. 2005. Development of STARlab: The Solar Thermal Applications Research Laboratory. In: *Solar World Congress*. D.Y. Goswami (ed). American Solar Energy Society, Orlando.

Brooks, M.J. and Roberts, L.W. 2009. Establishment of a broadband radiometric ground station on the South African east coast. In: *SPIE Optics and Photonics*. B.K. Tsai (ed). SPIE, San Diego.

Brooks, M.J. and Roberts, L.W. 2010. A data processing algorithm for the perforated shadow band incorporating a ray trace model of pyranometer exposure. In: *SPIE Optics and Photonics*. N.G. Dhere, J.H. Wohlgemuth and K. Lynn (eds). SPIE, San Diego.

Brooks, M.J., von Backström, T.W. and van Dyk, E.E. 2014. On the replacement of missing data in radiometric time series of high temporal resolution. In: *2nd Southern African Solar Energy Conference (SASEC)*, Port Elizabeth.

Bush, B.C., Valero, F.P.J., Simpson, A.S. and Bignone, L. 2000. Characterization of thermal effects in pyranometers: a data correction algorithm for improved measurement of surface insolation. *Journal of Atmospheric and Oceanic Technology*, 17, 165-175.

Chaabene, M. and Ben Ammar, M. 2008. Neuro-fuzzy dynamic model with Kalman filter to forecast irradiance and temperature for solar energy systems. *Renewable Energy*, 33, 1435-1443.

Ciolkosz, D. 2009. SASRAD: An hourly-timestep solar radiation database for South Africa. *Journal of Energy in Southern Africa*, 20, 25-34.

Craggs, C., Conway, E. and Pearsall, N.M. 1999. Stochastic modelling of solar irradiance on horizontal and vertical planes at a northerly location. *Renewable Energy*, 18, 445-463.

CSP Today. 2015. http://social.csptoday.com/tracker/projects (accessed on 2 February 2015).

Dazhi, Y., Jirutitijaroen, P. and Walsh, W.M. 2012. Hourly solar irradiance time series forecasting using cloud cover index. *Solar Energy*, 86, 3531-3543.

De Boor, C. 1978. *A Practical Guide to Splines*. Springer-Verlag.

de Castro, C., Mediavilla, M., Miguel, L.J. and Frechoso, F. 2013. Global solar electric potential: A review of their technical and sustainable limits. *Renewable and Sustainable Energy Reviews*, 28, 824-835.

de Gruijl, F.R. 1999. Skin cancer and solar radiation. *European Journal of Cancer*, 35, 2003-2009.

De Oliveira, A.P., Machado, A.J. and Escobedo, J.F. 2002. A new shadow ring for measuring diffuse solar radiation at the surface. *Journal of Atmospheric and Oceanic Technology*, 19, 698-708.

Delta-T Devices Ltd. 2006. Technical Manual for the Sunshine Pyranometer type SPN1. Cambridge, UK.

Delta-T Devices Ltd. 2007. User Manual for the Sunshine Pyranometer Type SPN1. Cambridge, UK.

Department of Energy. 2013. Integrated resource plan for electricity: update report. South African Government.

Diabate, L., Blanc, P. and Wald, L. 2004. Solar radiation climate in Africa. *Solar Energy*, 76, 733-744.

Drummond, A.J. 1956. On the measurement of sky radiation. 551.508.23, South African Weather Bureau, Pretoria.

Drummond, A.J. 1964. Comments on sky radiation measurement and correction. *Journal of Applied Meteorology*, 3, 810-811.

Duchon, C.E. and O'Malley, M.S. 1998. Estimating cloud type from pyranometer observations. *Journal of Applied Meteorology*, 38, 132-141.

Duffie, J.A. and Beckman, W.A. 1991. *Solar Engineering of Thermal Processes*. Wiley, New York.

Dutton, E.G., Michalsky, J., Stoffel, T., Forgan, B.W., Hickey, J.R., Nelson, D.W., Alberta, T.L. and Reda, I. 2001. Measurement of broadband diffuse solar irradiance using current commercial instrumentation with a correction for thermal offset errors. *Journal of Atmospheric and Oceanic Technology*, 18, 297-314.

Erbs, D.G., Klein, S.A. and Duffie, J.A. 1982. Estimation of the diffuse radiation fraction for hourly, daily and monthly-average global radiation. *Solar Energy*, 28, 293-302.

Espinar, B., Blanc, P., Gschwind, B., Menard, L., Wey, E., Thomas, C. and Saboret, L. 2012. HelioClim-3: a near-real time and long term surface solar irradiance database.

Fluri, T.P. 2009. The potential of concentrating solar power in South Africa. *Energy Policy*, 37, 5075-5080.

Fritsch, F.N. and Carlson, R.E. 1980. Monotone piecewise cubic interpolation. *SIAM Journal on Numerical Analysis*, 17, 238-246.

Frohlich, C. and Lean, J. 2004. Solar radiative output and its variability: Evidence and mechanisms. *Astronomy and Astrophysics Review*, 12, 273-320.

Gastón-Romeo, M., Leon, T., Mallor, F. and Ramírez-Santigosa, L. 2011. A Morphological Clustering Method for daily solar radiation curves. *Solar Energy*, 85, 1824-1836.

GeoModel Solar. 2014. Personal communication.

Giglmayr, S., Brent, A., Gauche, P. and Fechner, H. 2014. Utility-scaled PV power and energy outlook for South Africa in 2015. In: *2nd Southern African Solar Energy Conference (SASEC)*, Port Elizabeth.

Glasbey, C.A., Graham, R. and Hunter, A.G.M. 2001. Spatio-temporal variability of solar energy across a region: a statistical modelling approach. *Solar Energy*, 70, 373-381.

Gueymard, C. 2004. The sun's total and spectral irradiance for solar energy applications and solar radiation models. *Solar Energy*, 76, 423-453.

Gueymard, C. 2009. Direct and indirect uncertainties in the prediction of tilted irradiance for solar engineering applications. *Solar Energy*, 83, 432-444.

Gueymard, C. 2012. Clear-sky irradiance predictions for solar resource mapping and large-scale applications: Improved validation methodology and detailed performance analysis of 18 broadband radiative models. *Solar Energy*, 86, 2145-2169.

Gueymard, C. and Myers, D.R. 2008a. Solar radiation measurement: Progress in radiometry for improved modeling. In: *Modelling solar radiation at the Earth's surface*. V. Badescu (ed). Springer-Verlag.

Gueymard, C. and Myers, D.R. 2008b. Validation and ranking methodologies for solar radiation models. In: *Modelling solar radiation at the Earth's surface*. V. Badescu (ed). Springer-Verlag.

Gueymard, C. and Myers, D.R. 2009. Evaluation of conventional and high-performance routine solar radiation measurements for improved solar resource, climatological trends, and radiative modeling. *Solar Energy*, 83, 171-185.

Gueymard, C.A. 2001. Parameterized transmittance model for direct beam and circumsolar spectral irradiance. *Solar Energy*, 71, 325-346.

Gueymard, C.A. 2003a. Direct solar transmittance and irradiance predictions with broadband models. Part I: detailed theoretical performance assessment. *Solar Energy*, 74, 355-379.

Gueymard, C.A. 2003b. Direct solar transmittance and irradiance predictions with broadband models. Part II: validation with high-quality measurements. *Solar Energy*, 74, 381-395.

Gueymard, C.A. 2008. REST2: High-performance solar radiation model for cloudless-sky irradiance, illuminance, and photosynthetically active radiation – Validation with a benchmark dataset. *Solar Energy*, 82, 272-285.

Gueymard, C.A. and Wilcox, S.M. 2011. Assessment of spatial and temporal variability in the US solar resource from radiometric measurements and predictions from models using ground-based or satellite data. *Solar Energy*, 85, 1068-1084.

Harrouni, S. 2008. Fractal classification of typical meteorological days from global solar irradiance: Application to five sites of different climates. In:

Modeling solar radiation at the Earth's surface. V. Badescu (ed). Springer-Verlag, pp. 29-53.

Hickey, J.R., Frieden, R.G., Griffin, F.J., Cone, S.A., Maschhoff, R.H. and Gniady, J. 1977. The self-calibrating sensor of the Eclectic Satellite Pyrheliometer (ESP) program. In: *International Solar Energy Society Annual Meeting* Orlando.

Hottel, H.C. 1976. A simple model for estimating the transmittance of direct solar radiation through clear atmospheres. *Solar Energy*, 18, 129-134.

Ineichen, P. 2006. Comparison of eight clear sky broadband models against 16 independent data banks. *Solar Energy*, 80, 468-478.

Ineichen, P. 2008. Comparison and validation of three global-to-beam irradiance models against ground measurements. *Solar Energy*, 82, 501-512.

Ineichen, P., Gremaud, J.M., Guisan, O. and Mermoud, A. 1983. Study of the corrective factor involved when measuring the diffuse solar radiation by use of the ring method. *Solar Energy*, 31, 113-117.

International Energy Agency. 2013. *Renewable Energy Outlook*. http://www.worldenergyoutlook.org/publications/weo-2013/ (accessed on 13 March 2014).

Jacovides, C.P., Tymvios, F.S., Assimakopoulos, V.D. and Kaltsounides, N.A. 2006. Comparative study of various correlations in estimating hourly diffuse fraction of global solar radiation. *Renewable Energy*, 31, 2492-2504.

Joint Committee for Guides in Metrology. 2008. Evaluation of measurement data - Guide to the expression of uncertainty in measurement JCGM 100. GUM 1995 with minor corrections.

Journée, M. and Bertrand, C. 2011. Quality control of solar radiation data within the RMIB solar measurements network. *Solar Energy*, 85, 72-86.

Kandel, R. and Viollier, M. 2010. Observations of the Earth's radiation budget from space. *Comptes Rendus Geoscience*, 342, 286-300.

King, D.L., Boyson, W.E., Hansen, B.R. and Bower, W.I. 1998. Improved accuracy for low-cost solar irradiance sensors. In: *2nd World Conference and Exhibition on Photovoltaic Solar Energy Conversion*, Vienna.

Kipp & Zonen. 2014. *Solar energy guide*. http://www.kippzonen.com/Product/13/CMP-11-Pyranometer (accessed on 13 March 2014).

Kirk, T. 2013. Personal communication.

Kopp, G. and Lean, J.L. 2011. A new, lower value of total solar irradiance: Evidence and climatic significance. *Geophysical Research Letters*, 38, 1-7.

Kreyszig, E. 1988. *Advanced Engineering Mathematics*. 6th edn. John Wiley & Sons, New York.

Kudish, A.I. and Evseev, E.G. 2008. The assessment of four different correction models applied to the diffuse radiation measured with a shadow ring using global and normal beam radiation measurements for Beer Sheva, Israel. *Solar Energy*, 82, 144-156.

Kunene, K.R. 2011. *Broadband solar radiometric measurements in the greater Durban area.* MScEng Thesis, University of KwaZulu-Natal.

Kunene, K.R., Brooks, M.J., Roberts, L.W. and Zawilska, E. 2013. Introducing GRADRAD: The greater Durban radiometric network. *Renewable Energy,* 49, 259-262.

Kunene, K.R., Brooks, M.J. and Zawilska, E. 2012. Performance of solar radiometric decomposition models for Durban, South Africa. In: *1st Southern African Solar Energy Conference (SASEC),* Stellenbosch.

Lanini, F. 2010. *Division of global radiation into direct radiation and diffuse radiation.* Master's Thesis, University of Bern.

LeBaron, B.A., Michalsky, J.J. and Perez, R. 1990. A simple procedure for correcting shadowband data for all sky conditions. *Solar Energy*, 44, 249-256.

Leloux, J., Lorenzo, E., Garcia-Domingo, B., Aquilera, J. and Gueymard, C. 2014. A bankable method of assessing the performance of a CPV plant. *Applied Energy,* 118, 1-11.

Lysko, M.D. 2006. *Measurement and models of solar irradiance.* PhD Thesis, Norwegian University of Science and Technology.

Marion, W. and George, R. 2001. Calculation of solar radiation using a methodology with worldwide potential. *Solar Energy*, 71, 275-283.

Matsuo, Y., Yanagisawa, A. and Yamashita, Y. 2013. A global energy outlook to 2035 with strategic considerations for Asia and Middle East energy supply and demand interdependencies. *Energy Strategy Reviews*, 2, 79-91.

Maxwell, E.L. 1987. A quasi-physical model for converting hourly global horizontal to direct normal insolation. SERI/TR-215-3087, Solar Energy Research Institute, Golden.

Medhaug, I., Olseth, J.A. and Reuder, J. 2009. UV radiation and skin cancer in Norway. *Journal of Photochemistry and Photobiology B: Biology*, 96, 232-241.

Michalsky, J., Dutton, E.G., Nelson, D.W., Wendell, J., Wilcox, S.M., Andreas, A., Gotseff, P., Myers, D.R., Reda, I., Stoffel, T., Behrens, K., Carlund, T., Finsterle, W. and Halliwell, D. 2011. Am extensive comparison of commercial pyrheliometers under a wide range of routine observing conditions. *Journal of Atmospheric and Oceanic Technology*, 28, 752-766.

Michalsky, J., Dutton, E.G., Rubes, M., Nelson, D.W., Stoffel, T., Wesley, M., Splitt, M. and DeLuisi, J. 1999. Optimal measurement of surface shortwave irradiance using current instrumentation. *Journal of Atmospheric and Oceanic Technology*, 16, 55-69.

Michalsky, J.J., Berndt, J.L. and Schuster, G.J. 1986. A microprocessor-based rotating shadowband radiometer. *Solar Energy*, 36, 465-470.

Miller, D.G., Rivington, M., Matthews, K.B., Buchan, K. and Bellocchi, G. 2008. Testing the spatial applicability of the Johnson–Woodward method for estimating solar radiation from sunshine duration data. *Agricultural and Forest Meteorology*, 148, 466-480.

Moler, C. 2004. *Numerical computing with MATLAB*. Society for Industrial and Applied Mathematics.

Muneer, T. and Younes, S. 2006. The all-sky meteorological radiation model: proposed improvements. *Applied Energy*, 83, 436-450.

Muneer, T. and Zhang, X. 2002. A new method for correcting shadow band diffuse irradiance data. *Journal of Solar Energy Engineering*, 124, 34-43.

Muzathik, A.M., Bin Wan Nik, W.M.N., Bin Samo, K. and Ibrahim, M.Z. 2010. Reference solar radiation year and some climatology aspects of east coast of west Malaysia. *American Journal of Engineering and Applied Sciences*, 3, 293-299.

Myers, D.R. 2005. Solar radiation modeling and measurements for renewable energy applications: data and model quality. *Energy*, 30, 1517-1531.

Myers, D.R. 2010a. Personal communication.

Myers, D.R. 2010b. Seasonal variation in the frequency distributions of differences between radiometric data for solar resource assessment applications. In: *39th ASES National Solar Conference*, Phoenix, Arizona.

Myers, D.R. 2013. *Solar Radiation: Practical Modeling for Renewable Energy Applications*. Taylor and Francis Group.

Myers, D.R., Stoffel, T., Reda, I., Wilcox, S.M. and Andreas, A. 2002. Recent progress in reducing the uncertainty in and improving pyranometer calibrations. *ASME Journal of Solar Energy Engineering*, 124, 44-50.

Myers, D.R. and Wilcox, S.M. 2009. Relative accuracy of 1-minute and daily total solar radiation data for 12 global and 4 direct beam solar radiometers. In: *American Solar Energy Society Annual Conference*. National Renewable Energy Laboratory, Buffalo.

Ngoko, B.O., Sugihara, H. and Funaki, T. 2014. Synthetic generation of high temporal resolution solar radiation data using Markov models. *Solar Energy*, 103, 160-170.

NREL. 2014. *Baseline Measurement System.* http://www.nrel.gov/midc/srrl_bms/ (accessed on multiple dates).

Oliphant, A.J., Grimmond, C.S.B., Schmid, H.P. and Wayson, C.A. 2006. Local-scale heterogeneity of photosynthetically active radiation (PAR), absorbed PAR and net radiation as a function of topography, sky conditions and leaf area index. *Remote Sensing of Environment*, 103, 324-337.

Orgill, J.F. and Hollands, K.G.T. 1977. Correlation equation for hourly diffuse radiation on a horizontal surface. *Solar Energy*, 19, 357 - 399.

Orsini, A., Tomasi, C., Calzolari, F., Nardino, M., Cacciari, A. and Georgiadis, T. 2002. Cloud cover classification through simultaneous ground-based measurements of solar and infrared radiation. *Atmospheric Research*, 61, 251-275.

Pankratz, A. 1983. *Forecasting with univariate Box-Jenkins models: Concepts and cases*. John Wiley & Sons.

Paoli, C., Voyant, C., Muselli, M. and Nivet, M.-L. 2010. Forecasting of preprocessed daily solar radiation time series using neural networks. *Solar Energy*, 84, 2146-2160.

Parisi, A.V., Wong, J.C.F. and Randall, C. 1998. Simultaneous assessment of photosynthetically active and ultraviolet solar radiation. *Agricultural and Forest Meteorology*, 92, 97-103.

Perez, R., Ineichen, P., Maxwell, E.L., Seals, R.D. and Zelenka, A. 1992. Dynamic global-to-direct irradiance conversion models. *ASHRAE Transactions Research Series*, 98, 354-369.

Perez, R., Ineichen, P., Seals, R., Michalsky, J. and Stewart, R. 1990a. Modeling daylight availability and irradiance components from direct and global irradiance. *Solar Energy*, 44, 271-289.

Perez, R., Ineichen, P., Seals, R. and Zelenka, A. 1990b. Making full use of the clearness index for parameterizing hourly insolation conditions. *Solar Energy*, 45, 111-114.

Perez, R., Seals, R., Zelenka, A. and Ineichen, P. 1990c. Climatic evaluation of models that predict hourly direct irradiance from hourly global irradiance: Prospects for performance improvements. *Solar Energy*, 44, 99-108.

Pitz-Paal, R. and Hoyer-Klick, C. 2010. Introduction to solar resource measurements. German Aerospace Center Institute of Technical Thermodynamics.

PMOD-WRC. 2010. Annual Report. Physikalisch-Meteorologisches Observatorium Davos und Weltstrahlungszentrum, Davos.

Reda, I. 2010. Personal communication.

Reda, I. 2011. Method to calculate uncertainties in measuring shortwave solar irradiance using thermopile and semiconductor solar radiometers. NREL/TP-3B10-52194, National Renewable Energy Laboratory, Golden.

Reda, I. and Andreas, A. 2008. Solar position algorithm for solar radiation applications. NREL/TP-560-34302, National Renewable Energy Laboratory, Golden.

Reda, I., Hickey, J.R., Long, C., Myers, D.R., Stoffel, T., Wilcox, S.M., Michalsky, J., Dutton, E.G. and Nelson, D.W. 2005. Using a blackbody to calculate net longwave responsivity of shortwave solar pyranometers to correct for their offset error during outdoor calibration using the component sum method. *Journal of Atmospheric and Oceanic Technology*, 22, 1531-1540.

Reda, I., Myers, D.R. and Stoffel, T. 2008. Uncertainty estimate for the outdoor calibration of solar pyranometers: A metrologist perspective. *NCSLI Measure: The Journal of Measurement Science*, 3, 58-66.

Reda, I., Stoffel, T. and Myers, D.R. 2003. A method to calibrate a solar pyranometer for measuring reference diffuse irradiance. *Solar Energy*, 74, 130-112.

Rehman, S. and Ghori, S.G. 2000. Spatial estimation of global solar radiation using geostatistics. *Renewable Energy*, 21, 583-605.

Reikard, G. 2009. Predicting solar radiation at high resolutions: A comparison of time series forecasts. *Solar Energy*, 83, 342-349.

Reindl, D.T., Beckman, W.A. and Duffie, J.A. 1990. Diffuse fraction correlations. *Solar Energy*, 45, 1-7.

Ridley, B., Boland, J. and Lauret, P. 2010. Modelling of diffuse solar fraction with multiple predictors. *Renewable Energy*, 35, 478-483.

Santos, J.M., Pinazo, J.M. and Canada, J. 2003. Methodology for generating daily clearness index values Kt starting from the monthly average daily value KbarT. Determining the daily sequence using stochastic models. *Renewable Energy*, 28, 1523-1544.

Singh, O.P., Srivastava, S.K. and Gaur, A. 1996. Empirical relationship to estimate global radiation from hours of sunshine. *Energy Conversion Management*, 37, 501-504.

Skartveit, A. and Olseth, J.A. 1987. A model for the diffuse fraction of hourly global radiation. *Solar Energy*, 38, 271-274.

Skartveit, A., Olseth, J.A. and Tuft, M.E. 1998. An hourly diffuse fraction model with correction for variability and surface albedo. *Solar Energy*, 63, 173-183.

SoDa. 2013. *Solar Radiation Data*. http://www.soda-is.com/eng/helioclim/helioclim3_uncertainty_eng.html#threshold200 (accessed on 28 September 2013).

SolarGIS. 2013. SolarGIS version 1.8: Specifications of solar radiation and meteo database.

Sproul, A.B. 2007. Derivation of the solar geometric relationships using vector analysis. *Renewable Energy*, 32, 1187-1205.

Stine, W.B. and Harrigan, R.W. 1985. *Solar energy fundamentals and design: with computer applications*. John Wiley & Sons, New York.

Stoffel, T., Renne, D., Myers, D.R., Wilcox, S.M., Sengupta, M., George, R. and Turchi, C. 2010. Best practices handbook for the collection and use of solar resource data. NREL/TP-550-47465.

Tapakis, R. and Charalambides, A.G. 2013. Equipment and methodologies for cloud detection and classification: A review. *Solar Energy*, 95, 392-430.

Tomson, T., Russak, V. and Kallis, A. 2008. Dynamic behavior of solar radiation. In: *Modelling solar radiation at the Earth's surface*. Viorel Badescu (ed). Springer-Verlag, pp. 257-281.

Torres, J.L., De Blas, M., Garcia, A. and de Francisco, A. 2010. Comparative study of various models in estimating hourly diffuse solar irradiance. *Renewable Energy*, 35, 1325-1332.

Tovar-Pescador, J. 2008. Modelling the statistical properties of solar radiation and proposal of a technique based on Boltzmann statistics. In: *Modelling solar radiation at the Earth's surface*. V. Badescu (ed). Springer-Verlag, pp. 55-91.

Trenberth, K.E., Fasullo, J.T. and Kiehl, J.T. 2009. Earth's global energy budget. *Bull. Am. Meteorol. Soc.*, 90, 311-323.

US Department of Energy. 2013. ARM Climate research facility management plan.

Utrillas, M.P., Marín, M.J., Esteve, A.R., Estellés, V., Gandía, S., Núnez, J.A. and Martínez-Lozano, J.A. 2013. Ten years of measured UV Index from the Spanish UVB Radiometric Network. *Journal of Photochemistry and Photobiology B: Biology*, 125, 1-7.

Viebahn, P., Lechon, Y. and Trieb, F. 2011. The potential role of concentrated solar power (CSP) in Africa and Europe—A dynamic assessment of technology development, cost development and life cycle inventories until 2050. *Energy Policy*, 39, 4420-4430.

Vignola, F. 1999. Solar Cell Based Pyronometers: Evaluation of the Diffuse Response.

Vignola, F., Michalsky, J. and Stoffel, T. 2012. *Solar and Infrared Radiation Measurements* CRC Press, Boca Raton.

Voyant, C., Paoli, C., Muselli, M. and Nivet, M.-L. 2013. Multi-horizon solar radiation forecasting for Mediterranean locations using time series models. *Renewable and Sustainable Energy Reviews*, 28, 44-52.

Wilcox, S.M. and Myers, D.R. 2008. Evaluation of radiometers in full-time use at the National Renewable Energy Laboratory Solar Radiation Research Laboratory. NREL/TP-550-44627.

Wilcox, S.M. and Stoffel, T. 2009. Solar Resource and Meteorological Assessment Project (SOLRMAP) solar and meteorological station options: configurations and specifications. National Renewable Energy Laboratory, Golden, CO.

World Meteorological Organization. 1987. *International Cloud Atlas: Vol II*. World Meteorological Organization, Montreaux.

Yang, K., Huang, G.W. and Tamai, N. 2001. A hybrid model for estimating global solar radiation. *Solar Energy*, 70, 13-22.

Zawilska, E. and Brooks, M.J. 2011. An assessment of the solar resource for Durban, South Africa. *Renewable Energy*, 36, 3433-3438.

Zawilska, E., Brooks, M.J. and Meyer, A.J. 2012. A review of solar resource assessment initiatives in South Africa: the case for a national network. In: *The World Renewable Energy Forum,* Colorado.

Zelenka, A., Perez, R., Seals, R. and Renne, D. 1999. Effective accuracy of satellite-derived hourly irradiances. *Theoreatical and Applied Climatology*, 62, 199-207.

Zhang, T., Stackhouse Jr, P.W., Gupta, S.K., Cox, S.J., Colleen Mikovitz, J. and Hinkelman, L.M. 2013. The validation of the GEWEX SRB surface shortwave flux data products using BSRN measurements: A systematic quality control, production and application approach. *Journal of Quantitative Spectroscopy and Radiative Transfer*, 122, 127-140.

APPENDIX A: Reference instrument histories

Tables A-1 to A-3 provide details of the sensors used over the course of the PB test programme at NREL's Solar Radiation Research Laboratory (NREL, 2014).

Table A-1: Instrument history of NREL SRRL reference sensors for GHI.

Kipp & Zonen CM22 (GHI) serial number	Sensitivity [W/m^2/mV]	Date installed	Date removed
10034	91.776	05/31/2006	06/13/2007
10046	107.52	06/13/2007	05/23/2008
10034	91.660	05/23/2008	07/06/2009
10046	107.19	07/06/2009	06/30/2010
10034	91.905	06/30/2010	-
10034	92.018	07/27/2010	(recalibration)
10034	91.871	05/05/2011	(recalibration)
10034	91.630	05/04/2012	(recalibration)

Table A-2: Instrument history of NREL SRRL reference sensors for DHI.

Kipp & Zonen CM22 (DHI) serial number	Sensitivity [W/m^2/mV]	Date installed	Date removed
10046	108.45	08/04/2001	05/27/2005
10034	91.673	05/27/2005	05/31/2006
10046	107.72	05/31/2006	06/13/2007
10034	91.704	06/13/2007	05/23/2008
10046	107.56	05/23/2008	07/06/2009
10034	91.905	07/06/2009	06/30/2010
10046	107.19	06/30/2010	05/26/2011
100174	102.92	05/26/2011	06/07/2012
10046	107.61	06/07/2012	08/27/2013

Table A-3: Instrument history of NREL SRRL reference sensors for DNI.

Kipp & Zonen CH1 (DNI) serial number	Sensitivity [W/m^2/mV]	Date installed	Date removed
10256	91.797	08/04/2001	05/27/2010
80033	111.82	05/27/2010	08/02/2010
10256	91.927	08/02/2010	-
10256	92.472	05/05/2011	(recalibration)
10256	92.241	05/04/2012	(recalibration)

APPENDIX B: Extract of NREL perforated shadow band maintenance log

Routine maintenance was performed on the PB system by staff of the Solar Radiation Research Laboratory throughout this study to ensure data quality. All actions were logged and are available online through NREL's Baseline Measurement System website. An extract of the log from June 2010 is given in Figure B-1, indicating the date and time of each inspection, the state of the instrument and band, the shading pattern observed, the name of the NREL staff member responsible for the inspection and the action taken. The NREL designation for the perforated band is *ZEBRA*, derived from 'Zonal Exposure to BRoadband RAdiation'.

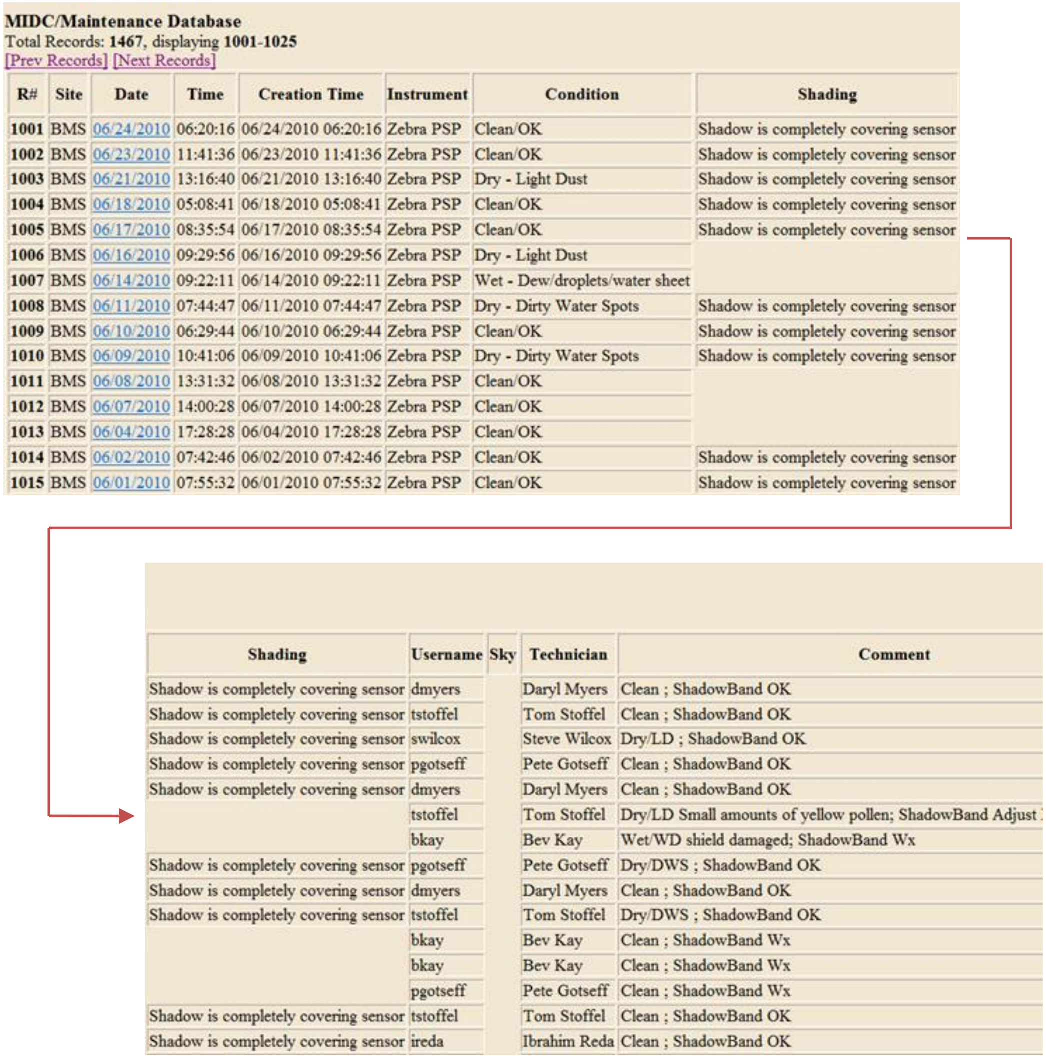

MIDC/Maintenance Database
Total Records: **1467**, displaying **1001-1025**
[Prev Records] [Next Records]

R#	Site	Date	Time	Creation Time	Instrument	Condition	Shading	Username	Sky	Technician	Comment
1001	BMS	06/24/2010	06:20:16	06/24/2010 06:20:16	Zebra PSP	Clean/OK	Shadow is completely covering sensor	dmyers		Daryl Myers	Clean ; ShadowBand OK
1002	BMS	06/23/2010	11:41:36	06/23/2010 11:41:36	Zebra PSP	Clean/OK	Shadow is completely covering sensor	tstoffel		Tom Stoffel	Clean ; ShadowBand OK
1003	BMS	06/21/2010	13:16:40	06/21/2010 13:16:40	Zebra PSP	Dry - Light Dust	Shadow is completely covering sensor	swilcox		Steve Wilcox	Dry/LD ; ShadowBand OK
1004	BMS	06/18/2010	05:08:41	06/18/2010 05:08:41	Zebra PSP	Clean/OK	Shadow is completely covering sensor	pgotseff		Pete Gotseff	Clean ; ShadowBand OK
1005	BMS	06/17/2010	08:35:54	06/17/2010 08:35:54	Zebra PSP	Clean/OK	Shadow is completely covering sensor	dmyers		Daryl Myers	Clean ; ShadowBand OK
1006	BMS	06/16/2010	09:29:56	06/16/2010 09:29:56	Zebra PSP	Dry - Light Dust		tstoffel		Tom Stoffel	Dry/LD Small amounts of yellow pollen; ShadowBand Adjust
1007	BMS	06/14/2010	09:22:11	06/14/2010 09:22:11	Zebra PSP	Wet - Dew/droplets/water sheet		bkay		Bev Kay	Wet/WD shield damaged; ShadowBand Wx
1008	BMS	06/11/2010	07:44:47	06/11/2010 07:44:47	Zebra PSP	Dry - Dirty Water Spots	Shadow is completely covering sensor	pgotseff		Pete Gotseff	Dry/DWS ; ShadowBand OK
1009	BMS	06/10/2010	06:29:44	06/10/2010 06:29:44	Zebra PSP	Clean/OK	Shadow is completely covering sensor	dmyers		Daryl Myers	Clean ; ShadowBand OK
1010	BMS	06/09/2010	10:41:06	06/09/2010 10:41:06	Zebra PSP	Dry - Dirty Water Spots	Shadow is completely covering sensor	tstoffel		Tom Stoffel	Dry/DWS ; ShadowBand OK
1011	BMS	06/08/2010	13:31:32	06/08/2010 13:31:32	Zebra PSP	Clean/OK		bkay		Bev Kay	Clean ; ShadowBand Wx
1012	BMS	06/07/2010	14:00:28	06/07/2010 14:00:28	Zebra PSP	Clean/OK		bkay		Bev Kay	Clean ; ShadowBand Wx
1013	BMS	06/04/2010	17:28:28	06/04/2010 17:28:28	Zebra PSP	Clean/OK		pgotseff		Pete Gotseff	Clean ; ShadowBand Wx
1014	BMS	06/02/2010	07:42:46	06/02/2010 07:42:46	Zebra PSP	Clean/OK	Shadow is completely covering sensor	tstoffel		Tom Stoffel	Clean ; ShadowBand OK
1015	BMS	06/01/2010	07:55:32	06/01/2010 07:55:32	Zebra PSP	Clean/OK	Shadow is completely covering sensor	ireda		Ibrahim Reda	Clean ; ShadowBand OK

Figure B-1: Extract from NREL's perforated band maintenance log for June 2010 (NREL, 2014).

APPENDIX C: Data file format

The radiometric data files used in datasets #1 and #2 include three types of information: i) text headers in row 1; ii) information used to process the file in rows 2 and 3 and iii) measurement data at 1 minute intervals from row 4 onwards. A sample is given in Table C-1 below.

With respect to the measurement data, columns A to K are obtained from the NREL Baseline Measurement System archive, while columns M to R are generated by the NREL Solar Position Algorithm (Reda and Andreas, 2008) and comprise geometric data needed for implementation of the ray trace model. An explanation of the contents of the spread sheet for length of N_s rows is given in Table C-2. Sample files from both datasets are available on request from the author.

Table C-1: Extract from 18-column NREL data file for 26 November 2011 in spread sheet format.

	A	**B**	**C**	**D**	**E**	**F**	**G**	**H**	**I**
1	DATE	MST	Global CM22 Vent [W/m^2]	Global Extraterrestrial (calc) [W/m^2]	Direct CH1 [W/m^2]	Direct Extraterrestrial (calc) [W/m^2]	Diffuse CM22 Vent [W/m^2]	Zebra PSP [W/m^2]	Atmos Net Infrared PIRs [W/m^2]
2	330	144				116.68	1.027		
3	39.74	440	482.0	0.76	969.2	0.000635	52.4		
4	40143	07:01	7.24	3.64	0.00	1403.6290	5.10	2.67	-95.07
5	2009/11/26	07:02	8.84	7.27	0.00	1403.6290	5.63	3.10	-96.20
6	2009/11/26	07:03	10.19	10.93	0.00	1403.6290	6.16	3.61	-94.62
7	2009/11/26	07:04	11.23	14.61	0.00	1403.6310	6.68	3.86	-94.22

	J	**K**	**L**	**M**	**N**	**O**	**P**	**Q**	**R**
1	Zenith Angle [degrees]	Azimuth Angle [degrees]	TO [W/m^2]	Date	Time	Topocentric zenith angle [degrees]	Top. azimuth angle (westward from S) [degrees]	Topocentric local hour angle [degrees]	Hour angle (-E/+W) [degrees]
2									
3									
4	89.85	117.56	-7.04	2009/11/26	07:01:00	89.85	-62.44	288.22	-71.78
5	89.70	117.71	-7.13	2009/11/26	07:02:00	89.70	-62.29	288.47	-71.53
6	89.55	117.87	-7.01	2009/11/26	07:03:00	89.55	-62.13	288.72	-71.28
7	89.40	118.03	-6.98	2009/11/26	07:04:00	89.40	-61.97	288.97	-71.03

Table C-2: Daily data file content for spread sheet of N_s rows.

Cell range	Description	Use
A4:AN_s	Date (C4 is in number format)	Date-stamp
B4:BN_s	Mountain Standard Time	Time-stamp
C4:CN_s	DNI from Kipp and Zonen CH1	Reference DNI
D4:DN_s	Extra-terrestrial GHI (calculated)	Data filter and calculation of k_{tday}
E4:CN_s	DHI from Kipp & Zonen CM22	Reference DHI
F4:FN_s	Extra-terrestrial DNI (calculated)	Data filter
G4:CN_s	GHI from Kipp & Zonen CM22	Reference GHI
H4:HN_s	Eppley PSP under PB	Source of perforated band data
I4:IN_s	Atmospheric net infrared irradiance	Calculation of thermal offset
J4:JN_s	Zenith angle	Solar position
K4:KN_s	Azimuth angle	Solar position
L4:LN_s	Thermal offset (calculated)	Reduce uncertainty in PB data
M4:MN_s	Date	Date-stamp (from SPA; repeat)
N4:NN_s	Mountain Standard Time	Time-stamp (from SPA; repeat)
O4:ON_s	Zenith angle	From SPA; repeat
P4:PN_s	Azimuth angle	From SPA; alternate convention
Q4:QN_s	Hour angle	Ray trace model
R4:RN_s	Hour angle	Alternate convention
A2	Day number	Shadow band correction factor
A3	Geographic latitude	Bird clear sky model
B2:B3	Start and end row for $Z < 70°$	For information
C3, E3, G3	Averages for GHI, DNI and DHI	For information
D3	Daily clearness index, K_{T_day}	For information
F2:F3	Eppley PSP calibration factor and sensitivity factor	Calculation of thermal offset
G2	Shadow band correction factor	Adjust for sky blocking effect

APPENDIX D: Statistical metrics

Standard deviation

Standard deviation (SD) is the square root of the variance, and although similar to RMSD is less commonly used. It permits the expression of confidence intervals of a measurand's estimate about the population mean, and is calculated as follows (Joint Committee for Guides in Metrology, 2008):

$$\mathrm{SD} = \sqrt{\frac{1}{(N-1)}\sum_{i=1}^{N}[E_{mod} - \bar{E}_{meas}]^2} \tag{D-1}$$

For a normally distributed dataset, the SD may be combined with the mean $\bar{E}$ to give the confidence interval of the estimated irradiance, E_{mod}, as follows:

$$E_{mod} = \bar{E}_{mod} + k.SD \tag{D-2}$$

For a normally distributed sample, the confidence intervals of 68%, 95% and 99.7% correspond to k values of 1, 2 and 3 respectively. In this study, the Lilliefors test was performed to determine whether the irradiance data created by the interpolation schemes conformed to a normal distribution. Tests for kurtosis and skewness were also performed.

Expanded uncertainty

Gueymard (2012) uses standard deviation and RMSD to calculate a combined uncertainty, u_c, from which an expanded uncertainty with 95% confidence level for radiometric models can be determined:

$$U_{95} = k_x\sqrt{\mathrm{SD}^2 + \mathrm{RMSD}^2} \tag{D-3}$$

In equation (D-3), k_x is a coverage factor that equals 1.96 for large datasets (Reda, 2011). SD and RMSD are calculated in percentages. The smaller the value of U_{95}, the better the model performs.

APPENDIX E: Additional data: Cloudy sky conditions

Chapter 5 focused on the statistical uncertainty of the best performing PB interpolation schemes, but omitted the results for those that do poorly. As addenda to Tables 5.1, 5.2 and 5.4, Figures E-1 to E-4 provide a qualitative indication of the relative performance of all interpolation schemes tested for DHI, GHI and DNI respectively. The data are taken from dataset #1 and classified according to clearness index in each chart. Uncertainty is given in terms of root mean square difference as a percentage for DHI and GHI, and in [W/m^2] for DNI.

Certain trends are noteworthy. In Figure E-1 the decomposition models, which are grouped to the left of the graph, are effective in generating diffuse horizontal irradiance at low clearness indices as stated in the main text. The gradual rise in their uncertainties as cloud levels decline is noticeable looking towards the rear of the graph.

The low plateau located to the left of centre of the Figure E-1 corresponds to the suppression of uncertainty by the adaptive interpolation schemes, most of which do well across the full range of sky conditions. Most of the ARIMA models perform well throughout but particularly so under clearer conditions.

In Figure E-2, the adaptive schemes once again give rise to a low area on the graph that indicates their good performance in filling data gaps for global horizontal irradiance. To the far left the GeD interpolation technique returns low uncertainties in bins 1 and 2 but loses its effectiveness as K_{T_day} increases.

Figures E-3 and E-4 are representations of the same data, viewed from two sides for readability. For most schemes there is a clear rise in DNI uncertainty over the mid-clearness index bins, with lower values recorded under clear and overcast skies. This was also seen in the ‘hump-back’ shapes of Figures 5.5 and 5.10. As with the GHI results, the adaptive methodology reduces RMSD uncertainty. Since DNI is composed of DHI and GHI data, the B_AIS_Best scheme positioned between B_AIS_20 and 37 represents the results for B_AIS schemes 21 to 28 respectively, given in Table 5.3. These result from the combination of the best DHI and GHI results from each clearness index category and are graphed here as one result per bin, that is B_AIS_21 is B_AIS_Best applied to bin 1, 22 applies to bin 2 and so on. In most cases, the use of the Bird clear sky model (denoted with a C appended to scheme name) reduces uncertainty, although this effect is reduced somewhat for the adaptive schemes that already benefit from the use of better-performing GHI and DHI components.

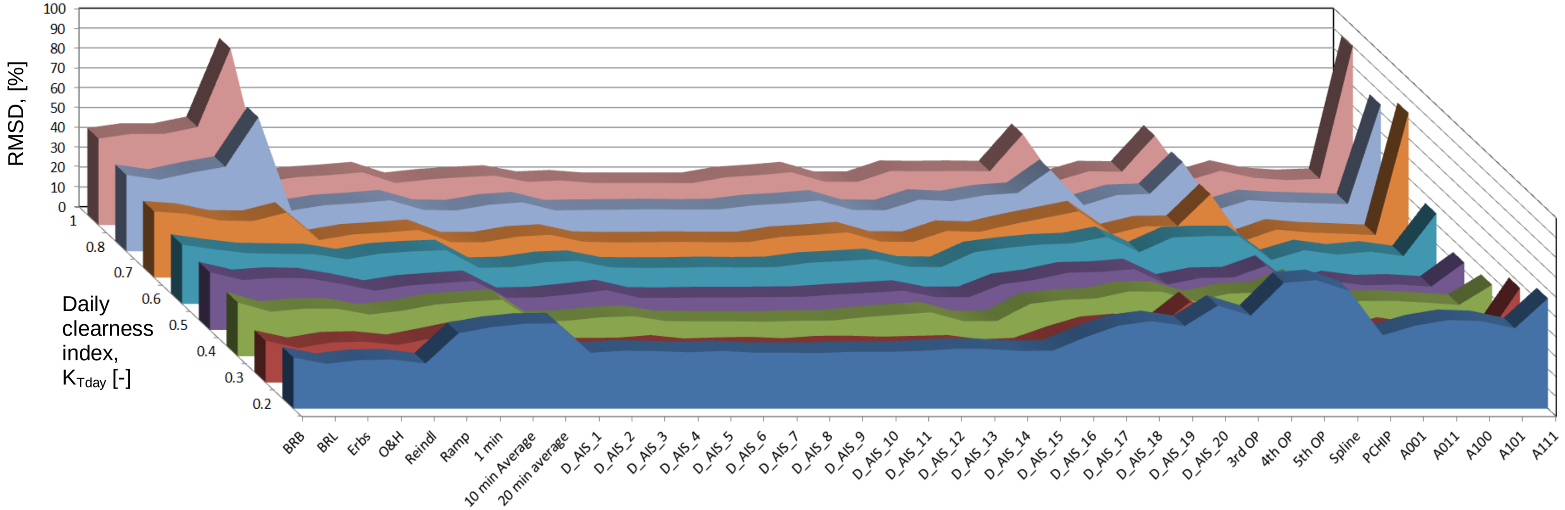

Figure E-1: Percentage root mean square difference of DHI interpolation schemes across all eight clearness index bins (dataset #1).

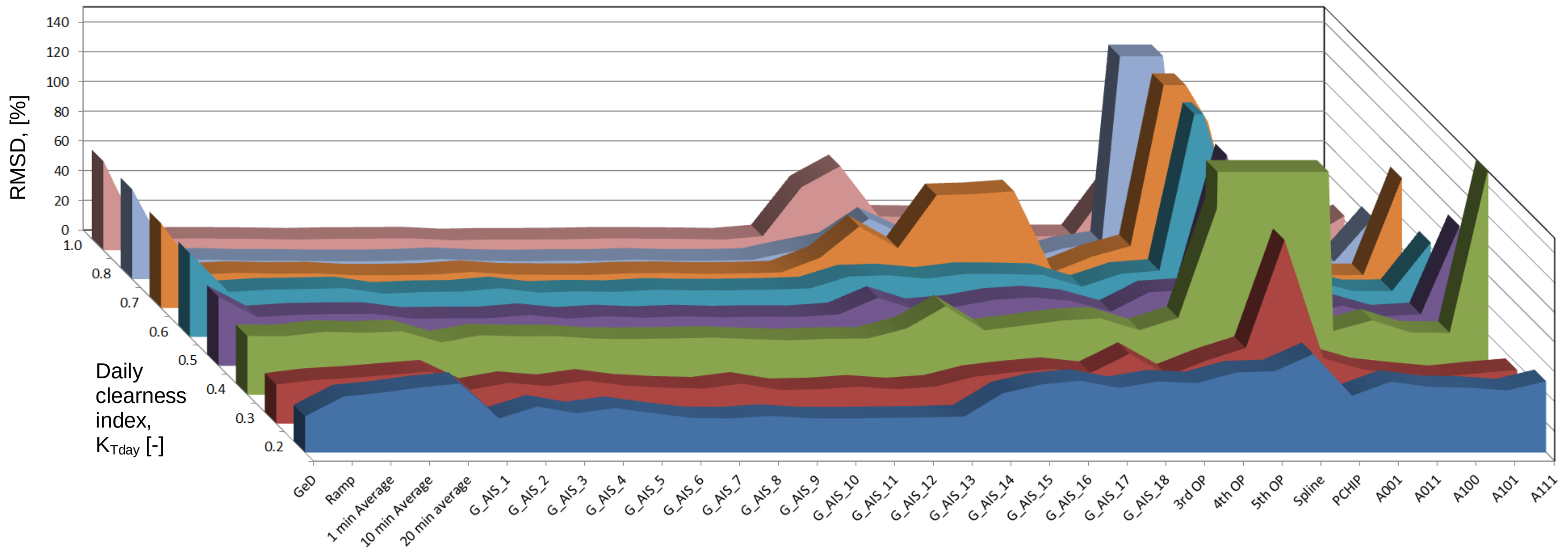

Figure E-2: Percentage root mean square difference of GHI interpolation schemes across all eight clearness index bins (dataset #1).

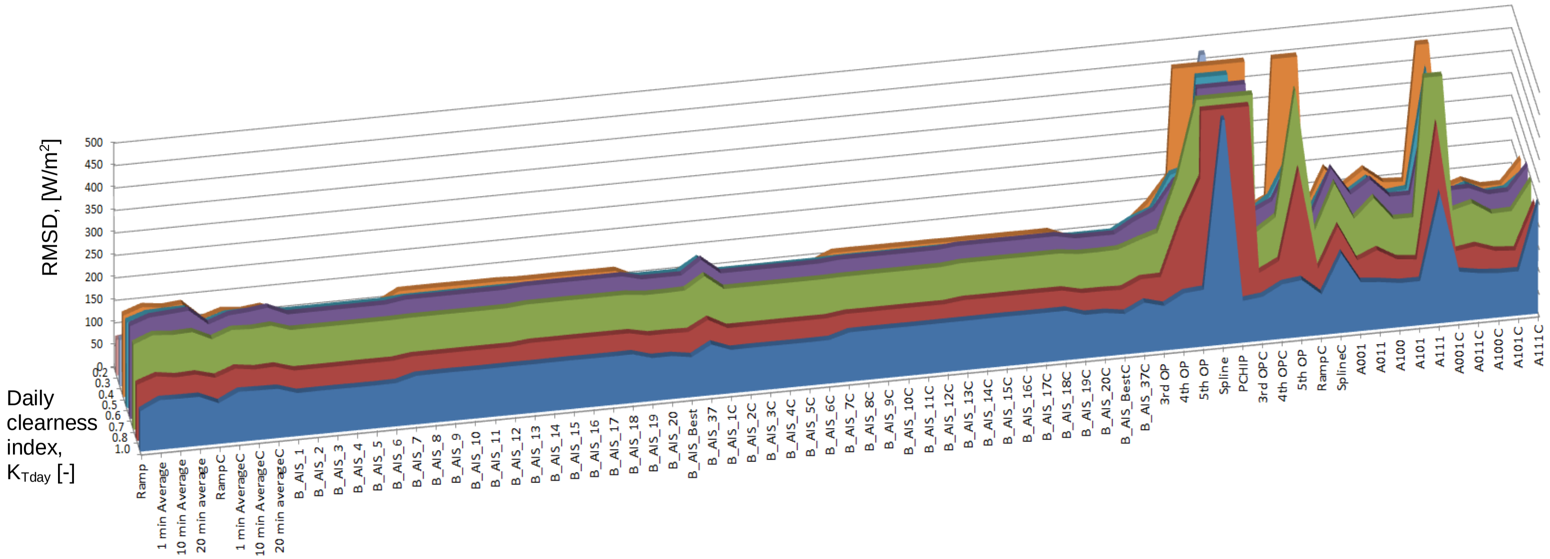

Figure E-3: Root mean square difference of DNI interpolation schemes across all eight clearness index bins in dataset #1 (bin 1 at rear).

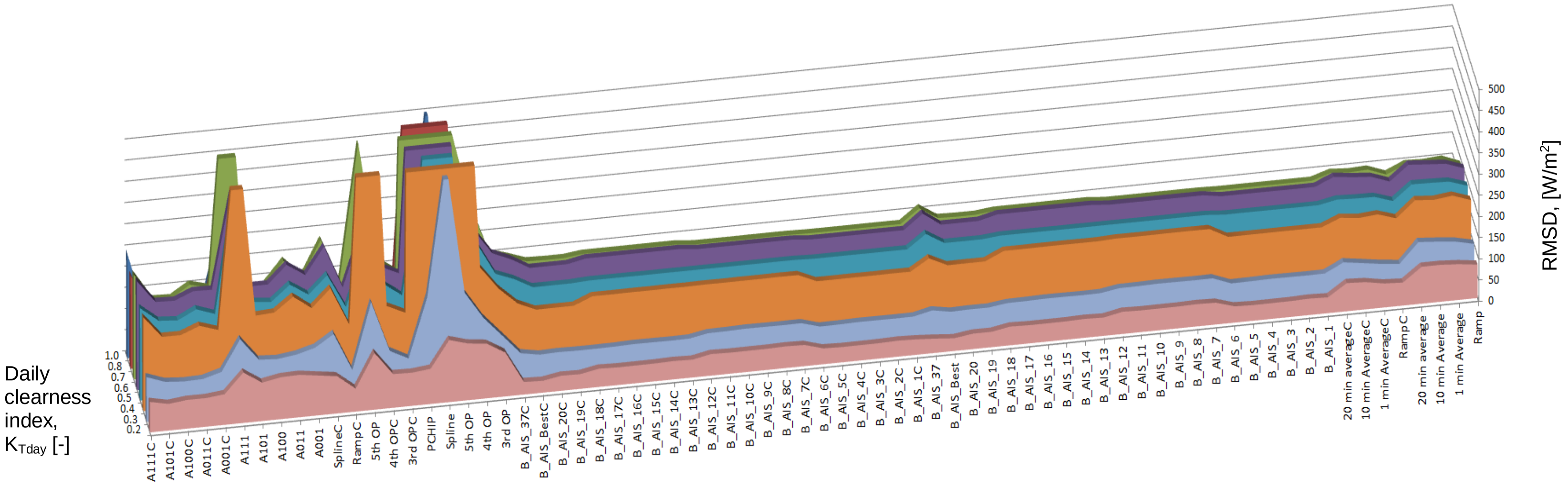

Figure E-4: Root mean square difference of DNI interpolation schemes across all eight clearness index bins in dataset #1 (bin 1 at front).